HAL
open science

Spin dynamics and structural modifications of Co2MnSi Heusler alloys by helium ions irradiation

Iman Abdallah

To cite this version:

Iman Abdallah. Spin dynamics and structural modifications of Co2MnSi Heusler alloys by helium ions irradiation. Physics [physics]. Université Paul Sabatier - Toulouse III, 2016. English. NNT : 2016TOU30079 . tel-02073985v3

HAL Id: tel-02073985

https://theses.hal.science/tel-02073985v3

Submitted on 16 Dec 2016

HAL is a multi-disciplinary open access archive for the deposit and dissemination of scientific research documents, whether they are published or not. The documents may come from teaching and research institutions in France or abroad, or from public or private research centers.

L'archive ouverte pluridisciplinaire **HAL**, est destinée au dépôt et à la diffusion de documents scientifiques de niveau recherche, publiés ou non, émanant des établissements d'enseignement et de recherche français ou étrangers, des laboratoires publics ou privés.

Université Fédérale
Toulouse Midi-Pyrénées

THÈSE

En vue de l'obtention du

DOCTORAT DE L'UNIVERSITÉ DE TOULOUSE

Délivré par :

Université Toulouse 3 Paul Sabatier (UT3 Paul Sabatier)

Présentée et soutenue par :
Iman ABDALLAH
le lundi 23 mai 2016

Titre :

Spin dynamics and structural modifications of Co2MnSi Heusler alloys by Helium ions irradiation

---

École doctorale et discipline ou spécialité :
ED SDM : Physique - COR 02

Unité de recherche :
CEMES-CNRS

Directeur/trice(s) de Thèse :
Nicolas BIZIERE
Etienne SNOECK

Jury :

Philippe LECOEUR Rapporteur IEF Orsay
Matthieu BAILLEUL Rapporteur IPCMS Strasbourg
Marc RESPAUD Examinateur LPCNO-INSA Toulouse
Pascale BAYLE-GUILLEMAUD Examinatrice INAC-CEA Grenoble
Gérard BENASSAYAG Invité CEMES-CNRS Toulouse

Acknowledgments

Here comes the moment to thank the people who devoted their time and knowledge for this work to be completed and published. After tremendous hard work and continues effort, this is the fruit of the three past years. I am thankful to my thesis directors Nicolas BIZEIRE and Etienne SNOECK for endorsing me to achieve this work.

First I thank the members of the jury for reviewing and commenting on my manuscript and giving me this opportunity to publish this work. I want to thank the rapporteurs Dr. Philippe LECOUER from IEF in Orsay and Dr. Matthieu BAILLEUL from IPCMS in Strasbourg for their comments and positive evaluations. I thank as well Dr. Marc RESPAUD, the president of the jury, from INSA in Toulouse and Dr. Pascale BAYLE-GAUILLEMAUD from INAC-CEA in Grenoble for their fruitful comments on the manuscript.

I want to express my gratitude to my advisor Nicolas Biziere for his continues support, coordination and friendly encouragement during the past three years to achieve this work. Thank you for offering me this opportunity to work on this diverse subject. Thank you for putting me on the right tracks and for all the professional and social discussions we had. I thank as well Etienne Snoeck for his coordination and immense help in the microscopy part.

I want as well to thank many researchers whom without this work wasn't possible to be completed. Thank you Gerard BENASSAYAG for all the discussions, simulations and massive help in the ion irradiation part. Thank you for being a part of this work. I thank a well Beatrice PECASSOU for the ion irradiation experiments. I would like also to thank Jean-Francois BOBO for his mentoring and guidance to use the sputtering machine. I want to thank Nicolas RATEL-RAMOND and Alexandre ARNOULT for X-ray Diffraction experiments and their tremendous help to achieve the results we wanted. I last want to thank both César Magen from for the STEM experiments at LMA-INA, Zaragoza-Spain and my friend Luis Alfredo RODRIGUEZ for the Lorentz microscopy experiments done at CEMES.

Family and friends, without your support and courage during the whole period of stay in France from the beginning of the journey in Strasbourg to its end in Toulouse, I couldn't make it without you. From a personal perspective, I need to thank the people who I am with became a better person. My parents, Sobhi and Zeinab, I am grateful for what you have raised me to become a better person in this world no matter what difficulties someone may encounter in life. My two brothers Salam and Ali and their lovely families, my lovely sister Ahlam and her family, thank you for all the encouragement and support throughout the years. Ahmad, Mariam, Hadi and Karam, this thesis is dedicated for you my beloved ones.

Special thanks go to my friends from CEMES and IPCMS in Strasbourg. Thank you for the support and for being a part in my life. I want to thank in person, Fatima Ibrahim, Ali HALLAL, Mohammad HAIDAR, Ferdaous BEN ROMDHANE, Ahmed MAGHRAOUI, Wasim JABER, Rania NOUREDDINE, Batoul SROUR, Imane Malass, Luis Alfredo RODREGEUZ, David REYES, Thibaud DENNEULIN, Marion CASTIELA, XIAOXIAO FU and all my friends and colleagues I have met. At the end I wish all the luck to Ines ABID, Barthelemy PRADINS and Thomas GARANDEL in their last year of PhD.

Iman ABDALLAH,

Toulouse, the 23rd of May 2016.

Table of contents

Introduction **4**

Chapter 1: Heusler alloys *State of the Art* **7**

1.1 Crystalline structure of Co-based Heusler alloys 8

1.2 Half-metallic behavior 10

1.3 Magnetic behavior 12
1.3.1 Origin of magnetism in Heusler alloys 12
1.3.2 Curie temperature 14

1.4 Several effects on half-metallicity and magnetic behavior of Heusler alloys. 15
1.4.1 Effect of atomic disorder 15
1.4.2 Effect of surface and interface 16

1.5 Ion irradiation/implantation 18

1.6 Applications of Heusler alloys 19

1.7 Choice of Co_2MnSi Heusler compound 20
1.7.1 Saturation Magnetization 20
1.7.2 Magneto-crystalline anisotropy constant 21
1.7.3 Exchange constant 21
1.7.4 Magnetic damping factor 21

Chapter 1 References: 23

Chapter 2: Magnetization Dynamics **29**

2.1 Basics of Magnetism 29

2.2 Micro-magnetic energy terms of ferromagnetic thin films 32
2.2.1 Zeeman Energy 32
2.2.2 Exchange energy 32
2.2.3 Demagnetization energy 34
2.2.4 magneto-crystalline Anisotropy energy 34

2.3 Magnetization dynamics 37
2.3.1 Equation of motion LLG and its solution 37
2.3.2 Ferromagnetic resonance in thin films 41

2.4 Spin waves 44
2.4.1 Magnetostatic regime 45
2.4.1.1 Magnetostatic modes 45
2.4.2 Spin waves in the exchange regime 49
2.4.2.1 Standing Spin waves (SSW) 50

2.5 Magnetization relaxation mechanism 51
2.5.1 Intrinsic relaxation processes 52
2.5.2 Extrinsic relaxation processes 55

Chapter 2 References: 58

Chapter 3: Experimental techniques 61

3.1 Deposition Techniques 61
3.1.1 Sputtering 62
3.1.1.1 Presentation of PLASSYS sputtering chamber 64

3.2 CMS Thin film deposition procedure 65

3.3 Structural characterization techniques 66
3.3.1 Basics of crystallography diffraction 67
3.3.2 Reflection High Energy Electron Diffraction (RHEED) 68
3.3.3 X-ray Diffraction (XRD) 69
3.3.4 Transmission Electron Microscopy (TEM) 72
3.3.4.1 High Resolution Electron Microscopy (HRTEM): 75
3.3.4.2 Scanning Transmission Electron Microscopy (STEM): 77
3.3.4.3 Geometric Phase Analysis (GPA): 78
3.3.4.4 Lorentz Microscopy (LM): 79

3.4 Magnetic characterization techniques 84
3.4.1 Physical Property Measurement System (PPMS) 84
3.4.2 Magneto-Optical Kerr Effect (MOKE) 84
3.4.3 Ferromagnetic Resonance (FMR) 86
3.4.3.1 FMR Experimental set-up 87

3.5 Ion irradiation/implantation technique 91
3.5.1 Ion-Solid interaction 92

Chapter 3 References: 93

Chapter 4: Structural and magnetic properties of as deposited CMS samples 95

4.1 Structural properties of CMS samples 96
4.1.1 Determination of deposition conditions 96
4.1.2 Atomic disorder by X-ray Diffraction 98
4.1.3 Structural investigation by HRTEM and HAADF-STEM 107

4.2 Magnetic properties 114
4.2.1 MOKE measurements: switching field mechanisms 114
4.2.2 Domain walls observation by Lorentz microscopy 124
4.2.3 FMR Dynamic properties measurements 125
4.2.3.1 Extraction of magnetic parameters 126
4.2.3.2 Study of dynamic relaxation: anisotropic damping 138

4.3 Conclusion 146

Chapter 4 References: 148

Chapter 5: Effect of He^+ ions irradiation on structural and magnetic properties of CMS Heusler alloys 150

5.1 Irradiation with Helium ions (He^+) at 150 keV 151
5.1.1 Simulation of Co_2MnSi irradiation with He^+ ions 151

5.2 Induced atomic disorder by X-ray diffraction and STEM 153

5.3 Modifications of magnetic properties by He^+ ions irradiation 161

5.3.1 Static magnetic properties 161

5.3.2 FMR measurements of irradiated samples: effect of irradiation on magnetic parameters 163

5.3.3 Effect of He^+ irradiation on the Gilbert Damping 176

Chapter 5 References: 187

Conclusion and Perspective 189

Introduction

Spintronic, which involve electron's spin for data storage and processing, has emerged from the discovery of *Giant magnetoresistance* (GMR) by A. Fert and P. Grunberg in 1988 [1 Baibich, 2 Binasch] few years after the prediction of *Tunneling magnetoresistance* (TMR) by M. Julliere in 1975 [3 Julliere, 4 Miyazaki, 5 Moodera]. This discovery, rewarded by a Nobel Prize in 2007, has revolutionized the field of sensor devices, allowing for very weak magnetic field detection. The highest TMR reached today at room temperature is 604% by suppression of Ta diffusion on CoFeB/MgO/CoFeB [6 Ikeda]. Among the numerous applications of magneto-resistive effects, one of the most famous is the development of Magnetic Random Access Memories (MRAM) for data storage and processing, developed in the 2000's. Another very active topic in spintronics deals with the spin transfer torque (STT) effect [7 Slonczewski, 8 Berger] which relates the effect of a spin polarized current upon the magnetization of a nanostructure. Indeed, for sufficiently high current density, one can switch the magnetization of a nanomagnet or induce its precession in the GHz or THz range. Similarly to magneto-resistive effects, STT is now the basis of numbers of devices such as ST-MRAM or microwave devices.

The basic mechanism of GMR and TMR relies on the spin polarization, *i.e.* the difference between majority and minority spins at the fermi level, of the material. STT effect also depends on spin polarization but also on the dynamic damping coefficient which opposes the STT. Indeed, the current density to switch the magnetization of a nanomagnet is proportional to the Gilbert damping constant and inversely proportional to the spin polarization. Therefore there is today an intense research to find materials with both high spin polarization and low damping coefficient. In this research field, one promising route concerns Heusler alloys which are predicted to be half metals, meaning theoretically 100% spin polarization, with a weak Gilbert damping coefficient below 10^{-3}, about one order of magnitude below the usual ferromagnetic material used in microelectronic.

After the discovery of Heusler alloys by F. Heusler [9 Heusler], half metallicity proof of NiMnSb half-Heusler compound was reported by *de Groot et al.* [10 de Groot] leading to a great interest in investigating different kinds of Heusler alloys. Nowadays, the improvement of structural and magnetic properties of Heusler alloys has become a major topic in spintronics.

In this work we offer to study the correlations between the structural and magnetic properties of the particular Co_2MnSi Heusler alloy. The interests for this material are multiple. First it is predicted to be half metallic when ordered in the $L2_1$ or B2 crystal phases. Also, it has been predicted to show very low damping coefficient down to $6x10^{-4}$ which is about one order of magnitude lower than the usual ferromagnetic materials. Its high Curie temperature up to 800° K provides stability for devices working at room temperature. Last, the deposition conditions of this alloy are compatible with microelectronics processes. Therefore it shows multiple advantages for the development of new generation of spintronic devices.

To achieve our goal, we study the evolution of the static and dynamic magnetic parameters of the Co_2MnSi when submitted to He^+ ion irradiation at 150 KeV. Ion irradiation is a particular efficient method to control and/or modify the structure of magnetic alloys. For

example, the improvement of long range $L1_0$ order of FePt and FePd alloys was demonstrated by ion irradiation in the early 2000's. More recently, Gaier *et al.* [11 Gaier] showed in 2009 that He^+ ion irradiation improves the long range B2 order in Co_2MnSi. Our work is an extension of the one of Gaier. Our initial objectives are twofold. The first is to study the possibility to use ion irradiation to enhance the structural order and magnetic properties of the Co_2MnSi, even in the most ordered $L2_1$ phase, and to decrease the microwave losses in the Gigahertz range. The second objective is more fundamental as it consists in studying the intrinsic and extrinsic contributions of the dynamic relaxation as a function of the atomic order. Our goal is to get a better understanding of the intrinsic mechanisms controlling the magnetic dynamic relaxation.

To reach these different objectives, we combined several experimental techniques. We grow Co_2MnSi Heusler alloys by magnetron sputtering on MgO substrates. These samples are then irradiated with light He^+ ions. The structural properties of the samples are studied by X-ray diffraction, in normal and anomalous conditions, and with Transmission Electron Microscopy (TEM) techniques, in particular HAADF-STEM imaging mode. This part of our study has been realized in collaboration with the LAAS-CNRS Laboratory in Toulouse and with the INA-ARAID laboratory at the University of Zaragoza (Spain). The evolution of the static and dynamic magnetic properties of the samples has been measured by means of Magneto Optic Kerr Effect (MOKE), Physical Properties Measurements System (PPMS) at the LPCNO laboratory in Toulouse and Ferromagnetic Resonance (FMR). The FMR set-up has been developed at the CEMES during this PhD.

The manuscript is organized as follow:

- In chapter 1 we give an overview of the state of the art about full X_2YZ Heusler alloys and in particular the structural and magnetic behavior of Co_2MnSi. In this chapter, we also include some features affecting the half metallicity as well as the magnetic behavior. In particular a review of the effect of atomic disorder and deposition conditions on the magnetic properties is addressed.

- In chapter 2 we present some basics of magnetism starting with the micromagnetic energy terms involved in the understanding of the static and magnetic behavior of ferromagnetic films. Then magnetization dynamics is presented and spin waves concept is introduced. At the end of this chapter, we introduce the concept of intrinsic and extrinsic dynamic relaxation mechanisms.

- The chapter 3 presents the different experimental techniques that we used in this work for the deposition of thin films and irradiation processes as well as experimental methods for structural and magnetic characterization of the thin films.

- In chapter 4, we present the structural and magnetic properties of 3 different series of CMS samples, showing different initial structural and magnetic properties. In this chapter we address the problem of the determination of the static and magnetic parameters due to the observed atomic disorder.

- The chapter 5 is devoted to the study of the effect of He^+ ion irradiation on the three series of samples. We will show how the irradiation modifies both the mechanical strain in the material as well as the chemical arrangement. Then the effect of these structural modifications on the magnetic properties will be addressed, with a highlight on the variation of the crystal anisotropy in the samples. In the final part of this chapter, preliminary results on the effect of atomic disorder on the evolution of the intrinsic and extrinsic dynamic relaxation parameters will be presented. We will show that the B2 and $L2_1$ orders shows different evolution under irradiation, leading to different behavior of their magnetic properties.

References:

[1] M. N. Baibich, J. M. Broto, A. Fert, F. N. Van Dau, F. Petroff, P. Etienne, G. Creuzet, A. Friederich, et J. Chazelas, « Giant magnetoresistance of (001) Fe/(001) Cr magnetic superlattices », *Phys. Rev. Lett.*, vol. 61, nº 21, p. 2472, 1988.

[2] G. Binasch, P. Grünberg, F. Saurenbach, et W. Zinn, « Enhanced magnetoresistance in layered magnetic structures with antiferromagnetic interlayer exchange », *Phys. Rev. B*, vol. 39, nº 7, p. 4828, 1989.

[3] M. Julliere, « Tunneling between ferromagnetic films », *Phys. Lett. A*, vol. 54, nº 3, p. 225‑226, sept. 1975.

[4] T. Miyazaki et N. Tezuka, « Giant magnetic tunneling effect in Fe/Al2O3/Fe junction », *J. Magn. Magn. Mater.*, vol. 139, nº 3, p. L231‑L234, janv. 1995.

[5] J. S. Moodera, L. R. Kinder, T. M. Wong, et R. Meservey, « Large magnetoresistance at room temperature in ferromagnetic thin film tunnel junctions », *Phys. Rev. Lett.*, vol. 74, nº 16, p. 3273, 1995.

[6] S. Ikeda, J. Hayakawa, Y. Ashizawa, Y. M. Lee, K. Miura, H. Hasegawa, M. Tsunoda, F. Matsukura, et H. Ohno, « Tunnel magnetoresistance of 604% at 300K by suppression of Ta diffusion in CoFeB/MgO/CoFeB pseudo-spin-valves annealed at high temperature », *Appl. Phys. Lett.*, vol. 93, nº 8, p. 082508, août 2008.

[7] « J. Slonczewski, Journal of Magnetism and Magnetic Materials, vol. 159, page L1 (1996) ».

[8] L. Berger, « A simple theory of spin-wave relaxation in ferromagnetic metals », *J. Phys. Chem. Solids*, vol. 38, nº 12, p. 1321‑1326, janv. 1977.

[9] F. Heusler, W. Starck, and E. Haupt, Verh. DPG 5, 220 (1903) .

[10] R. A. De Groot, F. M. Mueller, P. G. Van Engen, et K. H. J. Buschow, « New class of materials: half-metallic ferromagnets », *Phys. Rev. Lett.*, vol. 50, nº 25, p. 2024–2027, 1983.

[11] O. Gaier, « A study of exchange interaction, magnetic anisotropies, and ion beam induced effects in thin films of Co2-based Heusler compounds », Ph. D. dissertation, Technical University of Kaiserslautern, 2009.

Chapter 1: Heusler alloys
State of the Art

In 1903 F. Heusler has discovered a new class of intermetallic materials that exhibit a ferromagnetic order although none of its constituent elements are magnetic in Cu_2MnAl alloy [1 Heusler]. These alloys are ternary compounds and divided into two categories, *Half Heusler* (XYZ) and *Full Heusler* alloys (X_2YZ) where, X, Y are transition metals elements and Z belong to *sp* elements group (Table 1.1).

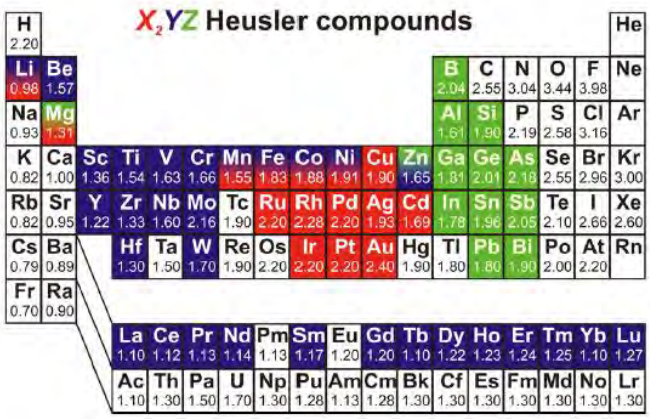

Table 1.1: periodic table of elements showing the different species of Heusler alloys. Adapted from [2 Graf]

Enormous investigations were conducted to study Heusler alloys for spintronic applications, in the last two decades, due to two main magnetic properties. The first one is the half metallic behavior which means that the material behaves as an insulator or a semiconductor for one spin orientation and as a metal for another orientation. The other important property, which is of particular interest in this thesis manuscript, is the low Gilbert damping coefficient that is predicted to be below 10^{-3}. The mentioned properties were first investigated by *ab-intio* calculations [3 de Groot]. De Groot *et al.* have shown the half metallic behavior in NiMnSb Heusler compounds; this discovery led to a great interest in studying Heusler alloys. Since then, different atomic combinations have been tested as for example Co-based Heusler compounds. During the last 10 years, experimental work focused on the growth quality and the different magnetic properties of Heusler alloys.

The advantages of Heusler alloys are their electronic, magnetic and magneto-optical properties along with high thermal stability. Half Heusler alloys gained a lot of interest in the thermoelectric and solar applications [4 Bartholomé]. On the other hand, full Heusler alloys were specially investigated in spintronic applications. Examples on some applications of half and full Heusler alloys are given at the end of this chapter. In this work we focus on

the magnetic properties and especially the dynamic properties, of Co_2MnSi which is predicted to be half metallic with a very low damping ≈ 0.6 x 10^{-4} [5 Liu]. Moreover, its high Curie temperature (around 980 K) [6 Webster] makes it compatible with micro-electronic processes and promotes it as a promising candidate for spintronic devices.

In this chapter, we will present the general structural and magnetic properties of Heusler alloys, with a particular insight on Co-based Heusler compounds. Half metallicity and magnetic behavior will be presented. Then, we will present the influence of structural ordering on the magnetic properties and the half metallicity. The discussion about the damping will be presented in chapter 2. Then, the effect of ion irradiation on the Heusler alloys properties will be addressed and some examples of industrial applications with half and full Heusler alloys will be given. Finally, we give a summary of the reported values in literature for several magnetic parameters of the particular Co_2MnSi Heusler alloy which is the topic of our work.

1.1 Crystalline structure of Co-based Heusler alloys

Full Heusler alloys of general composition Co_2YZ preferably crystallize in $L2_1$ structure (space group $Fm\bar{3}m$). The cubic unit cell is made up of four interpenetrating FCC sublattices and atoms are placed following Wyckoff positions. Co atoms are placed at (1/4, 1/4, 1/4) position of the unit cell, Y and Z atoms are placed at (0, 0, 0) and (1/2, 1/2, 1/2) respectively, as shown in (Fig.1.1-a). $L2_1$ phase is the most ordered phase of Heusler alloys. If the atoms are misplaced or occupied randomly in the unit cell, the ordered phase is no longer valid. Heusler alloys also exist in three other crystalline phases, the partially disorder B2 and $D0_3$ phases, and the completely disordered A_2 phase. The B2 phase is formed by a random distribution of the Y and Z atoms positions in the unit cell but keeping Co atoms at their initial positions (Fig.1.1-b). The interchange of Co and Y atoms in the unit cell results in a formation of $D0_3$ structure (Figure 1.1-c). The completely disordered phase A_2 is formed when all atoms are randomly occupied in the unit cell (Fig.1.1-c) [7 Bacon and Plant, 6 Webster, 8 Trudel]. In our work we focused on the Co_2MnSi alloy which preferentially grows in the $L2_1$ order. However, it is important to note that it can grow into the chemically disordered B2 and (A2) structures depending on the deposition conditions.

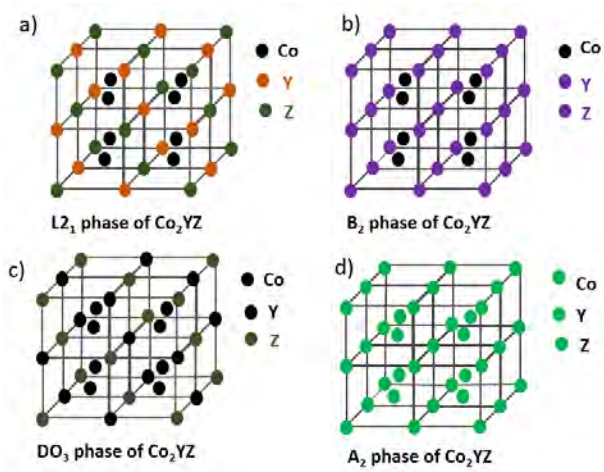

Figure 1.1: schematic presentation of Co_2YZ crystalline structure: a) $L2_1$, b) B2, c) $D0_3$ and A2 phases.

The stability of $L2_1$ crystal order in Heusler alloy depends on the elements occupying X, Y and Z. Kobayashi *et al.* showed that the B2/ $L2_1$ transition temperature for the Co_2YGa (Y=Ti, V, Cr) alloys monotonically decreases with increasing electron concentration of the Y site, whereas the transition temperature is almost constant at 1100±100 K for (Y=Mn, Fe) [9 Kobayashi]. This behavior may be related to the interaction between Y atoms and Ga.

Also, Z atoms can affect the ordering structure of Co based Heusler alloys, for example, Co_2MnSi and Co_2MnAl tend to crystallize in the $L2_1$ and B_2 order respectively and this is due to different bonding energy between Si or Al atoms and the transition metals [10 kandpal]. The nature of the Z atom has also an influence on the lattice parameter of Co based Heusler alloys. As an example ,table 1.2 presents the different lattice parameters for Co2MnZ alloys that ranges from 5.6 to 5.7 [6 Webster, 11 Elmers, 12 Wurmehl].

Heusler compounds	Lattice parameter ***a*** ($\dot{A}$)	Crystalline structure	Curie temperature (K°)
Co_2MnSi	5.654 [6 Webster]	$L2_1$	985 [6 Webster,13 Brown]
Co_2MnAl	5.756 [6 Webster]	B2	693 [6 Webster,14 Bushow]
Co_2MnGe	5.743 [6 Webster]	$L2_1$	905 [6 Webster, 14 Bushow]
Co_2FeAl	5.730 [10 Kandpal]	B2	1000 [14 Bushow]
Co_2FeSi	5.640 [12 Wurmel]	$L2_1$	1100 [12 Wurmel]

Table 1.2: crystalline structure and lattice parameters of some Co based Heusler alloys.

The structural properties of Co based Heusler alloy are very sensitive to the deposition condition and especially on the nature of the substrate in order to minimize lattice mismatch defined as: $\frac{a_{deposited\ film}-a_{substrate}}{a_{substrate}}$.

In literature, different substrates have been used to grow Co-based Heusler alloys like Ge (001) [15 Li], n-type Ge (111) [16 Nahid], GaAs and MgO (001). One of the major interest of using MgO substrate is for Magnetic tunnel junctions (MTJs) applications, while GaAs substrates allow for spin injection in semiconductor applications. GaAs has a lattice parameter of 5.65 Å while that of MgO is 4.21 Å (Figure 1.2). This leads to a better lattice mismatch for GaAs where the Co based Heusler alloys grow cube on cube. For MgO, epitaxial growth is achieved via a 45° rotation of the CMS axis with respect to MgO <100> direction. The lattice mismatch of Co_2MnSi on MgO is ≈ - 5.1% (Figure 1.2-a).

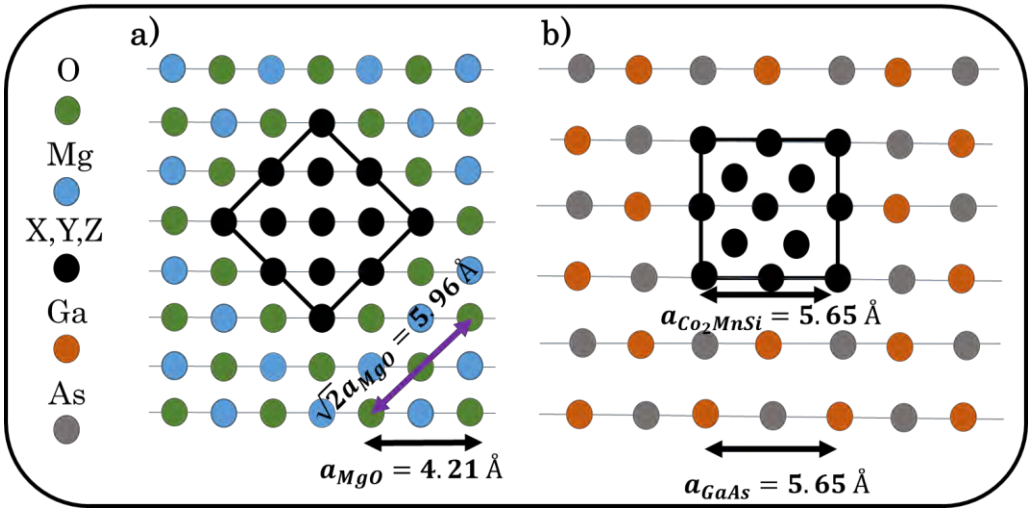

Figure 1.2: schematic presentation of the epitaxial growth of Co_2MnSi on a) MgO and b) GaAs.

Many groups have introduced Cr as a seed layer between the substrate and the deposited Heusler films [17 Ortiz, 18 Gaier, 8 Trudel]. The use of seed layers [19 Magen] and a single crystalline substrate [20 Garcia], improves the crystalline quality of the deposited thin film. For example, with the Cr seed layer, the lattice mismatch between the Cr/MgO and for Co_2MnSi/Cr is reduced to -2.4 % and -2.6 % respectively. Cr deposition is useful to reduce the strain at the interfaces and therefore enhance the magnetic properties of Co_2MnSi compared to films deposited directly on MgO substrates [17 Ortiz].

In the next section, we provide more details about the effects of surface termination and interface on the half metallicity and magnetic properties of Co-based Heusler compounds with a particular focus on Co_2MnSi which is the material studied in the framework of this thesis.

1.2 Half-metallic behavior

As mentioned before, high spin polarization at the Fermi energy is crucial to realize efficient TMR-based spintronic devices. Half metallic materials match this criteria. Several materials are known to be half metallic such as Cr oxides, magnetite Fe_3O_4, manganite ($La_{0.7}Se_{0.3}MnO_3$) [21 Soulen], the double perovskites (Sr_2FeReO_6) [22 Kato] and the pyrites (CoS_2) [23 Shishido]. Besides these materials, Heusler alloys attracted a lot of interest for being half metallic. In this section, origin of band gap and some effects on half metallicity are discussed.

Half-metallic materials exhibit a unique band structure. For one spin channel they are metallic while for the other they are semiconductors or insulators due to the gap in the density of states (DOS) at the Fermi energy level (Figure 1.3). This leads to a 100% spin polarization $\boldsymbol{P}$ of the conduction spin channel.

$$\boldsymbol{P} = \frac{D\uparrow(E_f) - D\downarrow(E_f)}{D\uparrow(E_f) + D\downarrow(E_f)}$$

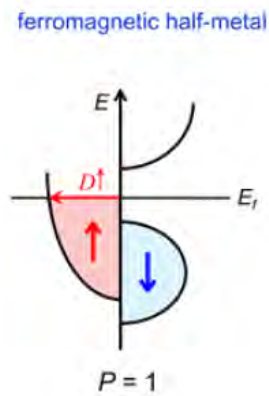

Figure 1.3: schematic presentation of the DOS of half metallic ferromagnetic, P=1 from electron's spin polarization at the Fermi level. Adapted from [24]

The half metallic behavior of Heusler alloys were first predicted by spin-dependent band structure ab-initio calculations of NiMnSb and PtMnSb by de Groot *et al*. [3 de Groot]. After this discovery, many Co-based Heusler alloys were theoretically predicted to be half-metallic. As an example, Figure 1.4 shows the total Density of States (DOS) for different Co_2MnZ alloys. It is clearly visible that no states at the fermi level are available for minority spin except for Z = Ga for which the DOS is not zero at Fermi energy.

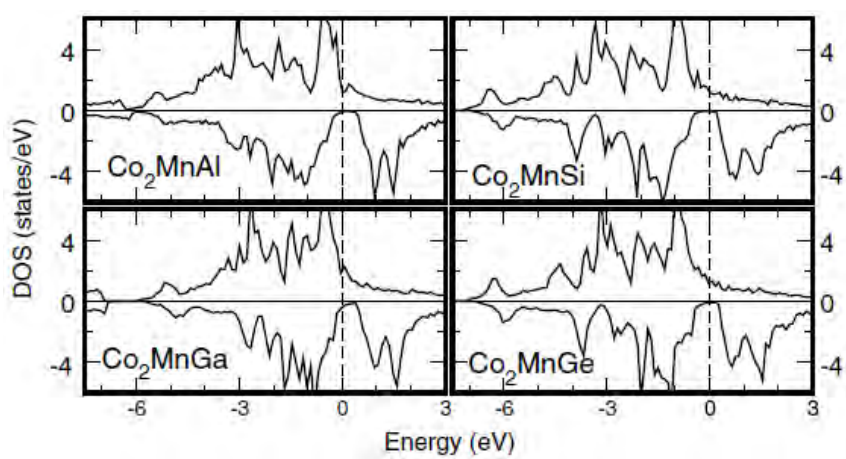

Figure 1.4: Spin resolved DOS for Co_2MnZ compounds with Z=Al,Ga,Si and Ge. Taken from [25 Galanakis].

The origin of the band gap for minority spins in these alloys have been studied in details by Galanakis in 2002 [25 Galanakis]. The starting point is the hybridization between Co-Co *d*-states and the Mn *d*-orbitals. The hybridization between Co-Co *d*-states is schematized in Figure 1.5-a leading to bonding (eg, t_{2g}) and antibonding (eu, t_{1u}) orbitals. Let's note that this mechanism is strongly dependent on the distance between the two Co atoms. Then these degenerated orbitals couple with the *d* states of the Mn atoms (Figure 1.5-b) to create bonding and antibonding orbitals below and above the fermi level. It is noteworthy that only minority spins are represented here. However for majority spins, the exchange

energy decreases the energy of the majority *d* spin states of Mn atoms which couple with the Co *d* states and avoid the energy gap.

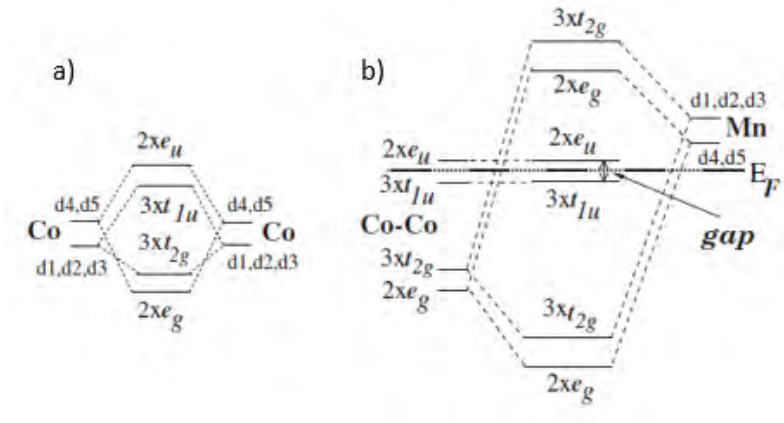

Figure 1.5: schematic presentation of the origin of band gap in Heusler alloys [26 Galanakis]. a) Hybridization between Co-Co atoms and b) with the Mn states. d1, d2 and d3 indicates $d_{x,y}$, d_{yx} and d_{zx} t_{2g} orbitals respectively. d_4 and d_5 stands for d_{z^2} , $d_{x^2-y^2}$ e_g orbitals. The number in front of the orbitals is the degeneracy of each orbital.

The scenario proposed by Galanakis is now commonly accepted in the Heusler community. It is, however, interesting to note that in this mechanism the *sp*-elements are not responsible for the existence of the minority gap. This is due to the fact that Z atoms introduce a deep lying *s*-*p*-bands below the center of the *d*-bands [26 Galanakis]. However the *sp* element modifies the position of the fermi level by changing the total number of valence electrons as it has been shown by Galanakis *et al.* in Co_2MnZ alloys with Z being Si, Sn, Ga, Ge or Al (Figure 1.4).

1.3 Magnetic behavior

1.3.1 Origin of magnetism in Heusler alloys

Half metallic Heusler alloys exhibit an interesting magnetic behavior along with high curie temperatures. Heusler alloys can be ferromagnetic, ferrimagnetic or antiferromagnetic [27 Picket, 28 Casper]. However, the majority of Heusler alloys have a ferromagnetic behavior.

Magnetic properties of Co-based Heusler alloys will be presented with a focus on magnetic moments, anisotropy field, and exchange interaction constant in Co_2MnSi alloys. In this alloy the exchange interaction responsible for the stability of ferromagnetism originates from the Mn-Co interaction [31 Kurtulus]. We will discuss the origin of magnetic moments in Co-based Heusler alloys and compare the theoretical and experimental reported values. The interesting characteristic of Co_2MnZ Heusler alloys is that the spin magnetic moment has an integer value. Calculated magnetic moments of some Co_2MnZ Heusler alloys are summarized in Table 1.3.

The mentioned mechanism of half metallicity, discussed in Section 1.3, explains the magnetic behavior and especially the value of the magnetic moment as a function of the

valence number of electrons in Co_2MnZ alloys. Indeed, it has been demonstrated that the magnetic moment of such alloys follow a Slater Pauling rule with an integer number of μ_B per unit cell (Figure 1.6).

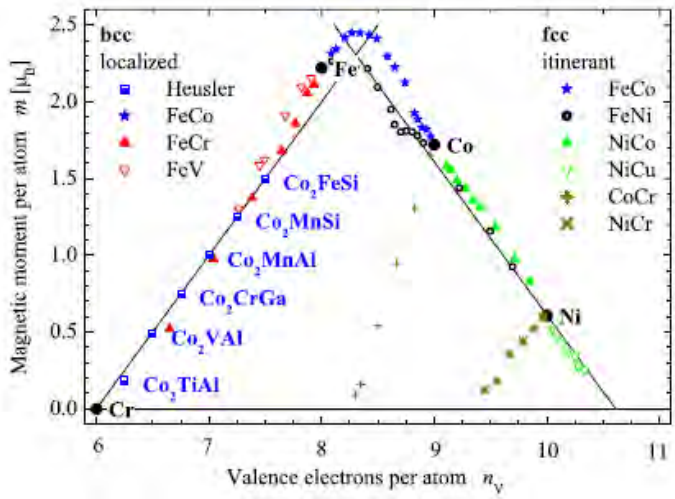

Figure 1.6: Slater–Pauling curve for 3*d* transition metals and their alloys. Experimental values for selected Co2-based Heusler compounds are given for comparison. (Note: the $A1{-}xBx$ alloys are given as AB in the legend, for short.) Image adapted from [10 kandpal]

The Slater-Pauling rule infers a linear dependence of the magnetic moment vs. the valence electron number [29 Slater and 30 Pauling]. The reason for such behavior relies on the finite number of minority spins electrons state. Within the mechanism proposed by Galanakis, the total number of minority states is 12 (2 for *s* states, 3 for *p*, 2 for eg, 3 for t_2g and 3 for t1u). Therefore, writing the total magnetic moment of the unit cell as $m = N_\uparrow - N_\downarrow$ and the total number of valence electrons as $N_v = N_\uparrow + N_\downarrow$ one gets $m = N_v - 2 * N_\downarrow$. Therefore the magnetic moment per atom is estimated by the following relation:

$$\boldsymbol{m = N_v - 24}$$

While the Slater Pauling rule of Co_2MnZ demonstrates that we have localized magnetic moments in Co based Heusler alloys, ab-initio calculations allow to get a deeper insight into the repartition of the magnetic moment on each atoms. For example, [25 Galanakis, 31 Kurtulus, 32 Fujii, 6 Webster] and many others have demonstrated that most of the magnetic moment value is carried out by Mn atoms, $\approx (3\mu_B)$, while the magnetic moment of Co atoms is about 1 μ_B. For *sp* atoms like Si, they possess a small negative moment and barely contribute to the total moment [10 Kandpal]. Then the total magnetic moment of Co_2MnSi is expected to be around 5 μ_B for a perfectly $L2_1$ crystalline structure [25 Galanakis].

$m^{spin}(\mu_B)$	Co	Mn	Z	Total theoretical
Co_2MnAl	0.768	2.530	-0.096	3.970
Co_2MnGa	0.688	2.775	-0.093	4.058
Co_2MnSi	1.021	2.971	-0.074	4.940
Co_2MnGe	0.981	3.040	-0.061	4.941
Co_2MnSn	0.920	3.203	-0.078	4.984

Table 1.3: Calculated spin magnetic moments per unit cell of some Co_2MnZ alloys. [26 Galanakis]

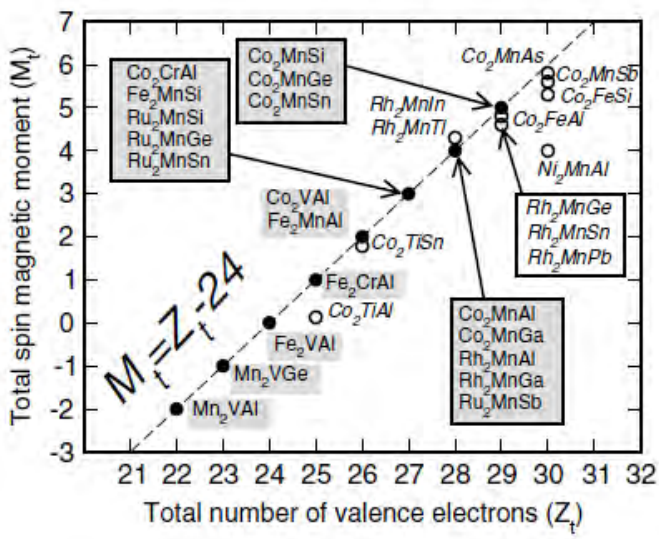

Figure 1.7: Calculated total spin moments for Heusler alloys, the dashed line represents the Slater-Pauling behavior. The open circles are deviated from the curve. Adapted from [26 Galanakis].

Figure 1.7 presents the total magnetic moment of several Heusler alloys as a function of the valence electron N_v (Z_t in Figure 1.7). The figure is divided into two regions; depending if the alloy possess a positive or negative magnetic moment. In the latter case, the spin down band (spin down) has more occupied states than the spin up band.

1.3.2 Curie temperature

The Curie temperature T_C is important for the stability of magnetic materials and for microelectronic processes. Above T_C, a ferromagnetic material becomes paramagnetic, *i.e.* the net magnetic moment is zero due to random thermal fluctuations of the magnetic moments.

Heusler compounds exhibit remarkable high curie temperatures T_C (Table 1.2). Fig 1.8-a shows a linear dependence of the Curie temperature on the valence electrons except for

N_v=27. The origin of the linear dependence between T_C and N_v is investigated by *kübler et al.* by means of ab-intio calculations [33 kübler]. Similarly, the same linear trend is viewed as a function of the magnetic moments. Figure 1.8-a and 1.8-b show the linear trend of curie temperature as a function of valence electrons and magnetic moments, respectively of Co-based Heusler alloys. The linear dependence between T_C and N_v is described by the following equation [33 Kübler]:

$$k_B T_c = \frac{2}{3}\sum_{\tau} \mathcal{L}_\tau{}^2 \left[\frac{1}{N}\sum_{qn}\frac{1}{j_n(q)}\right]^{-1}$$

Where $\mathcal{L}_\tau$ and $j_n(q)$ are the local moment ($\mathcal{L}_\tau{}^2 = s(s+1)$ or $\mathcal{L}_\tau{}^2 = M_s{}^2$) and the exchange interaction functions, respectively. T_c is determined by both the magnetic moments and the average exchange value.

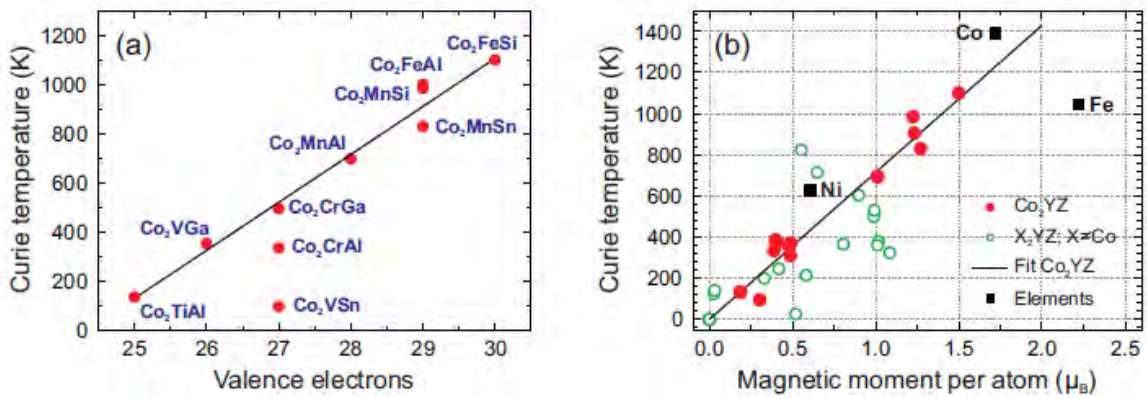

Figure 1.8: calculated curie temperatures for Co-based Heusler alloys as a function of a) valence electrons and b) magnetic moments. Adapted from [33 Kübler, 34 Fecher, 18 Gaier].

1.4 Several effects on half-metallicity and magnetic behavior of Heusler alloys.

1.4.1 Effect of atomic disorder

Theoretically, Heusler alloys are predicted to be half metals, however, experiments report a spin polarization less than 100 %. Many authors have pointed out the impact of atomic disorder on the half metallicity and magnetic properties [35 Ebert and Shcutz, 36, 37 Orgassa, 38 Picozzi].

For example, Orgassa *et al.* studied two types of atomic disorder in NiMnSb: the partial interchange between Ni and Mn atoms and vacancies. In the first case, they show that 5 % of interchange decreases the spin polarization down to 52%. In the second case, vacancies have been shown to destroy half metallicity with a spin polarization of only 24% in NiMnSb. This reduction in spin polarization is due to the appearance of disorder-induced states in the minority spin gap, resulting in narrowing the band gap and consequently a reduction of spin polarization at the fermi level [36 Orgassa] [37 Orgassa]. Therefore, for half Heusler alloys, a

suppression of antisite disorder and structural analysis is important to obtain high spin-polarization [2 Graf].

Galanakis *et al.* pointed out that the *sp* elements are not responsible of the minority gap but important for the structure stability of Heusler alloys. This is illustrated by substituting Sb in NiMnSb by Sn,In or Te that leads to the destruction of half metallicity [26 Galanakis].

For full Heusler alloys, several groups also studied the effect of atomic disorder on half metallicity in Co_2FeSi [39 Gercsi and Hono], Co_2MnGe and Co_2MnSi [38 Picozzi]. We will focus on the atomic disorder and defects effect on the half metallicity in Co_2MnSi.

Picozzi *et al.* investigated different types of defects in Co_2MnSi, such as antisites and atomic swaps in terms of energy formation and defect induced electronic and magnetic properties. They have found that Mn antisites (Co atoms being replaced by Mn) have the lowest energy formation and retain the half metallicity character, but the magnetic moment is reduced by $2\,\mu_B$. Whereas for Co antisites (Mn atoms being replaced by Co), they have a slightly higher energy formation and half metallicity is destroyed due to Co antisite *d* states and the total magnetic moment is also reduced. For both Mn-Si and Mn-Co swaps, they have high energy formation and half metallicity is unaffected but the magnetic behavior shows a reduction down to $4\,\mu_B$ for Mn-Co swap while the Mn-Si one is not affected and their values are equal to the ideal $L2_1$ phase. [40 Picozzi].

Picozzi *et al.* have also studied the effect of changing lattice parameters in Co_2MnZ (Z=Si, Ge, Sn) induced by applied pressure. The lattice constant increases as Z atomic number increases (by 1.8% substituting Ge for Si and by 3.7% substituting Sn for Ge). Thus, the volume compression leads to an increase of the minority band gap and the fermi energy is shifted from the valence band into the band gap [38 Picozzi].

1.4.2 Effect of surface and interface

The half metallicity can be lost due to the introduction of surface and interface states at the fermi level in the minority spin channel. Many theoretical investigations by Ab initio calculations were performed for half and full Heusler alloys. NiMnSb and Co_2MnSi surface and interface properties were thoroughly studied by several groups [41 Galanakis, 42 Ishida, 43 Nagao, 44 Miura, and 45 Hashemifar]. It is important to note that, experimentally, few groups have been able to study the surface and interface effects on half metallicity due to homogeneity, deposition quality conditions, and segregation of atoms to the surface during the growth of thin films [46 Ristoiu].

Galanakis studied the effect of surface termination on the properties of half (NiMnSb, CoMnSb and PtMnSb) and full Heusler (Co_2MnSi, Co_2MnGe and Co_2CrAl) alloys [41 Galanakis]. For Co terminated surfaces, a displacement in the spin down state peak near the fermi level results in a negative state polarization as shown in figure (1.9 c-d). In the case of Mn(Ge, Si or Cr) terminated surfaces, this strong peak no longer appears as shown in figure (1.9 a-b). Therefore, it is preferable to have Mn(Ge,Si,Cr) surface termination than Co ones.

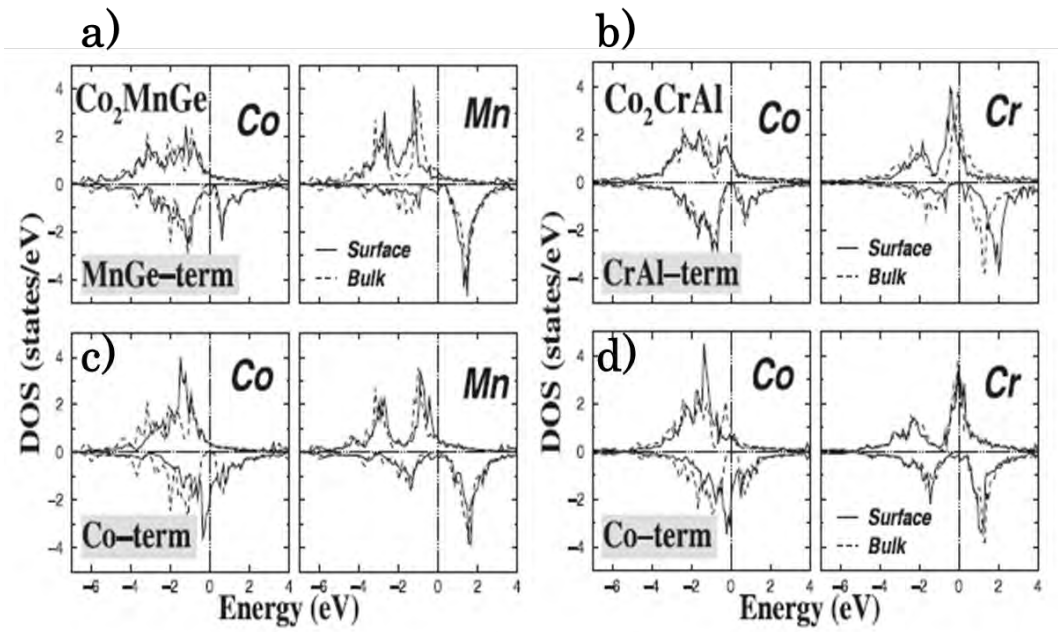

Figure 1.9: DOS of Co_2MnGe and Co_2CrAl as function of energy for different terminated surfaces [41 Galanakis].

Similarly, Ishida *et al.* have reported that, for Mn-Si surface termination, the half metallic character is preserved while it is destroyed for Co terminated surface [42 Ishida]. In their study, they considered two types of planes at the surface of (001) films, the Co and the MnSi planes. For the Co surface plane, no energy band gap is found for one of the two spin states, whereas a band gap is found for the MnSi surface plane and hence the half metallicity is preserved in this surface termination. Hashemifar *et al.* studied the stability and electronic structure for different termination surface for Co_2MnSi. They have found that the pure Mn termination preserves the half metallicity of the system [45 Hashemifar].

Besides the surface termination effects on half metallic behavior, the interface role is of particular importance for spintronic devices where the transport of spin polarized electrons and holes from one material to another is crucial. As mentioned before, GaAs and MgO are the two substrates widely used for the deposition of Co_2MnSi thin films. For Co_2MnSi/GaAs, Nagao *et al.* obtained a high spin polarization at (110) CoSi-AsGa interface and a nearly half metallic behavior is monitored [43 Nagao]. Half metallicity is lost for Mn-Si surface termination of Co_2MnSi/MgO according to Miura *et al.* [44 Miura]. These effects are related to the appearance of interface states in the half metallic gap and these states can be filled by the electrons from the minority valence band [18 Gaier].

Effect of half metallicity on gilbert damping factor

The damping behavior is of particular importance in this thesis and it is important to shed light on the relation between half metallicity and the gilbert damping factor. More details about gilbert damping will be discussed in the magnetization dynamics chapter.

In ferromagnetic materials, the Gilbert damping factor α is generally accounted to be proportional to the square of spin orbit coupling, which allows for spin flip transition. The low damping value α is closely related to the half metallicity since the spin gap for minority spins

is supposed to avoid spin-flip transition for dynamic magnetic relaxation. The lowest damping factor obtained theoretically, using extended Hückel tight binding (ETH-TB) model, for Co_2MnSi is $0.6*10^{-4}$ [5 liu] and experimentally $9*10^{-4}$ [47 Qiao]. Kubota *et al.* have studied the half metallic behavior and gilbert damping factor for $Co_2Fe_xMn_{1-x}Si$ alloys. In their work, they monitored the increase in minority DOS at the fermi level and at some point the loss of half metallic behavior which is accompanied by an increase in gilbert damping factor [48 Kubota]. The gilbert damping factor was found to vary from 0.005 for Co_2MnSi (x=0) to 0.02 for Co_2FeSi (x=1) and accompanied by a disappearance of half metallicity for $x \geq 0.8$.

1.5 Ion irradiation/implantation

In our work, we used ion irradiation to modify the structural properties of Co_2MnSi and study the effect of the structural modifications on the magnetic properties of the alloy as it will be presented in chapter 5. The purpose of this section is to give an overview of the work done on different materials by ion irradiation/implantation and its modifications on their magnetic properties. Additional details about ion irradiation technique will be given in chapter 3.

Controlling and pattering the magnetic properties of ferromagnetic materials is now a field of interest for magnonic crystal applications for example. Ion irradiation is a promising technique that can modify the magnetic behavior through direct modification of the structure of the investigated material. Irradiation can be done by either heavy or light ions depending on the mass to charge ratio of the selected ions and the energy of the accelerated ions. For example, Bonder *et al.* have reported that irradiation of Ar^+ ions at 80 KeV with doses from 10^{14} to 10^{16} ions/cm^2, is shown to cause intermixing of Co/Pt layers resulting in the magnetization switching from perpendicular to in plane direction [49 Bonder]. Structural properties modifications by light ion irradiation, for example, irradiation with He^+ ions, of an energy range of 5-150 KeV due to energy loss of ions trajectory in the solid results in magnetic patterning as well as interfacial mixing [50 Chappert, 51, 52 Devolder, and 53 Fassebender].

Ion irradiation/implantation have gained interest in studying the modifications of magnetic materials. Several groups [54 Folks, 55 Fassbender and McCord] have reported the modification of magnetic parameters upon implantation. For example, Folks *et al.* have reported the change in magnetic phase from ferromagnetic state of NiFe alloy films to a paramagnetic one by Cr ions implantation. As a result, they have patterned continuous $Ni_{80}Fe_{20}$ films into separate regions of ferromagnetic and paramagnetic behavior. Fassbender and McCord have reported a modification of static and dynamic magnetic properties in $Ni_{81}Fe_{19}$ by 30 KeV Ni implantation.

Alternatively, He^+ irradiation induces an enhancement in the chemical order of FePt and FePd thin films by increasing the long range $L1_0$ order parameter at room temperature [56 Ravelosona, 58 Bernas]. The enhancement of the chemical ordering by He^+ ions was done by Gaier *et al.* on Heusler alloys and in particular Co_2MnSi. In their study they have shown an improvement of the long range order in the B2 phase [57 Gaier]. This enhancement has been attributed to the Mn-Co and Co-Si exchanges due to mobile vacancies induced by irradiation [58 Bernas]. As discussed in this chapter, the disorder influences the structural and magnetic

properties and since Heusler alloys exhibit unique magnetic properties, tailoring them is of particular interest for technological applications.

Another aspect of ion implantation/irradiation is to control the magnetic gilbert damping coefficient. Several groups have seen an increase in gilbert damping due to ion implantation/ irradiation by Ni and Cr ions respectively [59 Obry, 60 King]. The origin for this increase relies on local modification of the chemical order in addition to modification of the local effective field. More details will be given in chapter 5 about the effect of ion irradiation on the magnetic properties of Heusler alloy Co_2MnSi.

1.6 Applications of Heusler alloys

Heusler alloys are known for their high spin polarization, and they have attracted much interest in the field of spin electronics for their potential application for tunneling magnetoresistance (TMR) and Giant magnetoresistance (GMR) devices. The half metallic materials act as a spin filter in such devices which leads to a huge magnetoresistance (MR) effect [61 Yakushiji]. Tunneling devices with high MR effect can be reached nowadays either by an engineered insulator barrier or by developing a 100 % spin polarization electrode materials. The potential candidates for the latter are ferromagnetic oxides or Heusler alloys [2 Graf]. Several groups have studied Co-based Heusler alloys as electrodes for MTJ, GMR and for spin injection from ferromagnetic materials into semiconductor. Besides technological applications, Half Heusler alloys were investigated for energy usages such as Solar cells and thermoelectric convertors. In the next two paragraphs, a brief description of the mentioned studies is given.

Tunneling magnetoresistance based on Heusler alloys electrodes was experimentally reported by Inomata in 2003. In their work, lower $Co_2Cr_{0.6}Fe_{0.4}Al$ and upper CoFe electrodes were used with AlO barrier, thus obtaining a 16 % room temperature rate and 26.5 % at 5 K [62 Inomata]. Ishikawa *et al.* have obtained a relatively high TMR ratios of 90% at room temperature and 192% at 4.2 K using Co-based Heusler alloy MTJs with Co_2MnSi as a lower electrode, MgO as a tunnel barrier prepared by sputtering and $Co_{50}Fe_{50}$ as an upper electrode respectively [63 Ishikawa]. Tsunegi *et al.*, in 2009, reported a higher TMR ratio of 217 % at room temperature and 753 % at 2K for the Co_2MnSi/MgO/CoFe TMJs with MgO as a barrier prepared by sputtering and electron beam evaporation system. The different in reported values in Co_2MnSi/MgO/CoFe TMJs results from the coherent tunneling process through the crystalline MgO barrier [64 Tsunegi]. Another application for Heusler alloy is the spin polarized carriers injection into semiconductors. They are considered important in designing spin injection devices due to several characteristics; such as, high spin polarization at Fermi energy, high Curie temperature along with large magnetic moments, and their lattice constants that is close to the III-V semiconductors which makes them ideal for epitaxial contacts [65 Ambrose, 66 Dong, 67 Lund, and 68 X.Y Dong]. Dong *et al.* in 2005 have reported an electrical spin injection of 27% at 2 K for Co_2MnGe into $Al_{0.1}Ga_{0.9}As$/GaAs light emitting diode hetero structures. However, Co_2MnSi with larger minority gap might be an effective injector than that of Co_2MnGe [68 Dong].

Heusler alloys are also useful for energy applications such as solar cells and thermoelectric convertor. First, for solar cells applications, turning sunlight into electric energy, Cu-based chalcopyrite semiconductors are used as light absorber materials for low

cost thin films. In these conventional chalcopyrite, a CdS buffer layer is sandwiched between the light absorber and a ZnO window layer. The use of CdS increased the performances of such devices with record efficiency of 19.9 %. The use of CdS meets the needs for a perfect contact between the absorber and the other layers with the avoidance of absorption losses, but CdS is found to be a very toxic material. Therefore, it is needed to replace CdS in solar systems with new materials of similar crystalline structure to that of chalcopyrite. LiZnP, LiMgZ (Z=As, P, Pb) and many other half-Heusler alloys fit such category where the electric conductivity has been shown to increase [69 casper].

Second, thermoelectric convertors (TEC) for power generation aim at reducing CO_2 emission which converts industrial furnaces, gas pipes, waste heat generated by engines and many more to electricity. The importance of TEC stems from the direct conversion of heat into electricity leading to a decrease in the reliance on fossil fuels. The existing TEC are inefficient and expensive at the same time. For that, half-Heusler alloys are interesting for TEC like n-type NiTiSn, p-type CoTiSb, Sb-doped NiTiSn materials For the latter, power factor can be reached up to 70 μW $(cmK^2)^{-1}$ at 650 K [70 Bhattacharya].

1.7 Choice of Co_2MnSi Heusler compound

Among Heusler alloys, we are interested in studying Co_2MnSi compounds because of their potential compatibility with microelectronic processes, high magnetic moment and Curie temperature and low damping coefficient. In this section, a brief overview on the magnetic properties such as saturation magnetization, magneto-crystalline anisotropy, exchange interaction and damping factor is given.

1.7.1 Saturation Magnetization

Saturation magnetization (M_s) can be defined as the maximum magnetization of a ferromagnetic material, this results when all the magnetic dipoles are aligned with an external field or at a remanence state for hard materials. In Table 1.4, we present experiment vs calculation values of the saturation magnetization of Co_2MnSi. The total magnetic moment experimental values are slightly different from ab-intio calculations.

M_s in Table 1.4 is expressed in $\mu_b\ /f.u\ (formula\ unit)$ (μ_B is Bohr's magneton=9.27×10^{-24} A.m^2), A/m in SI units or Tesla. To convert from μ_B to A/m or vice versa, we can do the following:

M_s (A/m) = number of atoms/m^3 $\times 9.27 \times 10^{-24} \times$ (the value of magnetization in μ_B)

Where the number of atoms/m^3 for Co_2MnSi = $\frac{4\ atoms\ per\ unit\ cell}{a^3} = \frac{4}{5.65^3} = 2.21 \times 10^{28}$.

$m^{spin}(\mu_B\ /f.u)$ Co_2MnSi Calculation	5.00 [32 Fujii], [38 Picozzi]	4.96 [13 Brown]	4.94 [25 Galanakis,]	5.008 [26 Galanakis],[71 Galanakis]	
$m^{spin}(\mu_B\ /f.u)$ Co_2MnSi Experiment	5.07 [6 Webster]	5.10±0.04 [72 Raphael]	4.95±0.25 [73 Singh]	4.7 [74 *Kämmerer*]	5.0 [75 Wang]

Table 1.4: calculated and experimental spin magnetic moments per unit cell for Co_2MnSi.

1.7.2 Magneto-crystalline anisotropy constant

In ferromagnets, the magnetization is generally aligned in a preferential direction, called the easy axis. The origin of this anisotropy for the direction of the magnetization can be either from the symmetry of the crystal (magneto crystalline anisotropy) or from dipolar interaction in the case of shape anisotropy. Our focus will be on the magneto-crystalline anisotropy of Co_2MnSi obtained by several groups.

Magneto-crystalline anisotropy is a consequence of the interaction between orbital moments and the spins of electrons. In Heusler, the spin-orbit interaction of the localized d-electrons results in the magneto-crystalline anisotropy. The magnetization will preferentially align with symmetry axes of the crystal. Anisotropy is described by the anisotropy constant ***K*** which can be experimentally obtained from Ferromagnetic Resonance (FMR), Brillouin light scattering (BLS) and Magneto-optical Kerr effect (MOKE) and other techniques. In this thesis, we have employed FMR. In CMS the anisotropy is cubic and the anisotropy constant ***K*** is negative where the easy axis of magnetization lies in the diagonal of the cube. The values of ***K*** range from – 8 KJ/m^3 [76 Gaier] to -25 KJ/m^3 [77 Ortiz]. . The increase in the anisotropy constant is related to several effects such as induced strain at the MgO/Co_2MnSi interfaces and to annealing temperatures.

1.7.3 Exchange constant

The origin of the exchange constant will be presented in chapter 2. The purpose of this paragraph is to give a comparison about the exchange constant obtained for Co_2MnSi by several groups. Ritchie *et al.* [78 Ritchie] and Rameev *et a*l. [79 Rameev] reported values of A= 19.3 pJ/m and A= 9.7 pJ/m. Hamrle *et al.*, by BLS measurements, obtained an exchange value, A= 23.5 pJ/m [80 Hamrle]. By FMR measurements, Pandey *et al.*, Belmeguenai *et al.* and Ortiz *et al.* have reported an exchange value of 21 pJ/m, 27 pJ/m and 19 pJ/m, respectively [81 Pandey, 82 Belmeguenai, 77 Ortiz]. The differences in reported values are generally assumed to rely on deposition conditions and substrates effects.

.

1.7.4 Magnetic damping factor

In this thesis, a particular interest is attributed to the study of the magnetic Gilbert damping factor α. The latter reflects the time needed for the magnetization pointed out of its equilibrium position to get back to equilibrium through different kind of relaxation processes. The dimensionless coefficient α is theoretically predicted to be less than 10^{-3} for Heusler alloys [5 Liu]. Experimentally, several groups have obtained the Gilbert damping factor, for example, in the previous work of Ortiz *et al.*, they have found the damping factor value between $3*10^{-3}$ and $7*10^{-3}$ [77 Ortiz]. The mentioned values are in agreement with experimental review about Co-based Heusler alloys by Trudel *et al.* [8 Trudel]. Chapter two will give some basics of relaxation mechanisms and chapter 4 and 5 will present the results obtained on the dynamic magnetic properties and specially the Gilbert damping factor.

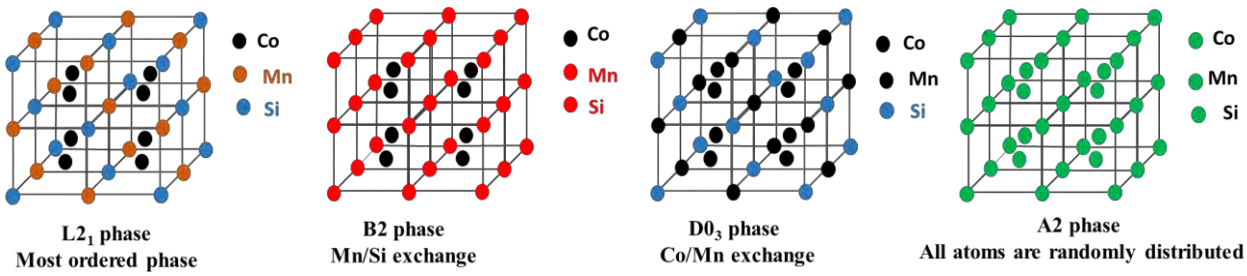

Figure 1.10: schematic presentation of Co_2MnSi crystalline structure: a) $L2_1$, b) B2, c) $D0_3$ and A2 phases.

In conclusion of this section, the magnetic behavior of these alloys depend strongly on their structural properties (figure 1.10). The magnetic behavior of $L2_1$ and B2 phases are similar, at least for the magnetic moment and spin polarization but no information is given on their respective anisotropy nor on the damping in the B2 order. Theoretically Picozzi et al [6 Picozzi] have shown that in the $L2_1$ phase, the value of magnetization is 5 $\mu_b\ /f.u.$ (1.3 T) and also when Mn and Si swap their positions in the lattice to form the B2 phase. The half metallicity of CMS is shown theoretically with a band gap at the fermi level for the $L2_1$ phase (0.81 eV) [38 Picozzi]. Furthermore [5 Liu] has calculated with the Fermi Breathing method a low Gilbert damping coefficient of $6*10^{-5}$ for this phase. Whereas a cubic crystal anisotropy is present in CMS, the anisotropy constant is negative leading to a magnetic easy axis oriented in the diagonal of the cube (<111>) and the hard axis along the edge of the cube (<100>). While there are many information about the $L2_1$ and B2 phases, insufficient literature is conducted on both $D0_3$ and A2 phases. Theoretically, Picozzi also studied the effect $D0_3$ order on the average magnetization when Co and Mn swap their positions. He also shows a decrease in the saturation magnetization to 4.5 $\mu_b\ /f.u.$ (1.16 T) whereas no information about the cubic anisotropy nor the damping relaxation terms is given. For the A2 phase no information was found about the magnetic behavior of this completely disordered phase.

Chapter 1 References:

[1] "F. Heusler, W. Starck, and E. Haupt, Verh. DPG 5, 220 (1903)."

[2] T. Graf, C. Felser, and S. S. P. Parkin, "Simple rules for the understanding of Heusler compounds," Prog. Solid State Chem., vol. 39, no. 1, pp. 1–50, May 2011.

[3] R. A. De Groot, F. M. Mueller, P. G. Van Engen, and K. H. J. Buschow, "New class of materials: half-metallic ferromagnets," Phys. Rev. Lett., vol. 50, no. 25, pp. 2024–2027, 1983.

[4] K. Bartholomé, B. Balke, D. Zuckermann, M. Köhne, M. Müller, K. Tarantik, and J. König, "Thermoelectric Modules Based on Half-Heusler Materials Produced in Large Quantities," J. Electron. Matter., vol. 43, no. 6, pp. 1775–1781, Nov. 2013.

[5] C. Liu, C. K. A. Mewes, M. Chshiev, T. Mewes, and W. H. Butler, "Origin of low Gilbert damping in half metals," Appl. Phys. Lett., vol. 95, no. 2, p. 022509, 2009.

[6] P. J. Webster, "Magnetic and chemical order in Heusler alloys containing cobalt and manganese," J. Phys. Chem. Solids, vol. 32, no. 6, pp. 1221–1231, 1971.

[7] G. E. Bacon and J. S. Plant, "Chemical ordering in Heusler alloys with the general formula A2BC or ABC," J. Phys. F Met. Phys., vol. 1, no. 4, p. 524, Jul. 1971.

[8] S. Trudel, O. Gaier, J. Hamrle, and B. Hillebrands, "Magnetic anisotropy, exchange and damping in cobalt-based full-Heusler compounds: an experimental review," J. Phys. Appl. Phys., vol. 43, no. 19, p. 193001, 2010.

[9] K. Kobayashi, K. Ishikawa, R. Y. Umetsu, R. Kainuma, K. Aoki, and K. Ishida, "Phase stability of B2 and L21 ordered phases in Co2YGa (Y=Ti, V, Cr, Mn, Fe) alloys," J. Magn. Magn. Mater., vol. 310, no. 2, Part 2, pp. 1794–1795, Mar. 2007.

[10] H. C. Kandpal, G. H. Fecher, and C. Felser, "Calculated electronic and magnetic properties of the half-metallic, transition metal based Heusler compounds," J. Phys. Appl. Phys., vol. 40, no. 6, p. 1507, Mar. 2007.

[11] H. J. Elmers, S. Wurmehl, G. H. Fecher, G. Jakob, C. Felser, and G. Schonhense, "Field dependence of orbital magnetic moments in the Heusler compounds Co 2 FeAl and Co 2 Cr 0.6 Fe 0.4 Al," Appl. Phys. Mater. Sci. Process., vol. 79, no. 3, pp. 557–563, Aug. 2004.

[12] S. Wurmehl, G. H. Fecher, H. C. Kandpal, V. Ksenofontov, C. Felser, H.-J. Lin, and J. Morais, "Geometric, electronic, and magnetic structure of Co 2 FeSi : Curie temperature and magnetic moment measurements and calculations," Phys. Rev. B, vol. 72, no. 18, Nov. 2005.

[13] P. J. Brown, K. U. Neumann, P. J. Webster, and K. R. A. Ziebeck, "The magnetization distributions in some Heusler alloys proposed as half-metallic ferromagnets," J. Phys. Condens. Matter, vol. 12, no. 8, p. 1827, 2000.

[14] K. H. J. Buschow, P. G. van Engen, and R. Jongebreur, "Magneto-optical properties of metallic ferromagnetic materials," J. Magn. Magn. Matter., vol. 38, no. 1, pp. 1–22, août 1983.

[15] G. Li, T. Taira, K. Matsuda, M. Arita, T. Uemura, and M. Yamamoto, "Epitaxial growth of Heusler alloy Co2MnSi/MgO heterostructures on Ge(001) substrates," Appl. Phys. Lett., vol. 98, no. 26, p. 262505, Jun. 2011.

[16] M. a. I. Nahid, M. Oogane, H. Naganuma, and Y. Ando, "Epitaxial growth of Co2MnSi thin films at the vicinal surface of n-Ge(111) substrate," Appl. Phys. Lett., vol. 96, no. 14, p. 142501, Apr. 2010.

[17] G. Ortiz, A. García-García, N. Biziere, F. Boust, J. F. Bobo, et E. Snoeck, « Growth, structural, and magnetic characterization of epitaxial Co2MnSi films deposited on MgO and Cr seed layers », *J. Appl. Phys.*, vol. 113, nº 4, p. 043921, 2013..

[18] O. Gaier, "A study of exchange interaction, magnetic anisotropies, and ion beam induced effects in thin films of Co2-based Heusler compounds," Ph. D. dissertation, Technical University of Kaiserslautern, 2009.

[19] C. Magen, E. Snoeck, U. Lüders, and J. F. Bobo, "Effect of metallic buffer layers on the antiphase boundary density of epitaxial Fe3O4," J. Appl. Phys., vol. 104, no. 1, p. 013913, Jul. 2008.

[20] A. García-García, J. A. Pardo, P. Štrichovanec, C. Magén, A. Vovk, J. M. D. Teresa, G. N. Kakazei, Y. G. Pogorelov, L. Morellón, P. A. Algarabel, and M. R. Ibarra, "Tunneling magnetoresistance in epitaxial discontinuous Fe/MgO multilayers," Appl. Phys. Lett., vol. 98, no. 12, p. 122502, Mar. 2011.

[21] "Soulen R J Jr et al 1998 Science 282 85."

[22] H. Kato, T. Okuda, Y. Okimoto, Y. Tomioka, K. Oikawa, T. Kamiyama, and Y. Tokura, "Structural and electronic properties of the ordered double perovskites A 2 M ReO 6 (A =Sr,Ca; M =Mg,Sc,Cr,Mn,Fe,Co,Ni,Zn)," Phys. Rev. B, vol. 69, no. 18, May 2004.

[23] T. Shishidou, A. J. Freeman, and R. Asahi, "Effect of GGA on the half-metallicity of the itinerant ferromagnet CoS 2," Phys. Rev. B, vol. 64, no. 18, Oct. 2001.

[24] "http://www.nims.go.jp/apfim/halfmetal.html."

[25] I. Galanakis, P. H. Dederichs, and N. Papanikolaou, "Slater-Pauling behavior and origin of the half-metallicity of the full-Heusler alloys," *Phys. Rev. B*, vol. 66, no. 17, p. 174429, Nov. 2002.

[26] I. Galanakis, P. Mavropoulos, and P. H. Dederichs, "Electronic structure and Slater–Pauling behaviour in half-metallic Heusler alloys calculated from first principles," J. Phys. Appl. Phys., vol. 39, no. 5, pp. 765–775, Mar. 2006.

[27] W. E. Pickett, "Single spin superconductivity," Phys. Rev. Lett., vol. 77, no. 15, p. 3185, 1996.

[28] F. Casper, T. Graf, S. Chadov, B. Balke, and C. Felser, "Half-Heusler compounds: novel materials for energy and spintronic applications," Semicond. Sci. Technol., vol. 27, no. 6, p. 063001, Jun. 2012.

[29] J. C. Slater, "The Ferromagnetism of Nickel. II. Temperature Effects," Phys. Rev., vol. 49, no. 12, pp. 931–937, juin 1936.

[30] L. Pauling, "The nature of the interatomic forces in metals," Phys. Rev., vol. 54, no. 11, p. 899, 1938.

[31] Y. Kurtulus, R. Dronskowski, G. Samolyuk, and V. Antropov, "Electronic structure and magnetic exchange coupling in ferromagnetic full Heusler alloys," Phys. Rev. B, vol. 71, no. 1, Jan. 2005.

[32] S. Fujii, S. Sugimura, and S. Asano, "Hyperfine fields and electronic structures of the Heusler alloys Co2MnX (X= Al, Ga, Si, Ge, Sn)," J. Phys. Condens. Matter, vol. 2, no. 43, p. 8583, 1990.

[33] J. Kübler, A. R. William, and C. B. Sommers, "Formation and coupling of magnetic moments in Heusler alloys," Phys. Rev. B, vol. 28, no. 4, pp. 1745–1755, août 1983.
J. Kübler, "Ab initio estimates of the Curie temperature for magnetic compounds," *J. Phys. Condens. Matter*, vol. 18, no. 43, p. 9795, 2006.

[34] G. H. Fecher, H. C. Kandpal, S. Wurmehl, C. Felser, and G. Schönhense, "Slater-Pauling rule and Curie temperature of Co2-based Heusler compounds," J. Appl. Phys., vol. 99, no. 8, p. 08J106, Apr. 2006.

[35] H. Ebert and G. Schütz, "Theoretical and experimental study of the electronic structure of PtMnSb," J. Appl. Phys., vol. 69, no. 8, pp. 4627–4629, Apr. 1991.
[36] D. Orgassa, H. Fujiwara, T. C. Schulthess, and W. H. Butler, "First-principles calculation of the effect of atomic disorder on the electronic structure of the half-metallic ferromagnet NiMnSb," Phys. Rev. B, vol. 60, no. 19, pp. 13237–13240, Nov. 1999.
[37] D. Orgassa, H. Fujiwara, T. C. Schulthess, and W. H. Butler, "Disorder dependence of the magnetic moment of the half-metallic ferromagnet NiMnSb from first principles," J. Appl. Phys., vol. 87, no. 9, pp. 5870–5871, May 2000.
[38] S. Picozzi, A. Continenza, and A. J. Freeman, "Co_2MnX (X=Si, Ge, Sn) Heusler compounds: An ab-initio study of their structural, electronic, and magnetic properties at zero and elevated pressure," Phys. Rev. B, vol. 66, no. 9, p. 094421, Sep. 2002.
[39] Z. Gercsi and K. Hono, "Ab initio predictions for the effect of disorder and quarternary alloying on the half-metallic properties of selected Co2Fe-based Heusler alloys," J. Phys. Condens. Matter, vol. 19, no. 32, p. 326216, Jul. 2007.
[40] S. Picozzi, A. Continenza, and A. Freeman, "Role of structural defects on the half-metallic character of Co2MnGe and Co2MnSi Heusler alloys," Phys. Rev. B, vol. 69, no. 9, Mar. 2004.
[41] I. Galanakis, "Surface properties of the half-and full-Heusler alloys," J. Phys. Condens. Matter, vol. 14, no. 25, p. 6329, Jul. 2002.
[42] S. Ishida, T. Masaki, S. Fujii, and S. Asano, "Theoretical search for half-metalliic films of Co2MnZ (Z = Si, Ge)," Phys. B Condens. Matter, vol. 245, no. 1, pp. 1–8, Jan. 1998.
[43] K. Nagao, Y. Miura, and M. Shirai, "Half-metallicity at the (110) interface between a full Heusler alloy and GaAs," Phys. Rev. B, vol. 73, no. 10, p. 104447, Mar. 2006.
[44] Y. Miura, H. Uchida, Y. Oba, K. Nagao, and M. Shirai, "Coherent tunnelling conductance in magnetic tunnel junctions of half-metallic full Heusler alloys with MgO barriers," J. Phys. Condens. Matter, vol. 19, no. 36, p. 365228, Sep. 2007.
[45] S. J. Hashemifar, P. Kratzer, and M. Scheffler, "Preserving the Half-Metallicity at the Heusler Alloy C o 2 M n S i (001) Surface: A Density Functional Theory Study," Phys. Rev. Lett., vol. 94, no. 9, Mar. 2005.
[46] D. Ristoiu, J. P. Nozières, C. N. Borca, T. Komesu, H. –. Jeong, and P. A. Dowben, "The surface composition and spin polarization of NiMnSb epitaxial thin films," EPL Europhys. Lett, vol. 49, no. 5, p. 624, Mar. 2000.
[47] S.-Z. Qiao, J. Zhang, Y.-F. Qin, R.-R. Hao, H. Zhong, D.-P. Zhu, Y. Kang, S.-S. Kang, S.-Y. Yu, G.-B. Han, S.-S. Yan, and L.-M. Mei, "Structural and Magnetic Properties of Co 2 MnSi Thin Film with a Low Damping Constant," Chin. Phys. Lett., vol. 32, no. 5, p. 057601, May 2015.
[48] T. Kubota, S. Tsunegi, M. Oogane, S. Mizukami, T. Miyazaki, H. Naganuma, and Y. Ando, "Half-metallicity and Gilbert damping constant in Co2FexMn1−xSi Heusler alloys depending on the film composition," Appl. Phys. Lett., vol. 94, no. 12, p. 122504, Mar. 2009.
[49] M. J. Bonder, N. D. Telling, P. J. Grundy, C. A. Faunce, T. Shen, and V. M. Vishnyakov, "Ion irradiation of Co/Pt multilayer films," J. Appl. Phys., vol. 93, no. 10, pp. 7226–7228, May 2003.
[50] C. Chappert, "Planar Patterned Magnetic Media Obtained by Ion Irradiation," *Science*, vol. 280, no. 5371, pp. 1919–1922, Jun. 1998.
[51] T. Devolder, "Light ion irradiation of Co/Pt systems: structural origin of the decrease in magnetic anisotropy," *Physical Review B*, vol. 62, no. 9, p. 5794, 2000.

[52] T. Devolder, J. Ferré, C. Chappert, H. Bernas, J.-P. Jamet, and V. Mathet, "Magnetic properties of He + -irradiated Pt/Co/Pt ultrathin films," *Physical Review B*, vol. 64, no. 6, Jul. 2001

[53] J. Fassbender, D. Ravelosona, and Y. Samson, "Tailoring magnetism by light-ion irradiation," J. Phys. Appl. Phys., vol. 37, no. 16, p. R179, Aug. 2004.

[54] L. Folks, R. E. Fontana, B. A. Gurney, J. R. Childress, S. Maat, J. A. Katine, J. E. E. Baglin, and A. J. Kellock, "Localized magnetic modification of permalloy using Cr+ ion implantation," J. Phys. Appl. Phys., vol. 36, no. 21, p. 2601, 2003.

[55] J. Fassbender and J. McCord, "Control of saturation magnetization, anisotropy, and damping due to Ni implantation in thin Ni[sub 81]Fe[sub 19] layers," Appl. Phys. Lett., vol. 88, no. 25, p. 252501, 2006.

[56] D. Ravelosona, C. Chappert, V. Mathet, and H. Bernas, "Chemical order induced by ion irradiation in FePt (001) films," Appl. Phys. Lett., vol. 76, no. 2, p. 236, 2000.

[57] O. Gaier, J. Hamrle, B. Hillebrands, M. Kallmayer, P. Pörsch, G. Schönhense, H. J. Elmers, J. Fassbender, A. Gloskovskii, C. A. Jenkins, C. Felser, E. Ikenaga, Y. Sakuraba, S. Tsunegi, M. Oogane, and Y. Ando, "Improvement of structural, electronic, and magnetic properties of Co2MnSi thin films by He+ irradiation," Appl. Phys. Lett., vol. 94, no. 15, p. 152508, Apr. 2009.

[58] H. Bernas, J.-P. Attané, K.-H. Heinig, D. Halley, D. Ravelosona, A. Marty, P. Auric, C. Chappert, and Y. Samson, "Ordering Intermetallic Alloys by Ion Irradiation: A Way to Tailor Magnetic Media," Phys. Rev. Lett., vol. 91, no. 7, Aug. 2003.

[59] B. Obry, T. Meyer, P. Pirro, T. Brächer, B. Lägel, J. Osten, T. Strache, J. Fassbender, and B. Hillebrands, "Microscopic magnetic structuring of a spin-wave waveguide by ion implantation in a Ni81Fe19 layer," Appl. Phys. Lett., vol. 102, no. 2, p. 022409, 2013.

[60] J. A. King, A. Ganguly, D. M. Burn, S. Pal, E. A. Sallabank, T. P. A. Hase, A. T. Hindmarch, A. Barman, and D. Atkinson, "Local control of magnetic damping in ferromagnetic/non-magnetic bilayers by interfacial intermixing induced by focused ion-beam irradiation," Appl. Phys. Lett., vol. 104, no. 24, p. 242410, Jun. 2014.

[61] K. Yakushiji, K. Saito, S. Mitani, K. Takanashi, Y. K. Takahashi, and K. Hono, "Current-perpendicular-to-plane magnetoresistance in epitaxial Co2MnSi/Cr/Co2MnSi trilayers," Appl. Phys. Lett., vol. 88, no. 22, p. 222504, May 2006..

[62] K. Inomata, N. Ikeda, N. Tezuka, R. Goto, S. Sugimoto, M. Wojcik, and E. Jedryka, "Highly spin-polarized materials and devices for spintronics," Sci. Technol. Adv. Mater., vol. 9, no. 1, p. 014101, Jan. 2008.

[63] T. Ishikawa, T. Marukame, H. Kijima, K.-I. Matsuda, T. Uemura, M. Arita, and M. Yamamoto, "Spin-dependent tunneling characteristics of fully epitaxial magnetic tunneling junctions with a full-Heusler alloy Co2MnSi thin film and a MgO tunnel barrier," Appl. Phys. Lett., vol. 89, no. 19, p. 192505, Nov. 2006.

[64] S. Tsunegi, Y. Sakuraba, M. Oogane, N. D. Telling, L. R. Shelford, E. Arenholz, G. van der Laan, R. J. Hicken, K. Takanashi, and Y. Ando, "Tunnel magnetoresistance in epitaxially grown magnetic tunnel junctions using Heusler alloy electrode and MgO barrier," J. Phys. Appl. Phys., vol. 42, no. 19, p. 195004, Oct. 2009.

[65] T. Ambrose, J. J. Krebs, and G. A. Prinz, "Epitaxial growth and magnetic properties of single-crystal Co2MnGe Heusler alloy films on GaAs (001)," Appl. Phys. Lett., vol. 76, no. 22, pp. 3280–3282, May 2000.

[66] J. W. Dong, L. C. Chen, C. J. Palmstro/m, R. D. James, and S. McKernan, "Molecular beam epitaxy growth of ferromagnetic single crystal (001) Ni2MnGa on (001) GaAs," Appl. Phys. Lett., vol. 75, no. 10, pp. 1443–1445, Sep. 1999.

[68] M. S. Lund, J. W. Dong, J. Lu, X. Y. Dong, C. J. Palmstrøm, and C. Leighton, "Anomalous magnetotransport properties of epitaxial full Heusler alloys," Appl. Phys. Lett., vol. 80, no. 25, pp. 4798–4800, Jun. 2002.

[68] X. Y. Dong, C. Adelmann, J. Q. Xie, C. J. Palmstrøm, X. Lou, J. Strand, P. A. Crowell, J.-P. Barnes, and A. K. Petford-Long, "Spin injection from the Heusler alloy Co2MnGe into Al0.1Ga0.9As⁄GaAs heterostructures," Appl. Phys. Lett., vol. 86, no. 10, p. 102107, Mar. 2005.

[69] F. Casper, T. Graf, S. Chadov, B. Balke, and C. Felser, "Half-Heusler compounds: novel materials for energy and spintronic applications," *Semicond. Sci. Technol.*, vol. 27, no. 6, p. 063001, Jun. 2012.

[70] S. Bhattacharya, A. L. Pope, R. T. L. Iv, T. M. Tritt, V. Ponnambalam, Y. Xia, and S. J. Poon, "Effect of Sb doping on the thermoelectric properties of Ti-based half-Heusler compounds, TiNiSn1−xSbx," Appl. Phys. Lett., vol. 77, no. 16, pp. 2476–2478, Oct. 2000

[71] I. Galanakis, "Orbital magnetism in the half-metallic Heusler alloys," *Phys. Rev. B*, vol. 71, no. 1, Jan. 2005

[72] M. P. Raphael, B. Ravel, Q. Huang, M. A. Willard, S. F. Cheng, B. N. Das, R. M. Stroud, K. M. Bussmann, J. H. Claassen, and V. G. Harris, "Presence of antisite disorder and its characterization in the predicted half-metal Co 2 MnSi," *Phys. Rev. B*, vol. 66, no. 10, Sep. 2002.

[73] L. J. Singh, Z. H. Barber, Y. Miyoshi, W. R. Branford, and L. F. Cohen, "Structural and transport studies of stoichiometric and off-stoichiometric thin films of the full Heusler alloy Co2MnSi," *J. Appl. Phys.*, vol. 95, no. 11, pp. 7231–7233, Jun. 2004

[74] S. Kämmerer, A. Thomas, A. Hütten, and G. Reiss, "Co2MnSi Heusler alloy as magnetic electrodes in magnetic tunnel junctions," *Appl. Phys. Lett.*, vol. 85, no. 1, pp. 79–81, Jul. 2004

[75] W. H. Wang, M. Przybylski, W. Kuch, L. I. Chelaru, J. Wang, Y. F. Lu, J. Barthel, H. L. Meyerheim, and J. Kirschner, "Magnetic properties and spin polarization of ${\mathrm{Co}}_{2}\mathrm{MnSi}$ Heusler alloy thin films epitaxially grown on GaAs(001)," *Phys. Rev. B*, vol. 71, no. 14, p. 144416, avril 2005.

[76] O. Gaier, J. Hamrle, S. J. Hermsdoerfer, H. Schultheiß, B. Hillebrands, Y. Sakuraba, M. Oogane, and Y. Ando, "Influence of the $L2_1$ ordering degree on the magnetic properties of Co2MnSi Heusler films," *J. Appl. Phys.*, vol. 103, no. 10, p. 103910, May 2008

[77] G. Ortiz, A. Garcia, J. Ben Youssef, N. Biziere, F. Boust, J. Bobo, E. Snoeck, and N. Vukadinovic, "Broadband Ferromagnetic Resonance Study of Thin Films: Effect of the Film Thickness," *IEEE Trans. Magn.*, vol. 49, no. 3, pp. 1037–1040, Mar. 2013

[78] L. Ritchie, G. Xiao, Y. Ji, T. Y. Chen, C. L. Chien, M. Zhang, J. Chen, Z. Liu, G. Wu, and X. X. Zhang, "Magnetic, structural, and transport properties of the Heusler alloys Co 2 MnSi and NiMnSb," *Phys. Rev. B*, vol. 68, no. 10, Sep. 2003.

[79] B. Rameev, F. Yildiz, S. Kazan, B. Aktas, A. Gupta, L. R. Tagirov, D. Rata, D. Buergler, P. Gruenberg, C. M. Schneider, S. Kämmerer, G. Reiss, et A. Hütten, « FMR

investigations of half-metallic ferromagnets », *Phys. Status Solidi A*, vol. 203, nº 7, p. 1503‑1512, mai 2006.

[80] J. Hamrle, O. Gaier, S.-G. Min, B. Hillebrands, Y. Sakuraba, and Y. Ando, "Determination of exchange constants of Heusler compounds by Brillouin light scattering spectroscopy: application to Co2MnSi," *J. Phys. Appl. Phys.*, vol. 42, no. 8, p. 084005, Apr. 2009.

[81] H. Pandey, P. C. Joshi, R. P. Pant, R. Prasad, S. Auluck, and R. C. Budhani, "Evolution of ferromagnetic and spin-wave resonances with crystalline order in thin films of full-Heusler alloy Co2MnSi," *J. Appl. Phys.*, vol. 111, no. 2, p. 023912, Jan. 2012.

[82] M. Belmeguenai, F. Zighem, D. Faurie, H. Tuzcuoglu, S.-M. Chérif, P. Moch, K. Westerholt, and W. Seiler, "Structural and magnetic properties of Co2MnSi thin films," *Phys. Status Solidi A*, vol. 209, no. 7, pp. 1328–1333, juillet 2012.

Chapter 2: Magnetization Dynamics

In this chapter, we start with the Basics of magnetism presented in section 2.1, then the different magnetic energies in a ferromagnetic system are introduced in section 2.2. Section 2.3 presents the theoretical aspects of magnetization dynamics along with the solution equation of motion with and without relaxation mechanisms. Ferromagnetic resonance, magnetostatic modes and spin waves will be discussed in section 2.4. Finally we will focus on the extrinsic and intrinsic relaxation processes of magnetization relaxation in section 2.5. The reader is addressed to these several books for additional information regarding the mentioned topics [1 Coey, 2 Blundel, 3 Stancil and Prabhakar, 4 Gurevich and Melkov, 5 Vonsovskii, and 6 Getzlaff].

2.1 Basics of Magnetism

A magnetic dipole moment is formed when an electron orbits around the nucleus, creating a current loop of an area $\boldsymbol{A}$, and expressed as $\boldsymbol{\mu} = \boldsymbol{I}\,\boldsymbol{A}$ **.** The magnetic moment can be also expressed by the orbital angular momentum of electrons, $\boldsymbol{L}$, then the magnetic dipole moment can be written as $\boldsymbol{\mu} = -\frac{\boldsymbol{e}}{\boldsymbol{2m}}\boldsymbol{L}$ **.** For an electron, the angular momentum $\boldsymbol{L}$ is due to orbital motion of the electron $\vec{\boldsymbol{l}}$ and to an intrinsic property called spin' $\vec{\boldsymbol{S}}'$ (Figure 2.1).

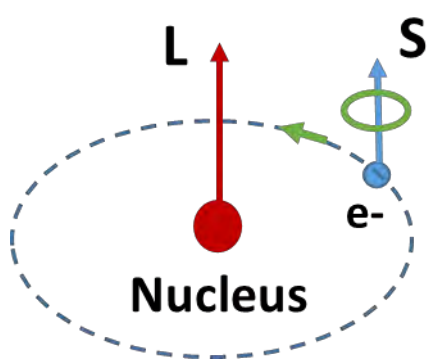

Figure 2.1: The magnetic moment of an atom is contributed by both the orbital and spin magnetic motion of the electron.

Both the orbital and spin angular momentum contribute to the magnetic moment of an electron. We can define $\boldsymbol{\mu_l}$ and $\boldsymbol{\mu_s}$ as the orbital magnetic moment and spin magnetic

moment, respectively. To derive both $\boldsymbol{\mu_l}$ and $\boldsymbol{\mu_S}$ expressions, the angular momentum $\boldsymbol{L}$ is described by quantum mechanical theory, $\boldsymbol{L} = \boldsymbol{m_l}\,\hbar$ where $\boldsymbol{m_l}$ is an orbital quantum number that varies from $-\boldsymbol{l}$ to $\boldsymbol{l}$. Substituting $\boldsymbol{m_l}\,\hbar$ in the expression of magnetic dipole moment we get:

$\boldsymbol{\mu_l} = -\,\boldsymbol{\mu_B}\,\boldsymbol{m_l}$ is the orbital magnetic moment and $\boldsymbol{\mu_B} = \frac{\boldsymbol{e}\,\hbar}{\boldsymbol{2m}} = 9.27 \times 10^{-24}\ A.m^2$, is the Bohr magneton.

$\boldsymbol{\mu_S} = -\,\boldsymbol{g}\,\boldsymbol{\mu_B}\,\boldsymbol{m_s}$ is the spin magnetic moment, $\boldsymbol{m_s}$ is the electron spin quantum number and $\boldsymbol{g} \approx \mathbf{2.003}$ is the Landé factor or also called the spectroscopic splitting factor.

Therefore, from the above two expressions we can define the total magnetic moment, due to both orbital and spin contribution, as:

$$\boldsymbol{\mu_{Total}} = -\ \boldsymbol{\mu_B}\left(\textstyle\sum_i \boldsymbol{m_l} + \boldsymbol{g}\sum_i \boldsymbol{m_s}\right). \tag{2.1}$$

The magnetization **M** (A.m) is defined as the sum of all magnetic moments per unit volume **V**.

$$\boldsymbol{M} = \frac{\sum \boldsymbol{\mu_{Total}}}{\boldsymbol{V}} \tag{2.2}$$

Let us consider a material placed in a magnetic field, the response of the atomic moments to that external field will define the material's magnetic behavior. The magnetic behavior of any matter in an external field is dived into the following categories (Figure 2.2):

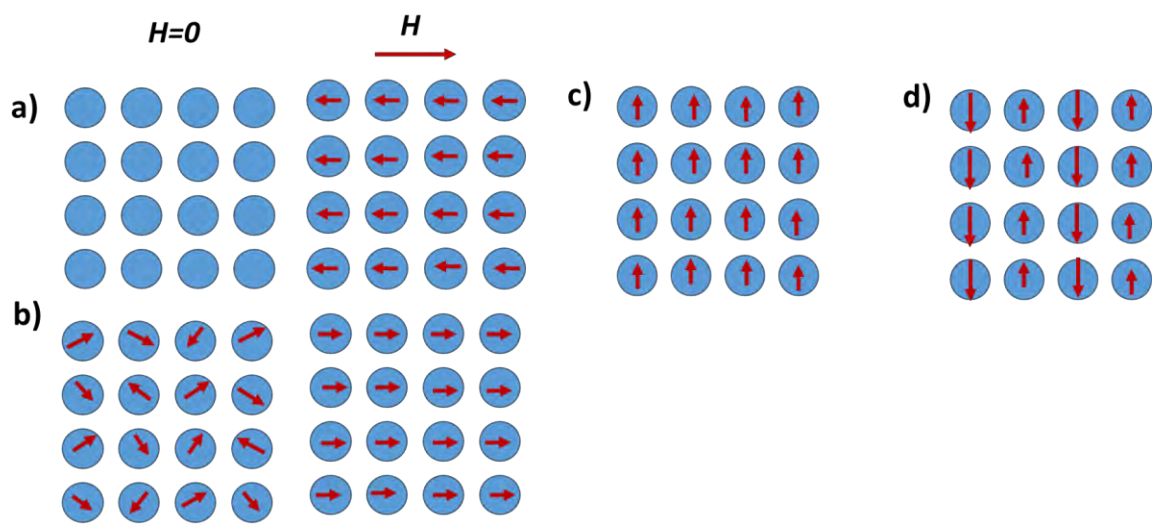

Figure 2.2: a) the atomic dipole moment for a *a)* diamagnetic and *b)* paramagnetic material with and without an external magnetic field. The alignment of magnetic moments in c) ferromagnetic and d) antiferromagnetic materials.

Diamagnetic materials: In the absence of the external magnetic field, no dipoles exist; but in the presence of an external magnetic field, magnetic dipoles are induced to counterbalance the applied magnetic flux. They align in opposite direction to the applied field resulting in a

negative non-zero magnetic moment. The magnetic susceptibility is then negative for such materials and of the order of 10^{-6} to 10^{-5}.

Paramagnetic materials: in the absence of external magnetic field, the paramagnetic materials possess magnetic moments that are randomly distributed due to thermal agitations. When applying an external magnetic field, these atomic dipoles align with the applied field and a positive net magnetization appears. The susceptibility is positive with values between 10^{-5} and 10^{-4}.

Ferromagnetic materials: In these materials, the exchange interaction (see below) is responsible for the parallel alignment of the magnetic moments on a length scale called the exchange length. The order of magnitude of exchange length is few nanometers (for example: 1.5 nm for Fe and 3.37 nm for Co). At the macroscopic scale, ferromagnetic materials can either present a net magnetization or not. In the latter case, the magnetization is organized in domains with different orientations in order to minimize the magnetic stray field. So even with a zero net magnetization, there is a local magnetization in each domain.

The susceptibility of ferromagnetic materials is generally from 10 to several thousands. These materials are classified as soft or hard depending on their ability to switch the magnetization from one direction to another opposite one.

Magnetic materials can be characterized by a hysteresis loop as shown in Figure 2.3. Moreover, the thermal behavior of ferromagnetic materials is important; above a given temperature, called the *Curie temperature*, the exchange interaction is not sufficient to maintain the alignment of the magnetic moments and therefore the material becomes paramagnetic.

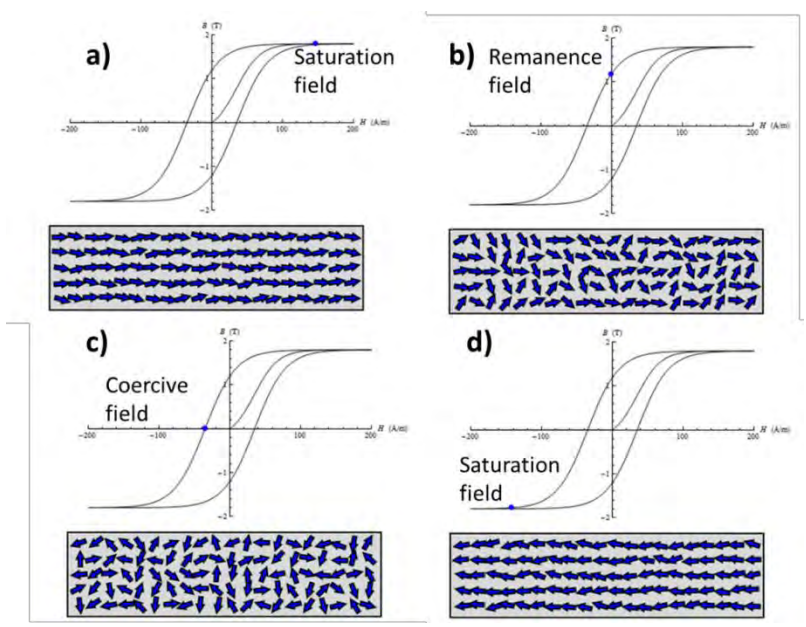

Figure 2.3: a) A sufficient magnetic field is applied to reach saturation magnetization inside a ferromagnetic material, then in b), the magnetic field is being reduced until there is no external field where a part of the material still have a residual magnetization. In c), to

completely demagnetize the material a significant field is needed and is called coercive field. In d) the sample is saturated in the opposite direction.

Ferri and Antiferro magnetic materials: these materials are generally composed of two ferromagnetic sub-lattices that are coupled antiparallel. If each sub-lattice presents the same magnetic moment (+M and –M) then the net magnetization is null and we have an antiferromagnetic material. Unlike ferromagnets, above a temperature called Neel temperature, they become paramagnetic. If the two sub-lattices moments are uncompensated we have then a nonzero net magnetization. These materials are called ferrimagnetic.

2.2 Micro-magnetic energy terms of ferromagnetic thin films

In a ferromagnetic material, the equilibrium position of the magnetization is found when the magnetization is aligned with the effective field defined as:

$$\boldsymbol{H_{eff}} = -\frac{\mathbf{1}}{\boldsymbol{\mu_0}}\frac{\boldsymbol{\delta E_{tot}}}{\boldsymbol{\delta M}} \tag{2.3}$$

$\boldsymbol{E_{tot}}$ is the total free energy of a ferromagnetic material, $\boldsymbol{\mu_0}$ is the vacuum permeability ($\boldsymbol{\mu_0} = 4\pi * 10^{-7}$) and $\boldsymbol{M}$ is the total magnetization. Different energy terms contribute the total energy of a ferromagnetic material. A stable state is reached when the energy is minimized. The main energy terms we will focus on are the Zeeman, exchange, demagnetization, and magneto-crystalline energies.

$$\boldsymbol{E_{tot}} = \boldsymbol{E_{Zeeman}} + \boldsymbol{E_{exchange}} + \boldsymbol{E_{demag}} + \boldsymbol{E_{anisotropy}} \tag{2.4}$$

2.2.1 Zeeman Energy

The magnetic moments within the sample will align parallel to an applied field to minimize the energy of the system. This behavior is known as the Zeeman energy expressed in the following equation:

$$\boldsymbol{E_{zeeman}} = -\boldsymbol{\mu_0} \int \vec{\boldsymbol{H}}_{\boldsymbol{ext}}.\vec{\boldsymbol{M}}\boldsymbol{dV} \tag{2.5}$$

2.2.2 Exchange energy

The exchange interaction is mediated by different mechanisms depending on the material system. In ferromagnetic material, the parallel alignment of the spins is the direct exchange interaction. This one comes from the competition of the coulomb interaction of the two electrons and the Pauli Exclusion Principle.

Considering two spins ($\vec{s_i}$ *and* $\vec{s_j}$), the Hamiltonian of the system including the exchange interaction can be expressed as:

$$\boldsymbol{H_{ij}} = -\mathbf{2}\,\boldsymbol{J}\,\boldsymbol{S_i}\boldsymbol{S_j} \tag{2.6}$$

$\boldsymbol{H_{ij}}$ is the exchange Hamiltonian for two interacting spins $\boldsymbol{S_i}$ *and* $\boldsymbol{S_j}$, $\boldsymbol{J}$ is the exchange integral that depends on the material and the interatomic distances (*i.e.* Orbital overlap). If $\boldsymbol{J}$ is positive, then the energy is minimum for parallel alignment of the spins, leading to the ferromagnetic order. If $\boldsymbol{J}$ is negative, then the minimum energy results in an antiparallel alignment of the spins and hence an antiferromagnetic behavior. This is illustrated by the Bethe-Slater curve in Figure 2.4 [6 Getzlaff].

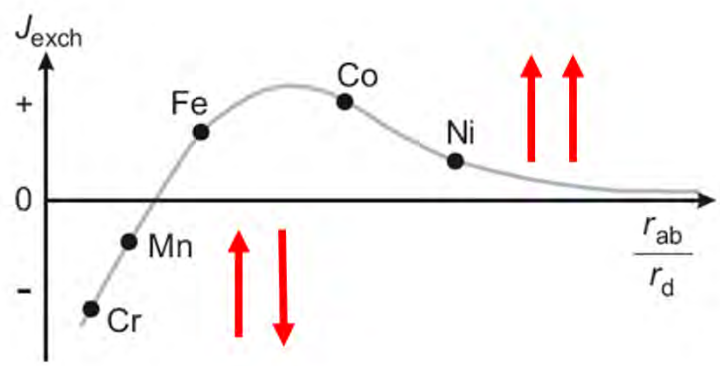

Figure 2.4: The Bethe-Slater curve. Exchange integral vs. the ratio of interatomic distance $\boldsymbol{r_{ab}}$ to the radius of d shell $\boldsymbol{r_d}$ [fundamentals of magnetism]. Mn and Cr are examples of an antiferromagnetic materials with negative exchange integral while Fe,Co and Ni are ferromagnetic with a positive exchange integral.

In the general case of two spins presenting a relative angle, the cost in exchange energy can be expressed as:

$$\boldsymbol{E_{exchange} = -2\,J\,S^2 \sum_{ij} Cos\theta_{ij}} \tag{2.7}$$

Where $\boldsymbol{\theta_{ij}}$ is the angle between the spins $\boldsymbol{i}$ and $\boldsymbol{j}$. In the continuum approach defining the micro magnetism, the exchange energy, in a certain volume of a crystal, is written as:

$$\boldsymbol{E_{exchange} = A \int (\nabla m_x + \nabla m_y + \nabla m_z)^2\, dV} \tag{2.8}$$

$\boldsymbol{m_x}$, $\boldsymbol{m_y}$ and $\boldsymbol{m_z}$ are the direction cosines of magnetization with respect to the crystal axis. $\boldsymbol{A}$ is the exchange stiffness constant of the material. $\boldsymbol{A = (c\,J\,S^2)/a}$, $\boldsymbol{c}$ is a crystallographic structure dependent constant and $\boldsymbol{a}$ is the lattice parameter. $\boldsymbol{A}$ is expressed in Joules/meters.

The above equation can be written as a function of the exchange field $\vec{H}_{exchange}$ defined as follows:

$$\boldsymbol{E_{exchange} = -\mu_0\, \vec{H}_{exch} \,.\, \vec{M}} \tag{2.9}$$

$$\boldsymbol{\vec{H}_{exch} = \frac{2A}{\mu_0 M_s} \nabla^2 \vec{M}} \tag{2.10}$$

2.2.3 Demagnetization energy

The demagnetization energy (also called dipolar energy or magnetostatic energy) is related to the magnetic field generated from the magnet itself. Due to the Maxwell relation div B= 0, magnetic poles at the boundaries of the sample arise and create a field called demagnetization field H_d opposite to the magnetization. The demagnetizing field is at the origin of domain formation in ferromagnets and it is expressed as follows:

$$\vec{H}_d = -\mu_0[N_d].\vec{M} \tag{2.11}$$

With $\mathbf{N_d}$ is a 3x3 dimensionless demagnetizing tensor. It depends on the shape of the material. In the case of an ellipsoid, the coordinate system is oriented along its axis such as $[\mathbf{N_d}] = \mathbf{N_x} + \mathbf{N_y} + \mathbf{N_z}$. In the case of a sphere, $\mathbf{N_x} = \mathbf{N_y} = \mathbf{N_z} = \mathbf{1/3}$. In our case, we have the shape of a an infinitely thin film with the normal to the surface parallel to Z-axis, then, $\mathbf{N_x} = \mathbf{N_y} = \mathbf{0}$ and $\mathbf{N_z}$=1.

The energy associate with the demagnetizing field is expressed as follows:

$$E_{dem} = -\frac{\mu_0}{2}\int \vec{H_d}.\vec{M}dV \tag{2.12}$$

Substituting H_d in (2.12), where m_x, m_y, and m_z are the component of the magnetization in the x y z directions, we get the following relation:

$$E_{dem} = \frac{\mu_0 M^2 V}{2}(\mathbf{N_x}m_x{}^2 + \mathbf{N_y}m_y{}^2 + \mathbf{N_z}m_z{}^2) \tag{2.13}$$

Taking into account the case of thin films where $\mathbf{N_x} = \mathbf{N_y} = \mathbf{0}$ and $\mathbf{N_z}$=1, the demagnetization energy is written as:

$$\mathbf{E_{dem}} = +\frac{\mu_0 V}{2}(\mathbf{M}^2) \tag{2.14}$$

2.2.4 magneto-crystalline Anisotropy energy

Experimentally, the magnetization align naturally in a certain direction called easy axis. In the opposite case, the direction for which the applied field is maximum to align the magnetization is called the hard axis.

Magneto-crystalline anisotropy:

The magneto-crystalline anisotropy arises from the spin-orbit interaction [15 Van Vleck]. This interaction is due to the coupling of the electron's orbital moment, which reflects the symmetry of the crystal, and the spin angular momentum. Then, depending upon the symmetry of the crystal, the material will exhibit different easy axis directions. For example hexagonal material will show a uniaxial anisotropy while cubic materials will show four perpendicular easy axis directions.

In Figure 2.5, the *easy axis* requires low magnetic field to saturate the sample while the *hard axis* needs a higher magnetic field to rotate the magnetic moments to the corresponding direction.

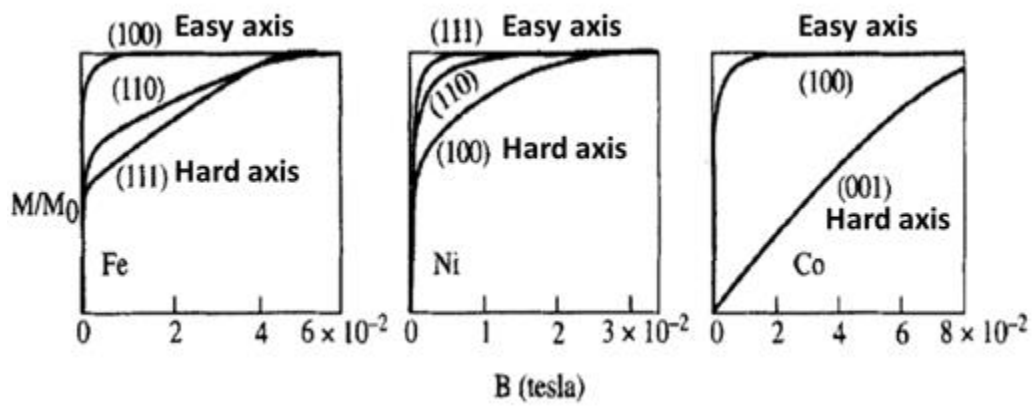

Figure 2.5: Magnetization in Fe, Co and Ni for applied fields in the easy and hard directions. The 110 direction for both Fe and Ni is known as the intermediate axis [2 Blundell].

i) Uniaxial anisotropy

Uniaxial anisotropy usually appears in hexagonal system and it is expressed by the following relation:

$$\boldsymbol{E_{uniax} = k_{u1} \sin \beta^2 + k_{u2} \sin \beta^2 + \cdots} \tag{2.15}$$

k_{ui} is the ith order anisotropy constant and β is the angle between the magnetization and the uniaxial anisotropy direction (i.e. single axis).

The sign of the anisotropy constant determine the direction of the easy and hard directions. To minimize the energy, if $\boldsymbol{k_{ui} > 0}$, then the minimum energy is achieved when $\theta = 0$ *or* $\theta = \pi$, therefore the easy axis direction will be along the anisotropy axis. But, if $\boldsymbol{k_{ui} < 0}$, then the minimum energy is achieved when $\theta = \pi/2$, then the easy axis lies perpendicular to the anisotropy axis.

Considering Z as the anisotropy axis, Figure 2.6 presents the energy landscape in the case of K >0.

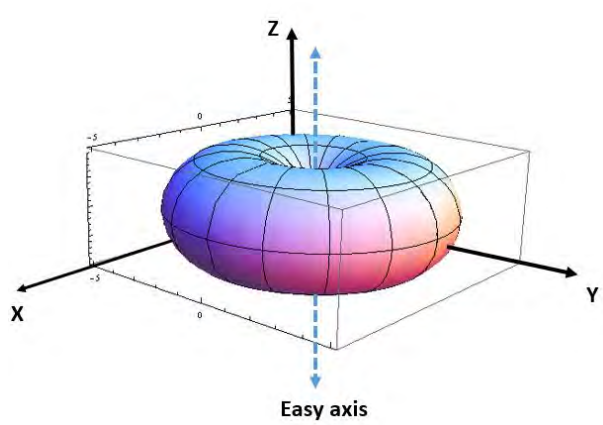

Figure 2.6: uniaxial anisotropy with $\boldsymbol{k_{ui} > 0}$.

ii) Cubic anisotropy

In the case of cubic material the cubic anisotropy can be expressed as:

$$\boldsymbol{E_{cubic} = K_{c1}\left(\alpha_x{}^2\alpha_y{}^2 + \alpha_y{}^2\alpha_z{}^2 + \alpha_z{}^2\alpha_x{}^2\right) + K_{c2}\,\alpha_x{}^2\alpha_y{}^2\alpha_z{}^2 + \cdots} \tag{2.16}$$

With K_{Ci} is the ith order cubic anisotropy constant and α_j are the director cosines defined as follows:

$$\boldsymbol{\alpha_x = \frac{M_x}{M_s} = \sin\theta\cos\varphi} \tag{2.17}$$

$$\boldsymbol{\alpha_y = \frac{M_y}{M_s} = \sin\theta\sin\varphi} \tag{2.18}$$

$$\boldsymbol{\alpha_x = \frac{M_x}{M_s} = \cos\theta} \tag{2.19}$$

If we replace the above relations in the $\boldsymbol{E_{cubic}}$, we get the first order $\boldsymbol{E_{cubic}}$ term:

$$\boldsymbol{E_{cubic} = K_{c1}\sin\theta^2\left(\cos\theta^2 + \sin\theta^2\cos\varphi^2\sin\varphi^2\right)} \tag{2.20}$$

The representation of the energy landscape, for $\boldsymbol{K_{c1} < 0}$ and $\boldsymbol{K_{c1} > 0}$, is shown in Figure 2.7. In the case of $\boldsymbol{K_{c1} < 0}$, the easy axes are the <110> directions. While for $\boldsymbol{K_{c1} > 0}$, they are along the <100> axes. The unit of anisotropy constant, in SI units, is J/meters^3.

In the next section, we will show how the difference in anisotropy constant sign and value affect the resonance frequency of a magnetic sample placed in an external magnetic field.

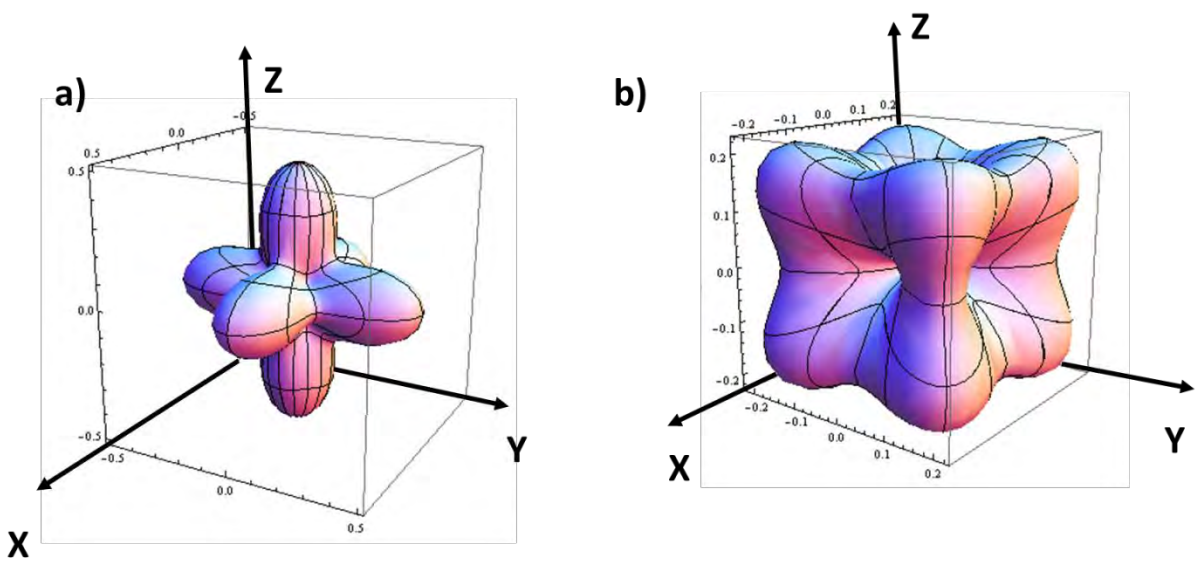

Figure 2.7: 3D presentation of the cubic anisotropy for a) $\boldsymbol{K_{c1} < 0}$ and b) $\boldsymbol{K_{c1} > 0}$.

2.3 Magnetization dynamics

In this section, the response of magnetization to a weak alternating field of several GHz is obtained from the Landau-Lifshitz-Gilbert equation of motion presented in subsection 2.3.1. We will discuss the effect of the relaxation mechanism.

2.3.1 Equation of motion LLG and its solution

When the magnetization in a ferromagnet is removed from its equilibrium position, it will undergo a precession around the direction of the effective field. The torque exerted on the magnetization is equal to $\vec{M} \wedge \vec{H}_{eff}$. Figure 2.8-a. The equation of motion governing the precession is expressed by:

$$\frac{d\vec{M}}{dt} = -\gamma\, \mu_0\, \vec{M} \wedge \vec{H}_{eff} \tag{2.21}$$

$\gamma = g\frac{|e|}{2m}$ is the gyromagnetic ratio for an electron of mass **m**. g is the Landé factor, without dimensions. It depends on the nature on the particle and on its environment via the orbital moment. In the case of a ferromagnetic material, the orbital moment is mainly quenched by the crystal field and then g is close to 2 (2.01 for $Ni_{84}Fe_{16}$ for example). In the case of a free electron, $\gamma/2\pi = 28\ GHz/T$.

Equation (2.21) doesn't take into account the energy losses, yet it shows that the magnetization will precess around an effective magnetic field for infinite time and this can't be true. At last, the radiation of the electromagnetic field in free space will lose energy. Many other mechanisms in ferromagnet are responsible for the energy losses during the precession of the magnetization in order that it get back to equilibrium after a few ns. In order to take this mechanisms into account. Landau and Lifshitz in 1935, [16 Landau and Lifshitz], introduced a relaxation coefficient λ, equivalent to a viscosity term, in the equation of motion:

$$\frac{d\vec{M}}{dt} = -\gamma\, \mu_0\, \vec{M} \wedge \vec{H}_{eff} - \frac{\gamma\mu_0\lambda}{{M_s}^2}\vec{M} \wedge (\vec{M} \wedge \vec{H}_{eff}\ ) \tag{2.22}$$

In (LL) equation (2.22); M_s is the magnetization saturation and λ is the relaxation factor and has the dimension of a magnetic field unit (A/m). Moreover, In 1955, and after the development of ferromagnetic resonance experiments [17 Bloembergen], Gilbert [18 Gilbert] added the phenomenological damping term, α, and the LL equation is transformed into LLG equation (2.23):

$$\frac{d\vec{M}}{dt} = -\gamma\, \mu_0\, \vec{M} \wedge \vec{H}_{eff} + \frac{\alpha}{M}\left(\vec{M} \wedge \frac{d\vec{M}}{dt}\right) \tag{2.23}$$

Where α, is a dimensionless phenomenological relaxation coefficient. The second term describes the time the magnetization takes to retain equilibrium position, parallel to $\vec{H}_{eff}$, The LLG equation is valid mainly in the case of small (linear approximation) perturbation of the magnetization. For large oscillation amplitude, other models have to be considered such as the Bloch Bloembergen relaxation term which is derived from the nuclear magnetic resonance relaxation. In this model, two relaxation times are considered, T_1 which

corresponds to the relaxation of the longitudinal component of the magnetization and T_2 which corresponds to the relaxation of the transverse component. However, in this work we only work in the small excitation regime and only the LLG equation will be used (Figure 2.8-b).

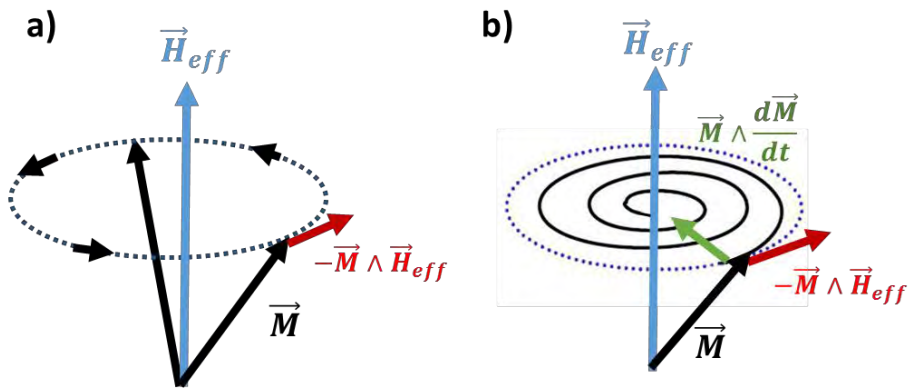

Figure 2.8: The magnetization precession on a constant orbit around an effective field a) without damping. The magnetization in b) is a damped motion to retain equilibrium position.

We are now interested in solving the LLG equation (2.23) in the case of small oscillation amplitude. We will first solve the equation without the damping term and then we will consider the effect of relaxation [3 Stancil and Prabhakar].

I. Solution of equation of motion without relaxation mechanism:

Let us consider a ferromagnetic material that is excited by an alternating microwave field applied perpendicular to the static magnetic field. Both the total external field and magnetization can be described as a time dependent perturbation expressions, $\vec{h}(t)$ and $\vec{m}(t)$ as follows:

$$\begin{cases} \vec{M} = \vec{M}_s + \vec{m}(t) \\ \vec{H} = \vec{H}_{ext} + \vec{h}(t) \end{cases} \tag{2.24}$$

Where $\vec{m}(t)$ and $\vec{h}(t)$ are small perturbation to the equilibrium magnetization and static applied field $\vec{M}_s$ and $\vec{H}_{ext}$, respectively.

By replacing (2.24) in (2.21), we get:

$$\frac{\partial \vec{m}}{\partial t} = -\gamma\, \mu_0 (\vec{M}_s \wedge \vec{H}_{ext} + \vec{M}_s \wedge \vec{h}(t) + \vec{m}(t) \wedge \vec{H}_{ext} + \vec{m}(t) \wedge \vec{h}(t)\,) \tag{2.25}$$

For single domain materials without anisotropy, $\vec{M}_s$ and $\vec{H}_{ext}$ are aligned together and their cross product will cancel. Also the last term in eq. 2.25 is neglected since $\vec{m}(t)$ *and* $\vec{h}(t)$ are

small in magnitude compared to the static terms. So we keep only linear terms in $\vec{m}(t)$ *and* $\vec{h}(t)$ .Equation (2.25) becomes:

$$\frac{\partial \vec{m}}{\partial t} = -\gamma\, \mu_0 (\vec{M}_s \wedge \vec{h}(t) + \vec{m}(t) \wedge \vec{H}_{ext}) \tag{2.26}$$

Assuming the static equilibrium field is along the Z axis, and the time dependence of $\vec{m}(t)$ *and* $\vec{h}(t)$ is of the form $e^{-i\omega t}$. Then the equation of motion for $\vec{m}(t)$ can be written as follows:

$$i\omega\vec{m} = -\gamma\, \mu_0\, \vec{h} \wedge \vec{M}_s + \gamma\, \mu_0 \vec{m} \wedge \vec{H}_{ext} \tag{2.27}$$

We define the following: $\omega_M = \gamma\, \mu_0\, M_s$ and $\omega_0 = \gamma\, \mu_0\, H_{ext}$. Equation 2.27 becomes:

$$i\omega\vec{m} = -\omega_M\, \vec{h} \wedge \vec{e}_z + \omega_0\, \vec{m} \wedge \vec{e}_z \tag{2.28}$$

In Cartesian coordinates, we get:

$$\begin{cases} i\omega\vec{m}_x = -\omega_M \vec{h}_y + \omega_0 \vec{m}_y \\ i\omega\vec{m}_y = +\omega_M \vec{h}_x - \omega_0 \vec{m}_x \\ i\omega\vec{m}_z = 0 \end{cases} \tag{2.29}$$

It is then possible to define the susceptibility that relates the dynamic magnetization to the oscillating field such as:

$$\vec{m} = \bar{\chi}.\, \vec{h} \tag{2.30}$$

$\bar{\chi}$ is the Polder tensor and is expressed as follows:

$$\bar{\chi} = \begin{bmatrix} \chi & i\kappa \\ -i\kappa & \chi \end{bmatrix} \tag{2.31}$$

With,

$$\chi = \frac{\omega_0 \omega_M}{\omega_0{}^2 - \omega^2} \qquad \textit{and} \qquad \kappa = \frac{\omega \omega_M}{\omega_0{}^2 - \omega^2} \tag{2.32}$$

The resonance conditions corresponds to the discriminant of the susceptibility tensor equal to zero, *i.e.* $\omega = \omega_0$. When the resonance conditions are fulfilled χ and κ diverge and so the component of the dynamic magnetization. In the next section, we demonstrate that the effect of damping avoids this divergence and majors the amplitude of the susceptibility component [3 Stancil and Prabhakar].

II. *Solution of equation of motion with relaxation mechanism:*

Starting with the eq. (2.23) and including the damping term we get:

$$i\omega\vec{m} = -\gamma\, \mu_0\, \vec{h}(t) \wedge \vec{M}_s + \gamma\, \mu_0 \vec{m}(t) \wedge \vec{H}_{ext} + \frac{i\omega\alpha}{M_s} \vec{m} \wedge \vec{M}_s \tag{2.33}$$

In analogy to equation 2.29, the above expression is written in Cartesian coordinates, and the static magnetic field is along the Z direction. Then 2.33 can be written:

$$i\omega\vec{m} = -\,\omega_M\,\vec{h}(t)\wedge\vec{e}_z + \;\omega_0\,\vec{m}(t)\wedge\vec{e}_z + i\omega\alpha\,\vec{m}(t)\wedge\vec{e}_z \tag{2.34}$$

Likewise equation 2.29, we get:

$$\vec{h} = (\overline{\chi})^{-1}.\,\vec{m}$$

$$\begin{pmatrix}\vec{h}_x\\ \vec{h}_x\end{pmatrix} = \frac{1}{\omega_M}\begin{pmatrix}\omega_0 + i\,\omega\alpha & i\,\omega\\ -i\,\omega & \omega_0 + i\,\omega\alpha\end{pmatrix}\begin{pmatrix}\vec{m}_x\\ \vec{m}_y\end{pmatrix} \tag{2.35}$$

The Polder susceptibility tensor $\overline{\chi}$ including the damping can be expressed as,

$$\overline{\chi} = \frac{1}{([\,\omega_0{}^2-\omega^2(1+\alpha^2)]^2+4\omega^2\,\omega_0{}^2\alpha^2)}\begin{bmatrix}\chi & i\kappa\\ -ik & \chi\end{bmatrix} \tag{2.36}$$

With,

$$\begin{cases}\chi = \omega_M\,\omega_0\left[\,\omega_0{}^2 - (1-\alpha^2)\omega^2\right] - i\,(\alpha\omega_M\omega\left[\,\omega_0{}^2 + (1+\alpha^2)\omega^2\right])\\ k = \omega_M\omega\left[\,\omega_0{}^2 - (1+\alpha^2)\omega^2\right] - i\,(2\alpha\omega_M\omega^2\,\omega_0)\end{cases} \tag{2.37}$$

The susceptibility χ is divided into a real χ' and an imaginary χ'' Part. In Figure 2.9, χ is calculated with Permalloy sample values ($\mu_0\,M_s = 1T, \gamma = 29 * 2\pi\frac{GHz}{T}, \omega = 9\,GHz$ *and* $\alpha = 0.01$). The real part of χ changes its sign, while the imaginary part passes through a maximum which indicates the resonance absorption field.

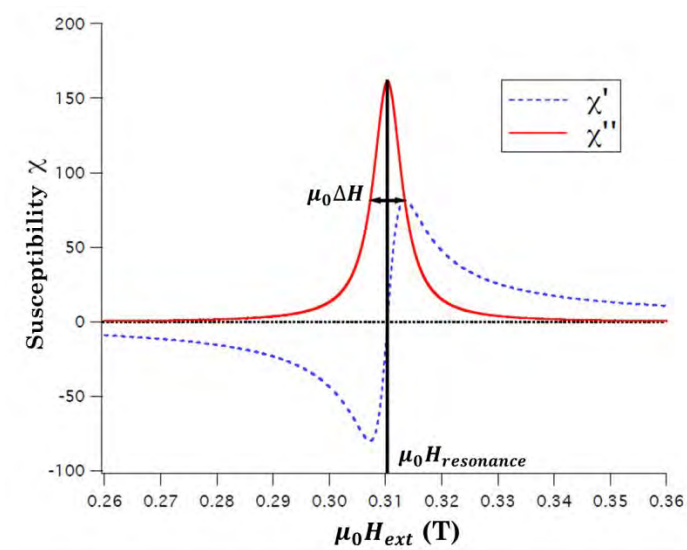

Figure 2.9: Real and imaginary part of the susceptibility tensor χ, adapted from [19 Ortiz].

The line width in a ferromagnetic resonance experiment is directly related to the damping term α through the relation:

$$\Delta\mathrm{H}_{\mathrm{Gilbert}} = \frac{\alpha}{\frac{\partial(2\pi f)}{\partial H}}\frac{\gamma}{M_S}\left(E_{\theta\theta} + \frac{1}{sin^2\theta_{eq}}E_{\varphi\varphi}\right) \tag{2.38}$$

The above expression is reduced to $\Delta\mathrm{H}_{\mathrm{Gilbert}} = \frac{2\alpha\omega}{\mu_0\gamma}$ for symmetric axes. In the case where additional, *i.e* extrinsic, contribution to the relaxation mechanisms is considered, the line width can be written as:

$$\Delta\mathrm{H} = \Delta\mathrm{H}_{\mathrm{Gilbert}} + \Delta H_0 \tag{2.39}$$

Where the extrinsic contribution, $\Delta H_0 = \Delta\mathrm{H}_{\mathrm{inh}} + \Delta\mathrm{H}_{\mathrm{mos}} + \Delta\mathrm{H}_{2\mathrm{mag}}$, will be discussed in section 2.5.

2.3.2 Ferromagnetic resonance in thin films

The ferromagnetic resonance corresponds to the uniform excitation of the magnetization in a ferromagnet with a small oscillating microwave field. Following equation 2.23, one has to replace the static field by the effective field that contains the exchange, the demagnetizing and crystal anisotropy fields:

$$\vec{H}_{eff} = \vec{H}_{ext} + \vec{H}_{demag} + \vec{H}_{anisotropy} + \vec{H}_{exchange} \tag{2.40}$$

The solution of the LLG equation for an arbitrary direction of the magnetization defined by the polar and azimuthal angle θ and φ has been given by Smit and Beljers [20 Smit and Belgers] and Suhl [21 Suhl]. Vectors $\vec{M}$, $\frac{d\vec{M}}{dt}$ and $\vec{H}_{eff}$ are expressed as follows:

$$\begin{cases} \vec{M} = M_s\vec{e}_r \\ \frac{d\vec{M}}{dt} = M_s\frac{d\theta}{dt}\vec{e}_\theta + M_s\sin\theta\frac{d\varphi}{dt}\vec{e}_\emptyset \\ \vec{H}_{eff} = -\frac{1}{\mu_0}\frac{\partial E_{tot}}{\partial M} = -\frac{1}{\mu_0}\left(\frac{E_{tot}}{M_s}\vec{e}_r + \frac{1}{M_s}\frac{\partial E_{tot}}{\partial\theta}\vec{e}_\theta + \frac{1}{M_s\sin\theta}\frac{\partial E_{tot}}{\partial\varphi}\vec{e}_\varphi\right) \end{cases} \tag{2.41}$$

To simplify equation (2.41), we define the following terms:

$$\begin{cases} \theta_H = -\frac{1}{\mu_0 M_s}\frac{\partial E_{tot}}{\partial\theta} = -\frac{1}{\mu_0 M_s}E_\theta \\ \varphi_H = -\frac{1}{\mu_0 M_s\sin\theta}\frac{\partial E_{tot}}{\partial\varphi} = -\frac{1}{\mu_0 M_s\sin\theta}E_\varphi \end{cases} \tag{2.42}$$

LLG equation (2.23) in spherical coordinates becomes:

$$\begin{pmatrix} 0 \\ M_s\frac{d\theta}{dt}\vec{e}_\theta \\ M_s\sin\theta\frac{d\varphi}{dt}\vec{e}_\varphi \end{pmatrix} = -\mu_0\gamma\begin{pmatrix} 0 \\ -M_s\varphi_H\vec{e}_\theta \\ M_s\theta_H\vec{e}_\varphi \end{pmatrix} + \frac{\alpha}{M_s}\begin{pmatrix} 0 \\ -{M_s}^2\sin\theta\frac{d\varphi}{dt}\vec{e}_\theta \\ {M_s}^2\frac{d\theta}{dt}\vec{e}_\varphi \end{pmatrix} \tag{2.43}$$

Replacing equation (2.42) in (2.43), we get the LLG equation of motion in spherical coordinates:

$$\begin{cases} \frac{d\theta}{dt} = (-\frac{\gamma}{M_s \sin\theta} E_\varphi - \frac{\alpha\gamma}{M_s} E_\theta)\vec{e}_\theta \\ \frac{d\varphi}{dt} = (\frac{\gamma}{M_s \sin\theta} E_\theta - \frac{\alpha\gamma}{M_s (\sin\theta)^2} E_\varphi)\vec{e}_\varphi \end{cases} \tag{2.44}$$

The interest in finding the equilibrium orientation of magnetization in the presence of an external field leads to the determination of the resonance frequency. The equilibrium conditions are achieved when the free energy of the system, F, is minimum with respect to the angles that determines the direction of magnetization, θ_{eq} and φ_{eq}, such that:

$$E_\theta = \frac{\partial E}{\partial \theta}\Big|_{\theta=\theta_{eq},\varphi=\varphi_{eq}} = 0 \; and \; E_\varphi = \frac{\partial E}{\partial \varphi}\Big|_{\theta=\theta_{eq},\varphi=\varphi_{eq}} = 0 \tag{2.45}$$

To obtain the resonance frequency, first we need to deviate the magnetization away from equilibrium and the above condition is not valid. In analogy to equation (2.24), $\boldsymbol{\theta}$ and $\boldsymbol{\varphi}$ will be expressed by a small harmonic oscillation around the equilibrium values:

$$\begin{cases} \theta - \theta_{eq} = \theta_A e^{-i\omega t} \\ \varphi - \varphi_{eq} = \varphi_A e^{-i\omega t} \end{cases} \tag{2.46}$$

Where θ_A and φ_A are amplitudes constants. Before proceeding with the calculation, equation (2.44) is converted as follows using Taylor expansion:

$$\begin{cases} \frac{d\theta}{dt} = (-\frac{\gamma}{M_s \sin\theta}(E_{\theta\varphi}\theta + E_{\varphi\varphi}\varphi) - \frac{\alpha\gamma}{M_s}(E_{\theta\theta}\theta + E_{\theta\varphi}\varphi)) \\ \frac{d\varphi}{dt} = (\frac{\gamma}{M_s \sin\theta}(E_{\theta\theta}\theta + E_{\theta\varphi}\varphi) - \frac{\alpha\gamma}{M_s (\sin\theta)^2}(E_{\theta\varphi}\theta + E_{\varphi\varphi}\varphi)) \end{cases} \tag{2.47}$$

Where $E_{\theta\varphi}$, $E_{\theta\theta}$ and $E_{\varphi\varphi}$ are the second derivative of the total energy with respect to $\boldsymbol{\theta}$ and $\boldsymbol{\varphi}$. Expression (2.46) is inserted in (2.47) to derive the following set of equations:

$$\begin{bmatrix} -i\omega + \frac{\gamma}{M_s \sin\theta_{eq}} E_{\theta\varphi} + \frac{\alpha\gamma}{M_s \sin\theta_{eq}} E_{\theta\theta} & \frac{\gamma}{M_s \sin\theta_{eq}} E_{\varphi\varphi} + \frac{\alpha\gamma}{M_s} E_{\theta\varphi} \\ -\frac{\gamma}{M_s \sin\theta_{eq}} E_{\theta\theta} + \frac{\alpha}{M_s (\sin\theta_{eq})^2} E_{\theta\varphi} & -i\omega - \frac{\gamma}{M_s \sin\theta_{eq}} E_{\theta\varphi} + \frac{\alpha\gamma}{M_s (\sin\theta_{eq})^2} E_{\varphi\varphi} \end{bmatrix} \begin{bmatrix} \theta \\ \varphi \end{bmatrix} = 0 \tag{2.48}$$

From the above equation, we can obtain the resonance frequency when the determinant is zero:

$$-\omega^2 + \left(\frac{\gamma^2}{{M_s}^2 (\sin\theta_{eq})^2} + \frac{\alpha^2\gamma^2}{{M_s}^2 (\sin\theta_{eq})^2}\right)\left(E_{\theta\theta}E_{\varphi\varphi} - {E_{\theta\varphi}}^2\right) - i\omega\frac{\alpha\gamma}{M_s}\left(\frac{E_{\varphi\varphi}}{(\sin\theta_{eq})^2} + E_{\theta\theta}\right) = 0 \tag{2.49}$$

In the case of $\alpha = 0$, the resonance frequency is obtained:

$$\omega_{res} = \frac{\gamma}{M_s \sin\theta_{eq}}\left[\left(E_{\theta\theta}E_{\varphi\varphi} - {E_{\theta\varphi}}^2\right)\right]^{1/2} \tag{2.50}$$

The above equation (2.50) is called Smit-Beljers formula. The result of this equation in the case of thin films considering $N_x = N_Y = 0$ and $N_Z = 1$, then demagnetizaion and Zeeman energy becomes:

$$E_{demag} = \frac{1}{2}\mu_0 M_s{}^2 (\cos\theta)^2 \tag{2.51}$$

$$E_{zeman} = -\mu_0 M_s H_{ext}[\cos\theta\cos\theta_H + \sin\theta\sin\theta_H\cos(\varphi - \varphi_H)] \tag{2.52}$$

Where θ, θ_H, φ and φ_H are defined in Figure 2.10.

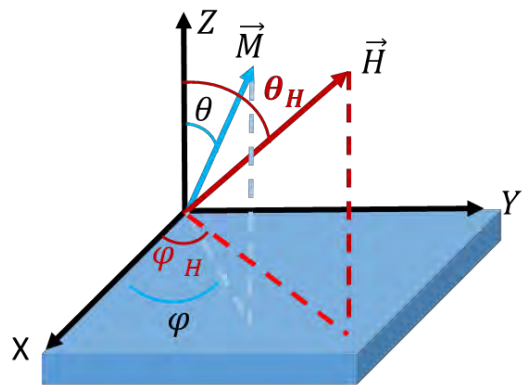

Figure 2.10: representation of magnetization $\vec{M}$ and the external magentic $\vec{H}_{ext}$ in cartesian coordinates.

The total energy in thin films is written as:

$$E = \frac{1}{2}\mu_0 M_s{}^2 (\cos\theta)^2 - \mu_0 M_s H_{ext}[\cos\theta\cos\theta_H + \sin\theta\sin\theta_H\cos(\varphi - \varphi_H)] + K_{c1}\sin\theta^2\left(\cos\theta^2 + \sin\theta^2\cos\varphi^2\sin\varphi^2\right) \tag{2.53}$$

Substituting equation (2.53) in Smit-Beljers formula (2.50), we get:

I. In plane magnetization: Parallel to X-axis ($\theta = \frac{\pi}{2}, \varphi = 0$)

$$\omega_{res} = \mu_0\gamma[(H_{ext} + H_k)(H_{ext} - \frac{H_k}{2} + M_s)]^{1/2} \tag{2.54}$$

II. In plane magnetization: 45° from the X-axis ($\theta = \frac{\pi}{2}, \varphi = \frac{\pi}{4}$)

$$\omega_{res} = \mu_0\gamma[(H_{ext} - H_k)(H_{ext} - H_k + M_s)]^{1/2} \tag{2.55}$$

III. Out-of-Plane magnetization: : Parallel to Z-axis ($\theta = 0$)

$$\omega_{res} = \mu_0\gamma(H_{ext} - H_k - M_s) \tag{2.56}$$

With $H_k = \frac{2|K_{c1}|}{M_s}$ is the anisotropy magnetic field. The above three equations are valid for $K_{c1} < 0$. If $K_{c1} > 0$, then a negative sign must be replaced in the equation before H_k. In the next paragraph, a schematic presentation of equations (2.54) and (2.55) for different negative K_{c1} is shown in Figures 2.11.

In Figure 2.11, the resonance frequency is plotted as a function of the external magnetic field at 0 and 45° rom the x-axis. The easy and hard axes of magnetization are found with a 45° orientation with respect to each other.

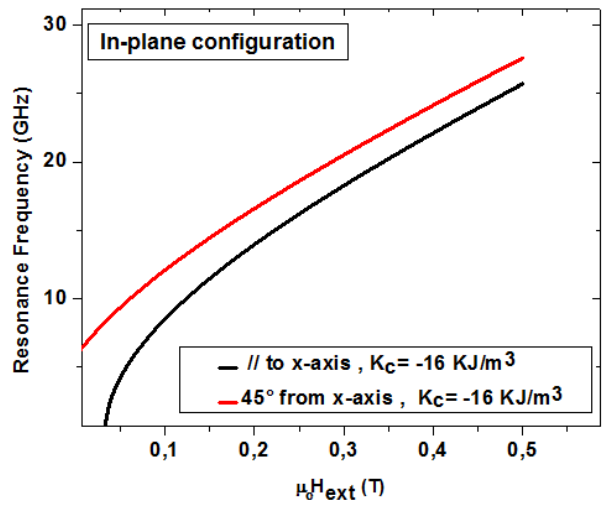

Figure 2.11: Resonance frequency as a function of an applied external field for in-plane configuration (θ=90°). The solid black lines represent the in-plane orientations when ϕ=0°, while the red line represents the in-plane orientations when ϕ=45° from x-axis. Simulation was done with M_s=1.25 T, $\frac{\gamma}{2\pi} = 28.7\ GHz/T$, and K_c=-16 Kj/m3.

For out-of-plane magnetization, for an applied field sufficient to saturate the magnetization, the resonance frequency has a linear behavior following equation (2.56), Fig 2.12. The slope of the frequency as a function of external magnetic field curve is equal to the gyromagnetic ratio $\boldsymbol{\gamma}$.

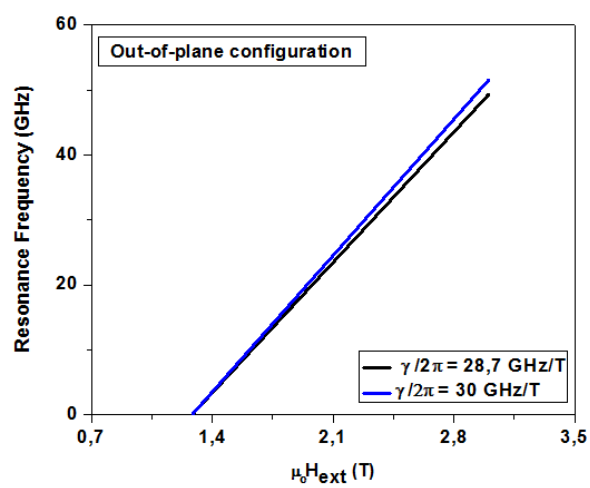

Figure 2.12: Resonance frequency as a function of an external magnetic field for out-of-plane configuration (θ=0°). The blue line is corresponds to $\frac{\gamma}{2\pi} = 30\ GHz/T$, while the black line corresponds to $\frac{\gamma}{2\pi} = 28.7\ GHz/T$.

2.4 Spin waves

In the previous section, we have presented the fundamental mode or (uniform mode) of magnetization dynamics. This was described by the uniform precession of magnetic

moments around the effective field when it is subjected to a small uniform microwave excitation field. In this case all the spins precess in-phase at the same frequency and are not propagative (*i.e.* the wave vector $\vec{\boldsymbol{K}} = \mathbf{0}$) as shown in Figure 2.13-a. In the case of a non-uniform microwave excitation, the spins will not oscillate spatially in phase anymore. The phase perturbation will then propagate in the material with a wave vector $\vec{\boldsymbol{K}} \neq \mathbf{0}$. That is what is called spin waves. In this case, the neighboring spins will precess with a phase shift at a given frequency which leads to a propagation of the spins as shown in Figure 2.13-b. Spin waves were first introduced by Bloch in 1930's [22 Bloch] and they are described as an elementary excitation in a ferromagnetic material. In this section, we will briefly present the magnetostatic regime as well as the main contribution to spin waves theory.

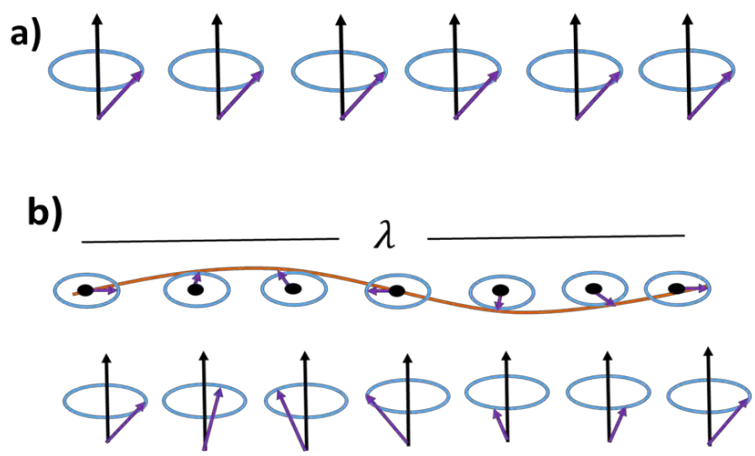

Figure 2.13: a) uniform mode of magnetic excitation and b) spin waves with a wave length $\boldsymbol{\lambda}$.

2.4.1 Magnetostatic regime

In order to obtain the *dispersion relation* ($\omega = f(\vec{K})$), we use both the susceptibility expression and the continuity conditions of Maxwell's equation for electromagnetic waves. Let's consider the spin wave amplitude to be of the following form:

$$\boldsymbol{A}(\vec{\boldsymbol{r}}) = \boldsymbol{exp}^{(i\vec{\boldsymbol{k}}.\vec{\boldsymbol{r}})}\boldsymbol{U_K}(\vec{\boldsymbol{r}}) \tag{2.57}$$

$\vec{\boldsymbol{k}}$ is the wave vector and has a magnitude of $|K| = \frac{\boldsymbol{2\pi}}{\boldsymbol{\lambda}}$ with $\boldsymbol{\lambda}$ being the spin wave wavelength. $\boldsymbol{U_K}(\vec{\boldsymbol{r}})$ is a periodic function that satisfy the crystal periodicity. In the next subsection, we will follow the method introduce in [23 Damon and Eshbach] to find the dispersion relation in the magnetostatic regime.

2.4.1.1 Magnetostatic modes

Before, we didn't take into consideration the electrical variable influence on the magnetization dynamics analysis. Here, we will show how the magnetic and electrical variables are related.

Considering the Maxwell equations:

$$\begin{cases} \vec{\nabla} \wedge \vec{H} = \frac{\partial \vec{D}}{\partial t} + \vec{J} \\ \vec{\nabla} \wedge \vec{E} = -\frac{\partial \vec{B}}{\partial t} \\ \vec{\nabla} . \vec{D} = \rho \\ \vec{\nabla} . \vec{B} = 0 \end{cases} \tag{2.58}$$

Where, $\vec{H}$ is the magnetic field in (A/m),$\vec{D}$ is the electric displacement in (C/m^2), $\vec{J}$ is the electric current density in (A/m^2), $\vec{E}$ is the electric field in (V/m), ρ is the electric charge density in (C/m^3) and $\vec{B}$ is the magnetic induction field in (T). $\vec{B}$ is related to the magnetic field $\vec{H}$ and polder tensor $\bar{\chi}$ by the following relation:

$$\vec{B} = \mu_0(\vec{H} + \vec{M}) = \mu_0(\bar{I} + \bar{\chi})\vec{H} = \bar{\mu}\vec{H} \tag{2.59}$$

Where $\bar{I}$ an identity matrix and μ is the permeability. $\bar{I} + \bar{\chi}$ can be expressed, after the Polder tensor derived in equation (2.31), as follows:

$$\bar{I} + \bar{\chi} = \bar{\mu} = \mu_0 \begin{bmatrix} 1+\chi & i\kappa & 0 \\ -ik & 1+\chi & 0 \\ 0 & 0 & 1 \end{bmatrix} \tag{2.60}$$

The electric displacement and the current density are related to electric field by the following formula:

$$\begin{cases} \vec{D} = \epsilon \vec{E} \\ \vec{J} = \sigma \vec{E} \end{cases} \tag{2.61}$$

ϵ is the permittivity and σ is the electrical conductivity.

Let us consider that the different electrical and magnetic fields have a spatial and time dependent function of the form $exp^{i(\vec{k}.\vec{r}-\omega t)}$, Maxwell's equations can thus be written in the following form:

$$\begin{cases} i\vec{K} \wedge \vec{H} = -i\omega\vec{D} + \vec{J} \\ \vec{K} \wedge \vec{E} = -\omega\vec{B} \\ i\vec{K} . \vec{D} = \rho \\ \vec{K} . \vec{B} = 0 \end{cases} \tag{2.62}$$

By replacing equation (2.59) and (2.61) in the first two equations of (2.62) and crossing K into both sides, we get:

$$\vec{K} \wedge \vec{K} \wedge \vec{H} = -\omega^2\epsilon\mu_0(\bar{I} + \bar{\chi})\vec{H} - i\omega\sigma\,\mu_0(\bar{I} + \bar{\chi})\vec{H} \tag{2.63}$$

Equation (2.62) can be simplified as follows:

$$\vec{K} \wedge \vec{K} \wedge \vec{H} = -{k_0}^2(\bar{I} + \bar{\chi})\vec{H} \tag{2.64}$$

With,

$${k_0}^2 = \omega^2\mu_0(\epsilon + \frac{i\sigma}{\omega}) \tag{2.65}$$

Expression (2.65) refers to the wave number for a propagating wave in a non-magnetic medium. If $\boldsymbol{\epsilon} \gg \boldsymbol{\sigma}/\boldsymbol{\omega}$, then the material is said to be dielectric with a wave number $\boldsymbol{k_0} = \boldsymbol{\omega}/\boldsymbol{c}$, with $\boldsymbol{c}$ is the speed of light. Whereas, if $\boldsymbol{\epsilon} \ll \boldsymbol{\sigma}/\boldsymbol{\omega}$, the material behaves as a metal.

From equation (2.64), we can calculate the norm of curl $\vec{\boldsymbol{H}}$ as follows:

$$\left|\vec{\boldsymbol{\nabla}} \wedge \vec{\boldsymbol{H}}\right| = \left|\vec{\boldsymbol{K}} \wedge \vec{\boldsymbol{H}}\right| = \frac{\left|\vec{\boldsymbol{K}} \wedge \vec{\boldsymbol{K}} \wedge \vec{\boldsymbol{H}}\right|}{\left|\vec{\boldsymbol{K}}\right|} = \frac{\boldsymbol{k_0}^2}{K}\left|(\bar{\boldsymbol{I}} + \bar{\boldsymbol{\chi}})\vec{\boldsymbol{H}}\right| \tag{2.66}$$

From the previous equation, we note that for high values of K such that $\boldsymbol{K} \gg \boldsymbol{k_0}$, curl $\vec{\boldsymbol{H}} \rightarrow \boldsymbol{0}$. This approximation is called the magnetostatic approximation. In this case the magnetic and electric part are not coupled anymore. Maxwell's equations can then be written as:

$$\begin{cases} \vec{\boldsymbol{\nabla}} \wedge \vec{\boldsymbol{h}} = \boldsymbol{0} \\ \vec{\boldsymbol{\nabla}} \wedge \vec{\boldsymbol{e}} = \boldsymbol{i\omega}\vec{\boldsymbol{b}} \\ \vec{\boldsymbol{\nabla}}.\vec{\boldsymbol{b}} = \boldsymbol{0} \end{cases} \tag{2.67}$$

$\vec{\boldsymbol{h}}$, $\vec{\boldsymbol{b}}$, and $\vec{\boldsymbol{e}}$ are the time dependent dynamic components of $\vec{\boldsymbol{H}}$, $\vec{\boldsymbol{B}}$, and $\vec{\boldsymbol{E}}$, respectively.

As curl h = 0 we can define a magnetostatic potential $\boldsymbol{\psi}$ such as: $\vec{\boldsymbol{h}} = -\vec{\boldsymbol{\nabla}}\boldsymbol{\psi}$

Then $\vec{\boldsymbol{\nabla}}.\vec{\boldsymbol{b}}$ can be expressed as follows:

$$\vec{\boldsymbol{\nabla}}.\vec{\boldsymbol{b}} = \vec{\boldsymbol{\nabla}}\left((\bar{\boldsymbol{I}} + \bar{\boldsymbol{\chi}})\vec{\boldsymbol{\nabla}}\boldsymbol{\psi}\right) = \boldsymbol{0} \tag{2.68}$$

From equation (2.68) and assuming that $\boldsymbol{\chi}$ and $\boldsymbol{k}$ are independent on position, we deduce the following:

$$(\boldsymbol{I} + \boldsymbol{\chi})\left[\frac{\partial^2\boldsymbol{\psi}}{\partial x^2} + \frac{\partial^2\boldsymbol{\psi}}{\partial y^2}\right] + \frac{\partial^2\boldsymbol{\psi}}{\partial z^2} = \boldsymbol{0} \tag{2.69}$$

The previous equation is called the ***Walker's* equation** [24 Walker] and its solutions are referred to as the ***magnetostatic modes***.

If we consider that the magnetostatic potential $\boldsymbol{\psi}$ can be written in the form of $\boldsymbol{exp}^{(\boldsymbol{i}\vec{\boldsymbol{K}}.\vec{\boldsymbol{r}})}$, walker equation becomes:

$$(\boldsymbol{I} + \boldsymbol{\chi})\left[\boldsymbol{k_x}^2 + \boldsymbol{k_y}^2\right] + \boldsymbol{k_z}^2 = \boldsymbol{0} \tag{2.70}$$

Equation (2.70) clearly connects the wave vector $\boldsymbol{k}$ to the frequency (ω) in $\boldsymbol{\chi}$.

Now if we consider that the magnetic field is applied along Z-axis (the direction of external magnetic field), and the spin wave propagate with angle $\boldsymbol{\theta}$ with respect to Z axis. Here we consider an infinite medium Equation (2.70) becomes:

$$\begin{cases} \boldsymbol{k_x}^2 + \boldsymbol{k_y}^2 = \boldsymbol{k}^2\sin^2\boldsymbol{\theta} \\ \boldsymbol{k_z}^2 = \boldsymbol{k}^2\cos^2\boldsymbol{\theta} \end{cases} \tag{2.71}$$

Substituting equation (2.71) in (2.70) yields to:

$$\boldsymbol{\chi}\sin^2\boldsymbol{\theta} = -\boldsymbol{1} \tag{2.72}$$

This can be expressed in terms of frequency using equation (2.32) for $\boldsymbol{\chi}$. This gives the following:

$$\chi \sin^2 \theta = \frac{\omega_0 \omega_M \sin^2 \theta}{{\omega_0}^2 - \omega^2} \tag{2.73}$$

Simplifying equation (2.73), we get:

$$\omega = \left[\omega_0(\omega_0 + \omega_M \sin^2 \theta)\right]^{1/2} \tag{2.74}$$

We notice that equation (2.74) is independent of the wave vector $\boldsymbol{k}$. This is valid for an infinite medium. The correspondence between $\boldsymbol{\omega}$ and $\boldsymbol{k}$ will be found by applying the boundary conditions in the Maxwell equation. However, important comments can already be stated from 2.74. Indeed, the frequency of the spin waves depends on the propagation direction θ. We deduce that the resonance frequency is bounded between the two values [3 Stancil and Prabhakar]:

$$\omega_0 \leq \omega \leq [\omega_0(\omega_0 + \omega_M)]^{1/2} \tag{2.75}$$

The previous band of frequencies is called '*spin wave manifold*'.

In thin films, the magnetostatic modes are determined by the direction of the wave vector, $\boldsymbol{k}$, with respect to the applied external field in-plane or out-of-plane.

We are now interested in solving Walker's equation (2.69) to obtain the dispersion relation for magnetostatic spin waves propagating normally or tangentially in magnetized thin films. This leads us to the three principal configurations of magnetostatic waves in thin films, presented as follows:

2.4.1.1.1 Magnetostatic Forward Volume Wave (MSFVW):

In this case, the magnetic external field is applied perpendicular to the surface plane of the material and the magnetization, $\vec{M}$ is oriented out-of-plane ($\vec{M} \uparrow\uparrow \vec{H_0}$). If we have a propagative spin wave vector in the plane of the film such that (($\vec{M} \uparrow\uparrow \vec{H_0}$) $\perp \vec{k}$), then this configuration is known as the MSFVW.

For spin waves propagating in a thin film with a wave vector; $\vec{k} = \vec{k}_t + \vec{k}_z$ and $\vec{k}_t = \vec{k}_x + \vec{k}_y$; Kalinikos derived an explicit dispersion relation of the frequency $\boldsymbol{\omega}$ for the lowest order $\boldsymbol{n = 0}$ **,** where $\boldsymbol{n}$ is the stationary condition inside the film's thickness [25 Kalinikos]. The dispersion relation is then written as follows:

$$\omega^2 = \omega_0[\omega_0 + \omega_M(1 - \frac{1-exp^{-k_t d}}{k_t d})] \tag{2.76}$$

Where d is the thickness of the film.

2.4.1.1.2 Magneto static Backward Volume waves (MSBVW):

In this configuration the external magnetic field is applied parallel to the sample's plane. The magnetization, $\vec{M}$ is magnetized in-plane and the wave vector propagates in such a way that (($\vec{M} \uparrow\uparrow \vec{k}$). This configuration is called MSBVW.

The propagation spin wave vector this time has the form of $\vec{k} = \vec{k}_t + \vec{k}_y$ with $\vec{k}_t = \vec{k}_z$. Kalinikos also derived an explicit form of the dispersion relation for lowest order mode (fundamental mode) $n = 1$:

$$\omega^2 = \omega_0[\omega_0 + \omega_M(\frac{1-exp^{-k_z d}}{k_z d})] \tag{2.77}$$

Then, the phase and group velocities of MSBVW propagate in opposite direction.

2.4.1.1.3 Magnetostatic Surface Wave (MSSW):

We consider in this case that the propagating waves are perpendicular to an in-plane external magnetic field such that ($\vec{M} \perp \vec{K}$). This configuration is called the MSSW or the Damon-Eshbach mode [23 Damon and Eshbach]. The dispersion relation for MSSW is derived by solving the Walker's equation and is written as:

$$\omega^2 = \omega_0(\omega_0 + \omega_M) + \frac{\omega_M{}^2}{4}[1 - exp^{-2kd}] \tag{2.78}$$

Similarly to MSBVW this dispersion relation of MSSW clearly depends on the thickness of the magnetic film d and on the magnitude of the wave vector. One of the most important feature of MSSW is their evanescent character in the thickness of the film. This is why they are called surface waves. This also implies that depending on the direction of $\vec{K}$ with respect to $\vec{M}$, the wave will propagate on the upper or lower surface of the material. Finally, MSSW have group and phase velocities propagating in the same direction.

The graphical presentation of all three magnetostatic waves is presented in Figure 2.14.

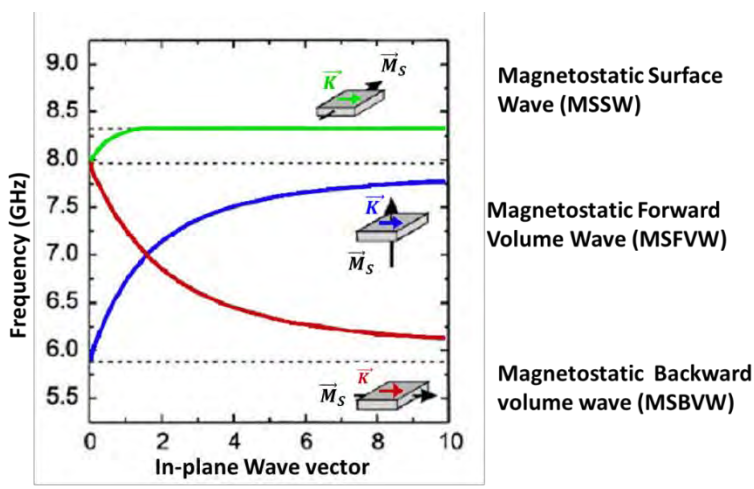

Figure 2.14: Topology of spin wave modes in a magnetic film as a function of the direction of magnetization and the in-plane wave vector [26 Demokritov].

2.4.2 Spin waves in the exchange regime

We are now interested in solving the dispersion relation (2.78) taking into account the exchange interaction term.

Starting from equation (2.9), the operator ∇^2 could be replaced by $-\boldsymbol{k^2}$. Then it is possible to replace the resonance frequency $\boldsymbol{\omega_0}$ by $\boldsymbol{\omega_0 + \gamma \frac{2A}{M_s} k^2}$. The dispersion relation thus becomes:

$$\boldsymbol{\omega^2 = \left(\omega_0 + \gamma \frac{2A}{M_s} k^2\right) + \left(\omega_0 + \omega_M \sin^2 \theta + \gamma \frac{2A}{M_s} k^2\right)} \tag{2.79}$$

Rado and Weertman [27 Rado & Weertman] have studied the modification of the spin waves ferromagnetic resonance due to the influence of exchange interaction. The exchange interaction is assumed to be at the interface of the magnetic layer where a surface uniaxial anisotropy exist. In this configuration, boundary condition are taken into account at the interface of the layer in addition to the electromagnetic ones in order to solve the equation of motion. Soohoo *et al.* have proposed a general exchange boundary conditions in their paper [28 Soohoo] such that:

$$\boldsymbol{\frac{\partial m_x}{\partial z} + p\, m_x \cos(2\theta) = 0 \;\; and \;\; \frac{\partial m_y}{\partial z} + p\, m_y \cos^2 \theta = 0} \tag{2.80}$$

$\boldsymbol{p}$ is the *pinning* factor and corresponds to the spin states at the interface. The condition $\boldsymbol{p=0}$ represents the free spins. A perfect pinning corresponds to $\boldsymbol{p \to \infty}$, which means that there is a complete blockage of spins at the interface [29 Kittel].

2.4.2.1 Standing Spin waves (SSW)

Standing Spin waves (SSW) were first predicted theoretically by Kittel [29 Kittel] and were first experimentally demonstrated by Seavey and Tannendwald [30 Seavey and Tannendwald]. SSW belongs to the stationary family of magnetostatic modes. The wave vector of SSW is parallel to the normal of the film. These waves undergo reflections at the interfaces leading to a stationary state. This state depends on the thickness of the layer "$\boldsymbol{d}$" and pinning conditions. Using condition (2.80), we can solve for k_z the two pinning parameters at each interface as follows:

$$\boldsymbol{\cot k_z d = \frac{{k_z}^2 - p_1 p_2}{k_z (p_1 p_2)}} \tag{2.81}$$

Where $\boldsymbol{p_1}$ and $\boldsymbol{p_2}$ are the pinning factors at the two films surfaces. If $\boldsymbol{p_1 = p_2 = p}$, expression (2.81) becomes:

$$\begin{cases} \boldsymbol{\cot\left(\frac{k_z d}{2}\right) = \frac{k_z}{p}} \\ \boldsymbol{-\tan\left(\frac{k_z d}{2}\right) = \frac{k_z}{p}} \end{cases} \tag{2.82}$$

From equation (2.79), if we consider only the exchange term into account, then the resonance frequency becomes:

$$\boldsymbol{\omega_n = \omega_0 - \omega_M + \gamma \frac{2A}{M_s} k_{z\,n}^2} \tag{2.83}$$

Equation (2.83) corresponds to the case when magnetization is out of plane. $k_{z,n}^2$ (For n=1, 2, 3 …) is the solution for the two equations in (2.82). Expression (2.83) can be written as:

$$\omega_n = \mu_0\gamma(H_0 - M_s + \frac{2A}{\mu_0 M_s} k_{z\,n}^2) \tag{2.84}$$

In the case of perfect pinning, $k_{z,n} = n\pi / d$ and if $p = 0$, $k_{z,n} = (n-1)\pi / d$.

If we consider the magnetization in the plane of the film, then we get the resonance frequency as:

$$\omega_n^2 = (\omega_M + \omega_0 + \gamma \frac{2A}{\mu_0 M_s} k_{z\,n}^2)(\omega_0 + \gamma \frac{2A}{\mu_0 M_s} k_{z\,n}^2) \tag{2.85}$$

One major interest in the measurement of such standing spin waves modes that it gives access to the exchange constant $\boldsymbol{A}$ value.

2.5 Magnetization relaxation mechanism

In this section, we will focus on the different mechanisms that contribute to the intrinsic and extrinsic relaxation processes of magnetization relaxation. The dissipative term in equation (2.23) described by the phenomenological damping coefficient $\boldsymbol{\alpha}$, contains contribution from both intrinsic and extrinsic relaxation mechanisms. Experimentally, $\boldsymbol{\alpha}$ is measured through the line width of the magnetic susceptibility in equation (2.39). The magnetization relaxation is governed by different energy dissipation mechanisms summarized in Figure 2.15.

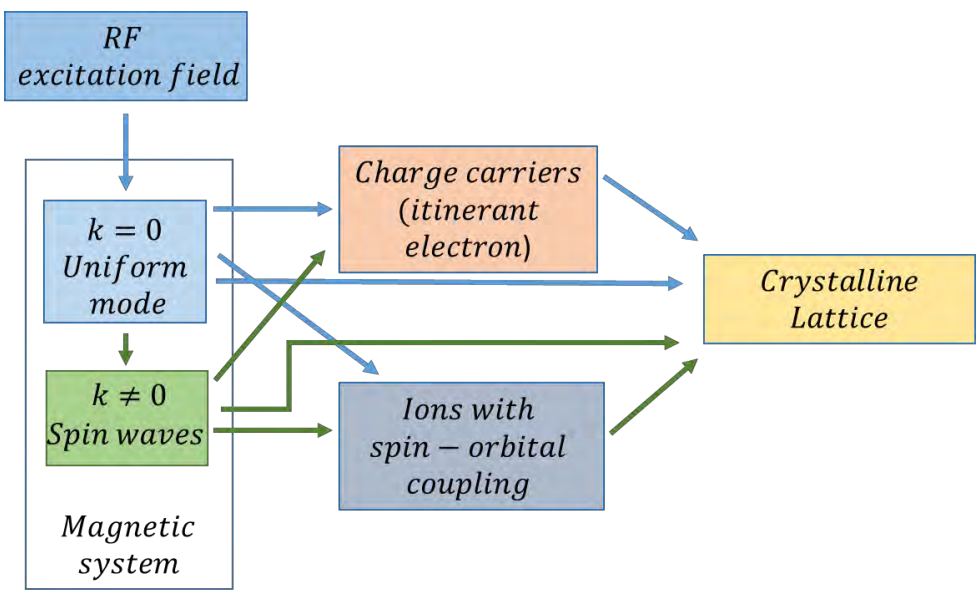

Figure 2.15: graphical presentation of the flow of energy from between the magnetic system and other systems when RF field excites the uniform modes [4 Gurevich and Melkov].

Relaxation processes, (energy dissipation), result from the energy distribution between the magnetic excitations (magnons) and the crystal vibrations (phonons) or the conduction electrons. Magnons-magnons relaxation is another relaxation mechanisms. These processes are divided into two configurations: the *spin-spin* and *spin-lattice* relaxation processes. The spin-spin relaxation processes can be caused by defects in the crystal [4 Gurevich and Melkov]. In most cases, the transferred energy to the lattice results in heating. The spin-lattice relaxation is divided into two processes: First, the *direct spin-lattice* process that is based on the direct energy transfer to the lattice upon the destruction of magnons and the creation of phonons. Second, the *indirect spin-lattice* process that is based on the energy transfer from magnons to the lattice by electron scattering.

In this section, we will present the basics of relaxation mechanisms in ferromagnets. As this is a very complicated topic a complete description is above the goal of this manuscript. For more details the reader is invited to refer to the references cited below.

2.5.1 Intrinsic relaxation processes

The intrinsic contribution to damping corresponds to the natural mechanisms allowing dissipation of the energy in order that the magnetization gets back to its equilibrium position. For example any precessing dipole radiates energy in free space and loses energy (radiation losses). In ferromagnets, there are more efficient dissipative processes. Then we have two main contributions, one corresponds to the relaxation of magnons by scattering with the conduction electrons and the second one corresponds to direct coupling of the magnetic modes with the phonons. We will also consider other mechanisms such as the dissipation due to eddy current which is the most important relaxation in thick metallic sample.

Let's note that there is no complete theory that describes the magnetic losses in dynamic experiments. However, several models have been developed for ferromagnets since the pioneering work of Kittel, Van Vleck or more recently by Heinrich or Kamberský [34-39].

- ***Collision of magnons with itinerant electrons***

In a metallic ferromagnet, the major source of damping is generally the electron-magnon interaction. Two mechanisms arise depending if the spin of the conduction is conserved or not. A very complete description of the different mechanisms can be found in [40 Woltersdorf].

1- *s-d* interaction: spin-flip scattering

Electron-magnon collision has been described by Berger in 1970's [31 Berger] as the collision of a magnon of energy $E = \hbar\omega_q$ with an itinerant electron of energy ε_K and spin state σ (σ can be $\pm\frac{1}{2}$). Figure 2.16 can be described as the creation and annihilation of electron-hole pair as a result of the collision of magnons and itinerant electrons by s-d exchange interaction. The itinerant electron is transferred to a higher energy defined as ε_{k+q} with a spin state σ'. Due to the conservation of angular momentum, itinerant electron has to flip its spin when coherently scattered by a magnon. If the electron hole pair undergoes a coherent scattering event, with a phonon for example, a coherent magnon will be reemitted. This mechanism leads to a renormalization of the landé *g*-factor [32 Heinrich]. The g-factor is related to both electron hole pair excitation spin flip time τ_{sf} and the momentum relaxation time τ_m as follows:

$$\frac{\tau_{sf}}{\tau_m} = \frac{1}{(g-2)^2} \tag{2.86}$$

Where time τ_{sf} is the electron hole pair excitation spin flip time and τ_m the momentum relaxation time. Details of obtaining τ_{sf} and τ_m can be found in [41 Dubois, 42 valet et Fert].

In the case where the electrons undergoes an incoherent scattering process (with a phonon or a magnon), the dephasing of the reemitted magnons leads to an average loss of coherence and then to damping. This process leads to a linear dependence of the linewidth with the frequency, in agreement with a Gilbert like term and can be expressed as a function of the density of states at fermi level Z_f , the spin flip time and the square of the g-factor [43 Pelzl].

Where τ is the electron scattering time.

In half metals such events are not possible due to the full spin polarization. This explains why the damping coefficient in these materials, such as Co_2MnSi are much lower than usual ferromagnetic (Fe, Ni, Co). However magnon-electron relaxation without spin flip is still occurring.

$$\alpha_{s-d} = (\gamma\hbar^2\pi/\mu_0 M_s)Z_f(g-2)^2/\tau \tag{2.87}$$

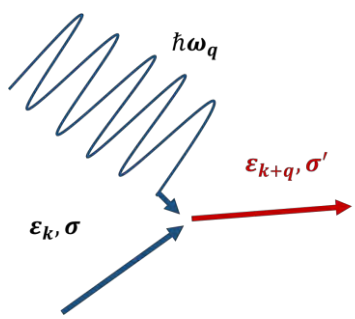

Figure 2.16: Collision between a Spin wave (a magnon) with energy $\hbar\omega_q$ and an itinerant electron with energy ε_K and spin state σ results in creation of an itinerant electron with momentum $k+q$ and spin orientation σ'.

2- Spin-Orbit relaxation: non spin-flip scattering

Electron-magnon scattering without spin flip is due to the spin orbit interaction. This effect has been described by Kamberský [33 Kamberský].

A classical representation of this effect is referred as the "breathing fermi surface". When the magnetization precesses, the Fermi surface has to be distorted periodically. However such a repopulation of the energy levels for the electrons can be done only with a timescale equal to momentum relaxation time T_m. Then a phase lag appears between the precessing magnetization and the Fermi surface oscillations leading to a global loss of coherence and then induces damping.

Recent work by Kamberský [35, 36, 37 Kamberský] and Gilmore [44 Gilmore] based on first principle calculations showed that the spin orbit relaxation is the dominant mechanism in relaxation processes in ferromagnetic materials. In this model, the relaxation rate is proportional to the spin-orbit coupling constant λ_{SO} and the damping factor. The corresponding damping coefficient is expressed as:

$$\alpha_{SO} = (\gamma\hbar\pi/\mu_0 M_s) Z_f \lambda_{SO}^2 (g-2)^2 * \tau \tag{2.88}$$

Following the approach of Kittel, the quantity $(g-2)$ can be expressed as the ratio of the orbital to spin moment ($g - 2 = 2\left(\frac{\mu_L}{\mu_s}\right)$). This is valid for small orbital moment but in ferromagnet this is valid due to the quenching of the orbital by the crystal field. Then from equation 2.88, we conclude that the Gilbert damping provides a sensitive probe of spin-orbit effects and if there is any shift in the g-factor that is related to the spin-orbit coupling [43 Pelzl].

- ***Intrinsic relaxation mechanisms induced by Eddy current***

In thick metallic sample, a major source of relaxation comes from the eddy current induced either by the oscillating pumping field or directly by the precessing magnetization itself.

It is possible to demonstrate that they induce a component of the spin wave vector perpendicular to the film surface. This additional wave vector is of the form $k = \frac{1+i}{\sqrt{2}\,|\delta|}$ with $\boldsymbol{\delta}$ the skin depth defined as:

$$\boldsymbol{\delta} = \sqrt{\frac{2}{\mu\omega\sigma}} \tag{2.89}$$

Where σ is the conductivity of any material and μ its permeability.

The imaginary part of the wave vector is responsible for the evanescence of the spin wave in the thickness of the film and then to a loss of coherence. For samples thicker than the skin depth $\boldsymbol{\delta}$, the contribution of eddy current are taken into account by integrating Maxwell's equation across the film thickness d. The contribution of the eddy current to the damping can be expressed as:

$$\boldsymbol{\alpha_{eddy} = \frac{1}{6} M_s \gamma \left(\frac{4\pi}{c}\right)^2 \sigma d^2} \tag{2.90}$$

Knowing the resistivity of CMS at room temperature to be 170 $\mu\Omega cm$ [10 Kämmerer], the skin depth calculated at 10 GHz for CMS is in the range of 260 nm which is much bigger than our studied CMS films (42 and 50 nm thickness layers). Thus, the contribution of eddy current damping term, in our case, is negligible.

- ***Magnon-phonon scattering***

The direct coupling of magnons and phonons is another source of energy dissipation for the precessing magnetization. A classical picture can be given as follows: let's consider a chain of spin localized on atoms. When a spin is precessing, the surrounding atoms will be periodically either attracted or repealed due to the dipolar coupling between the spins, leading

to phonons. Reciprocally the propagating phonon will perturb the phase of the spin wave leading to decoherence and consequently damping.

Detailed theories were developed by many groups but H. Suhl [45 Suhl] explicitly presented the relaxation by a phonon drag that can be applied to small geometries with homogeneous magnetization and lattice strain. The gilbert phonon damping is described as follows:

$$\boldsymbol{\alpha_{phonon}} = \frac{\boldsymbol{2\eta\gamma}}{\boldsymbol{M_s}}\left(\frac{\boldsymbol{B_2(1+\upsilon)}}{\boldsymbol{E}}\right)^{\boldsymbol{2}} \tag{2.91}$$

Where $\boldsymbol{\eta}$ is the phonon viscosity, B_2 is the magneto-elastic shear constant, E is the Young modulus and $\boldsymbol{\upsilon}$ is the Poisson ratio.

Finally one could discuss about intrinsic magnon-magnon interaction that leads to energy dissipation. These intrinsic mechanism are 3 and 4 magnons scattering. They have been described by Suhl to explain nonlinear effects in spin dynamics experiments such as additional absorption peaks or the saturation of the permeability.

The three magnon process, which is responsible for the subsidiary peak in high power experiments, corresponds to the relaxation of a uniform magnon with k_0 and energy ω_0 into two magnons with opposite wave vectors $+k$ and $-k$ of energy $\hbar\omega_0/2$. The four magnon process scattering corresponds to the annihilation of two magnons uniform modes with k_0 and ω_0 into two magnons with wave vector $+k$ and $-k$ and energy $\hbar\omega_0$. This is the source of the saturation for the susceptibility.

However, these effects mainly arises for nonlinear excitation of the magnetization. In our work, we only work in the small perturbation (linear) limit and then we will not discuss these two mechanisms. The reader is invited to refer to [3, 4, 46, and 47] for more details.

2.5.2 Extrinsic relaxation processes

Another source of energy losses comes from structural defects, interface effects or inhomogeneity of the magnetic parameters. In general such mechanisms are referred as extrinsic contribution to the damping as they are related to imperfections of the ideal material. Experimentally, the extrinsic contributions to the relaxation induce a non-zero linewidth at zero frequency ($\Delta\boldsymbol{H_0}$).

Different parameters can contribute to these extrinsic processes. The principal source of extrinsic relaxation is generally the two magnons scattering and the inhomogeneity of magnetic parameters. They have been described for example in Zakeri *et al.* [52 Zakeri].

- ***Inhomogeneity.***

The inhomogeneity of magnetic parameters is a main source of damping in materials. Indeed local variations of the effective field leads to the dephasing of the spins and then to the decoherence of the precession.

The linewidth broadening due to magnetic inhomogeneity can be calculated via a general formula:

$$\Delta H^{\mathrm{A}} = \left|\frac{\partial H_{res}}{\partial A}\right| \Delta A \tag{2.92}$$

Where ΔA is the average spread of a magnetic parameter of interest A, such as the amplitude of the magnetization M_s or anisotropy H_k. It can also correspond to the spreading of the easy axis direction φ_H due to the mosaicity of the material. This case is generally referred as ΔH_{mos}. This last term is generally one of the most important sources of linewidth broadening but vanishes for field applied parallel to easy and hard axis directions.

One of the most important feature of equation 2.92 is that the linewidth broadening due to magnetic inhomogeneity is frequency and angle independent.

- ***Two-magnon scattering***

In the two magnon relaxation process, the uniform mode of precession ($k = 0$) is scattered by a defect into a non-zero wave vector spin wave ($k \neq 0$) with the same energy. Two main points have to be mentioned here. First, the conservation of momentum is not required as long as the impurity can absorb the difference of momentum. Secondly, one crucial point is that the FMR mode has to be degenerated with a non-uniform mode. This implies a non-monotonous shape of the dispersion curve as shown in Figure 2.17.

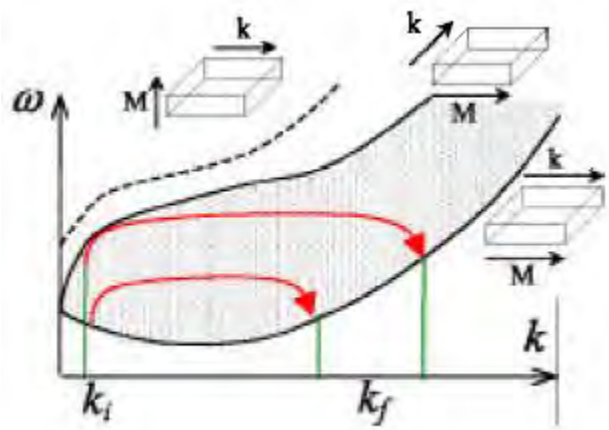

Figure 2.17: spin wave dispersion curves as a function of wave vector in the case of thin films. The gray region represents the case of tangentially magnetized thin film while the dashed line represents the case of a perpendicularly magnetized film [53 Bailleul].

Two magnon scattering is generally caused by geometrical defects, crystal defects or boundaries, etc... It is given by the following expression [54 Arias and Mills]:

$$\Delta H^{2\ \mathrm{magnon}} = \sum_{x_i} \Gamma_{x_i} \times \arcsin\left[\frac{f}{\sqrt{f^2+(f_0)^2}+f_0}\right] \tag{2.93}$$

With Γ_{x_i} is the strength of the two –magnon scattering along the in-plane crystalline direction x_i, $f_0 = \gamma M_{eff}$, and $M_{eff} = M_s - H_k/4\pi$.

It is important to note that for perpendicular configuration, *i.e.* a magnetic field applied perpendicular to the surface of the film, the dispersion relation shows no degenerate mode of the uniform mode with non-zero wave vector spin waves as long as θ, the angle between the magnetization and the normal of the surface is <45°. Experimentally, this gives a special signature of the ΔH vs θ curve (figure 2.18) [48-51].

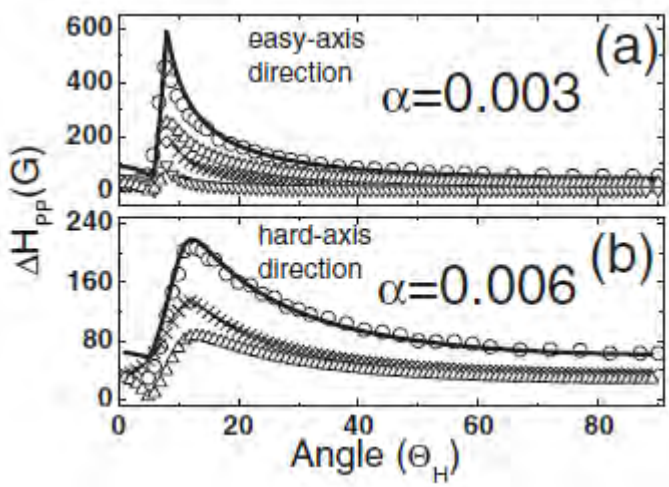

Figure 2.18: Angular dependence of linewidth ΔH_{pp} of FMR spectra in out of-Plane geometry for Co_2MnSi film. Panels (a) and (b) respectively depict line-width variations versus out-of-plane angle φ_H in the easy- and hard-axis directions [48 Yilgin].

After giving a brief description in this section about the intrinsic and extrinsic relaxation process of magnetization relaxation. A summery is given on the influence of these contribution on the magnetic parameters of the CMS Heusler alloys investigated in this manuscript.

The CMS thin films being studied later on in chapters 4 and 5 have a thickness less than 100 nm, and as noted earlier in this section, the eddy current contribution to the intrinsic relaxation process is then negligible. Whereas the magnon phonon damping factor couldn't be evaluated for CMS due to unknown parameters in literature such as the magneto-elastic shear constant, we will follow the assumption proposed by Kamberský stating that the damping of most of ferromagnetic material is due to electron-magnons scattering [37 Kamberský]. This leads the spin orbit interaction to be the dominant intrinsic contribution to relaxation mechanism where the damping factor depends on the spin orbit coupling through the relation 2.88.

The extrinsic relaxation processes are described by the frequency independent contribution to the linewidth. They are induced by crystal inhomogeneity such as defects, interface effects and magnetic inhomogeneity such as local variation of magnetization or anisotropy. Considering classical values of the extrinsic contributions to the linewidth observed in many studies on similar materials [49 Belmeguenai, 56 Qiao], the value of ΔH_0 is generally about 10 Oe. In our CMS samples, slightly higher values of ΔH_0 will be measured (see chapters 4 and 5). The most probable reason is a stronger contribution of the $\Delta \boldsymbol{H_{inhomogeneity}}$ **and** $\Delta \boldsymbol{H_{mosaicity}}$ as we will show that our samples have one or two crystal phase order as deposited. . Also 2 magnons scattering has probably a significant contribution to the linewidth, especially in our irradiated samples (chapter5) for which local defects are created at high fluence. However, this one is very difficult to estimate and requires

high field in and out-of-plane FMR measurements, the latter being not accessible within our stet-up.

Chapter 2 References:

[1] J. M. D. Coey, *Magnetism and magnetic materials*. Cambridge; New York: Cambridge University Press, 2009.

[2] S. Blundell, *Magnetism in condensed matter*, reprinted. Oxford: Oxford Univ. Press, 2003.

[3] D. Stancil and A. Prabhakar, *Spin Waves*. Boston, MA: Springer US, 2009.

[4] Guervich and Merkov, "Magnetization Oscillations and Waves,"

[5] S. V. Vonsovskii, *Ferromagnetic resonance: the phenomenon of resonant absorption of a high-frequency magnetic field in ferromagnetic substances*, vol. 4. Elsevier, 2013.

[6] M. Getzlaff, *Fundamentals of magnetism*. Berlin ; New York: Springer, 2008.

[7] M. A. Ruderman and C. Kittel, "Indirect exchange coupling of nuclear magnetic moments by conduction electrons," *Phys. Rev.*, vol. 96, no. 1, p. 99, 1954.

[8] T. Kasuya, "A theory of metallic ferro-and antiferromagnetism on Zener's model," *Prog. Theor. Phys.*, vol. 16, no. 1, pp. 45–57, 1956.

[9] K. Yosida, "Magnetic Properties of Cu-Mn Alloys," *Phys. Rev.*, vol. 106, no. 5, pp. 893–898, juin 1957.

[10] S. Kämmerer, S. Heitmann, D. Meyners, D. Sudfeld, A. Thomas, A. Hütten, et G. Reiss, « Room-temperature preparation and magnetic behavior of Co_2MnSi thin films », *J. Appl. Phys.*, vol. 93, n° 10, p. 7945, 2003..

[11] U. Falk, A. Furrer, J. K. Kjems, and H. U. Güdel, "Biquadratic Exchange in Cs Mn x Mg 1- x Br 3," *Phys. Rev. Lett.*, vol. 52, no. 15, p. 1336, 1984.

[12] N. L. Huang and R. Orbach, "Biquadratic Superexchange," *Phys. Rev. Lett.*, vol. 12, no. 11, pp. 275–276, Mar. 1964.

[13] I. Dzyaloshinsky, "A thermodynamic theory of 'weak' ferromagnetism of antiferromagnetics," *J. Phys. Chem. Solids*, vol. 4, no. 4, pp. 241–255, 1958.

[14] T. Moriya, "Anisotropic superexchange interaction and weak ferromagnetism," *Phys. Rev.*, vol. 120, no. 1, p. 91, 1960.

[15] J. H. van Vleck, "On the anisotropy of cubic ferromagnetic crystals," *Phys. Rev.*, vol. 52, no. 11, p. 1178, 1937.

[16] L. D. Landau and E. Lifshitz, "On the theory of the dispersion of magnetic permeability in ferromagnetic bodies," *Phys Z Sowjetunion*, vol. 8, no. 153, pp. 101–114, 1935.

[17] N. Bloembergen, "On the ferromagnetic resonance in nickel and supermalloy," *Phys. Rev.*, vol. 78, no. 5, p. 572, 1950.

[18] T. L. Gilbert and H. Ekstein, "Basis of the domain structure variational principle," *Bull. Amer. Phys. Soc.*, vol. 1, p. 25, 1956, and T. L. Gilbert, "A phenomenological theory of damping in ferromagnetic materials," *IEEE Trans. Magn.*, vol. 40, no. 6, pp. 3443–3449, Nov. 2004.

[19] G. Ortiz, A. García-García, N. Biziere, F. Boust, J. F. Bobo, and E. Snoeck, "Growth, structural, and magnetic characterization of epitaxial Co2MnSi films deposited on MgO and Cr seed layers," *J. Appl. Phys.*, vol. 113, no. 4, p. 043921, 2013.

[20] Smit, J. and H.G. Belgers, *Ferromagnetic resonance absorption in BaFe12O19, a highlyanisotropic crystal.* Philips Res. Rep., 1955. 10: p. 113-30.

[21] Suhl, H., "Theory of the magnetic damping constant", IEEE Trans. Magn. 34, 1834 (1998).

[22] F. Bloch, “Zur theorie des austauschproblems und der remanenzerscheinung der ferromagnetika,” *Z. Für Phys.*, vol. 74, no. 5–6, pp. 295–335, 1932.
[23] R. W. Damon and J. R. Eshbach, “Magnetostatic modes of a ferromagnet slab,” *J. Phys. Chem. Solids*, vol. 19, no. 3, pp. 308–320, mai 1961.
[24] L. R. Walker, “Magnetostatic Modes in Ferromagnetic Resonance,” *Phys. Rev.*, vol. 105, no. 2, pp. 390–399, Jan. 1957.
[25] B. A. Kalinikos, “Excitation of propagating spin waves in ferromagnetic films,” *Microw. Opt. Antennas IEE Proc. H*, vol. 127, no. 1, p. 4, 1980.

[26] S. O. Demokritov, B. Hillebrands, and A. N. Slavin, “Brillouin light scattering studies of confined spin waves: linear and nonlinear confinement,” *Phys. Rep.*, vol. 348, no. 6, pp. 441–489, 2001.

[27] G. T. Rado and J. R. Weertman, “Spin-wave resonance in a ferromagnetic metal,” *J. Phys. Chem. Solids*, vol. 11, no. 3, pp. 315–333, Oct. 1959.
[28] R. F. Soohoo, “General exchange boundary condition and surface anisotropy energy of a ferromagnet,” *Phys. Rev.*, vol. 131, no. 2, p. 594, 1963.
[29] C. Kittel, “Excitation of spin waves in a ferromagnet by a uniform rf field,” *Phys. Rev.*, vol. 110, no. 6, p. 1295, 1958.
[30] M. H. Seavey Jr and P. E. Tannenwald, “Direct observation of spin-wave resonance,” *Phys. Rev. Lett.*, vol. 1, no. 5, p. 168, 1958.
[31] L. Berger, “A simple theory of spin-wave relaxation in ferromagnetic metals,” *J. Phys. Chem. Solids*, vol. 38, no. 12, pp. 1321–1326, Jan. 1977.
[32] B. Heinrich, D. Fraitová, and V. Kamberský, “The Influence of s-d Exchange on Relaxation of Magnons in Metals,” *Phys. Status Solidi B*, vol. 23, no. 2, pp. 501–507, Jan. 1967.
[33] V. Kamberský, “On the Landau–Lifshitz relaxation in ferromagnetic metals,” *Can. J. Phys.*, vol. 48, no. 24, pp. 2906–2911, décembre 1970.

[34] V. Kamberskỳ, “On ferromagnetic resonance damping in metals,” *Czechoslov. J. Phys. B*, vol. 26, no. 12, pp. 1366–1383, 1976.
[35] V. Kamberskỳ, “Dissipative boundary conditions for ferromagnetic resonance equations,” *Czechoslov. J. Phys. B*, vol. 23, no. 6, pp. 627–635, 1973.
[36] V. Kamberskỳ, “FMR linewidth and disorder in metals,” *Czechoslov. J. Phys.*, vol. 34, no. 10, pp. 1111–1124, 1984.
[37] V. Kamberský, “Spin-orbital Gilbert damping in common magnetic metals,” *Phys. Rev. B*, vol. 76, no. 13, Oct. 2007
[38] B. Heinrich, J. F. Cochran, and R. Hasegawa, “FMR linebroadening in metals due to two-magnon scattering,” *J. Appl. Phys.*, vol. 57, no. 8, pp. 3690–3692, Apr. 1985.
[39] B. Heinrich, G. Woltersdorf, R. Urban, and E. Simanek, “Role of dynamic exchange coupling in magnetic relaxations of metallic multilayer films (invited),” *J. Appl. Phys.*, vol. 93, no. 10, p. 7545, 2003.
[40] G. Woltersdorf, “Spin-pumping and two-magnon scattering in magnetic multilayers,” Sinon Fraser University, 2004.
[41] S. Dubois, L. Piraux, J. M. George, K. Ounadjela, J. L. Duvail, and A. Fert. Evidence for a short spin diffusion length in permalloy from the giant magnetoresistance of multilayered nanowires. *Phys. Rev. B*, 60:477–484, 1999.
[42] T. Valet and A. Fert. Theory of the perpendicular magnetoresistance in magnetic multilayers. *Phys. Rev. B*, 48:7099–7113, 1993.

[43] J. Pelzl, R. Meckenstock, D. Spoddig, F. Schreiber, J. Pflaum, and Z. Frait, "Spin–orbit-coupling effects on g-value and damping factor of the ferromagnetic resonance in Co and Fe films," *J. Phys. Condens. Matter*, vol. 15, no. 5, p. S451, 2003.

[44] H. Keith Gilmore, "Gas sensors based on conducting polymers," *Sensors*, vol. 7, no. 3, pp. 267–307, 2007.

[45] H. Suhl, The theory of ferromagnetic resonance at high signal powers, J. Phys. Chem. Solids, 1 (1957), p. 209.

[46] J. T. Łopuszański, A. Pękalski, and J. Przystawa, Eds., *Magnetism in Metals and Metallic Compounds*. Boston, MA: Springer US, 1976.

[47] R. A. Lukaszew, *Handbook of Nanomagnetism: Applications and Tools*. CRC Press, 2015.

[48] R. Yilgin, Y. Sakuraba, M. Oogane, S. Mizukami, Y. Ando, and T. Miyazaki, "Anisotropic Intrinsic Damping Constant of Epitaxial Co_2MnSi Heusler Alloy Films," *Jpn. J. Appl. Phys.*, vol. 46, no. 9, pp. L205–L208, 2007.

[49] M. Belmeguenai, H. Tuzcuoglu, M. S. Gabor, T. Petrisor, C. Tiusan, D. Berling, F. Zighem, T. Chauveau, S. M. Chérif, and P. Moch, "Co2FeAl thin films grown on MgO substrates: Correlation between static, dynamic, and structural properties," *Phys. Rev. B*, vol. 87, no. 18, p. 184431, mai 2013.

[50] H. Kurebayashi, T. D. Skinner, K. Khazen, K. Olejník, D. Fang, C. Ciccarelli, R. P. Campion, B. L. Gallagher, L. Fleet, A. Hirohata, and A. J. Ferguson, "Uniaxial anisotropy of two-magnon scattering in an ultrathin epitaxial Fe layer on GaAs," *Appl. Phys. Lett.*, vol. 102, no. 6, p. 062415, 2013.

[51] H.-S. Song, K.-D. Lee, J.-W. Sohn, S.-H. Yang, S. S. P. Parkin, C.-Y. You, and S.-C. Shin, "Relationship between Gilbert damping and magneto-crystalline anisotropy in a Ti-buffered Co/Ni multilayer system," *Appl. Phys. Lett.*, vol. 103, no. 2, p. 022406, 2013.

[52] K. Zakeri, J. Lindner, I. Barsukov, R. Meckenstock, M. Farle, U. von Hörsten, H. Wende, W. Keune, J. Rocker, S. Kalarickal, K. Lenz, W. Kuch, K. Baberschke, and Z. Frait, "Spin dynamics in ferromagnets: Gilbert damping and two-magnon scattering," *Phys. Rev. B*, vol. 76, no. 10, Sep. 2007.

[53] M. Bailleul, Propagation et con_nement d'ondes de spin dans les microstructures magnétiques, Thèse de doctorat de l'Ecole Polytechnique,2002.

[54] R. Arias and D. L. Mills, "Extrinsic contributions to the ferromagnetic resonance response of ultrathin films," *Phys. Rev. B*, vol. 60, no. 10, pp. 7395–7409, Sep. 1999.

[55] S.-Z. Qiao, J. Zhang, Y.-F. Qin, R.-R. Hao, H. Zhong, D.-P. Zhu, Y. Kang, S.-S. Kang, S.-Y. Yu, G.-B. Han, S.-S. Yan, and L.-M. Mei, "Structural and Magnetic Properties of Co 2 MnSi Thin Film with a Low Damping Constant," Chin. Phys. Lett., vol. 32, no. 5, p. 057601, May 2015.

Chapter 3: Experimental techniques

In this chapter, we will introduce the different techniques used to study the structural and magnetic properties of 'as deposited' Co_2MnSi (CMS) Heusler alloy. Section 3.1 describes different deposition technique. In section 3.2 thin film deposition procedure of CMS will be presented. Section 3.3 the structural investigation by X-Ray Diffraction (XRD) and Transmission Electron Microscopy (TEM) is carried on the deposited CMS thin films. In section 3.4 Magneto Optical Kerr Effect (MOKE) and Ferromagnetic Resonance (FMR) spectroscopy experiments are used to study the static and dynamic magnetic properties of CMS. At the end of this chapter, Ion irradiation technique is introduced.

3.1 Deposition Techniques

Thin films fabrication are usually divided into two categories, the Chemical Vapor Deposition (CVD) and the Physical Vapor Deposition (PVD). In CVD process, the material to be deposited is in the gas or liquid form, the deposition is done by a chemical reaction on the substrate surface. While, PVD technique is based on the formation of a vapor state of the material to be deposited as thin films onto the substrate. To convert the material from solid to vapor state, is done by either thermal evaporation (*i.e.* heating) or sputtered/bombarded ions.

- ***PVD by thermal evaporation:***

It is one of the oldest methods to deposit thin films, metals are evaporated by heating and the evaporated material will form a thin layer on the used substrate. The ultra-high vacuum is necessary for film deposition ($< 10^{-8}$ Torr). Thermal evaporation can be divided into two parts: Filament evaporation and Electron-beam one. Filament evaporation is done by placing the desired metal on the filament directly (usually Tungsten, W), then the metal is evaporated as we increase the temperature of the filament. The rate of deposition is directly related to the temperature of the filament and it should be lower than the sublimation temperature to avoid contamination. In the case of electron-beam evaporation, electron beam is focused on the material to evaporate instead of heating it. Different techniques are used to elaborate thin films by evaporation, such as: Molecular Bean Epitaxy (MBE) and Pulsed laser deposition (PLD). The reader is invited to refer to [1,2,3,4 and 5] for more details about PLD and MBE.

- ***PVD by ionic bombardment:***

In this technique, ionic bombardment attack the material to be deposited (called target) and ejects the atoms from its surface. There exist two ways of ionic bombardment: either by direct application of ion beam on the target or by accelerated ionized gas (usually Argon Gas) that release the atoms from the target placed at a cathode, results in creating a plasma. An example of the former technique is Ion Beam Deposition (IBD) and the latter is the sputtering. Sputtering is the VPD technique used for elaborating CMS thin films and is detailed in the next paragraph.

3.1.1 Sputtering

This technique is used to deposit thin films by the creation of a gaseous plasma. The ionized gas in the plasma accelerate towards the target (the material to be deposited). Atoms are ejected from the target after being eroded by the energy transfer of the accelerating ions. After being ejected, the atoms will be deposited on a nearby surface (the substrate). The ionized gas used in our case is Argon, Ar. The use of neutral gas will avoid chemical reaction with the deposited material. Apart from the use of Argon to deposit metals and alloys, Oxygen ionized gas is used to deposit oxides. Compared to MBE (deposition rate of nm/hr), the rate of deposition of sputtering is higher and of order of one atomic layer per second. In this work we use face to face configuration for the CMS target in order to keep the stoichiometry of the material when it is deposited on the substrate. Now, we will present the different energy sources configurations to maintain the gaseous plasma.

- **DC configuration**

In the DC configuration of sputtering, the target is inside the vacuum chamber of ~ 10^{-7} mbar. Two electrodes are located inside the chamber to create the plasma. The target is fixed on the first negatively charged electrode (cathode) that carries a negative potential ranges from several volts to kilovolts. The second electrode (the anode) is placed on the substrate, placed at few centimeters from the target. To create the plasma, we introduce the Argon gas of 10^{-4} to 10^{-1} mbar, then, the free electrons will accelerate from the cathode and approach the outer shell electrons of the Ar atoms, this leaves the Ar atoms electrically unbalanced and forms ions instead, Ar^{+} ions. The positively charged ions will interact with the atoms on the negatively charged electrode (the cathode) leading to an energy transfer from the ions to free electrons and atoms of the target. The atoms will be deposited on the substrate while the free electrons will hit the outer electron shells of Ar^{+} ions, changing them into neutral gas. Due to the conservation of energy law, the Ar gas atoms that gained energy must be released, the released energy is in the form of photons. For this reason we see the glowing plasma (Figure 3.1).

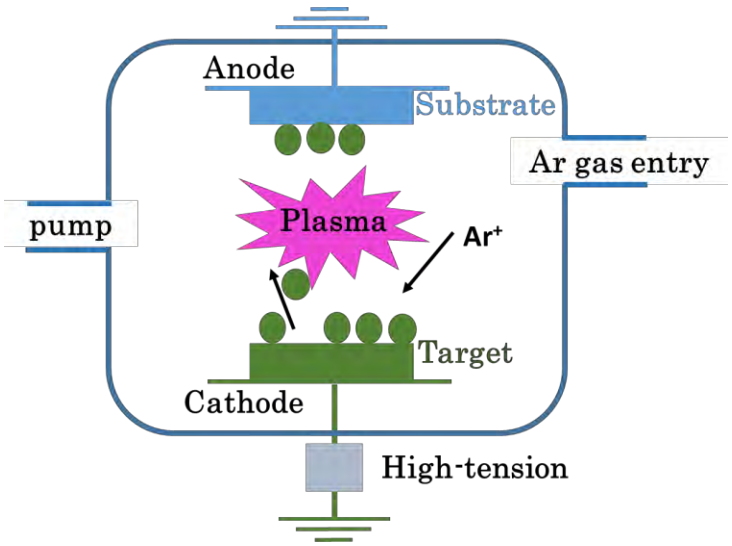

Figure 3.1: Graphical representation of sputtering configuration.

- **RF configuration**

The DC configuration is adapted to deposit conducting materials but it is not applicable to deposit dielectrics or oxides. The reason falls behind is that Ar^+ ions accumulate on the target surface and the electrons coming from the cathode can't neutralize the dielectric materials. To overcome this problem, both electrodes should be polarized by an alternating radio frequency (RF) potential. This leads to attract the electrons or the positive ions who discharged the surface. The RF operating at frequencies higher than 1 MHz, is sufficient for the positive ions to reach the electrodes. Usually, the used frequency is about 13.5 MHz to avoid interference with telecommunication waves.

- **Face to Face configuration**

Face to face configuration involves placing the two targets electrodes facing each other separated by few centimeters where the substrate is placed above them (Figure3.2). In this configuration, the two target electrodes are biased by RF potential. This configuration lower the deposition rates and the probability of high energy carbon contamination is reduced. Those two consequences of face to face target configuration allows us to have an epitaxial growth from stoichiometry targets. The stoichiometry of the targets can be only reserved by using the face to face configuration. In this thesis, face to face configuration is used to grow the Co_2MnSi Heusler alloys and MgO layers.

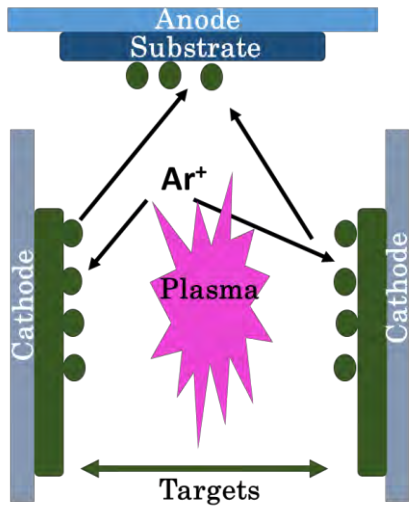

Figure 3.2: Graphical representation of the face to face configuration.

- **Magnetron configuration**

This configuration can be applied to both DC and RF energy sources. Using magnetron, any material can be deposited like dielectrics, oxides and conductors. This configuration (Figure 3.3) consists of placing a magnet below the (cathode) target. The free electrons will be trapped in the magnetic field above the target, causing them to not directly bombard the target as in the DC configuration. This will enhance the probability of deposition rate of the material.

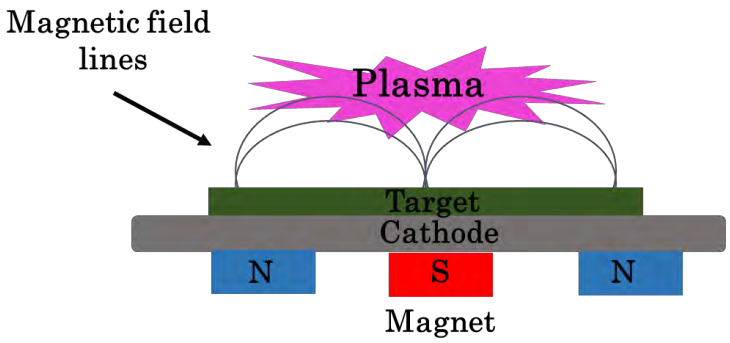

Figure 3.3: Graphical representation of magnetron sputtering configuration.

3.1.1.1 Presentation of PLASSYS sputtering chamber

The spattering chamber, PLASSYS-MPU-600S, located at CEMES-CNRS, Toulouse, is used to produce the studied samples for this thesis (Figure 3.4). It consists of the following:

- A cryogenic pump that ensures a high vacuum in the chamber (~10^{-8} mbar).
- Load lock high vacuum chamber (~10^{-7} mbar), permits to transfer the substrate inside the main chamber.
- Substrate heater holder (up to 1000° C), rotates 360° degrees and can be transferred from one position to another.
- Two 'face to face' targets connected to an alternative RF potential and 3 DC magnetron modes.
- Two flow meters controls for Argon and Oxygen gas (Ar and O_2).
- An electron canon and florescent screen that enable us to control and verify *in-situ* (during the growth procedure) the crystalline quality of the thin film by Reflective High Energy Electron Diffraction (RHEED).

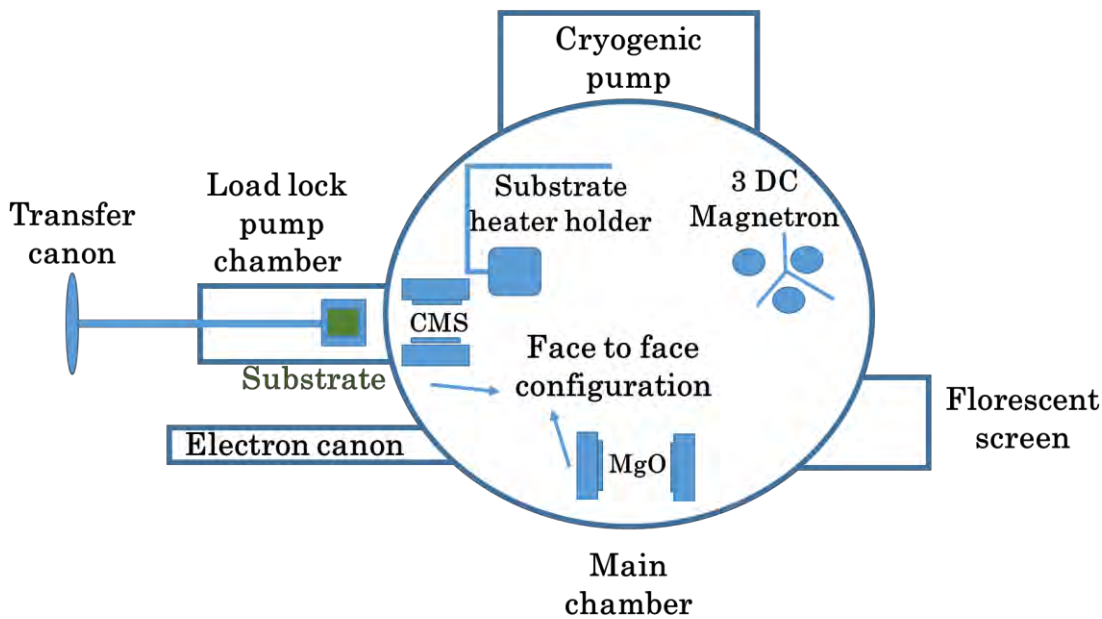

Figure 3.4: graphical representation of PLASSYS sputtering at CEMES.

3.2 CMS Thin film deposition procedure

In this section, we will present the different procedures to prepare CMS thin films starting from the substrate choice, the buffer layer, the deposition condition of CMS thin films and the last step by depositing a capping protection layer.

As presented in the first chapter, Heusler alloys can grow on different substrates and by different deposition techniques. GaAs and MgO substrates are widely used for the deposition of Heusler alloys. Although GaAs has a better mismatch for Heusler Co-based alloys, MgO substrates take advantage over GaAs for Magnetic tunnel Junctions applications. In our case, we use MgO substrates. CMS grows with a 45° angle rotation with respect to the (100) MgO plane and a lattice mismatch of -5.4 %, enabling epitaxial growth.

We use commercial monocrystalline MgO 10*10 or 20*20 mm^3 mm^2 *epi-polished* substrates, provided by NEYCO. MgO substrates when introduced in the main chamber of sputtering is annealing at 700° C for 1 hour to degas and reduce the roughness of the surface.

After annealing, a homo-epitaxial growth of MgO thin layer (~ 10 to 15 nm) is realized to reduce the defects and to insure a 2D thin film epitaxial growth of CMS layers. As mentioned in [6 Turban], a homo-epitaxial buffer layer blocks the diffusion of carbon atoms towards the surface substrate and consequently reduces the defects to obtain a 2D surface film for the epitaxial growth of CMS. MgO is deposited at 100° C using 'the face to face' configuration with a 100 Watts RF tension and a flow rate of 50 and 5.3 sccm for Ar and O_2, respectively. The MgO buffer layer surface was controlled by RHEED. RHEED images are shown in Figure 3.8.

After the deposition of the homo-epitaxial MgO layer, CMS thin films are deposited using also the face to face configuration. In this configuration the stoichiometry of the target consists of 50% Co, 25% Mn and 25% Si. The plasma in this case is formed by Ar gas only. The different depositions conditions (RF power of 100 w, Ar pressure flow of 50 sccm, CMS deposition and annealing temperatures of 600 °c and 800 °, respectively) have been optimized from the previous work of G. Ortiz [7 Ortiz].

The deposition rate is 1.5 nm/minute. In this work, the thickness of the CMS layer is always about 40 nm. This value has been chosen to avoid He^+ ions implantation during the irradiation process (see section 3.5). One crucial point in deposition procedure to achieve high crystalline CMS quality is the deposition and annealing temperature. The choice of the deposition and annealing temperature will be presented in chapter IV.

At the end of the process, a few nanometers of capping layer of MgO is deposited to prevent contamination and oxidation of the CMS layer when it is exposed to the normal atmosphere conditions. Moreover, it is important for the ferromagnetic resonance experiment to have a small insulating layer to avoid contact between the transmission line and the metallic surface.

In this thesis, we have fabricated many samples following the above deposition conditions. Among the different samples we had, even with the in-situ RHEED patterns verification, the decision to proceed with magnetic and structural characterization was based on the lowest peak to peak line width. Three samples have been selected and will be presented in the next chapters. .

3.3 Structural characterization techniques

In this section, we will present the different experimental techniques used to investigate the structural properties of CMS thin films. In this work, Reflection High Energy Electron Diffraction (RHEED) was in-situ used during the deposition procedures to control the film growth quality (2D vs 3D), normal and anomalous x-ray diffraction are used to define the structure order of the film and the probability to define the atomic positions in the unit cell. These characterization techniques have been correlated with Transmission Electron Microscopy (TEM) techniques to study, on the Nano meter scale, the crystal deformation after

He^+ irradiation using Geometric Phase Analysis (GPA) and direct observation of the local order by HAADF STEM.

We first recall some diffraction basics to introduce RHEED, X-ray diffraction techniques as well as describing the atomic disorder method used from x-ray diffraction peaks analysis. Then, TEM, HAADF STEM imaging technique is introduced and GPA analysis method is briefly described.

3.3.1 Basics of crystallography diffraction

By structural characterization, we study the topology and morphology of the crystal by sending beam of electrons or x-rays on the substrate surface. These methods vary from millimeter to nanometer scale. In this section we recall the theory of diffracted x-rays or electrons from a given surface for this, first we recall the crystallography basics of real and reciprocal space.

A crystal lattice is a solid material whose constituents (atoms, ions or molecules) are arranged in a highly ordered 3 dimensional periodic structure and symmetry. A unit cell is smallest volume of a crystal and defined by three neighboring atom unit vectors $\vec{a}, \vec{b}$ and $\vec{c}$ in the x,y and z axes, respectively. Atoms in the crystal can be defined as a point in the real pace lattice as $\vec{T} = u\,\vec{a} + v\vec{b} + w\vec{c}$, with $[uvw]$ is the real space direction integers.

For experimental techniques, we can't have access to the real space components of a crystal, but we can obtain a unit of inverse length. Thus, we define a reciprocal space lattice that is related to the real space. The unit vectors in the reciprocal space have a reciprocal relationship with the one of the real space by $\vec{G}(hkl) = h\,\vec{a}^* + k\vec{b}^* + l\,\vec{c}^*$, where $h, k\ and\ l$ are the miller indices of a plane (hkl), and $\vec{a}^*$, $\vec{b}^*$ and $\vec{c}^*$ are the reciprocal unit vectors, with

$$\boldsymbol{a}^* = \boldsymbol{2\pi}\frac{\boldsymbol{b}\wedge\boldsymbol{c}}{\boldsymbol{a}.(\boldsymbol{b}\wedge\boldsymbol{c})}\ ,\ \boldsymbol{b}^* = \boldsymbol{2\pi}\frac{\boldsymbol{c}\wedge\boldsymbol{a}}{\boldsymbol{a}.(\boldsymbol{b}\wedge\boldsymbol{c})} \text{ and } \boldsymbol{c}^* = \boldsymbol{2\pi}\frac{\boldsymbol{a}\wedge\boldsymbol{b}}{\boldsymbol{a}.(\boldsymbol{b}\wedge\boldsymbol{c})}.$$

For diffraction experimental techniques, electrons or x-rays behave as matter waves following the de Broglie relation $\lambda = h/p$ with $p = \frac{h}{2\pi}K$, where K is the wave vector expressed as, $k = 2\pi/\lambda$. The diffraction of a wave requires an incoming wave vector K_{IN} and a scattered wave vector K_{OUT}. Now we present how the wave vector can be diffracted using Bragg's relation and Ewald reconstruction.

Bragg's Relation:

Bragg had announced that waves behave as if they are reflected from the atomic planes and the wave vector K is related to the interplanar distance d_{hkl}. In Figure 3.5, an incoming vector incident on the first atomic plane with an angle θ_{in} is diffracted with an angle $\theta_{out} = \theta_{in} = \theta$. If the same wave vector hits the surface and diffracted from the second atomic plane, then the path length difference between the first and second ray is calculated as: $2d_{hkl}\sin\theta$. If the path-length difference is of an integer wavelength form, then we get Bragg's law:

$$\boldsymbol{2d_{hkl}\sin\theta = n\lambda} \tag{3.1}$$

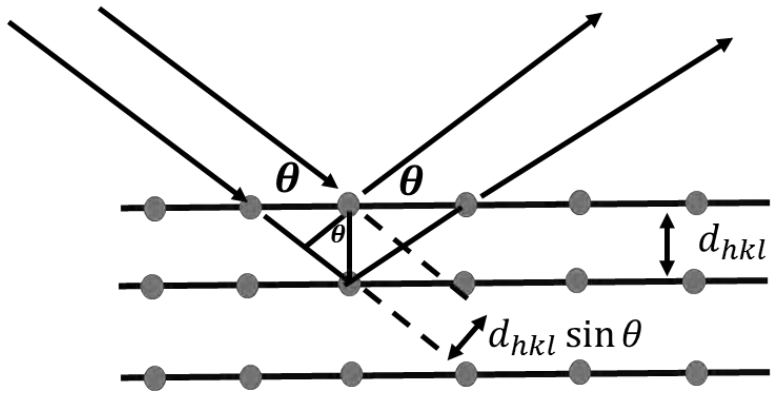

Figure 3.5: Schematic illustration of Bragg's law.

Ewald sphere

Ewald construction defines the direction of the diffracted wave by an intersection of two points. The first consists of incident wave vector with $|K_{in}| = 1/\lambda$. The second corresponds to the wave vector of reciprocal space$|g| = |K| - |K_{in}|$. Whenever a reciprocal lattice point touches the Ewald sphere, then the Bragg law is satisfied (Figure 3.6).

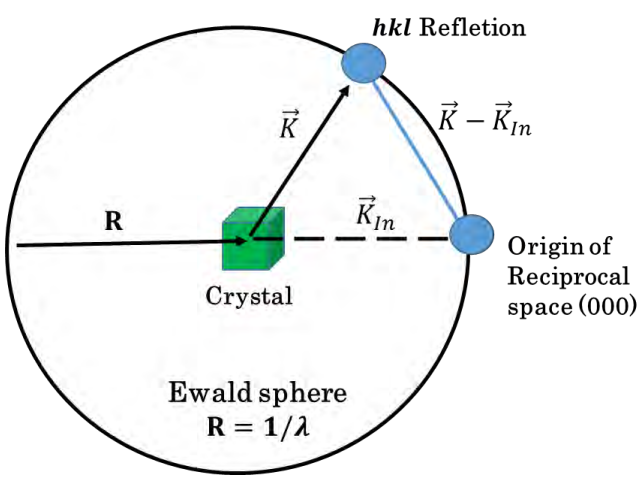

Figure 3.6: Ewald reconstruction sphere.

3.3.2 Reflection High Energy Electron Diffraction (RHEED)

RHEED technique is a useful technique for monitoring *in-situ* the epitaxial growth of the film at the end of each deposition process performed in the sputtering chamber. RHEED

provides information about the crystal structure surface, orientation and roughness surface to study the surface morphology and disorder.

The experimental principle consists of sending a coherent electron beam of kinetic energy, between 10 and 100 KeV, at a grazing angle (0° to 2°) relative to the plane of the layer, in our case a 20 KV accelerating voltage is used ($\lambda = 0.0086$ nm). The diffracted beam is then recovered using a fluorescent screen placed at a distance ($\boldsymbol{L = 38\ cm}$) from the substrate position.

The fact that incoming electrons have a very small incident angle with respect to the sample surface implies that only few atomic planes (the top layers of the sample) will contribute to the response of the diffracted wave. The electron wave is diffracted by a 2D lattice. In reciprocal space, the two dimensional array of the surface atoms are turned into vertical lines which are called the reciprocal rods. In a perfect case, the intersection of Ewald sphere and the planes of the 2D reciprocal lattices give fringes. But using RHEED, the incident electron beam is not perfectly focused and for this reason, the diffracted beam forms sticks or rods.

If we consider the fringes separation being $\mathbf{M}$, and $\boldsymbol{L = 38\ cm}$, then the interplanar distance, $\boldsymbol{d}$, is expressed as: $\boldsymbol{d = L\lambda/M}$. From the previous equation, we can have an approximation about the interplanar distance, $\boldsymbol{d}$, of MgO and CMS and consequently the lattice constant. The RHEED images are taken by a steady camera device located at few centimeters from the florescent screen. Figure 3.7 shows MgO RHEED patterns fulfill brag's diffraction with a 2D growth with the presence of Kikuchi lines. The latter are identified as strong patterns generated by the subsequent diffraction of inelastic scattered electrons. Kikuchi lines are distinguishable from the single brag diffraction intensity as they move in continuous manner as the crystal rotates.

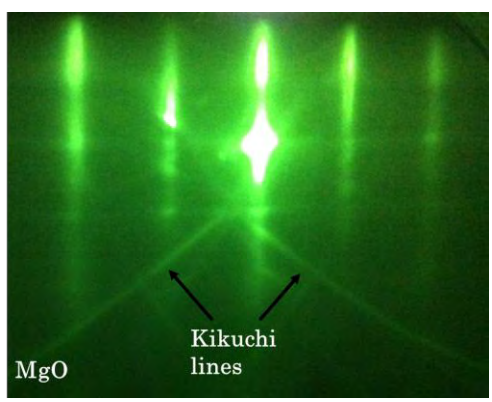

Figure 3.7: An example of MgO RHEED pattern in the [110] direction.

3.3.3 X-ray Diffraction (XRD)

A linearly polarized monochromatic X-ray electromagnetic wave incident on an atom with a free electron, induces the oscillation of the electron at the same frequency of the

incident wave, which in turns reemit electromagnetic radiation in all direction. This is the basic of the scattering of an electromagnetic wave by an atom, the so called Thomson scattering mechanism.

For every atom, the amplitude of the scattered electromagnetic wave depends on the energy of the incoming photons and is represented by a coefficient called the scattering factors which are complex quantities.

X-ray diffraction and reflectivity measurements were done at the LPCNO laboratory at INSA, Toulouse and LAAS-CNRS, Toulouse. A schematic presentation of the x-ray diffraction configuration is shown in figure 3.8. The diffractometer of LPCNO is Panalytical Empyrean equipped with a normal Cobalt Kα1 radiation source and a monochromator of Germanium Ge (220) with (λ=0.178 nm). LAAS diffractometer is a Bruker D8-Discover (Da-Vinci) diffractometer equipped with an anomalous Cu Kα_1 source (λ=0.154 nm).

In anomalous scattering, the incident radiation has sufficient energy to promote an electronic transition in an atom and leads to a modification of the amplitude of the scattering factor (especially the imaginary part of the scattering factor corresponding to the absorption component of the incident wave).

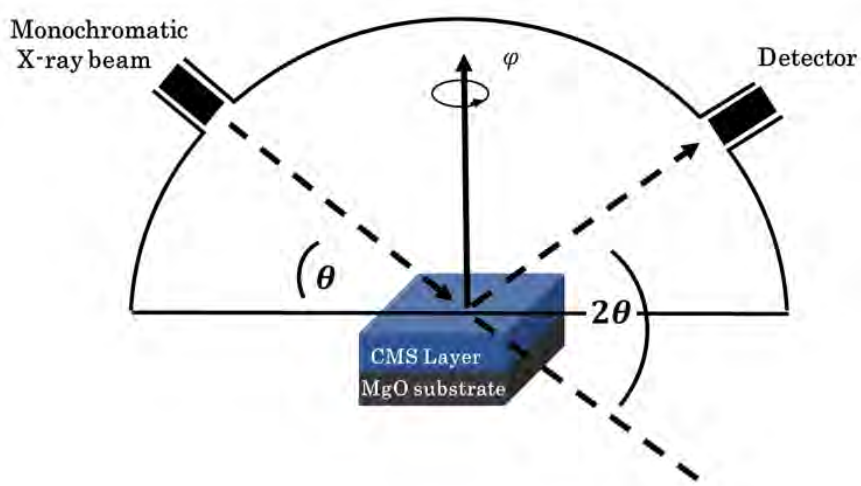

Figure 3.8: Schematic presentation of x-ray diffractometer in $\theta - 2\theta$ configuration.

We will show in chapter IV and V that diffraction at high angles permits us to analyze the crystal phases, determine in a good precision the lattice parameter and to evaluate the atomic disorder between Co, Mn and Si exchange atoms of Heusler alloys.

Using the method of Bragg-Brentano (divergent incident beam) ($\theta - 2\theta$) [8 Brentano], x-rays are diffracted from a crystal and the obtained pattern represents the intensity of the diffracted X'ray beam as a function of the detection angle (2θ). In this configuration, the diffracted planes are parallel to the substrate atomic planes. The angular positions of the diffracted lines are featured parameters of the crystal lattice. From the latter, we can have access to the interplanar distance and the lattice constant of our sample.

Now, we will present the Reflectivity, $\theta - 2\theta$ scan, and φ scan measurements:

- **Reflectivity measurements**

Reflectivity technique is purely optical and can be applied to all kinds of materials (liquid, crystal or amorphous samples) to determine the thickness of the sample. Intensity oscillations, called Kiessig fringes, result from constructive and destructive interference of X rays reflected from two interfaces. By performing X-ray reflectivity measurements, we can estimate the thickness of the sample from the frequency of oscillations, the density, from the total reflection critical angle and the surface roughness from the angular intensity decay. Figure 3.9 presents the reflectivity spectrum and a fitting simulation curve done with SimulReflec program, the estimated thickness is calculated to be 42 nanometers.

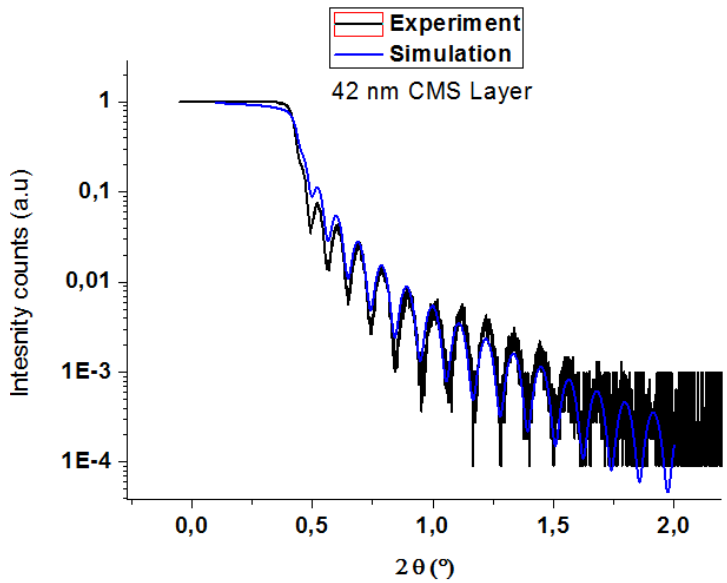

Figure 3.9: Reflectivity measurements of CMS layer.

- **$\boldsymbol{\theta - 2\theta}$ scan**

In $\theta - 2\theta$ scan, the x-ray beam is scattered from crystal planes parallel to the surface substrate because in this configuration, the detector moves in a circular path and substrate is placed at its center. The incident x-rays hit the surface of the substrate at an angle $\boldsymbol{\theta}$ and the reflect waves from its surface are collected by a detector placed at an angle $2\boldsymbol{\theta}$ relative to the incident beam. The intensity peaks that correspond to atomic planes positions are detected by performing $\boldsymbol{2\theta}$ angular scan (Figure 3.10-a). From Bragg's law, the detected angles and the interplanar atomic distances should satisfy the diffraction conditions. This technique allow us to acquire information about the lattice parameter, and the degree of disorder in the film.

- ***φ* scan**

In this configuration, $\boldsymbol{\theta}$ is kept constant (corresponds to a specific diffraction plane) and the substrate rotates 360° around its surface normal $\boldsymbol{\varphi}$ axis. If $\boldsymbol{\theta}$ is fixed at a value equivalent to the 022 diffracted plane, then for symmetric *hkl* reflections, we observe 4 peaks in the case of a cubic lattice. By doing $\boldsymbol{\varphi}$ scan for both the MgO substrate and the CMS film on top, we can confirm the epitaxial relationship and the in-plane 45° orientation. We have performed on our sample $\boldsymbol{\varphi}$ scan for two directions 022 and 111, it shows clearly the 45° orientation of CMS with respect to the MgO substrate (Figure 3.10-b).

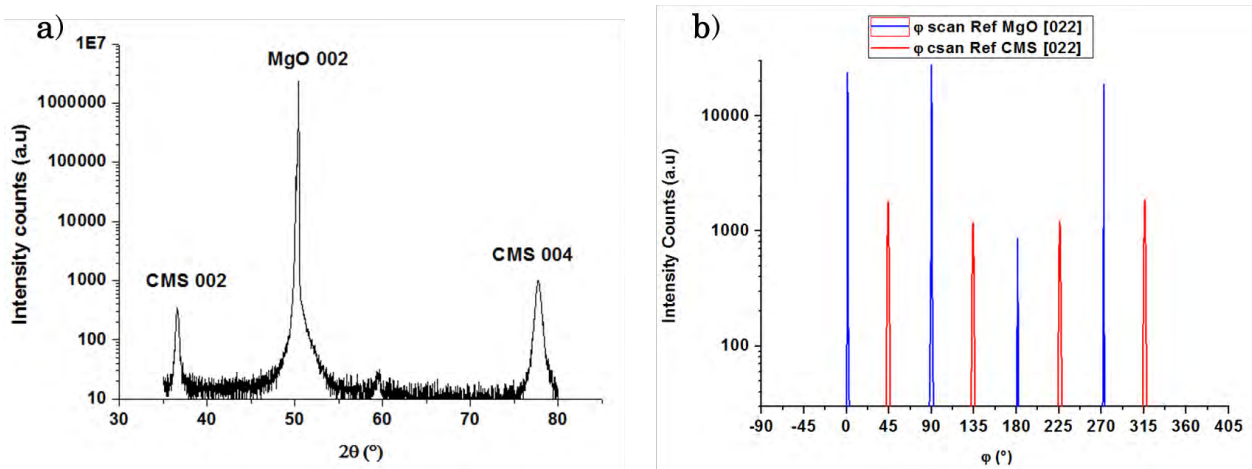

Figure 3.10: a) $\boldsymbol{\theta - 2\theta}$ X-ray diffraction scan showing the 002 and 004 peaks of CMS and 002 MgO peak. b) $\boldsymbol{\varphi}$ scan of the CMS with respect to the MgO substrate along the 022 direction clearly shows the 45° orientation.

3.3.4 Transmission Electron Microscopy (TEM)

The need in Nano materials sciences to image and examine details down to the atomic level have resulted in the development of electron microscopes that overcome the resolution limitation of an optical microscope imposed by the light wavelength. The first transmission electron microscope was developed by Max Knoll and Ernst Ruska in Germany in 1932. It consists of a highly energetic electron beam (> 100 keV) accelerated from an electron gun. This electron beam interacts with a thin sample (< 100 nm thickness) for electron transparency, before to be visualized on a fluorescent screen or recorded by a charge-coupled device (CCD) camera. The resulting image gives information about the material morphology as well as its physical and chemical properties. In this section, we present a general descriptive of a TEM used in our study. A schematic illustration of a transmission electron microscope (TEM) is presented in figure 3.11.

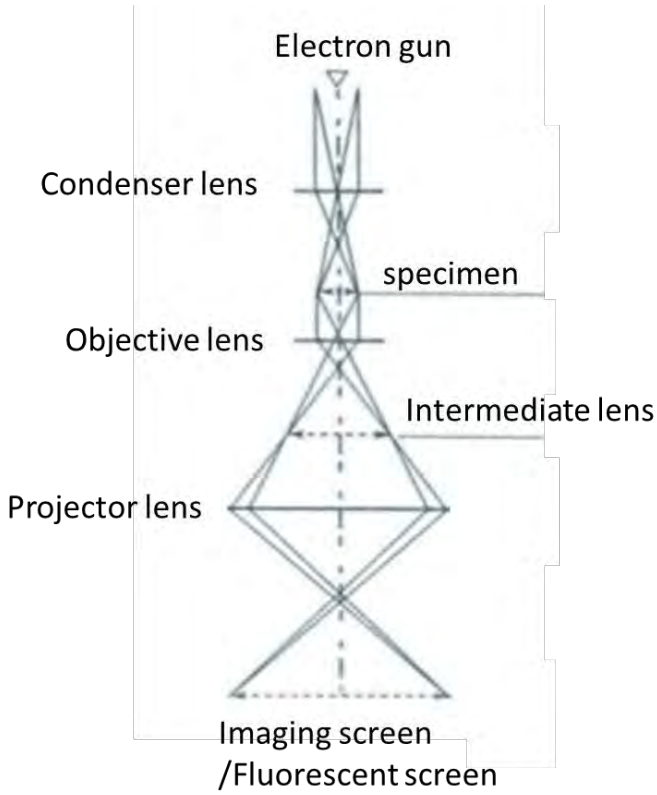

Figure 3.11: Schematic illustration of a transmission electron microscope.

The TEM column is described as:

- **An electron gun:** to generate the electron beam by either thermoionic gun or field emission gun (FEG). The thermoionic gun consists of the filament (cathode), a wehnelt and the anode. The electrons are generated by heating the metallic filament (Tungsten or LaB_6 crystal) and then accelerated passing them through the wehnelt, which acts as an electromagnetic lens, and the electron beam converges in a point called "cross-over", it will be then accelerated by an accelerator brought at the applied high tension. In the case of FEG, the electrons are produced by an electric potential applied between the source and the anode. Electrons are extracted by tunneling effect. Unlike the thermoionic gun, the electron beam doesn't pass by a cross-over, but comes directly from a tungsten filament and accelerated by a second anode. The two anodes play the role of electrostatic lens (which permits the convergence of the beam). An image of both thermoionic and FEG gun is presented in Figure 3.12.

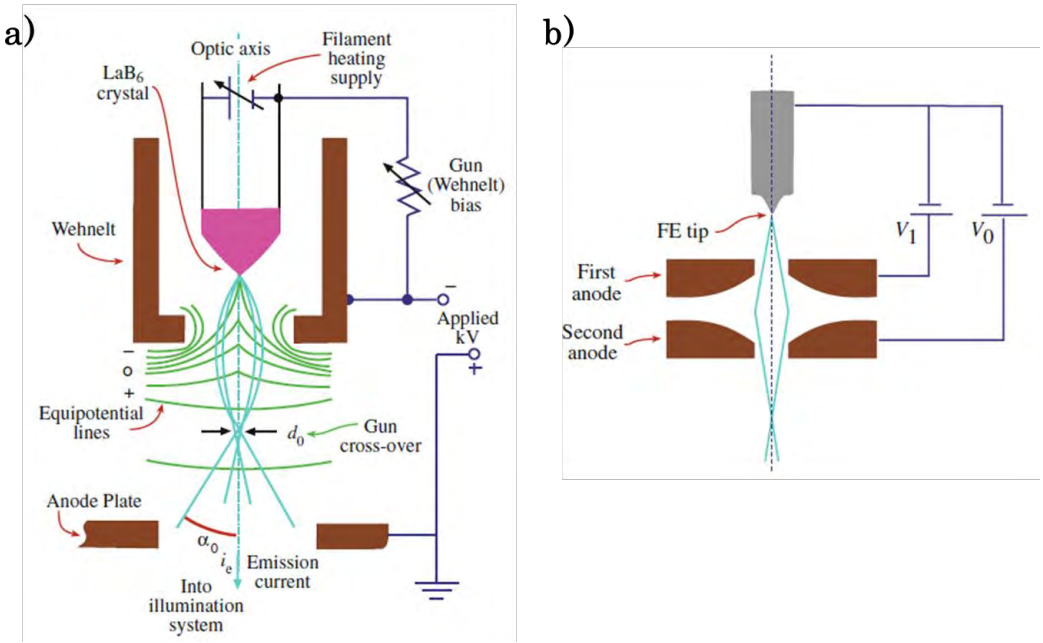

Figure 3.12: Schematic illustration of a) the thermoionic Gun principle and b) the field emission gun FEG [09 Williams and Carter].

- **Electronic lenses:** in the microscope, a converging electron beam is produced with the help of electromagnetic lenses. Three types of lenses exist in TEM: condenser, objective and projecting lenses.
  1- **The condenser lenses:** the system of condenser lenses are used to focus the electron beam on the studied sample either in a parallel or convergent configuration depending on if we are working in TEM or scanning transmission electron microscopy (STEM) mode, respectively. In addition, the use of apertures allows controlling the electron beam doses to reduce damage in the observed area.

  2- **Objective lense:** it is the most important lens in the column; it is used to form a magnified image of the specimen. But since electromagnetic lenses are not perfect, the image contains optical aberrations that limit the resolution of the microscope such as spherical aberration, chromatic aberration and astigmatism.

  3- **Projector lenses**: permits to transfer the image formed by the objective lens and project it on a fluorescent screen and the resulting light collected by a CCD camera.

In a TEM, the point resolution limit is determined by the lenses performance and the nature of the electron wave radiation. This is established as the smallest distance between two well-separated points and is proportional to the product $C_s^{1/4} * \lambda^{3/4}$, where Cs is the coefficient of spherical aberration and λ is the electron wavelength [10 Scherzer]. Thus, the TEM resolution is limited by the acceleration voltage of the electron beam and the ability to correct the

spherical aberration of the objective lens. The most modern TEM microscopes operated at 300 KV and equipped with Cs correctors are able to reach a point-to-point resolution down to 0.5 Å.

A transmission electron microscope has two operational modes: TEM and STEM modes. In the TEM mode, the image is recorded by using a parallel beam configuration where the electrons illuminate each point of the specimen at the same time, similar to an optical microscope. The beam interacts with the specimen and is magnified by the intermediate lens and then is focused onto an imaging device such as a fluorescent screen or a CCD camera. In STEM mode, the image is formed by scanning the specimen with a highly focused electron beam, similar to a scanning electron microscope (SEM).
The local electron-specimen interaction produces several secondary signals that are collected with different detectors to create a two-dimensional image of the object or analyzed in energy using a spectrometer to create Electron Energy Loss Spectra (EELS). This feature allows (S)TEM performing quantitative analysis of the chemical composition of the sample.

Electron-matter interaction:

When an incident electron beam penetrates the sample, electrons undergo elastic or inelastic scattering. Electrons will be diffused at (milli or micro radian) angles with respect to the incident electron beam. Inelastic scattering results when the incident electron beam interacts with the electron cloud of the sample. The energy loss due electron-electron interaction gives information about the chemical nature, bonding and degree of oxidation in the studied sample and can be detected using several techniques like Energy Dispersive X-ray Spectroscopy (EDX), Energy Filtered TEM (EFTEM) or Energy Electron Loss Spectroscopy (EELS). In elastic scattering process, electrons are scattered without energy loss. The elastic diffusion results from Coulomb interaction of electrons with the nucleus of the studied sample. Elastic scattering provides information about the crystalline geometry of the object.

In this thesis, two TEM modes are used to observe our CMS thin films, the high resolution TEM (HRTEM) and high angle annular dark field-scanning transmission electron microscopy (HAADF-STEM) modes. From both techniques we can acquire information regarding the crystalline structure of the sample depending on the contrast mechanism involved in the imaging processes. The mentioned modes are discussed in the following two paragraphs.

3.3.4.1 High Resolution Electron Microscopy (HRTEM):

Starting from the elastic scattering principle, HRTEM images are formed when the electron wave is phase shifted due a potential distribution within the sample. The electron wave contains structural characteristics of the sample.

From a mathematical point of view, the image formation by TEM is described as follows: according to quantum mechanics, a high energetic electron wave that is scattered from the interaction with the crystalline specimen can be described by the Schrodinger equation (also known as Dirac equation) with E, e and m are the energy, charge and mass of an electron:

$$\left[-\frac{\hbar^2}{2m}\nabla^2 - eV(r)\right]\psi(r) = E\psi(r) \tag{3.2}$$

By considering the negligible effect of the elastically scattered electrons and absorption by the thin specimen, the above equation is solved by considering $\psi(r)$ as a plane wave:

$$\psi(r) = A(r)exp^{i\varphi(r)} \tag{3.3}$$

$A(r)$ and $\varphi(r)$ being the amplitude and phase shift of the electron plane wave function. This electron wave propagates through the objective lens that creates a magnified image of the specimen in its image plane. The final image wave function, $\psi_{image}(\mathbf{r})$, contains information about both the specimen and the optical system. Mathematically speaking, $\psi_{image}(\mathbf{r})$ will correspond to the inverse Fourier transform of the product, in the reciprocal space, of the object electron wave ($\psi_{obj}(\mathbf{k})T(\mathbf{k})$) and the transfer function, $T(\mathbf{k})$, which contains all the optical transfer (including aberrations and defocus) of the microscope:

$$\psi_{image}(\mathbf{r}) = FT^{-1}\{\psi_{obj}(\mathbf{k})T(\mathbf{k})\} \tag{3.4}$$

where FT is the Fourier transform operator.

The recorded TEM image will be the intensity of $\psi_{image}(r)$, $I(r) = |\psi_{image}(r))|^2$. For an ideal microscope, the image intensity will correspond to the amplitude of $\psi_{image}(\mathbf{r})$ only. However, a suitable alteration of the transfer function will allow recovering the phase shift of the image electron wave. In this way, high-resolution TEM mode allows to get this phase shift, needed to resolve atomic columns.

The HF3300C 300 KV Cold FEG microscope (I^2TEM), developed between Hitachi and CEMES-CNRS, is used to acquire HRTEM images. It is equipped with a spherical aberration corrector located below the objective lens which achieve a spatial resolution of 80 pm [11 Snoeck]. An example of a TEM image for CMS sample is presented in figure 3.13.

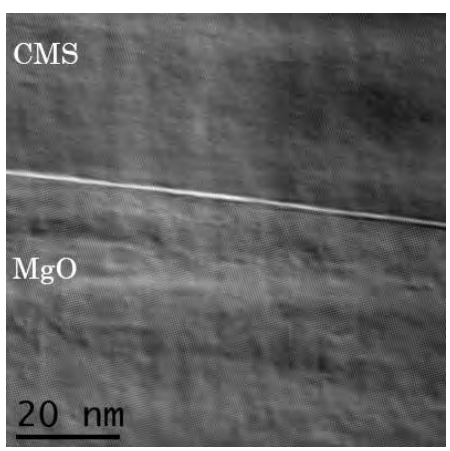

Figure 3.13: Intermediate-magnification HRTEM image for a cross-sectional CMS layer grown on MgO substrate.

3.3.4.2 Scanning Transmission Electron Microscopy (STEM):

HAADF STEM experiments were done by Dr. César Magen at LMA-INA, Zaragoza-Spain using FEI TITAN low-base microscope equipped with a spherical probe aberration corrector which is localized below the condenser lens system and above the objective lens.

In STEM mode, information is collected in a serial acquisition procedure. A small probe is scanned over the surface of the sample point by point. The image is formed after collecting signals at each position of the probe. Specific detectors will acquire the electrons scattered at various angle. There are three types of STEM detectors used: the Bright Field (BF) detector which permits to captures the unscattered electrons, the Dark Field (DF) detector collects the diffracted beam of angles between 10 and 40 mrad and the High Annular Dark Field (HAADF) detector that collects the high angles diffracted beams (angles>40 mrad) (Figure 3.14).

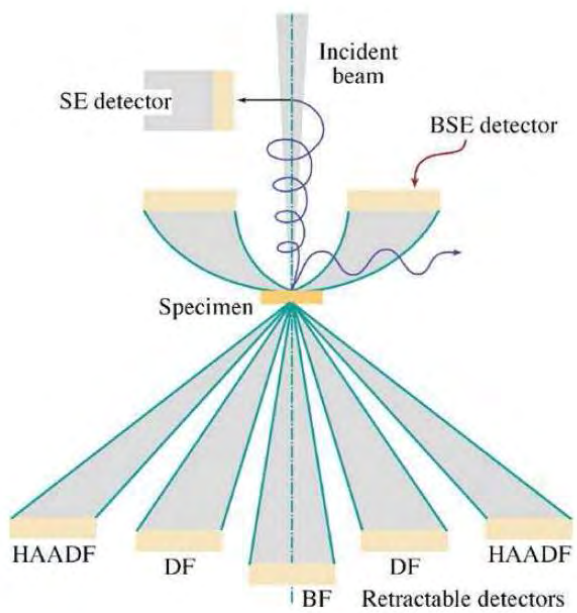

Figure 3.14: various electron detectors in STEM mode [9 William and Carter].

The HAADF detector collects the elastically incoherently scattered electrons resulting from interaction with the atomic nuclei of the sample [12 Peng]. The signal intensity collected by the HAADF detector is proportional to the atomic number (Z) of atoms that have interacted with the electron beam. It means that elements with high atomic number (Z=27 for Co) can be distinguished from lighter ones (Z=16 for Si). The intensity of the detector is expressed as:

$$I \sim m * t * Z^{\eta} \tag{3.5}$$

Where η is a constant between $\sqrt{2/3}$ and 2, m is a scaling constant and t is the sample thickness. η depends on many parameters: for example the convergence of the beam and the detector, the sample and the orientation of the sample. An example of an HAADF-STEM image of CMS layer is shown in figure 3.15

For more details about STEM technique, the reader is invited to check the following references [13-16].

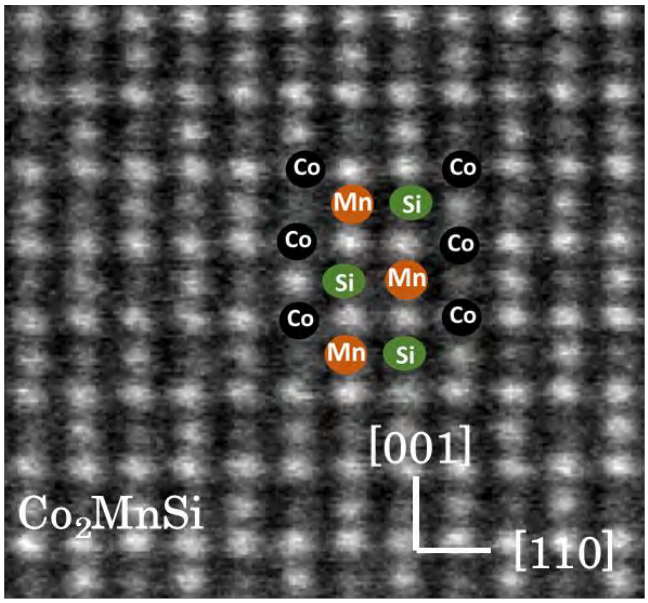

Figure 3.15: An HAADF-STEM image of CMS layer where the atomic columns of Co, Mn Si are clearly shown.

3.3.4.3 Geometric Phase Analysis (GPA):

Geometric Phase Analysis (GPA) is a quantitative method to study the local deformation field in crystalline materials. This method has been developed by M. Hÿtch and co-workers [17 Hÿtch, 18 Snoeck, 19 Rocher and Snoeck] and is described briefly as follows:

In a HRTEM/HAADF-STEM image, the different set of fringes can be considered as a Fourier series (summation of cosine functions). After applying a fast Fourier transform (FFT), the different sets of fringes are represented as g_{hkl} reflections in the reciprocal space, similar to a diffraction pattern. A mask is then applied to a $\vec{g}$ reflection in order to isolate the information corresponding to a single signal and an inverse Fourier transform (FFT^{-1}) is performed. A complex image is obtained from which we calculate the phase of the chosen signal (or set of fringes). The recovered phase information (so-called "*geometric phase*") is related to the displacement of the lattice plane by the following expression:

$$\varphi(g) = -2\pi\vec{g}.\vec{u}(\vec{r}) \tag{3.6}$$

where $\vec{g}$ is the Bragg periodicity and $\vec{r}$ is the position vector in the real space. The lattice deformation can then be calculated from the gradient of the phase image, in the direction of the chosen $\vec{g}$ vector. A 2D deformation field can also be calculated using at least two phase images reconstructed from two non-collinear $\vec{g}$ vectors. A more acquire result is obtained when ***GPA*** method is applied on HAADF-STEM images because of the signal-to-noise ratio is lower than those images obtained by HRTEM.

In Figure 3.16 we describe how we use GPA method for mapping the strain of the in-plane lattice parameter through the 220 plane: in a HAADF-STEM image obtained close to the CMS-MgO interface (Figure 3.16 (a)), we calculate the FFT image (Figure 3.16 (b)). Here we have selected the 220 spot using a cosine mask, as presented by a circle in the FFT. By solving equation 3.6, we reconstruct an image of the phase, taking as reference the lattice parameters of MgO, the color variation observed in the CMS layer evidences a lattice parameter difference between the MgO and CMS in-plane lattice parameters (Figure 3.16 (c)). In figure 3.16 (d) the strain is presented as the ε_{xx} in-plane deformation that is calculated from the phase gradient. Here a deformation of -4.6 % was measured in the CMS layer relative to the MgO substrate lattice parameters.

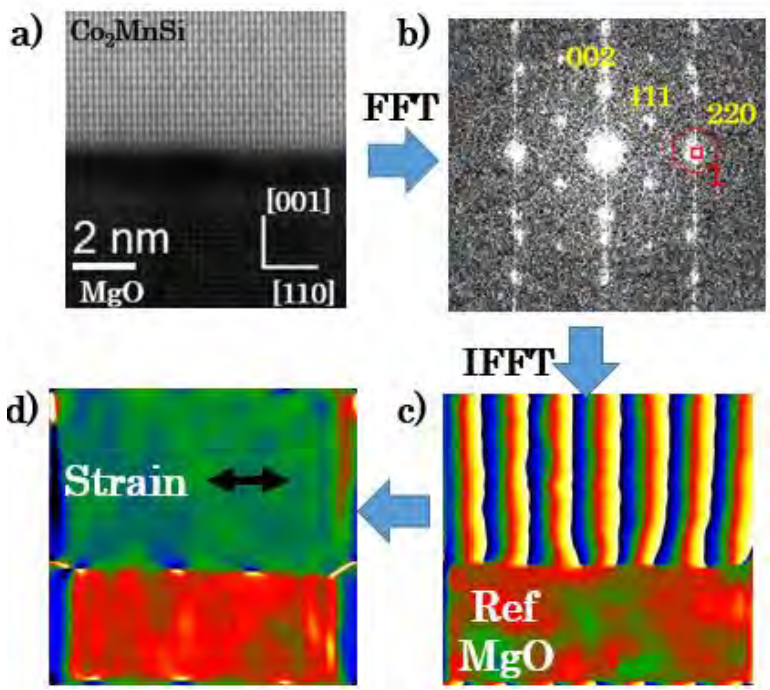

Figure 3.16: a) HAADF-STEM image of CMS/MgO and its corresponding b) FFT. c) The phase image and the d) strain mapping.

3.3.4.4 Lorentz Microscopy (LM):

The high spatial resolution of a TEM used to investigate the crystal structure and chemical composition of thin specimen at nanoscale can be also used to visualize, and quantitatively study the magnetic configuration of magnetic materials. Electron holography (EH) and Lorentz Microscopy (LM) are the most popular magnetic imaging TEM techniques that allow reconstructing the integrated magnetic induction along the electron trajectory and projected to the image plane, with spatial resolutions ranging from few nanometers (in the case of LM) to 1 nm (in the case of EH). Both techniques obtain the magnetic information of a magnetic specimen by retrieving the shift of the electron wave phase after it passes through

the sample. However, the way to get this phase shift is different in each case: in EH, the phase shift is recorded by making a interferometry experiment between two electron waves; in LM, the phase shift can be obtained by altering the transfer function of the microscope either by using a contrast aperture to select a particular magnetic deflection direction in the back focal plane (LM in Foucault mode [20 De Graef]) or by defocusing the image (LM in Fresnel mode). The later LM mode is a versatile method to get a rapid visualization of magnetic domains via the observation of magnetic domain walls (DWs). DWs were first observed by Hale in TEM in 1959 [21 Hale] and since then Lorentz microscopy technique gained a lot of success. The purpose of using this technique is to study the magnetic configuration of magnetic domains in our CMS thin films, as well as the determination of the exchange constant by measuring the DW width. In our study we use the LM in Fresnel mode and it is described as follows:

LM in Fresnel mode

From a classical approach, LM is based on the Lorentz force, $\mathbf{F_L}$, that experience the electrons travelling a velocity **v** when they pass through the electric (**E**) and magnetic (**B**) fields inside and around the ferromagnetic material:

$$\mathbf{F_L} = -e(\mathbf{E} + \mathbf{v} \times \mathbf{B}) \tag{3.7}$$

In absence of electric fields acting parallel to the image plane, the in-plane component of the magnetic induction will induce a deflection of the electron trajectory which is perpendicular to the in-plane magnetic induction direction ($\mathbf{B}_\perp = \mathbf{B}(x, y)$), according to the cross product. The electron deflection angle θ_L respect to the incoming electron trajectory can be calculated as:

$$\theta_L = \frac{e\lambda}{h} B_\perp t \tag{3.8}$$

Where t corresponds to the sample thickness. In presence of these magnetic domains with different orientations, the electron deflection process creates two bright and dark lines with excess and lack of electrons respectively imaging the domain wall (DW) separating neighboring magnetic domains (see figure 3.17). Therefore, in out-of-focus condition, a DW will produce a brighter and/or a darker contrasts in LM image, and this magnetic contrast can be inversed by changing the defocus sense. A schematic representation of the magnetic contrast formation due to DW in LM, in Fresnel mode, is shown in Figure 3.17. Thus LM is a powerful tool to perform a qualitative description of the magnetic configuration of ferromagnetic nanostructures by a direct visualization of DWs, and its versatility allows developing *in-situ* TEM experiments to follow the evolution of these DWs by the application of diverse stimuli like magnetic field, electric current, temperature and strain.

For a quantitative analysis, we need to make a more complex treatment that will permit getting the electron wave phase shift and understand the electron interference process around a DW that will allow measuring its width.

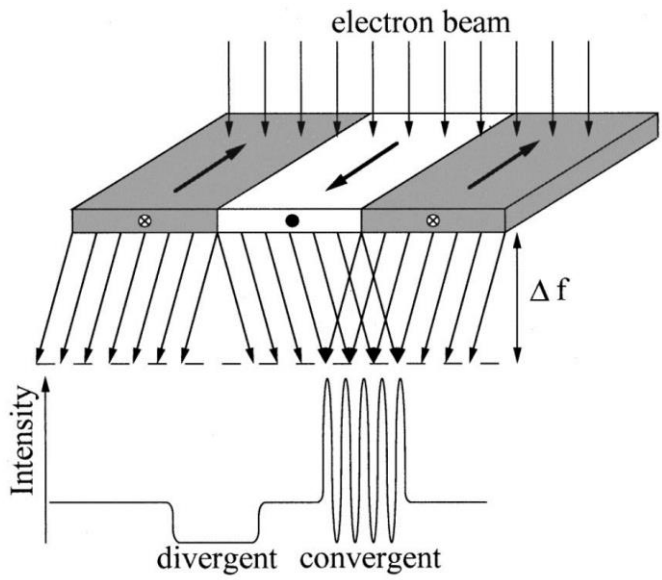

Figure 3.17. Schematic representation illustrating the mechanism of contrast formation by DWs in Fresnel mode. In top is represented the electron deflection process due to Lorentz force. In bottom is illustrated the resulting intensity profile traced perpendicular to DWs for a given defocus position $\Delta f = \Delta z \neq 0$. (Adapted from [22 Lloyd])

Quantitative magnetic information by TIE analysis

In LM, the phase shift is obtained by solving the following differential equation in the limit of small defocus, Δ_z:

$$-\frac{2\pi}{\lambda}\frac{\partial I(x,y,\Delta_z)}{\partial \Delta_z}\bigg|_{\Delta_z\to 0} = \nabla\cdot[I(x,y,0)\nabla\varphi(x,y)] \tag{3.9}$$

Equation 3.9 is the so-called transport of intensity equation (TIE) [23 Beleggia], and show how the phase shift gradient is proportional to the derivate of the intensity with respect to the defocus. This equation proposed by Van Dyck *et. al.* [24, 25 Van Dyck] arises by calculating the intensity of the image electron wave, $\psi_{ima}(\mathbf{r})$, considering a small alteration of the transfer function of the microscope due to a small defocus. Equation 3.9 can be solved by means of a focal series of Lorentz images, where images are recorded in-focus [$I(x, y, 0)$], under-focus [$I(x, y, -\Delta z)$] and over-focus [$I(x, y, \Delta z)$], conditions are used to calculate $\varphi(x, y)$ after rewriting the equation 3.9:

$$\nabla\varphi(x,y) = -\frac{\pi}{\lambda\Delta_z}\nabla^{-2}\nabla\left[\frac{1}{I(x,y,0)}\nabla\{\nabla^{-2}[I(x,y,\Delta_z)-I(x,y,-\Delta_z)]\}\right] \tag{3.10}$$

where ∇^{-2} is the two-dimensional inverse Laplacian operator. While Lorentz force describes the 'classical' movement of the electrons inside electromagnetic fields, in a quantum

mechanics approach the Aharanov-Bohm effect describes how the phase of the electron wave is shifted by the influence of these electromagnetic potentials:

$$\varphi(x,y) = C_E \int V(x,y,z)dz - \frac{e}{\hbar}\int A_z(x,y,z)dz \tag{3.11}$$

where C_E is a interaction constant that only depends on the acceleration voltage of the microscope, V is typically the electrostatic potential of the specimen and A_z is the z-component of the magnetic potential. If we assume that the specimen is chemically homogeneous and its thickness is constant, the phase shift gradient calculated by TIE method can be associated with the in-plane magnetic induction as:

$$\nabla\varphi(x,y) = -\frac{e}{\hbar}[\mathbf{n}_z \times t\mathbf{B}(x,y)] \tag{3.12}$$

where $\mathbf{n}_z$ is the z-component of the normal vector which is perpendicular to the sample plane. Equation 3.12 can be also expressed in term of $\mathbf{B}(x, y)$ as:

$$\mathbf{B}(x,y) = \left(B_x, B_y\right) = \frac{\hbar t}{e}\left(-\frac{\partial\varphi}{\partial y}, \frac{\partial\varphi}{\partial x}\right) \tag{3.13}$$

Thus the above vector expression will allow the reconstruction of vector maps of the in-plane magnetic induction, providing us a quantitative description of local magnetization orientation.

Measurement of DW width

By LM in Fresnel mode we can measure the width of DWs by taking advantage of the linear behavior between the width of magnetic contrast (W_c) and the defocus distance, where the magnetic contrast width increases with the increasing of the absolute value of the defocus distance. As commented previously, the different magnetization orientations of neighboring magnetic domains can produce either a bright contrast due to the accumulation of electrons or a dark contrast due to the deficient of them in the DW position. Another way to see this phenomenon is to think that a bright contrast is produced because of two images of both domains are moved toward the center of the DW, overlapping them, causing a *convergent image* interference, while a dark contrast is produced because of the two image are moved outside the center of the DW, separating them, causing a *divergent image* interference. As we see in Figure 3.18, while a divergent image interference induces a single valley, or inverted peak, in the intensity profile, a convergent image interference produces a fringe pattern due to the superposition of two electron waves that converge in the middle of the DW. Both contrast can be used to measure DW widths, but the bright one is more tricky because is more difficult to determine the width of the fringe pattern.

For Bloch walls, the domain wall width can be measured by using a simple analytical expression for convergent- and divergent-wall width versus defocus distance [26 Wade, 27 Volkov]:

$$W_C = W_{DW} + 2\theta_L\Delta_z \tag{3.14}$$

W_{DW} corresponds to the DW. Thus, W_{DW} can be calculated from the above equation by a straightforward extrapolation to $\Delta_z = 0$ of a linear regression of the function $W_C(\Delta_z)$. In addition, the linear regression slope gives us information about the deflection angle θ_L, parameter that can be also estimated from equation 3.8 if we know the magnetic induction of the specimen and the sample thickness around the DW. The main drawback of equation 3.8 is that we have to know previously the effective thickness, parameter that is not easy to obtain. Fortunately, there is a way to estimate the product $B_\perp t$ by measuring the fringe spacing created in the convergent image (Figure 3.18-d) for the bright magnetic contrast at high defocus values. If we assume that the magnetic field away from the DW is uniform so:

$$B_\perp t = \frac{h}{e}\frac{1}{2s} \tag{3.15}$$

Where 's' is the spacing of the fringes for a bright contrast. From equation 3.8 and 3.15 we can easily deduce that the slope of equation 3.14 is directly related with $1/s$ as:

$$2\theta_L = \frac{\lambda}{s} \tag{3.16}$$

Thus, equation 3.16 can be used as an accuracy parameter of linear regression to determine the DW width of Bloch walls. In the case of Néel wall, the DW width determination is not straightforward, because its magnetic structure is more complex and we do not know if the DW width measured by Lorentz Microscopy corresponds to either the width of the core or tail Néel wall.

An example of the CMS layer taken at different defocus values is presented in figure 3.18. In chapter 4, we will show the results of DW observed by LM technique.

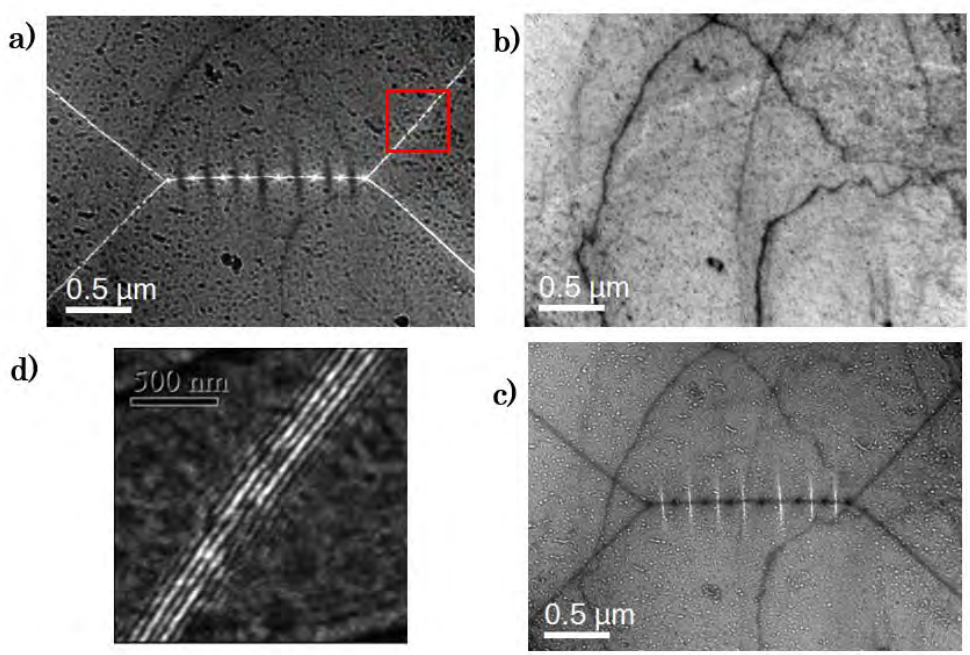

Figure 3.18: observation of domains walls in a) over-focus $\Delta_z > 0$ and c) under-focus ($\Delta_z < 0$). Image b) corresponds to the in-focus ($\Delta_z = 0$) observation where no magnetic domains are observed. Figure d) shows the fringe spacing of the red box in a)

3.4 Magnetic characterization techniques

Ferromagnetic resonance (FMR), Longitudinal Magneto-Optical Kerr Microscope (LMOKE) and Physical Property Measurement System (PPMS) are the techniques used in this thesis work to study the static and dynamic magnetic properties of CMS films. The mentioned techniques will be detailed as follows:

3.4.1 Physical Property Measurement System (PPMS)

Magnetic moment measurements of the CMS films have been performed at the "Laboratoire de Physique et Chimie des Nano-Objets" (LPCNO), Toulouse. These measurements have been performed with a PPMS-VSM device from Quantum Design. This magnetometry measurement is based on the variation of magnetic flux induced in two pickup coils by a vibrating sample. One of the main advantages of this device is the possibility to apply large fields up to 9 T and to perform measurements down to 2 K. However, our experiments have been performed in magnetic fields up to 1T at room temperature.

3.4.2 Magneto-Optical Kerr Effect (MOKE)

The interaction between light and a magnetic medium is known for more than a century since the discovery of the Faraday Effect in 1875 and the Kerr effect in 1877. The Faraday Effect corresponds to the rotation of the polarization axis of a linearly polarized electromagnetic wave travelling through a dielectric and simultaneously submitted to an external magnetic field parallel to the propagation direction. This effect is due to the difference of propagation velocity for the right and left handed waves composing the initial wave. In a simple approximation, the rotating electric field of the circularly polarized wave induces a circular electric polarization in the material, which in turn creates a magnetic field. Depending upon the polarization (right or left), the additional magnetic field oppose or add up to the magnetization (or magnetic field) and leads to a decrease or increase in the velocity. It is important to note that the rotation of the polarization is reversed if the magnetic field is reversed.

The Kerr effect is the equivalent of the Faraday Effect but for the reflected component of the incident wave. In the case of a magnetic sample, it is the magnetization of the sample which acts as the effective magnetic field. In this case we talk about the Magneto-Optical Kerr Effect (MOKE). In reflection, there is also a second effect that induces a rotation of the polarization and some ellipticity (Figure 3.19-b). It is called the Voigt effect and it is proportional to the square of the normalized component of the magnetization. However this effect is generally lower than the Kerr effect and is often neglected.

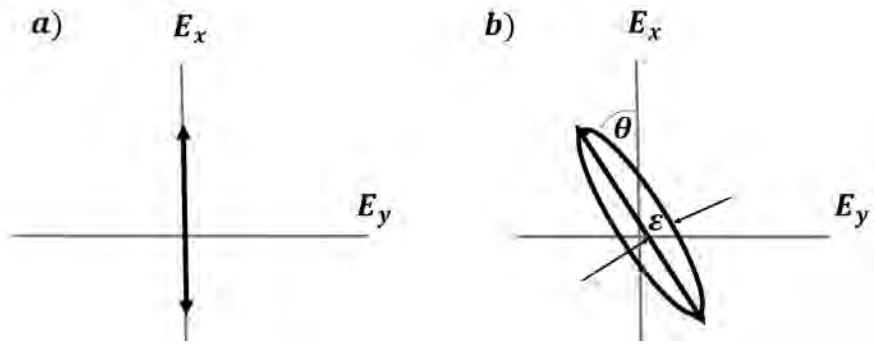

Figure 3.19: Schematic illustration of a polarized wave before a) and after b) the reflection.

Therefore, in a MOKE experiment, the polarization of a linearly polarized light reflected at the surface of a magnetic material will depend on the direction of the magnetization with respect to the propagating wave vector. Three experimental configurations are possible depending on the orientation of the magnetization with respect to the plane of incidence (see Figure 3.20). In the polar configuration (PMOKE) the magnetization is perpendicular to the plane of the layer and in the incident plane of the light. In the longitudinal configuration (LMOKE) the magnetization lies in plane of the layer and in the incident plane (Fig 3.20-b). In the transverse configuration (TMOKE or Quadratic MOKE QMOKE) the magnetization lies in the plane of the layer and is perpendicular to the incident plane (Fig 3.20-c).

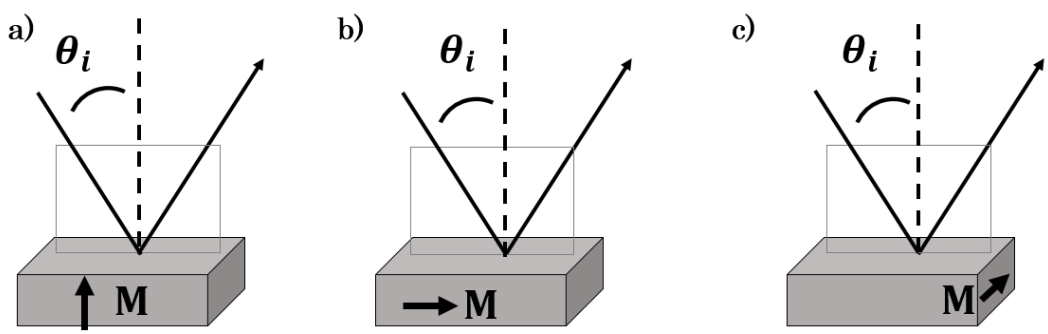

Figure 3.20: a) Polar, b) Longitudinal and c) Transverse configurations of MOKE.

In this work, the magnetization of the CMS films has been studied in the LMOKE configuration. The set-up is located on the ONERA campus. The experiment is schematized in Figure 3.21. It is composed of a Laser source He-Ne with a 5 mW power. Before the sample, a Glan-Thomson polarizer (P) allows to linearly polarize the light. A magnetic field is applied parallel to the plane of the sample by two Helmotz coils. The magnetic field can reach 450 Oe. The reflected wave is analyzed with an analyzer composed of a rotary retardation plate, set

to get a rotation of the polarization at 45° with respect to the polarization at the output of (P), and a Wollaston bi-prism. The latter allows to separate the reflected wave into two equal components. Finally each component will be measured by two PIN photo-diodes and their difference is recorded as a function of the applied field. Prior to the experiment, the intensity on each diode is set to be equal in absence of external field. Then the field is applied back and forth in a sequence zero->+saturation-> - saturation-> +saturation.

An example of a LMOKE measurement of the hysteresis curve on our sample is presented in Figure 3.22.

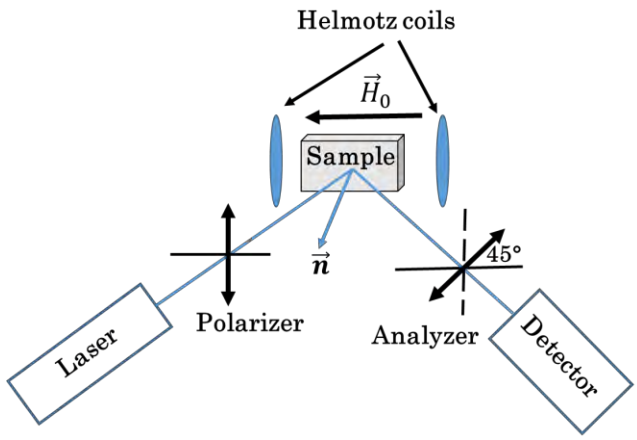

Figure 3.21: schematic illustration of MOKE experimental set-up.

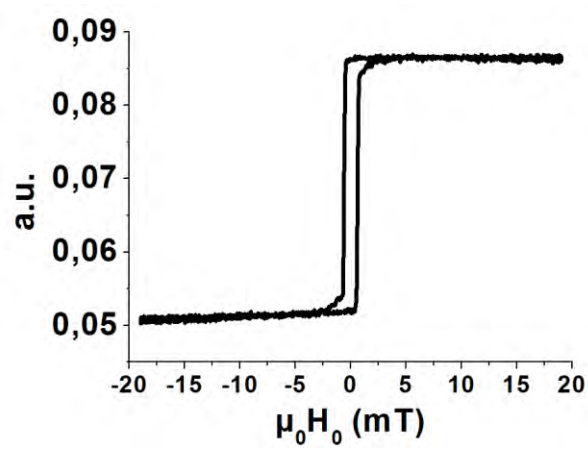

Figure 3.22: An example of Hysterises loop for LMOKE measurements.

3.4.3 Ferromagnetic Resonance (FMR)

Ferromagnetic resonance (FMR) spectroscopy is one of the techniques used to probe electrons spin magnetic moments and study magnetic properties and spin dynamics of

ferromagnetic materials. FMR was first discovered in 1911 by Arkadyév after he observed the absorption of Ultra High Frequency radiation in ferromagnetic materials. In 1923, the results of Arkad'yev were explained by Dorfman as an optical transition due to Zeeman splitting from which it provides a way to study ferromagnetic materials. As explained in chapter 2, FMR is based on the absorption of microwave field of a few GHz by a ferromagnetic material. This section provides an overview about the experimental setup used to extract the magnetic parameters in this work.

3.4.3.1 FMR Experimental set-up

During this PhD work, we have developed a FMR measurement set-up at the CEMES Lab. We used the well-known modulation technique, first because of the easiness to set, as it avoids complicated calibration procedure like in vectorial measurements, and also to get a good signal to noise ratio.

Our experiment is depicted and schematically illustrated in Figure 3.23. The principle of the measurement is the following. A microwave signal of given frequency is injected in a microstrip line above which the CMS sample is placed. In this work, the injected microwave power in the stripline is about -15 dBm. Such amplitudes of the microwave signal allows to stay in the linear regime of excitation of the spin dynamics. The microstrip line is placed in an electromagnet allowing for a static magnetic field to be applied. Additionally Helmholtz coils are fed with a low frequency current which allows modulating the static field. In this experiment the static magnetic field is swept and the frequency of the microwave signal is constant. At the resonance field, the magnetic sample absorbs some energy from the microwave field (called the pumping field). The decrease of the microwave amplitude is measured in transmission via a schottky diode and a lock in amplifier. All instruments are piloted via a homemade LabVIEW interface program.

The maximum static magnetic field that can be applied is equal to 0.7 T for a field applied in the plane of the layer and 1.5 T for a perpendicular applied field. This is achieved by changing the poles of the electromagnet. Also, our set-up allows for a rotation of the electromagnet from 0 to 180°.This allows to study the angle dependence of the FMR signal in plane. The low frequency generator feeds a Kepco current source which is connected to the Helmoltz coils. The frequency of the voltage signal sent by the generator to the Kepco and then the frequency of magnetic modulation is set to 73 Hz. The amplitude of the modulation field is of 2 Oe. The same voltage signal that feeds the Kepco is injected to the reference input of the lock-in for the demodulation measurement.

The microstrip line has been fabricated at ONERA-Toulouse clean room facility from a 350 μm thick Alumina wafer with a dielectric constant ≈ 10. The dielectric is fully covered by gold on one side in order to connect to the ground plane of the sample holder made of brass. On the other side of the dielectric, a gold line of 400 μm width has been realized by UV lithography. The width has been chosen in order to be as close as possible to 50 ohms and also to facilitate the connection with the central core of SMA connectors. As can be shown from the reflection and transmission measurement in Figure 3.24, the line is clearly not 50 ohms

adapted within all the frequency range. The periodic modulation of the transmitted S21 or reflected S11 signal, measured with an Anritsu MS4642A vector network analyzer, comes from the impedance mismatch between the line and the connectors. The S11 and S21 parameters corresponds to the coefficient of reflection and transmission, respectively of the incident microwave voltage signal. The most probable reason is a bad value of the dielectric constant considered to design the line. Due to the difficulty to get access to lithography facilities, all measurements presented in this work have been performed with this microstrip line.

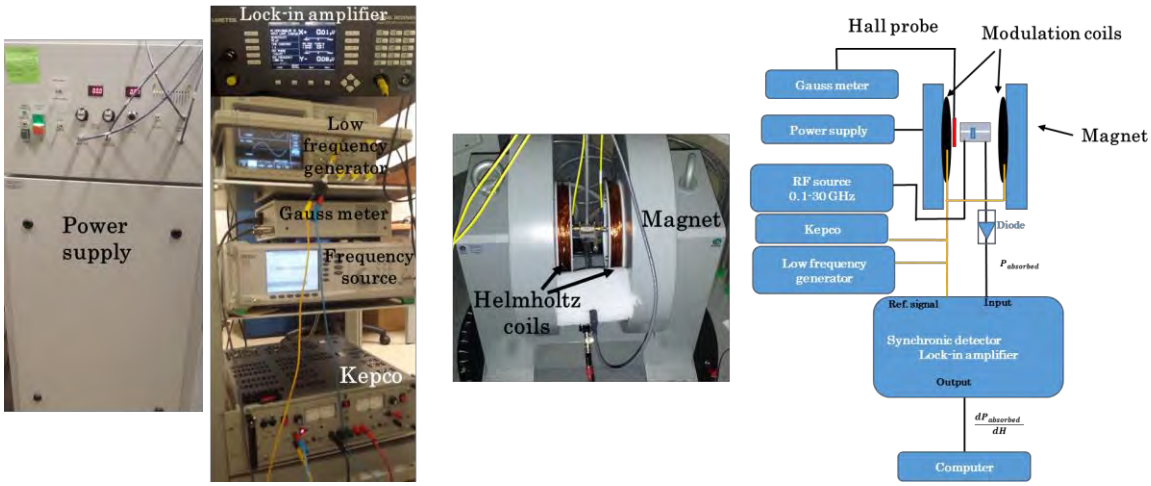

Figure 3.23: depicted presentation and schematic illustration of the FMR set-up.

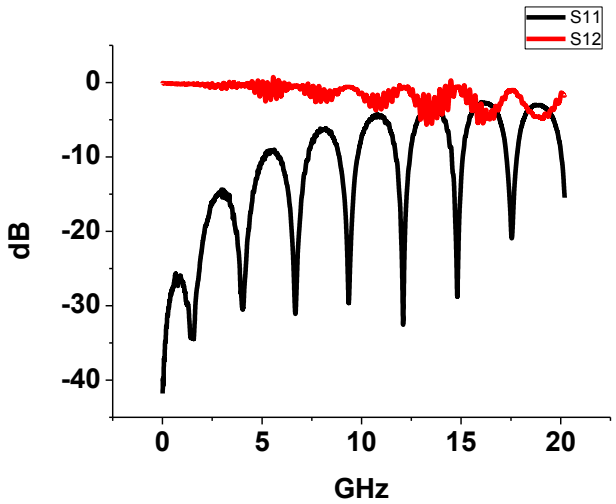

Figure 3.24: Reflection “S11” and transmission “S12” measurements of the transmission line.

Now let us study the response of magnetic material to electromagnetic radiation at a fixed frequency ω_0. As explained in chapter 2 (section 2.3.1), the magnetic susceptibility is complex and equals to $\chi' + i\,\chi''$. It is the imaginary part of the susceptibility that corresponds to the energy losses and to microwave absorption. However, modulating the value of the static field, the absorption is also modulated. Experimentally it corresponds to the measurements of the derivative of $\chi''(\omega)$

Let's consider the pumping field to be of the form $h(t,\omega) = h_0 e^{i\omega t}$. Following $m(t,\omega) = m(t,\omega)e^{i(\omega t+\delta)}$, the dynamic component of the magnetization is of the form $m(t,\omega) = (\chi' + i\chi'')h_0 e^{i\omega t}$. The variation of the free energy of the system can be written as dF=$-\mu_0$h.dm. Then the average power dissipated by the magnetic system can be written as:

$$P_{absorbed}^{tot} = \lim_{T\to\infty} \frac{\mu_0}{T}\int_0^T Re(h).Re\left(\frac{dm}{dt}\right)dt = \frac{1}{2}\mu_0\omega\chi''(\omega)\,h_0^2 \qquad (3.17)$$

Experimentally, we measure the variation of the transmitted voltage in the microstrip line due to the absorbed power in the magnetic film. The variation of voltage is due to the inductive coupling between the microstrip and the magnetic sample. Figure 3.25 gives a very simplified vision of the transmitted signal. We see that due to modulation of the static field at frequency, $f_{modulation}$, the amplitude of transmitted amplitude varies also as $f_{modulation}$ and is proportional to $d\chi''/dh$. Using a Shcottky diode allows to recover the envelop function (red line in Fig. 3.26) as the output voltage is given by $\sqrt{v(t)^2}$. This low frequency voltage is then injected at the input of the lock-in.

Therefore, the signal measured with the lock-in is proportional to the derivative of the susceptibility (Figure 3.26). This technique has the major advantage of increasing the signal to noise ratio and it is easy to set-up as it avoids complicated calibration process that must be performed for example with Vector Network Analyzer.

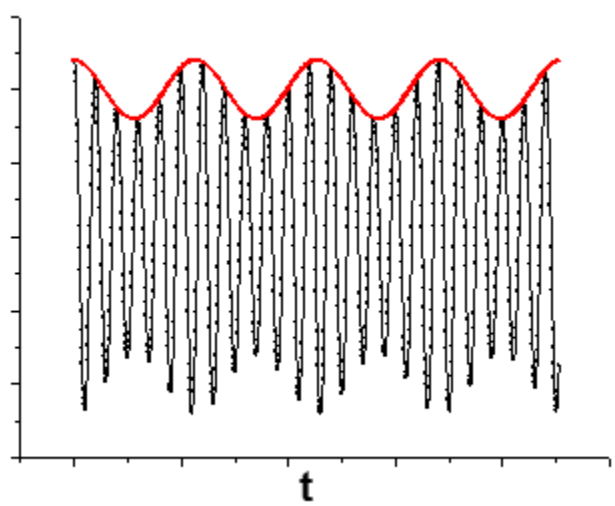

Figure 3.25: Transmitted signal with the red envelope curve.

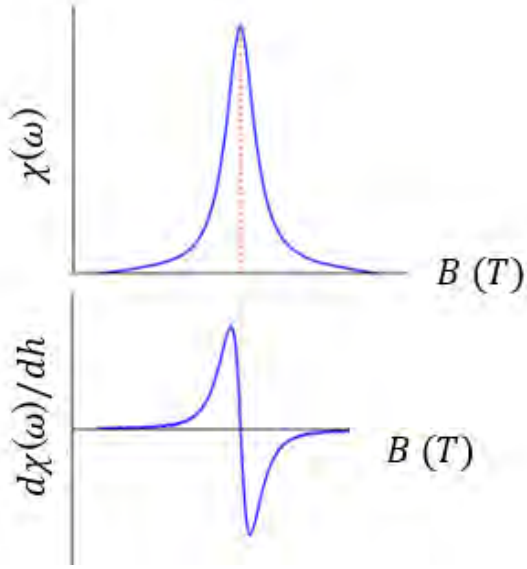

Figure 3.26: Microwave absorption and FMR derivative signal as a function of the applied external field.

From the measured signal, we can obtain the resonance magnetic field H_{res} and the linewidth ΔH. The resonance field is measured as the field for which the signal is crossing the zero. The full width at half maximum, i.e. the linewidth ΔH, is obtained from the peak to peak linewidth ΔH_{pp} as expressed in the following relation:

$$\Delta H = \sqrt{3}\,\Delta H_{pp} \tag{3.18}$$

However, this model describes the perfect case for a perfect 50 Ω microstrip line, for which the propagating mode is purely TEM (transverse electromagnetic), and in the case of small loses induced by the magnetic material. In this case the variation of the impedance ΔZ of the stripline is proportional to the variation of the inductance ΔL which is related to the imaginary part of the susceptibility χ''. In the perfect case of an accorded cavity for example, the relation is $\Delta L = \mu_0\,\chi''\,\frac{2d*l}{\omega}$, where d and l are the thickness of the magnetic film and its length. In reality we always have some mixing of the real and imaginary part of the susceptibility leading to an asymmetry of the measured signal. The asymmetry of the signal is due to several reasons. First, the propagating mode is never purely TEM and the coupling between the magnetic material and the microstrip modifies the propagating mode. Additionally the samples we measure are few mm long and so propagating effects cannot be completely neglected. By consequent, the measured signal are fitted with a function of the form $d\chi'/dH\ \sin(\varepsilon)+\ d\chi''/dH\ \cos(\varepsilon)$, with ε varying from 5° to 15° depending on the sample. In chapter 5, we will show some signals with a very pronounced asymmetry and we will show that it corresponds to the presence of multi resonance peaks.

3.5 Ion irradiation/implantation technique

Ion implantation/irradiation consists of accelerating energetic ions into a material with a fixed energy. The ions which are penetrating can induce some displacement within the sample in the irradiation regime or to be localized/implanted inside the material in the implantation regime. The two regimes depends on the kinetic energy of the incoming atoms. Ionic bombardment was first introduced by Shockley in 1954 at Bell laboratories but later in 1970's the ionic implantation technique was developed to introduce impurities in the studied systems. As mentioned in chapter 1, this technique is highly desired to modify the structural electronic and magnetic properties for electronic systems and industrial applications. The main application of this technique is the doping of semiconductor materials for the fabrication of integrated electronic devices. Implantation/irradiation can be done with almost all the elements such as Ga, He, Cr, Si and many others.

During this thesis, the ion irradiation of Heusler alloys is carried out at room temperature in CEMES laboratory using an ion implanter VARIAN 200-A2F. This ion implanter (Figure 3.27) consists of:

- Ion source: which converts the electrically neutral atoms (Arsine, Phosphorus or helium…) from the gas phase into an ion plasma and impurities. These ions are extracted with voltage of 25 kV.
- Mass spectrometer: consists of a magnetic sector which bends the ion beam through a right angle, spatially separate the different masses present in the beam and select desired ions species passing through a selection aperture before reaching the accelerator.
- Accelerator: It will increase the ion energy up to 200 KeV to the ions to be implanted.
- Focusing and Scanning system: a quadrupole lens and deflection plates in x and y directions to focus and scan the ion beam on the selected sample to produce uniform implantation/ irradiation with a desired fluence.

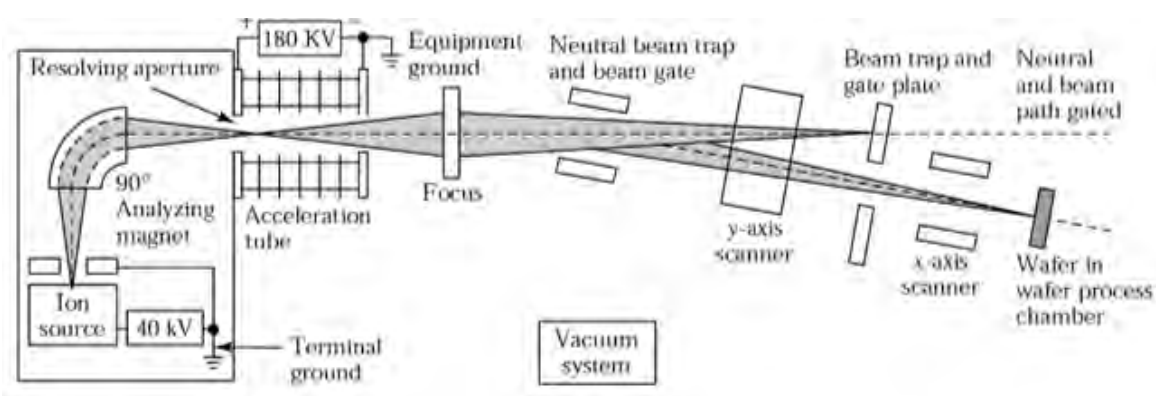

Figure 3.27: schematic illustration of ion implanter.

3.5.1 Ion-Solid interaction

When an ion beam bombards a solid material, several mechanisms will take place to slow down the accelerated ions and dissipate their energy. These mechanisms are divided into 1) nuclear energy losses which occur as a result of elastic collision where the energy is transferred from the kinetic incident ion to the target atoms, and 2) electronic energy losses which occur as a result of inelastic scattering where the electrons of the ions interact with the electrons of the target atoms [28 Giannuzzi]. The interaction mechanism is traditionally divided in a nuclear and an electronic stopping power. The ion energy loss is characterized by the sum of both terms. The contribution of each effect varied along the trajectory of the ions. Finally, both mechanisms define the stopping range of an ion energy loss in a path length and the final ion concentration distribution (figure 3.28). The stopping power range is expressed as follows:

$$S = \left(\frac{dE}{dx}\right)_{nuclear} + \left(\frac{dE}{dx}\right)_{electronic} \tag{3.19}$$

Nuclear energy losses are dominant to explain ion-solid interaction for low energy accelerated ions with high atomic number, but electronic energy losses becomes important for high energy accelerated ions with low atomic numbers. In nuclear energy loss process, the accelerated ions will transfer energy to the target atoms which can be displaced from their initial position (lattice sites) if the energy is high enough. These recoil atoms can also induce the displacement of the lattice sites as far as their energy is larger than a threshold value. This is known as the collision cascade. This leads to the movement of the ion to an interstitial site by leaving a vacancy in the target lattice site. The vacancy-interstitial pair is called the **Frenkel pair** or **Frenkel defect**. The displaced atoms can undergo further collisions in their way through the material which leads to other types of defects like dislocations characterized by local lattice heating of the target material. Electronic losses have less lattice disorder impact on the target lattice than the nuclear energy losses due to the small energy transfer collision [29 Gaier].

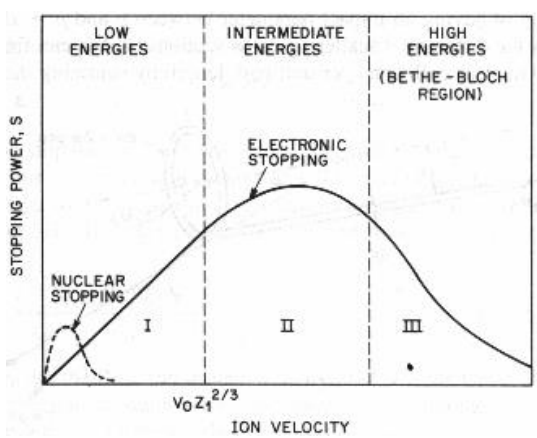

Figure 3.28: stopping range power as a function of ion velocity.

Chapter 3 References:

[1] D. K. Fork, D. B. Fenner, G. a. N. Connell, J. M. Phillips, and T. H. Geballe, "Epitaxial yttria-stabilized zirconia on hydrogen-terminated Si by pulsed laser deposition," *Appl. Phys. Lett.*, vol. 57, no. 11, pp. 1137–1139, Sep. 1990.

[2] A. Inam, C. T. Rogers, R. Ramesh, K. Remschnig, L. Farrow, D. Hart, T. Venkatesan, and B. Wilkens, "a-axis oriented epitaxial YBa2Cu3O7−x-PrBa2Cu3O7−y heterostructures," *Appl. Phys. Lett.*, vol. 57, no. 23, pp. 2484–2486, Dec. 1990.

[3] D. M. Hwang, T. Venkatesan, C. C. Chang, L. Nazar, X. D. Wu, A. Inam, and M. S. Hegde, "Microstructure of insitu epitaxially grown superconducting Y-Ba-Cu-O thin films," *Appl. Phys. Lett.*, vol. 54, no. 17, pp. 1702–1704, Apr. 1989.

[4] P. Willmott, "Deposition of complex multielemental thin films," *Prog. Surf. Sci.*, vol. 76, no. 6–8, pp. 163–217, Oct. 2004.

[5] Cho, A. Y.; J. R. Arthur, Jr. 'Molecular beam epitaxy. Prog. Solid State Chem., 10: 157–192. (1975).

[6] P. Turban, S. Andrieu, B. Kierren, E. Snoeck, C. Teodorescu, and A. Traverse, "Growth and characterization of single crystalline NiMnSb thin films and epitaxial NiMnSb/MgO/NiMnSb(001) trilayers," *Phys. Rev. B*, vol. 65, no. 13, Mar. 2002.

[7] G. Ortiz Hernandez, "Elaboration et étude des propriétés physiques de couches minces monocristallines d'alliage de Heusler à faible amortissement magnétique pour composants hyperfréquences," Université de Toulouse, Université Toulouse III-Paul Sabatier, 2013.

[8] J. Brentano, "Focussing method of crystal powder analysis by X-rays," *Proc. Phys. Soc. Lond.*, vol. 37, no. 1, p. 184, 1924.

[9] D. B. Williams and C. B. Carter, *Transmission electron microscopy: a textbook for materials science*, 2nd ed. New York: Springer, 2008.

[10] O. Scherzer, "The Theoretical Resolution Limit of the Electron Microscope," *J. Appl. Phys.*, vol. 20, no. 1, pp. 20–29, Jan. 1949.

[11] E. Snoeck, F. Houdellier, Y. Taniguch, A. Masseboeuf, C. Gatel, J. Nicolai, and M. Hytch, "Off-Axial Aberration Correction using a B-COR for Lorentz and HREM Modes," *Microsc. Microanal.*, vol. 20, no. S3, pp. 932–933, Aug. 2014.

[12] Y. Peng, P. D. Nellist, and S. J. Pennycook, "HAADF-STEM imaging with sub-angstrom probes: a full Bloch wave analysis," *J. Electron Microsc. (Tokyo)*, vol. 53, no. 3, pp. 257–266, 2004.

[13] H. Rose and C. F. Kisielowski, "On the Reciprocity of TEM and STEM," *Microsc. Microanal.*, vol. 11, no. S02, Aug. 2005.

[14] D. W. M.I. Den Hertog, "Characterization of silicon nanowires by transmission electron microscopy," *Acs Nano*, vol. 3, no. 10, pp. 3015–3022, 2009.

[15] S. Bals, R. Kilaas, and C. Kisielowski, "Nonlinear imaging using annular dark field TEM," *Ultramicroscopy*, vol. 104, no. 3–4, pp. 281–289, Oct. 2005.

[16] S. Bals, B. Kabius, M. Haider, V. Radmilovic, and C. Kisielowski, "Annular dark field imaging in a TEM," *Solid State Commun.*, vol. 130, no. 10, pp. 675–680, Jun. 2004.

[17] M. J. Hÿtch, E. Snoeck, and R. Kilaas, "Quantitative measurement of displacement and strain fields from HREM micrographs," *Ultramicroscopy*, vol. 74, no. 3, pp. 131–146, août 1998.

[18] E. Snoeck, B. Warot, H. Ardhuin, A. Rocher, M. J. Casanove, R. Kilaas, and M. J. Hÿtch, "Quantitative analysis of strain field in thin films from HRTEM micrographs," *Thin Solid Films*, vol. 319, no. 1–2, pp. 157–162, avril 1998.

[19] A. Rocher and E. Snoeck, "Misfit dislocations in (001) semiconductor heterostructures grown by epitaxy," *Mater. Sci. Eng. B*, vol. 67, no. 1–2, pp. 62–69, décembre 1999.

[20] "De Graef M 2001 Lorentz microscopy: Theoretical basis and image simulations Magnetic Imaging and Its Applications to Materials. Experimental Methods in the Physical Sciences vol 36 pp 27–67."

[21] *Hale M E, Fuller H W and Rubinstein H 1959 Magnetic Domain Observations by Electron Microscopy J. Appl. Phys. 30 789.* Springer Science & Business Media, 1998.

[22] S. J. Lloyd, N. D. Mathur, J. C. Loudon, and P. A. Midgley, "Magnetic domain-wall width in La 0.7 Ca 0.3 MnO 3 thin films measured using Fresnel imaging," *Phys. Rev. B*, vol. 64, no. 17, Oct. 2001.

[23] M. Beleggia, M. A. Schofield, V. V. Volkov, and Y. Zhu, "On the transport of intensity technique for phase retrieval," *Ultramicroscopy*, vol. 102, no. 1, pp. 37–49, Dec. 2004.

[24] D. V. Dyck, "High-speed computation techniques for the simulation of high resolution electron micrographs," *J. Microsc.*, vol. 132, no. 1, pp. 31–42, Oct. 1983.

[25] Van Dyck D and Op de Beek M 1993 A new approach to object wavefunction reconstruction in electron microscopy Optik (Stuttg). 3 103–7."

[26] R. H. Wade, "The Determination of Domain Wall Thickness in Ferromagnetic Films by Electron Microscopy," *Proc. Phys. Soc.*, vol. 79, no. 6, p. 1237, 1962.

[27] V. V. Volkov and Y. Zhu, "Magnetic structure and microstructure of die-upset hard magnets RE13.75Fe80.25B6 (RE=Nd, Pr): A possible origin of high coercivity," *J. Appl. Phys.*, vol. 85, no. 6, pp. 3254–3263, Mar. 1999.

[28] L. A. Giannuzzi, B. I. Prenitzer, and B. W. Kempshall, "Ion-solid interactions," in *Introduction to focused ion beams*, Springer, 2005, pp. 13–52.

[29] O. Gaier, "A study of exchange interaction, magnetic anisotropies, and ion beam induced effects in thin films of Co2-based Heusler compounds," Ph. D. dissertation, Technical University of Kaiserslautern, 2009.

Chapter 4: Structural and magnetic properties of as deposited CMS samples

As explained in the introduction of this thesis, the particular magnetic features of the Co_2MnSi, such as the half metallicity and low gilbert damping coefficient, are obtained in the most ordered crystal phase $L2_1$ even if half metallicity is also predicted for the B_2 order. Therefore, high crystalline quality of the CMS films is required.

In this work, our goal is to study how the structural order and magnetic properties in the CMS are correlated. Ion irradiation is used in order to modify and control the structure of the material and follow the evolution of the different magnetic parameters, especially in the dynamic range. We will show the results obtained on three series of CMS samples which, despite similar deposition conditions, show different structural and magnetic properties, either as deposited or under ion irradiation. Each series of samples corresponds to a thin film of CMS which is cut into few pieces, one is kept as the "reference" sample and the others pieces are irradiated at different fluences in order to follow the evolution of the structural and magnetic properties with irradiation and then with atomic disorder.

The three series of samples are denoted samples N°1, 2 and 3, each showing different interest and giving different insight into the correlation between the structure and magnetic properties of the CMS:

- Series N°1: the reference sample shows clearly two distinct crystal orders with distinct magnetic properties. Also the damping coefficient shows an anisotropic behavior for the reference sample (i.e. similar behavior in the 4 easy and hard axes). A complete magnetic and structural characterization of the four samples of this series has been performed.

- Series N°2: the reference sample shows a single crystal order with a lower magnetization value than observed for the reference sample of series N°1, but with a much stronger cubic and uniaxial anisotropy fields. The damping is also found to be anisotropic. Unfortunately only partial structural characterization could be performed on this series due to the small size of the samples.

- Series N° 3: it also shows two crystal orders for the reference sample with magnetic properties similar to those of the reference sample of series N°1. However, in opposite to series N°1, one of the crystal order is largely minority in the reference sample as it is barely visible in magnetic measurements. Furthermore, the reference sample shows an isotropic behavior of the damping coefficient. Here also only partial structural characterization could be performed on this series.

In this chapter we will focus on the structural and magnetic properties of the reference samples of each series. Those ones will be referred in this chapter as sample N°1, 2 and 3. We first present the methodology to determine the deposition conditions. Then a detailed study of the structural properties of the reference sample of series N°1 is presented and comments on the structural properties of samples N°2 and N°3 are given based on partial X-ray diffraction studies. The last part of this chapter will be devoted to the determination of the magnetic parameters of the 3 different samples.

4.1 Structural properties of CMS samples

In this section, we first present the deposition conditions of the CMS films studied in this work. Then we investigate its crystallographic properties by X-ray diffraction and HAADF-STEM imaging. X-ray allows getting access to the lattice parameters of the structure, degree of disorder. HAADF-STEM will be used for investigation of local chemical ordering of the alloy and the lattice mismatch with respect to the MgO substrate.

4.1.1 Determination of deposition conditions

We fabricated our samples with a sputtering chamber located at the CEMES laboratory (see chapter 3 for details). We present in this chapter the structural and magnetic properties of 3 samples deposited at 600° C and annealed at 700°C for one hour.

Our first task was to optimize the deposition conditions to fabricate high crystal order CMS films, *i.e.* the deposition and annealing temperature. We start from the PhD work of G. Ortiz [1 Ortiz] who developed the process of CMS thin films deposition with the same sputtering chamber used in this work. In our study we have also optimized the deposition conditions of CMS. Our methodology has been the following. First, we studied the effect of the deposition temperature. We start with a deposition temperature ranging from 400° and up to 700° with 50° step. Each film is annealed at 700° for 1 hour. In order to verify the "quality" of the film, we performed in-situ RHEED diffraction and ex-situ FMR measurements.

The interest in these two methods is simple. First RHEED gives information about the surface obtained with a 2 nm penetration depth of 20 kV accelerated electrons. RHEED is performed at each step of the process and allows for a direct observation of the nature of the growth (2D, 3D). An example of RHEED images is presented in Figure 4.1 for different deposition temperatures.

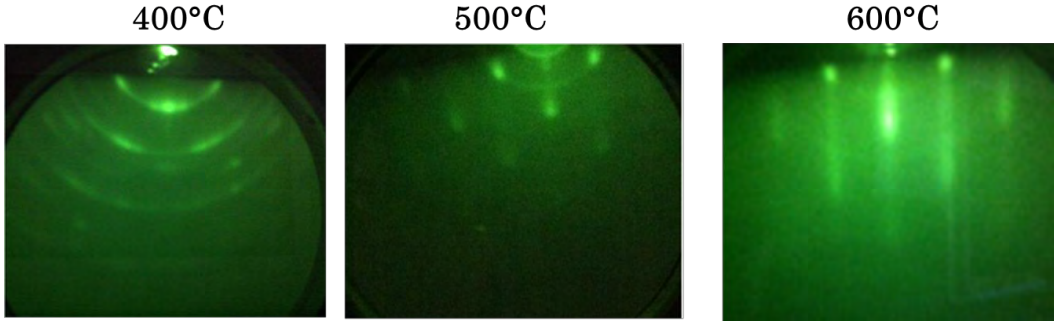

Figure 4.1: RHEED patterns of CMS at different deposition temperatures.

We observe that the diffraction patterns change from rings at 400°C to dots at 500° C and sticks at 600° C. The sticks formed in figure 4.1 represent a 2D monocrystalline surface, while the dots corresponds to a 3D monocrystalline rough surface. The rings patterns formed in figure 4.1 indicates a polycrystalline surface with a surface mosaicity. From the RHEED patterns observed at different deposition temperature, it is clear that deposition must be done above 600° C.

RHEED diffraction also allows to verify that the CMS films grow on the MgO substrate with the expected epitaxial relationship (001)[110]CMS//(001)[100]MgO, indicating a 45° rotation of the CMS on the MgO substrate in order to minimize the lattice mismatch. This is shown in Figure 4.2. The presence of sticks for both MgO and CMS layers is an indication of 2D growth. For the MgO substrate, the Kikuchi lines indicates the high crystalline quality. However, from CMS RHEED pattern at [110] direction, we observe some rings along with the rods and it might be explained as the film consists of textured grains in the monocrystalline layer.

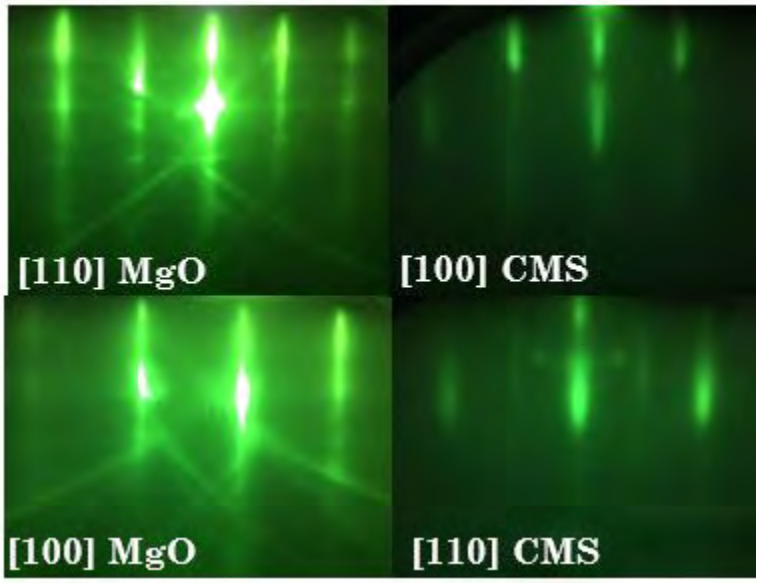

Figure 4.2: RHEED images of MgO buffer layer and the deposited CMS film along [110] and [100] directions.

Further study of the film "quality" is performed ex-situ via FMR linewidth measurement at 7 GHz. Indeed, according to theoretical prediction, the damping coefficient, and then the linewidth, decreases as the material gets more into the ordered $L2_1$ phase. An example of the FMR signal at 7 GHz for different deposition temperature is presented in figure 4.3. We observe a decrease of the linewidth as the deposition temperature is at 600°C. Once the deposition temperature is chosen, we studied the effect of the annealing temperature in a range between 600°C to 750°C with 50°C step. Annealing is always performed for 1 hour to increase the ordered crystalline structure of CMS.

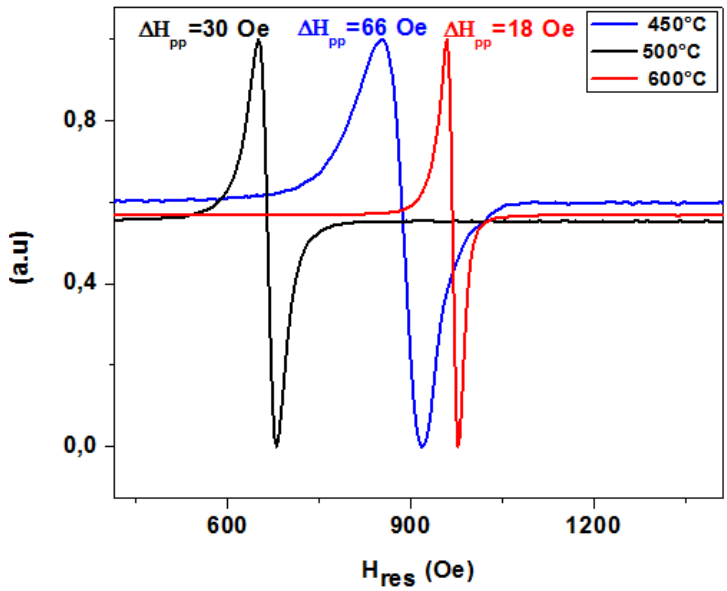

Figure 4.3: FMR absorption spectra for different deposition temperatures at 7GHz.

Therefore we found that the best compromise is to grow the CMS film at 600° with an annealing for one hour at 700°c.

In this manuscript, we have optimized the deposition conditions by both in-situ RHEED and ex-situ FMR line width measurements after many trials. We have decided to study three samples due to different magnetic and structural behavior although having similar deposition conditions (deposition and annealing temperatures, same RF power and Ar pressure). The three samples are named N°1, N°2 and N°3. Sample N°1 was the first to be fabricated, whereas samples N°2 and N°3 were fabricated after a renovation process of the sputtering chamber took place at CEMES laboratory in January 2015. After the renovation process, also an optimized study took place to retrieve the best optimized deposition conditions which were found to be the same as before.

In this chapter, we present the structural and magnetic properties for the three samples. A complete structural analysis, combining X-ray diffraction in normal and anomalous conditions and HAADF-STEM imaging, has only been performed on sample N°1 while only partial information on samples N°2 and N°3 has been obtained by X-ray diffraction in anomalous conditions.

4.1.2 Atomic disorder by X-ray Diffraction

X-ray diffraction is a powerful and common technique as it gives information about the phase order but also on the occupation site of the different atoms.

- **<u>Sample N°1:</u>**

X-rays reflectivity measurement gives a thickness value of 42 nm (Figure 4.4)

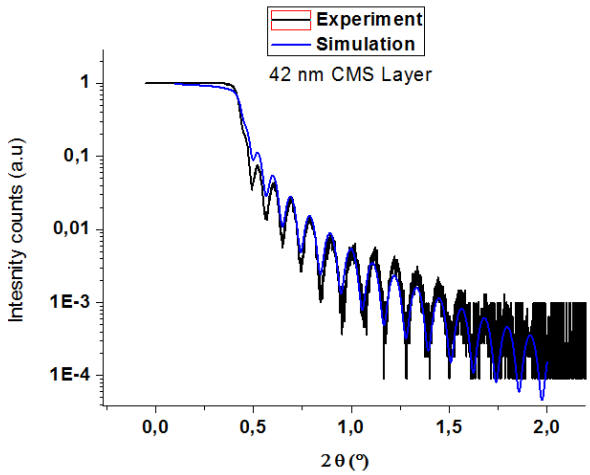

Figure 4.4: Reflectivity measurements of CMS layer.

The expected 45° rotation of the CMS layer with respect to the MgO in order to minimize the lattice mismatch (-5.1 %) is verified with φ scan as shown in Figure 4.5 for two different family of plane {111} and {022} for both the CMS and the MgO.

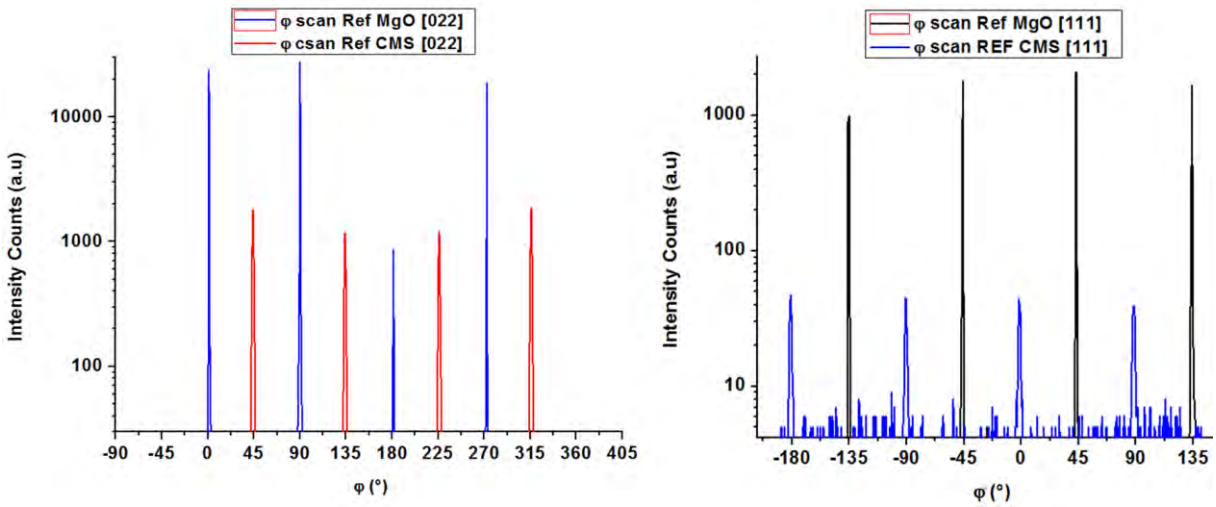

Figure 4.5: *φ* scan of the CMS with respect to the MgO substrate along the [022] and [111] directions clearly shows the 45° orientation.

The lattice parameters of the sample are obtained from the position of the reflection peaks in θ-2θ measurements (e.g: Figure 4.6). These values are obtained by fitting the diffraction peaks with (TOPAS) software. The result has shown that our film grow with a tetragonal symmetry with in-plane parameter a=5.63 Å and an out-of-plane parameter c=5.67 Å. We recall that in the perfect cubic structure, the lattice parameter is expected to be 5.65 Å. The lower value of the in plane lattice parameter is most probably due to the lattice

mismatch with the MgO substrate. Here we have the mismatch defined as $\frac{a_{CMS} - \sqrt{2}*a_{MgO}}{\sqrt{2}*a_{MgO}} = -5.4\%$ wich is in good agreement with the expected value of -5.2 %.

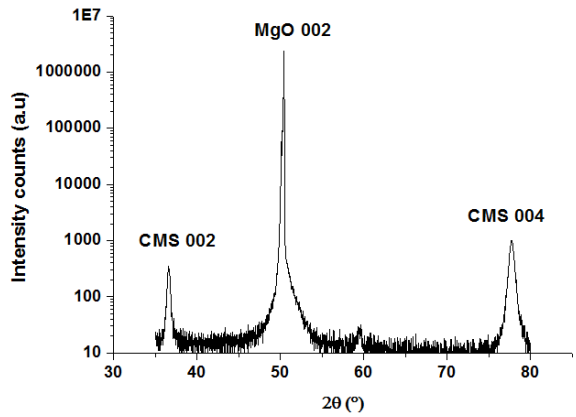

Figure 4.6: a) $\theta - 2\theta$ X-ray diffraction scan showing the 002 and 004 peaks of CMS and 002 MgO peak.

From X-ray diffraction intensity peaks, quantitative information can be extracted about the crystalline order of the CMS thin film. Different crystallographic phases of CMS Heusler alloys $L2_1$, B_2, $D0_3$ and A_2 can be identified by different X-ray diffraction peaks. Fundamental diffraction peaks appear for all CMS crystal phases and are characterized by the set of family planes $h + k + l = 4n$, n is integer, (e.g. 022 peak). In addition, superlattice (h,k,l) diffraction peaks when h, k and l are odd numbers, (e.g. 111), only appear when the $L2_1$ and/or $D0_3$ phases are present while diffraction peaks for planes $h + k + l = 4n$ +2 (e.g 002) appear for $L2_1$, $D0_3$ and B_2 phases.

Many groups have studied the order structure of CMS films based on the intensity peaks in different sets of planes obtained by X-ray diffraction [2 Gaier, 3 Pandey, 4 Belmeguanie and 5 Webster]. A majority of these studies consider that when the diffraction peak corresponding to the {111} family of plane is present then the material grows in the $L2_1$ order. However, one major problem consists in differentiating the different crystal order and more particularly the $D0_3$ and $L2_1$ phase that allows odd diffraction (hkl) peaks. Indeed, the scattering factors are very close at the Cu edge and therefore diffraction with diffractometers equipped with Cu-Kα1 source does not give all the information needed. To overcome this issue we performed experiments with two different sources for which different scattering factors appear. In this work we made diffraction experiments with a Co-Kα1 source because, due to anomalous diffraction of the Co at the K-edge, the Co and Mn scattering factor becomes distinguished and hence Co and Mn atoms can be differentiated

Thus, the different disorder parameters in CMS can be obtained combining diffraction measurements using Cu and Co Kα1 sources. The method employed here is based on a model proposed by Niculescu *et al* [6 Niculescu] and has recently been applied by Takamura *et al.* [7 Takumara] for the structural characterization of Co_2FeSi. In this model, α, β and γ are three disorder parameters. α corresponds to the number of Mn atoms located on Si sites and represents the Mn/Si substitution per CMS unit. Similarly β and γ corresponds to the number

of Co atoms on Si and Mn sites, respectively. Then, the structure factors for the different peak of interest are expressed as:

$$F_{111} \propto (1-2\alpha-\beta)(f_{Mn}-f_{Si})+(\gamma-\beta)(f_{Co}-f_{Mn}) \quad (4.1)$$

$$F_{002} \propto (1-2\beta)(f_{Co}-f_{Si})+(1-2\gamma)(f_{Co}-f_{Mn}) \quad (4.2)$$

$$F_{022} = F_{004} \propto 2f_{Co}+f_{Mn}+f_{Si} \quad (4.3)$$

Where f_{Co}, f_{Mn} and f_{Si} are the scattering factors of Co, Mn and Si respectively. We can see from equations 4.1 and 4.2, that if f_{Co} and f_{Mn} are close, as for Cu Kα source, the intensity of the diffraction peaks I_{111} ($\propto |F_{111}|^2$) and I_{002} ($\propto |F_{002}|^2$) are not sensitive to $D0_3$ order while it is for Co-Kα1 source in anomalous conditions. This is shown in figure 4.7 for which we calculated the modulus of the scattering factor of the Co, Mn and Si atoms for both the Co and Cu sources wavelengths.

To calculate the structure factor F_{hkl} for every diffraction peak, we need first to evaluate the atomic diffusion factor f_i for Co, Mn and Si atoms using the following relation:

$$f = (f^0 + f' + if'') * DW_{hkl} \quad (4.4)$$

f^0 is the Thompson factor, known as the normalized scattering curve. $f^0\left(\frac{\sin\theta}{\lambda}\right)$ expressed as:

$$f^0\left(\frac{\sin\theta}{\lambda}\right) = \sum_{i=1}^{4} a_i e^{-b_i(\frac{\sin\theta}{\lambda})^2} + c \quad (4.5)$$

Equation (4.5) is fitted to 9 parameters [8 Cromer] with a_i, b_i and c are presented in table 4.1 for each Co, Mn and Si. They are evaluated for each atom and their values are independent on the wavelength λ.

Co (z=27)	1	2	3	4
a	12.284	7.341	4.003	2.349
b	4.279	0.278	13.536	71.169
Constant C	1.012			

Mn (z=25)	1	2	3	4
a	11.282	7.357	3.019	2.244
b	5.341	0.343	17.867	83.754
Constant C	1.090			

Si (z=14)	1	2	3	4
a	6.2915	3.035	1.989	1.541
b	2.439	32.334	0.678	81.694
Constant C	1.141			

Table 4.1: Values of a_i, b_i and c for Co (Z=27), Mn (Z=25) and Si (Z=14). Values adapted from NIST database search forum and [9 MacGillavryy].

f' and f'' are additional contribution, corresponding to absorption and diffusion respectively. They can be estimated from attenuation and scattering cross section tables for

different atomic numbers Z and energies in KeV. For Cu source, $\lambda = 1.54$ Å, the equivalent energy is E= hc/λ = 8.066 KeV while for Co source, $\lambda = 1.78$ Å and the equivalent energy is 6.9435 KeV. The values of f' and f" for Co, Mn ad Si are presented in table 4.2.

Cu source 7.902 KeV	f' (electron per atom)	f" (electron per atom)
Co	-2.351	3.623
Mn	-0.5765	2.778
Si	0.2547	0.3316

Co source 6.915 KeV	f' (electron per atom)	f" (electron per atom)
Co	-2.012	0.5816
Mn	-2.035	3.592
Si	0.3016	0.4405

Table 4.2: corresponding energies, attenuation and scattering factors for Co, Mn and Si a) for Copper source and b) for Cobalt source. Values adapted from NIST database search forum and [9 MacGillavryy].

Finally, DW_{hkl} is the Debye-Waller expression with β is the Debye-Waller factor:

$$DW_{hkl} = e^{-\beta(\frac{sin\theta_{hkl}}{\lambda})^2} \tag{4.6}$$

The atomic scattering factors of Co, Mn and Si atoms for both Co and Cu Kα1 sources are plotted in figure 4.1 as a function of $\frac{sin\theta_{hkl}}{\lambda}$. We notice in figure 4.1 that, f_{CO} *and* f_{Mn} are almost the same for Cu kα source and thus the $D0_3$ disorder structure can't be distinguished from the $L2_1$ phase. On the other hand, we see a clear difference in the atomic scattering factors for Mn and Co using Co kα source.

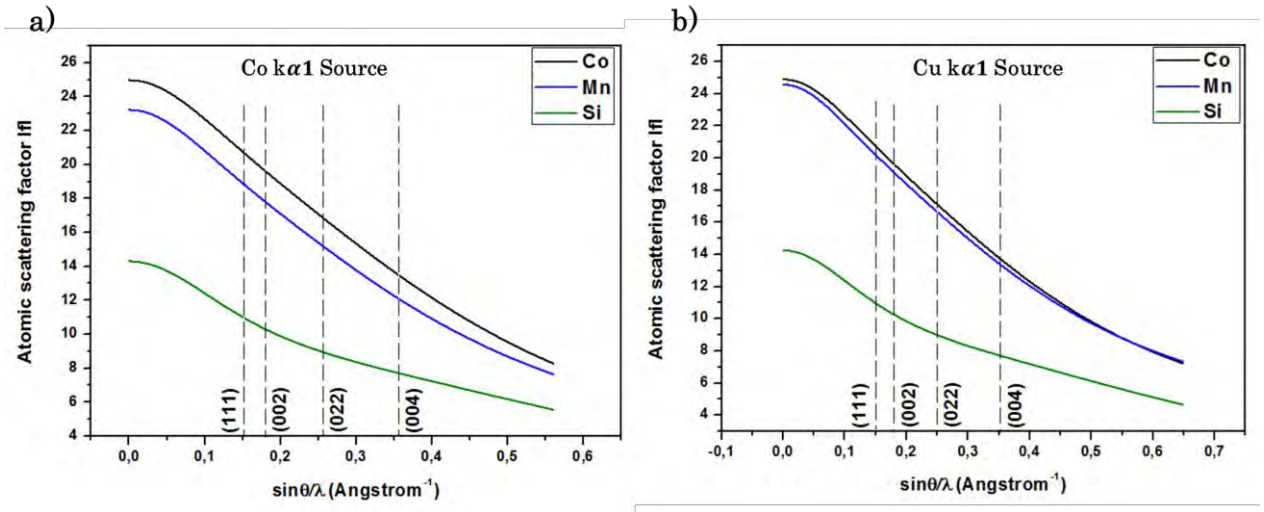

Figure 4.7: Atomic scattering factors of Co, Mn and Si atoms as a function of $\frac{sin\theta_{hkl}}{\lambda}$ for a) Co kα1 and b) Cu kα1 sources.

Then the intensity of the hkl peaks is expressed as follows:

$$I_{hkl} \approx L_{hkl(\theta)} P_{hkl(\theta)} |F_{hkl}|^2 \frac{1}{\sin\theta_{hkl}} \tag{4.7}$$

Where:

- $L_{hkl(\theta)}$ is the Lorentz factor equal to $L_{hkl(\theta)} = \frac{1}{\sin 2\theta_{hkl}}$.
- P is the polarization factor: $P_{hkl(\theta)} = \frac{1+A*\cos 2\theta_{hkl}}{1+A}$.
- A is the Attenuation factor, for Co source A= $\cos 53.13°$ and for Cu source A=$\cos 45.4°$.

In order, to obtain the different disorder parameters in equation 4.1, 4.2 and 4.3, we compare the experimental and calculated ratio of the superlattice diffraction peaks to the fundamental ones. As we have three unknown parameters we need four diffraction peaks. As already explained, experiments have been performed with two different diffractometers equipped with either a Co or Cu source to distinguish the Co/Mn exchange.
Measurements with the Co Kα_1 source have been performed in symmetric mode with a Panalytical Empyrean located at the LPCNO laboratory. It is equipped with a parallel plate collimator on the secondary lever which decreases the effect linked to the defocus of the X-ray beam when the sample is tilted. With this diffractometer, it has been possible to measure the (022) and (111) reflections in symmetric mode by tilting the sample at 45° and 54.74°, respectively. On the other hand, measurements with a Cu Kα_1 source have been realized at the LAAS laboratory with a Bruker D8-Discover (Da-Vinci) diffractometer. This instrument does not have the same collimator. Then the (022) and (111) reflections cannot be accessed in the symmetric mode due to the defocus of the X-ray beam. Moreover, they are not accessible as well in asymmetric mode due to geometrical constraint of the instrument. Therefore, only (002) and (004) in symmetric mode can be measured with the Cu Kα_1 source.

Taking this into account, our methodology is the following. We first calculate the ratio $I_{(002)}/I_{(004)}$ (Figure 4.8-d) obtained with the Cu Kα_1 source (λ=0.154 nm). According to equation

4.2 and 4.3, we get the value of β term. Let's note that we verify that the influence of the γ term, *i.e.* the exchange between the Co and Mn atoms, is negligible due to similar scattering factors.

Then the value of the β is injected in the calculation of the ratio $I_{(002)}/I_{(022)}$ (Figure 4.8-a and 4.8-c) obtained with the Co $K\alpha_1$ source (λ=0.179 nm). According to equation 4.2 and 4.3, we obtain the value of the γ. Finally the value of the α is obtained from the $I_{(111)}/I_{(022)}$ ratio also obtained with the Co $K\alpha_1$ source (according to equations 4.1 and 4.3).
The result of our method gives the following values:

$$\begin{cases} \alpha = 0.14 \pm 0.01 \; or \; 14\% \; \pm 1\% \\ \beta = 0.03 \pm 0.02 \; or \; 3\% \; \pm 2\% \\ \gamma = 0.01 \; \pm 0.01 \; or \; 1\% \; \pm 1\% \end{cases} \tag{4.8}$$

Let's note that the uncertainty is quite important. Typically we are not able to measure the value of Co/Mn exchange (γ) if less than 2%. Also, the uncertainty on β is important as compared to the nominal value. These uncertainties are mainly due to the fact that we are not using the same optics in the Co and Cu sources diffractometers.

From the disorder parameters we can calculate the probability of presence of each atom on its original site, considering a perfect $L2_1$ order as a starting structure. Indeed the probability of presence is calculated as follows in table 4.3 [7 Takamura]:

	X sites	Y sites	Z sites
Co	$2-\gamma-\beta$	γ	β
Mn	γ	$1-\alpha-\gamma$	α
Si	β	α	$1-\alpha-\beta$

Table 4.3: Probability of presence of each atom on the different atomic sites

The factor 2 on the Co site is due to the presence of two Co atoms per formula unit. We found values of 98, 86 and 83 % for the Co, Mn and Si respectively. Clearly our sample does not grow in the perfect L_{21} order. The values of the disorder parameters can be compared to the ones that we should have for the different crystal phase. The (α, β, γ) parameters for the $L2_1$, B_2, $D0_3$ and A_2 phase are respectively (0, 0, 0), (1/2, 0, 0), (0, 0, 2/3) and (1/4, 1/2, 1/2). While the Co/Mn and Co/Si exchange is very small in our films, we clearly see the presence of Mn/Si exchange. Neglecting the Co/Mn and Co/Si exchange, and taking into account that a fully B_2 order sample would show α = 0.5, we can conclude that we have about 0.14/0.5 ≈ 25% of B_2 order and ≈ 75% of $L2_1$ order in our films.

It is quite difficult to compare the quality of our films with the ones fabricated by other groups. As explained above, most of the structural studies performed with X-ray diffractions neglect this full analysis and consider a full $L2_1$ order of their films as long as the (111) diffraction peak is measured. However, we can state that our films show a high degree of order with almost 75% of the perfect order. This can be compared with the study of Takamura *et al.* on Co_2FeSi fabricated by rapid thermal annealing. Co_2FeSi is a very similar material as Co_2MnSi and is supposed to show similar magnetic behavior and crystal order. In figure 4 of Takamura article [7 Takamura], they show that (α, β, γ) is (0.12, 0.04, 0.10) for thermal

annealing at 700° while it decreases down to (0.06, 0.01, 0.04) for annealing at 800°. Then we see that for similar thermal annealing we get very similar values of disorder.

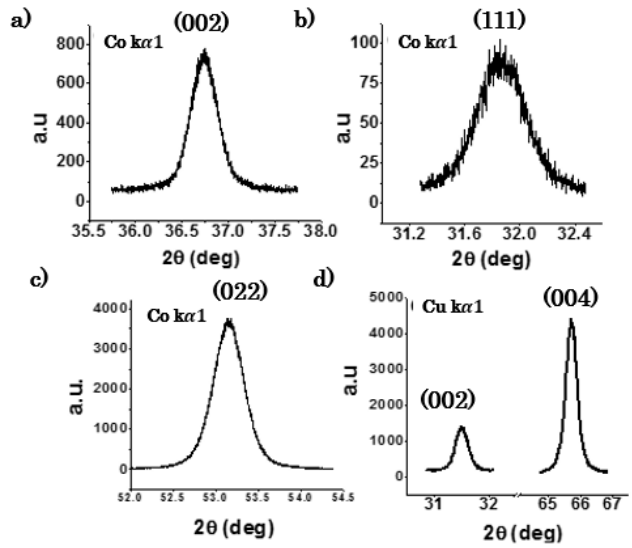

Figure 4.8: $\theta - 2\theta$ scan for Co Kα1 and Cu Kα1 sources at different diffraction peaks. (Values in ordinates are raw values indicating the number of photons received by the optical detector. The correction factors are included in the calibration process performed prior to the experiment).

X-ray diffraction were also performed on samples N°2 and N°3. Due to the small size of those samples, the obtained signal is weak and the diffraction peaks couldn't be detected by the Co source diffractometer located at the INSA.

Therefore, sample N°2 and N°3 has been studied with a new diffractometer (D8 discover equipped with Co micro source, berceau chi-phi,x, y z and scintillateur) installed recently at the CEMES Laboratory in November 2015. Reflectivity measurements gave a thickness of 42 ± 2 nm for sample N°2 and 50 ± 2 nm for sample N°3. The beam size of the diffractometer is of few mm² order allowing for the measurement of small size samples. However, the experiment is carried out without a monochromatic source and the X-ray beam is composed of both Kα1 and Kα2 edges radiation, which avoids any quantitative analysis about the atomic disorder on this sample.

The only experiment performed on the sample N°2 is a φ scan presented in figure 4.9, showing the (111) diffraction peak. According to the results obtained on sample N°1, we assume that this sample presents the $L2_1$ order. However, the amplitude of the signal is very weak, especially as compared to the sample N°3 (which has similar dimensions). Then, two assumptions can be made. Either the $L2_1$ is not the main crystal order in this sample, or it grows in the $L2_1$ phase but it present a high ratio of Co/Si exchange. The study of the magnetic parameters presented below is more favorable to the second assumption but it is most probable that the B2 order is present in this sample, similarly to the sample N°1 in section 4.2.3.

For sample N°3, we could perform diffraction experiments with the diffractometer equipped with the Cu source at the LAAS and on the new diffractometer installed at CEMES.

The measurement of the (111) peak with the CEMES diffractometer is also an indication of the $L2_1$ order presence in the alloy (figure 4.10-c). Additionally, the measurements of the (002) and (004) diffraction peaks, shown in figures 4.10-a) and 4.10-b respectively, with the Cu source diffractometer, allow to determine the out-of-plane lattice parameter and the Co/Si exchange parameter β. The lattice parameter is found to be 5.69 Å while β =0.06, which is slightly higher than the value obtained for sample N°1.

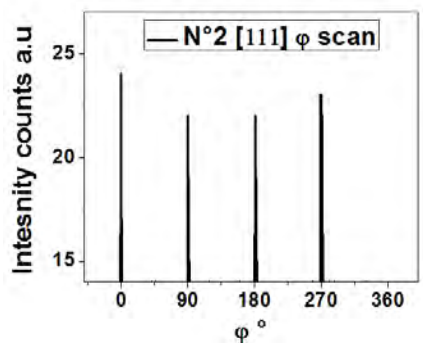

Figure 4.9: $\boldsymbol{\varphi}$ scan of N°2 sample along [111] direction using Co Kα source.

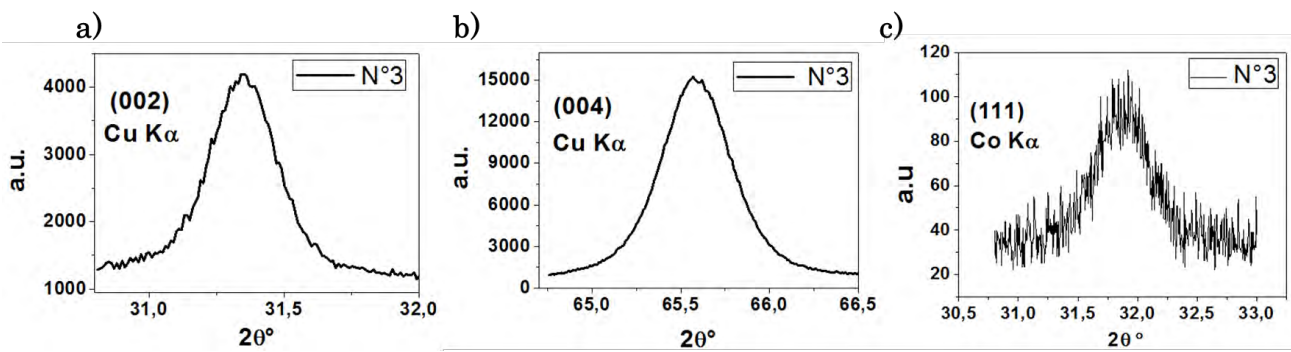

Figure 4.10: (002) and (004) diffraction peaks for sample N°3 measured with Cu Kα1 source in a) and b) respectively. c), (111) diffraction peak measured with the Co $K\alpha_{1,2}$ source diffractometer.

In conclusion, all of our three samples show some $L2_1$ crystal order. However, a complete study of the disorder parameter was only performed for sample N°1. This study have demonstrated that the B2 order is also present in sample N°1 and we can assume that similar feature is encountered for sample N°2 and N°3, with different amount of the respective crystal order. Additionally, Co-Si exchange is found to be slightly higher for the sample N°3 than for the sample N°1. Finally the crystal order for the sample N°2 is difficult to state as it is. Based on the results of samples N°1 and N°3, it is reasonable to think that this sample shows some $L2_1$ order along with the B2 order and Co/Si exchange. FMR measurements will show that the magnetization of this sample is lower than the two others samples, giving some credit to the potential strong Co/Si exchange.

While the X-ray diffraction experiments give access to the atomic ordering it doesn't give information about the local disorder organization in the material. For example, the question of a diluted disorder into a matrix or separate phase segregation cannot be answered.

In order to get such information, Transmission Electron Microscopy and especially High Resolution Transmission Electron Microscopy (HRTEM) and High Angle Annular Dark Field Scanning Transmission Electron Microscopy (HAADF-STEM) experiments have been performed to get the chemical arrangement at the atomic scale.

4.1.3 Structural investigation by HRTEM and HAADF-STEM

Electron microscopy offers numbers of complementary techniques to study the chemical composition, and the mechanical deformation or the crystal order at the atomic scale. HRTEM imaging has been performed using Hitachi HF3300 C 300KV cold FEG microscope (I^2TEM), developed between Hitachi and CEMES-CNRS. It is equipped with a spherical aberration corrector located below the objective lens. An example of a HRTEM image with its corresponding FFT diffractogram is presented in Figure 4.11. It allows us to verify both the thickness homogeneity of the sample and the thickness of the interface between the MgO and the CMS layer. The thickness of the film on this image is found to be 41 ± 1 nm with local variations at the upper surface. The interface between the CMS and the MgO is observed to have a thickness of 1.2 nm ± 0.2 nm.

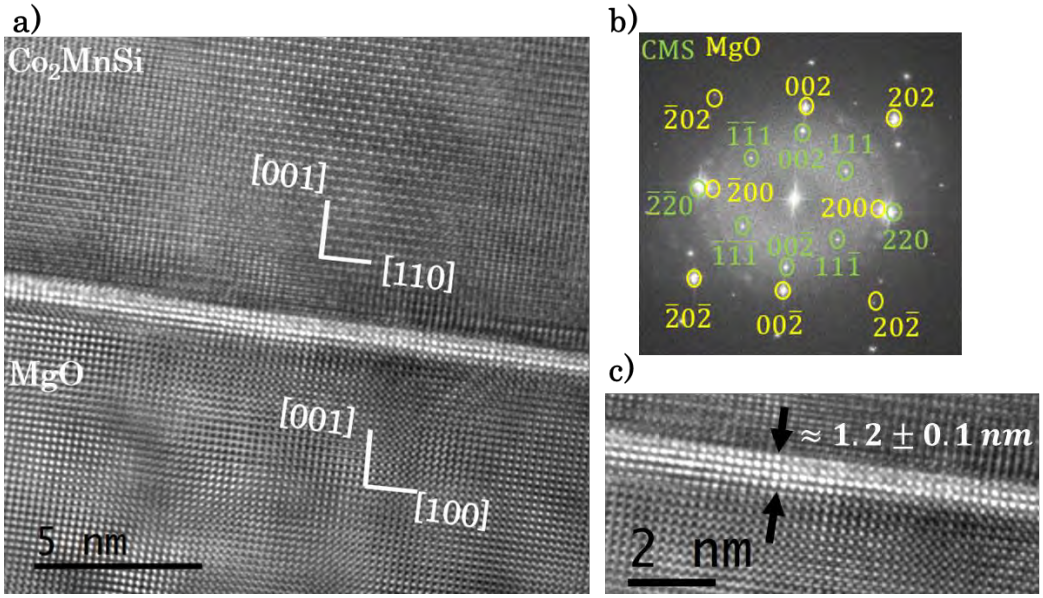

Figure 4.11: a) A HRTEM image, and b) its fast Fourier transform (FFT) for a cross-sectional CMS layer grown on MgO substrate. c) A zoom on the interface.

In order to make both chemical and structural analysis, HAADF-STEM experiments were performed at the TALEM laboratory, at the University of Zaragoza in Spain. As explained in chapter 3, one of the major interests for HAADF-STEM experiments is that the intensity of the atomic columns depends on its chemical nature. Then we have additional information as compared to HRTEM which is the possibility to observe the different chemical species on different atomic sites.

Measurements have been performed at 300 kV on a FEI Titan 60-300 microscope, equipped with a spherical aberration corrector for the probe. Samples N°1 and N°3 have been observed by HAADF-STEM:

- For sample N°1, a lamella have been prepared by FIB for observation in the [-110] zone axis direction. In this orientation, and for $L2_1$ order, the intensity of each atomic column, which increases with Z (Eq. 3.5 in chapter 3), corresponds to only one type of atoms.

- For sample N°3, 2 lamellas have been prepared by FIB. One for the observation in the [-110] and the second for observation [010] zone axes. In [010] zone axis, and for the $L2_1$ order, the Mn and Si atoms cannot be distinguished as both atoms alternate in the atomic columns.

An example of HAADF-STEM images of Sample N°3 is presented in Figure 4.12. The left column presents the reference sample observed in the [-110] zone axis while the right column presents the reference sample observed in the [010] zone axis. In Figure 4.12-a) and 4.12-e, low magnification allows to observe the MgO substrate at the bottom and the CMS at the top of the images. Clearly one can observe a difference of contrast as a function of the position. As the Magnesium (Z=12) and oxygen (Z=8) atoms have lower atomic numbers than Cobalt (Z=27) and Manganese (Z=25) atoms, the substrate appears more black as the intensity of the signal is lower than for the heavier atoms of CMS. We clearly see the different atomic arrangement as a function of the orientations of the crystal, as sketched in Figure 4.12-b and 4.12-f, showing the FCC structure of the material.

Figures 4.12-c and 4.12-g show a zoom on few atomic columns for each orientation. Figure 4.12-d and -h show the intensity profiles of STEM images taken along different lines reported in Figure 4.12-c and -g. In figure 4.12-d, the profiles clearly show the alternation of high and low peak intensities corresponding to Mn (Z = 25) and Si (Z = 14) columns, demonstrating the $L2_1$ order. We also note that the difference of intensity between Co and Mn columns is weak as expected from the Co and Mn atomic numbers (Z_{Co} = 27). Therefore and similarly to classical X-ray diffraction using a Cu $K\alpha_1$ source, HAADF-STEM is not very sensitive to the $D0_3$ disorder. In Figure 4.12-h, the intensity for the Mn/Si sites is constant. As the Wickoff positions of the Mn and Si atoms are (¼, ¼,¼) and (¼, ¾, ¼), respectively in the unit cell, each atomic column other than Co show the same intensity due to equal contribution from Si and Mn atoms.

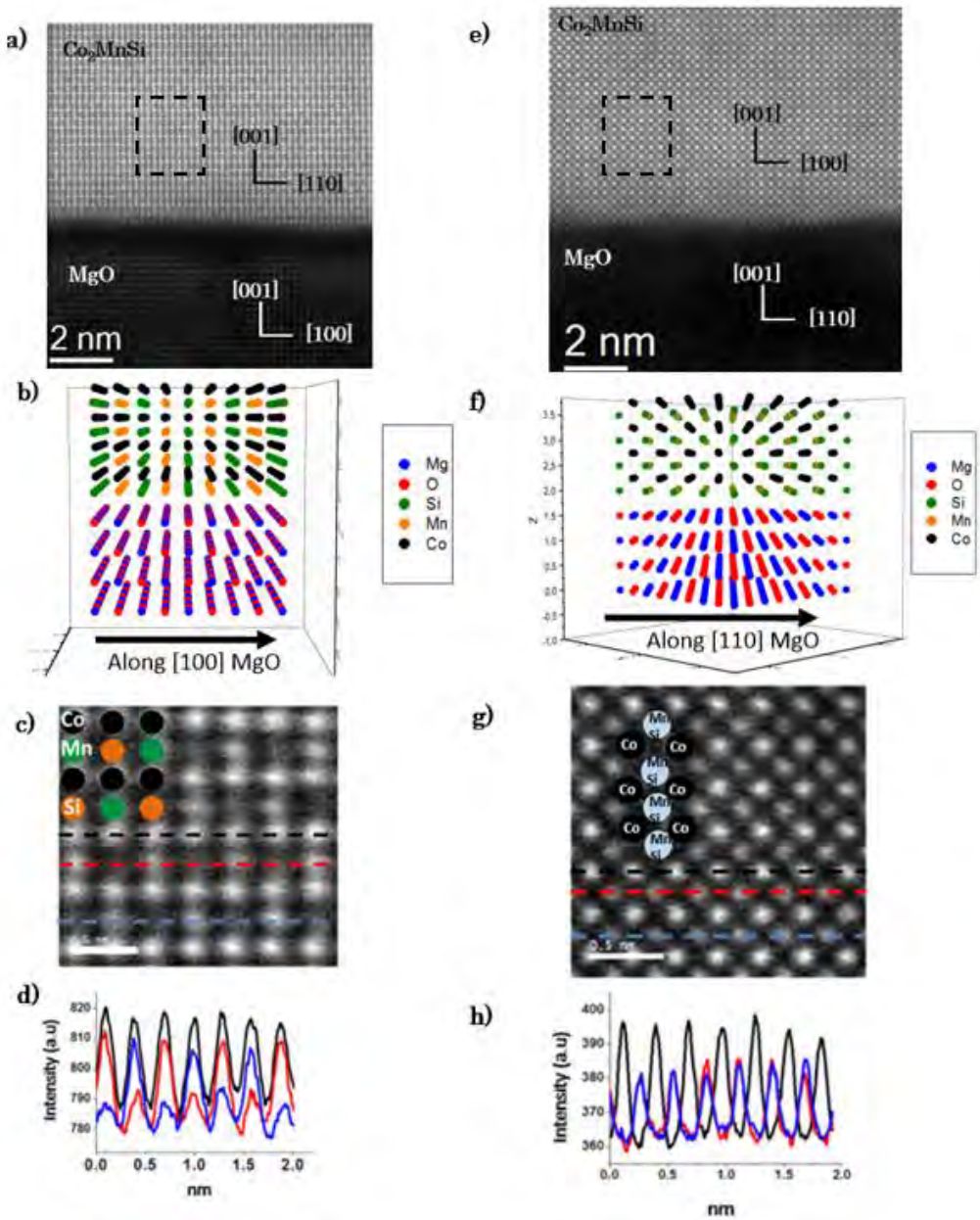

Figure 4.12: a) and e) are examples of HAADF-STEM of the reference sample N°3. b) and f) Sketched of the atomic arrangement in the different zone axis, considering the perfect $L2_1$ structure. C) and g) Zoom corresponding to the black boxes in a) and e) showing the Co, Mn and Si positions. D) and h) Intensity profile for the dotted lines in c) and g).

To go further in the structural analysis of the material, we performed a statistical analysis of the amplitude of the different atomic columns. This has been done for the two different samples:

- **Sample N°1 :**

An example of HAADF-STEM image is presented in Figure 4.13-a. The insert is a zoom on few atomic columns. The intensity profile of the lines denoted by the arrows in Figure 4.13-a shows the $L2_1$ order.

From the study of disorder parameters by X-ray diffraction, we claim the possibility that the material shows about 75% of $L2_1$ order and 25 % of B2 order. In order to demonstrate that the $L2_1$ order is the main phase of the sample, we performed a statistical analysis of maximum peak intensities of the HAADF-STEM images. Let's note that we have performed the statistics also on the intensity average value of pixels corresponding to the atomic columns with similar results.

Three distinct intensity distributions corresponding to the Co, Mn and Si atomic columns are observed (Fig 4.13-c). The values are normalized by the one of the Co intensity at the center of the Co distribution. The appearance of three different intensities in the HAADF-STEM image is in good agreement with the $L2_1$ order even if some spreading of the intensity distribution is observed. One source of spreading comes from the slight change of thickness across the lamella prepared for STEM experiment. This variation of thickness prevents any statistics over very large areas.

In some particular regions of the film other intensity distributions are observed, as the one reported in Figure 4.13-d which corresponds to statistical analysis performed on the black box in Figure 4.13-a. The inset in Figure 4.13-d shows that STEM intensities corresponding to the Mn and Si columns are very similar. Even if the statistical analysis is performed on a small number of atomic columns, it clearly shows that the STEM intensities corresponding to Mn and Si atomic columns converge to a single value, which could be associated to the appearance of the B2 order. This result has been observed in 5 HAADF-STEM images taken at different positions in the lamella. For each image, we found some regions composed of 10 to 15 atomic columns with similar B2 type ordering. Therefore, and based on the result obtained by X-ray diffraction, we make the assumption that very small grains with B2 order are distributed in the $L2_1$ matrix.

Dealing with the preliminary assumption that 25% of the layer should be in the B2 order, a natural question is to understand why we do not observe bigger regions of the sample in the B2 order. However we remind that HAADF-STEM images corresponds to a projection of the integrated intensity along the thickness of the lamella. Then if very small grains are diluted in the $L2_1$ matrix, they can be too small to induce significant changes in the intensity of the atomic columns of $L2_1$ order, at least within the noise of the signal which is mainly due to local variations of the thickness.

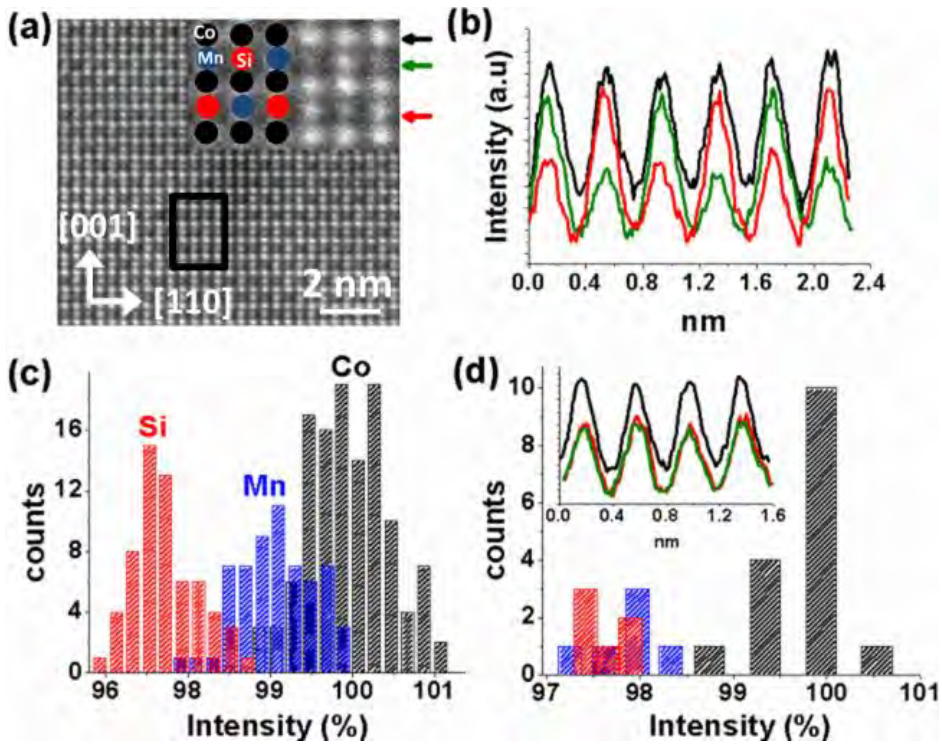

Figure 4.13: (a) HAADF-STEM image of CMS. The insert at top right is a zoom over 6x6 atomic columns. (b) Intensity profile of the lines denoted by the colored arrows in (a). (c) Statistical analysis of intensity profile obtained from (a) on a region of 11 x 23 atomic columns. (d) Statistical analysis of the area denoted by the black box in (a). In insert the intensity profile of the three central lines in the black box.

HAADF-STEM imaging also allows for mechanical strain studies in the CMS layer due to the lattice mismatch with the substrate. Starting from an HAADF-STEM low magnification image showing both the MgO and CMS (Figure 4.14-a), we performed a *GPA* analysis to observe the strain parallel and perpendicular to the MgO interface. The diffraction peaks selected in the FFT are the $MgO_{(200)}$ and $CMS_{(220)}$ spots for the calculation of the strain parallel to the interface ε_{xx}, and the $MgO_{(002)}$ and $CMS_{(002)}$ for the calculation of the out of plain strain ε_{zz}.

An example of the calculation is shown in Figure 4.14 for sample N°1. The average ε_{xx} strain is found to be -5.4 % in this zone of the lamella. Example of the difference of strain between the substrate and the CMS layer is shown in the profile in Figures 4.14-d and 4.14-e. Repeating the measurement on different images, it allows us to estimate an average value of the in-plane strain for the CMS to be -5.3% ± 0.3%. This result is in very good agreement with the expected lattice mismatch defined as $f = \frac{a_{CMS} - \sqrt{2} * a_{MgO}}{\sqrt{2} * a_{MgO}} = -5.4\%$. Similarly, the out of plane ε_{zz} strain is found to be in average 34 ± 1.2%, also in very good agreement with the expected value $\frac{c_{CMS} - a_{MgO}}{a_{MgO}} = 34.9\%$ calculated with the c parameters obtained from X-ray diffraction. Both ε_{xx} and ε_{zz} are very homogeneous within the CMS layer. We also observe at the interface some misfit dislocations (white points at the interface in Figure 4.14-b) with a quite periodic structure. The distance between two dislocations is found to range from 2.9 nm

and 4.3 nm on this image. This can be compared to the expected value of the periodicity of the dislocations defined as: $\frac{d_{[220]-CMS}}{|f|} = \frac{\frac{5.63}{\sqrt{8}}}{5.4} = 3.68\ nm$.

This is in good agreement with our observations. Therefore we can conclude that our CMS films are fully relaxed.

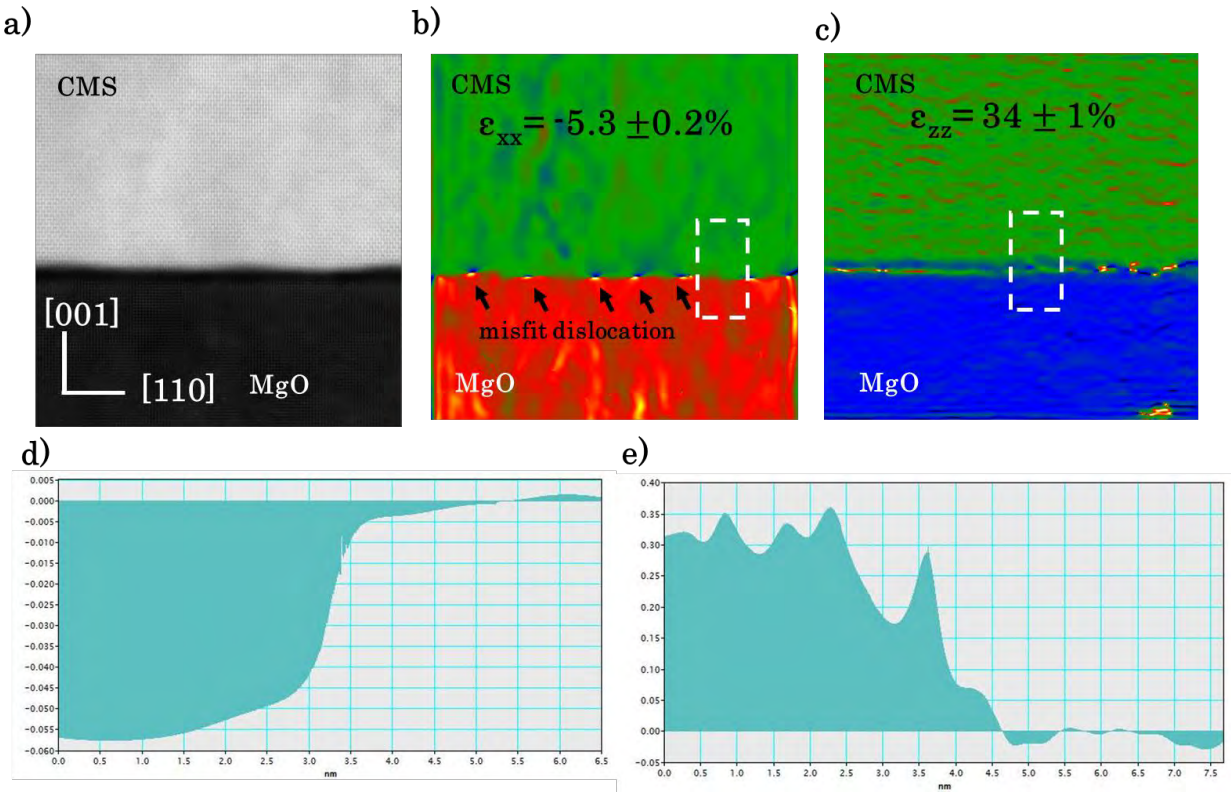

Figure 4.14: b) In-plane and c) out-of-plane Strain mapping derived from a) an HAADF-STEM for sample N°1. Profiles d) and e) corresponds to the strain value obtained from the selected box area in b) and c).

- **<u>Sample N°3 :</u>**

For sample N°3, the situation is very similar to sample N°1. For the lamella oriented in the [-110] zone axis, the statistics performed on the columns observed in Figure 4.15a clearly show the difference between the Si and Mn columns while the intensity for Mn and Co is very close. This is significant of $L2_1$ or $D0_3$ order. When the sample is observed in the [010] zone axis as in figure 4.15-c, the intensity of the Mn and Si columns are equal and below the intensity of Co. However, here the notion of Mn and Si columns is not relevant as both atoms are present in the same column. We simply make the statistics taking one out of every to atomic column as Mn and the other one as Si.

Let's note that we must not compare the relative intensity values between the different images. For example in Figure 4.15-c, the Si intensity was about 97% of the Co signal while in Figure 4.15-d, it is about 96%. The reason for this difference comes from the difference of background intensity (due to lamella thickness for example) from one image to another which naturally slightly modifies the relative amplitude of the atomic columns intensities with

respect to the Cobalt. Therefore, we must only compare the intensity of Co, Mn and Si column on every single image.

The main difference between sample N°3 and sample N°1 is that, in N°3, we were not able to detect any regions with a clear B_2 order. Therefore this sample most probably shows a high degree of $L2_1$ order as expected from the (111) x-ray diffraction peak in figure 4.10. Moreover, we expect to have a $L2_1$ order and not the $D0_3$ due to the result of atomic disorder obtained on sample N°1 and also based on the theoretical predictions which states that the $L2_1$ order is more energetically favorable than the DO_3 type. The values of the magnetization amplitude measured by FMR will confirm that the sample shows the $L2_1$ order.

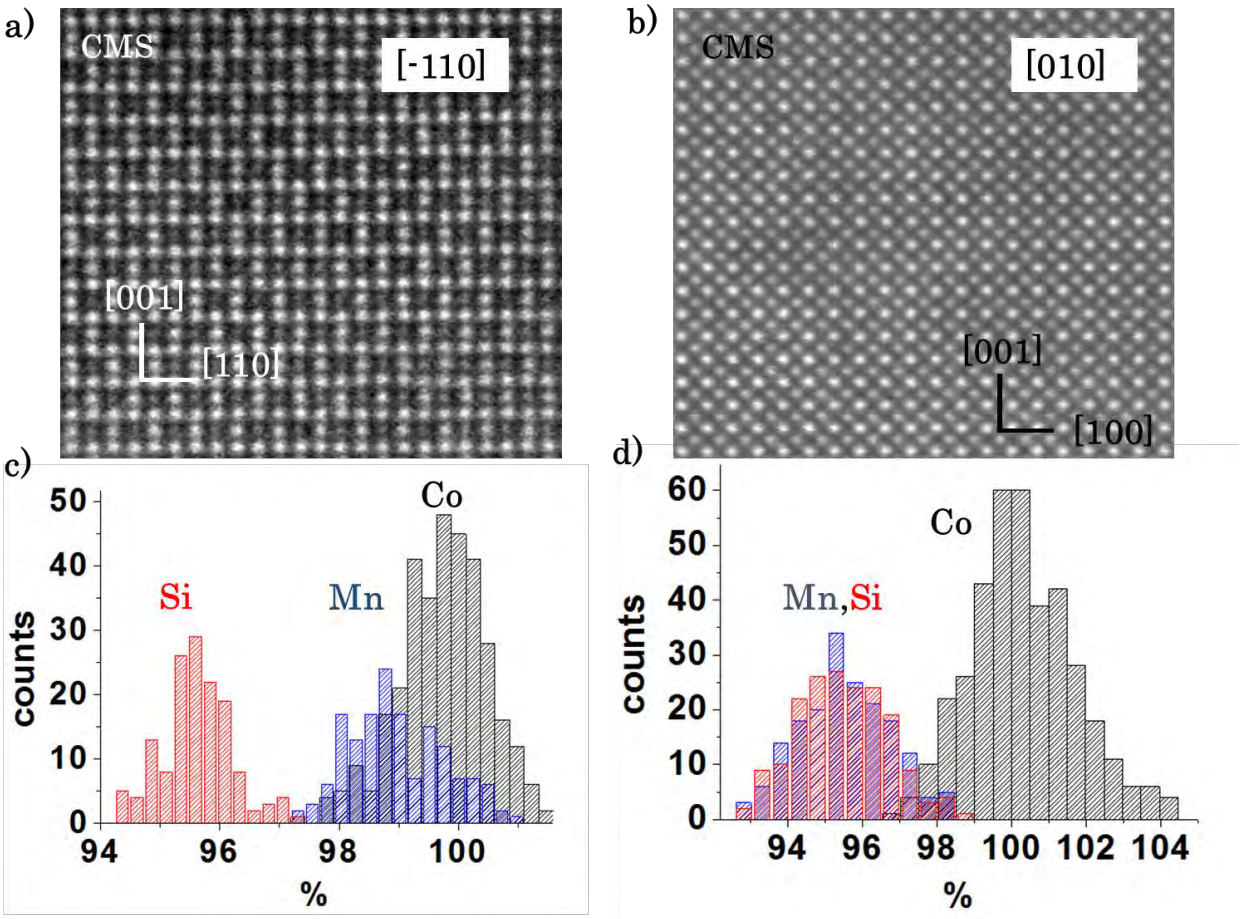

Figure 4.15: a) and b) HAADF-STEM images of sample N°3 observed in [-110] and [010] zone axes respectively. C) and d) show the statistics of the maximum intensity for each atomic column obtained from the STEM images presented in a) and b), respectively.

As a conclusion, XRD and TEM analysis have shown that the sample N°1 grows as a mixture of two phases corresponding to about 75% of $L2_1$ and 25 % B2. GPA analysis have shown that the sample is completely relaxed. We also measured a tetragonal distortion with respect to the expected perfect cubic lattice. The lattice parameters are found to be 5.63 Å in plane and 5.67 out of plane. Sample N°3 is somehow similar to sample N°1. A clear $L2_1$ order is demonstrated but a higher ratio of Co/Si exchange is observed as compared to sample N°1. Magnetic measurements will show that a second minority crystal phase is also present. Based

on the result of sample N°1 and despite it could not be observed with HAADF-STEM, we believe that this one, sample N°3, most probably corresponds to the B2 order. Furthermore we measured a larger out of plane lattice parameter for this sample (5.69 Å); we will show that it has an impact on the magnetic properties. Finally, for sample N°2, partial diffraction measurements shows a small amplitude (111) diffraction peak, suggesting the presence of the $L2_1$ phase based on the result obtained for the other two samples. However we will show that the magnetization and anisotropies amplitudes are different from the other two samples, suggesting a more complex structural disorder.

4.2 Magnetic properties

In this part, we present a study of the static and dynamic properties of the different CMS samples. Static measurements focused on the switching mechanism of the layers. Additionally, we will extract the magnetic parameters of the film such as the magnetization, exchange constant and anisotropy amplitudes from ferromagnetic resonance experiment. Finally, the last part of this section will be devoted to magnetic relaxations effects which are one of the most interesting features of these alloys.

4.2.1 MOKE measurements: switching field mechanisms

- **<u>SAMPLE N°1 :</u>**

Hysteresis cycles have been measured by Magneto-Optic Kerr Effect at the NMH-CEMES lab located on the ONERA Toulouse Campus. An example of MOKE cycle taken for sample N°1 is presented in Figure 4.16 for an external field applied parallel to an easy (a) or hard (b) axes. The measurements were performed with the magnetic field applied in the plane of the CMS sample. The external field is in the plane of incident light, which corresponds to the L-MOKE configuration. The sample is rotated manually via homemade sample holder within the Helmotz coils used to apply the field.

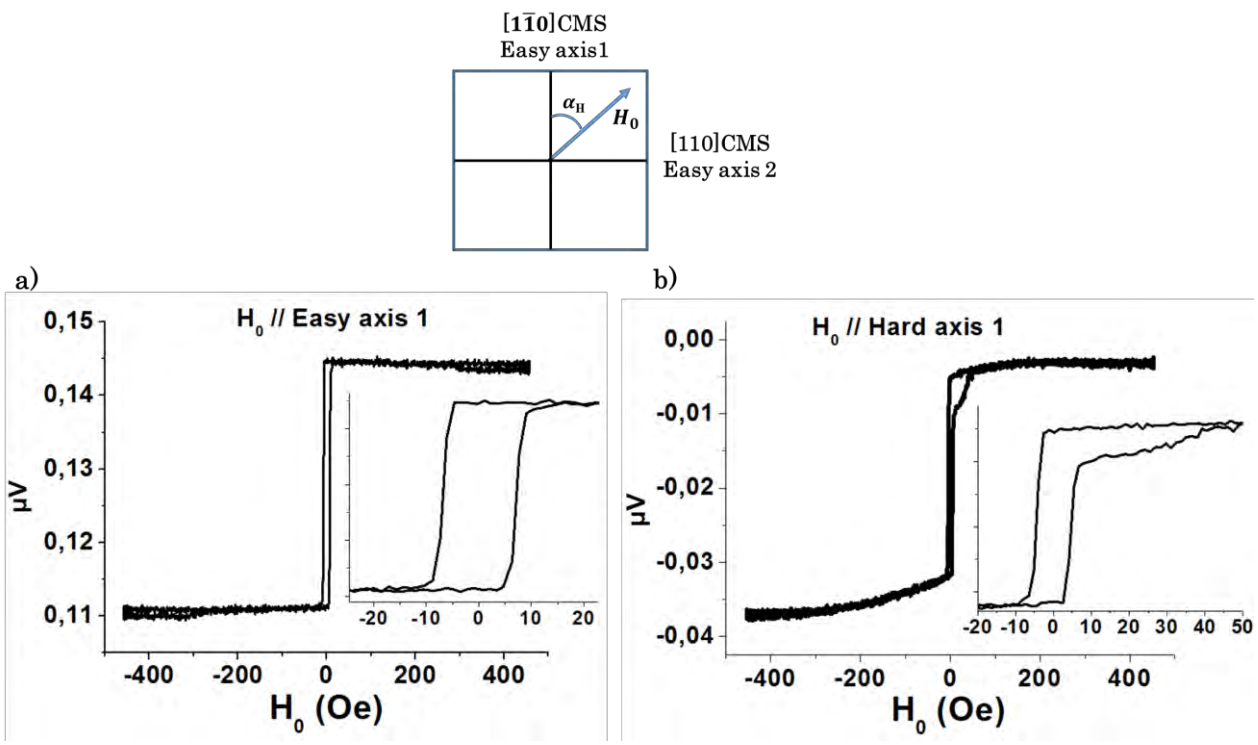

Figure 4.16: Hysteresis cycle for sample N°1 measured by MOKE. The external field is applied in the plane of the sample and parallel to a) an easy axis and b) a hard axis.

Raw measurements showed that coercive field values are of few Oe, typical for magnetic switching through nucleation/propagation of domains. However, some asymmetry between positive and negative fields is observed, avoiding a clear determination of the coercive field H_c. This is especially visible for fields applied with a non-zero relative angle with respect to the easy axis. This asymmetry for positive and negative fields is due to the quadratic contribution to the signal and due to the rotation of the magnetization perpendicularly to the applied field. In order to separate both the L- and Q-MOKE, we follow the procedure developed by Mewes *et al.* [10 Mewes] and also developed in O. Gaier PhD work [2 Gaier]. Only the basics of the symmetry process is presented here. More details can be found in the cited references.

First we write the rotation of the polarization axis due to the Kerr effect θ_{Kerr} as:

$$\theta_{Kerr} = \theta_{Kerr}^{Long} . M_{//} + \theta_{Kerr}^{Quad} . M_{//} M_{\perp} \tag{4.9}$$

Where θ_{Kerr}^{Long} and θ_{Kerr}^{Quad} are the longitudinal and quadratic proportionality factors of the Kerr rotation. $M_{//}$ and $M_{\perp}$ are the in-plane magnetization components parallel and perpendicular to the plane of incidence of light, respectively. To separate both contribution, we consider the symmetry of the two terms in equation 4.9. For the same value of applied external field, with a 180° sample rotation, the longitudinal contribution $M_{//}$ to the Kerr angle changes sign while the quadratic contribution ($M_{//} M_{\perp}$) remains the same. Therefore, the authors have shown that longitudinal and quadratic contributions can be separated by applying the following procedure:

$$\theta_{Kerr}^{long} = [\theta_{Kerr}(\alpha_H) - \theta_{Kerr}(\alpha_H + 180°)]/2 \quad (4.10)$$

$$\theta_{Kerr}^{Quad} = [\theta_{Kerr}(\alpha_H) + \theta_{Kerr}(\alpha_H + 180°)]/2 \quad (4.11)$$

Where α_H is the angle between the easy axis of the CMS and the direction of the applied field. The main complication of this process is that MOKE cycles have to be applied for directions between 0° and 360°. This is not achievable with our set-up since we have a 180° rotation planetary. Another possibility to recover the longitudinal and quadratic contributions is to calculate the following quantities:

$$\theta_{Kerr}^{long} = [\theta_{inc}(H) - \theta_{dec}(-H)]/2 \quad (4.12)$$

$$\theta_{Kerr}^{Quad} = [\theta_{inc}(H) + \theta_{dec}(-H)]/2 \quad (4.13)$$

The result of this process is shown in Figure 4.17, for an applied field at α_H= 45° from the easy axis, *i.e.* in the hard axis direction. The longitudinal and quadratic contributions are calculated for a field swept from negative to positive values. Two advantages come from the analysis of the longitudinal component. First, it allows for a direct renormalization of the curves without any additional treatment. Second, a precise measurement of the coercive field H_c can be obtained and the value of the saturation field in the direction of the hard axis, as a first approximation, equals to the value of the crystalline anisotropy field.

Results of the measured coercive field for α_H ranging from 0° to 180° is presented in Figure 4.18-a. The coercive field values range between 4.7 and 6.5 Oe (0.47 and 0.65 mT). Let's note that the uncertainty due to the symmetry process is about 1 Oe. Then no clear variation with respect to α_H is observed and the expected fourfold anisotropy is only visible for the saturation field H_{sat}, as shown in Figure 4.18-b (in the figure only a twofold symmetry arises since α_H ranges only between 0 and 180°). Here, the saturation field along the two hard axes directions (i.e. α = 45 and 135°) is evaluated to be around 350 Oe (=35 mT). However, when looking carefully at the hysteresis cycles, small differences arise depending on the angle of the external field α_H. For example, we can see on Figure 4.19 that for angles above 45° (typically between 50° and 70°), some small "plateaus" appear while they are absent for angles below 45° (see Figure 4.19-a and 4.19-b). This reflects the presence of a very small uniaxial anisotropy superposed on the easy axis 1. The difference of switching mechanism as a function of α will be detailed in the switching mechanisms below.

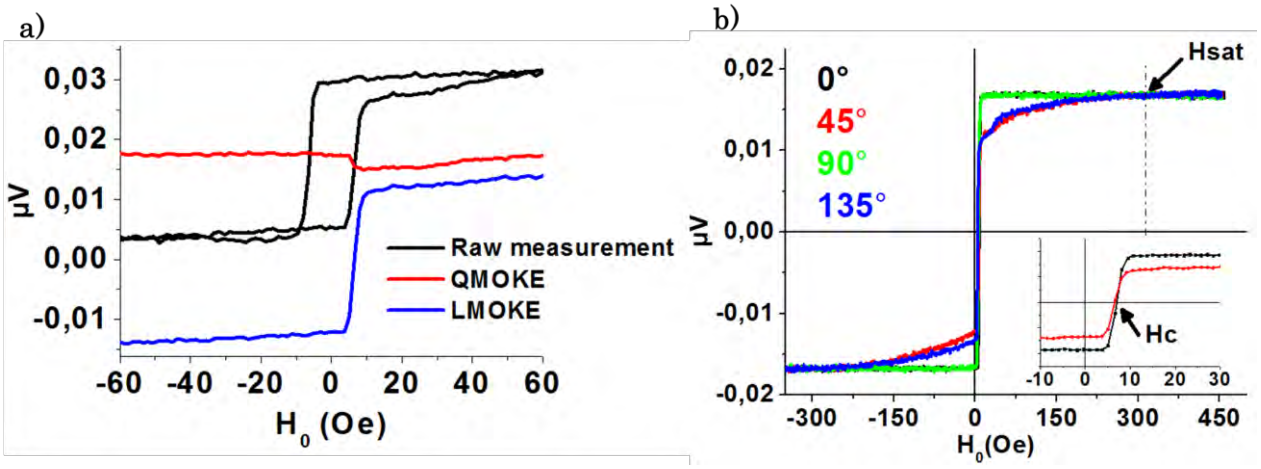

Figure 4.17: Sample N°1 a) recovery of Q- and L-MOKE from Raw measurements and b) LMOKE cycle at different external applied field angles.

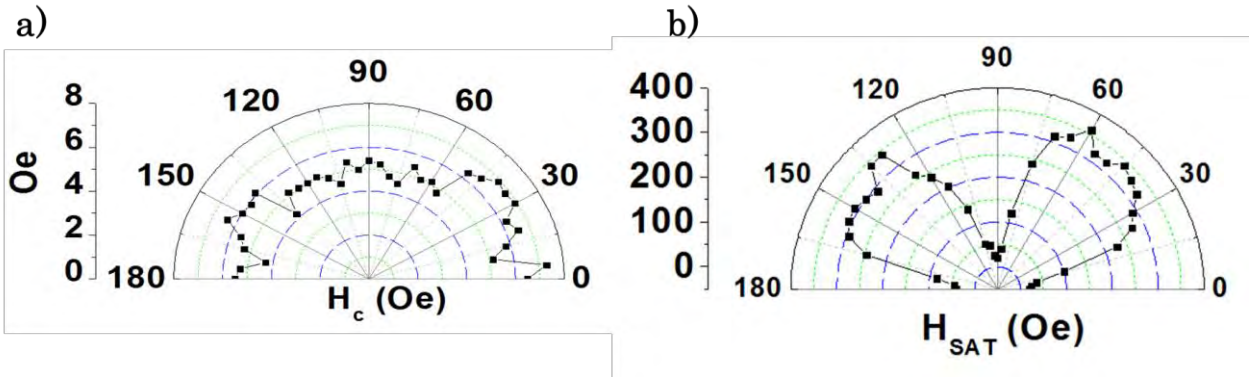

Figure 4.18: Sample N°1 twofold symmetry for a) coercive and b) saturation fields from 0° to 180°.

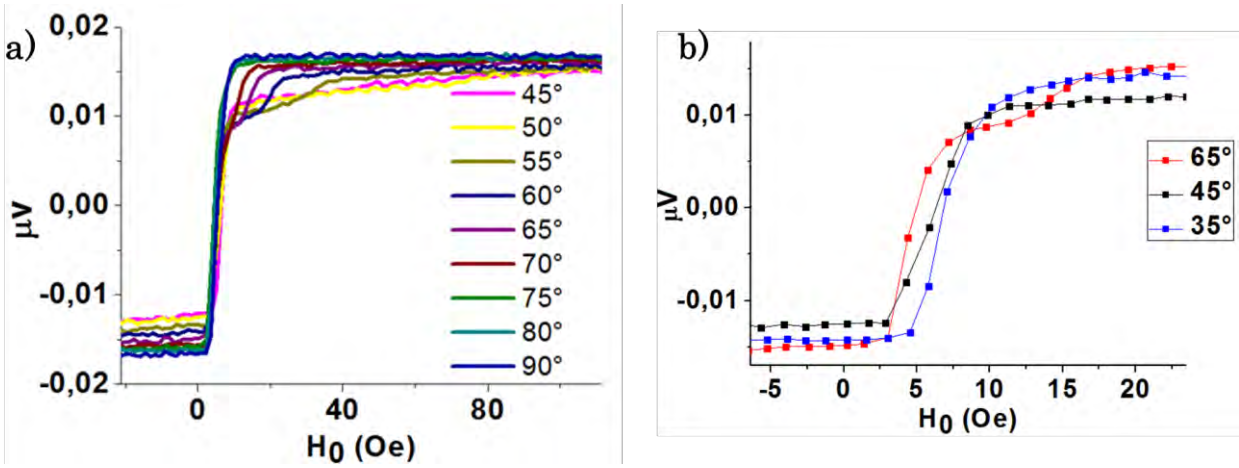

Figure 4.19: a) Evolution of the LMOKE component for sample N°1 at different angle α. The field is swept from negative to positive fields. We clearly observe some "plateau" for angles between 50° and 70°. However, in b) the "plateaus" are absent for angles below 45°.

- **SAMPLE N°2 :**

MOKE measurements have been also performed on sample N°2 only in few directions and then similar representation of the coercive field or saturation vs. the angle α cannot be presented. Figure 4.20 shows different raw measurements for different directions of the applied field α_H where 0° and 90° corresponds to the easy axis directions of the sample. Similarly to sample N°1, the cubic anisotropy is observed in the saturation field values at 45° and 135°. Here the value of the saturation field is evaluated to be around 450 Oe (45 mT). However, the shape of the hysteresis cycles differs from sample N°1 around the coercive field value, as shown in the inset of Figure 4.20. Indeed there is a clear difference between the two easy axes.

In order to compare the different cycles, we applied the symmetric procedure as explained for sample N°1. The result of the LMOKE signal is shown in Figure 4.21. The field is scanned from negative to positive values. For α_H=0°, we observe an abrupt decrease of the magnetization with an almost complete switching, which is typical for an applied field in the easy axis direction with a corresponding coercive field of 5 Oe (0.5 mT). However for α_H=90°, we observe that the magnetization amplitude component along the field direction goes down to zero at $\mu_0 H_0$ = - 2 Oe, so before the direction of the field is reversed. It is followed by a plateau with a constant value of magnetization until the field is reversed down to the coercive field of 6.5 Oe. This is typical for the presence of an additional uniaxial anisotropy along the easy axis 2 (α_H =0°). Indeed, the plateau corresponding to a zero net magnetization means that the magnetization rotates at 90° from the applied field; *i.e.* in the easy axis 2 direction.

Similarly to sample N°1, the magnetic switching process for 0° < α_H < 45° and 45° < α_H< 90° are different. This is observed in Figure 4.22 showing the longitudinal component of the magnetization for α_H = 30, 45 and 60°. Typically only for α_H > 45°, "plateaus" are observed. Here we have even observed two plateaus before saturation. Once again, this is typical due to the presence of a uniaxial anisotropy. Details about the switching mechanisms processes are given in the next sub-section.

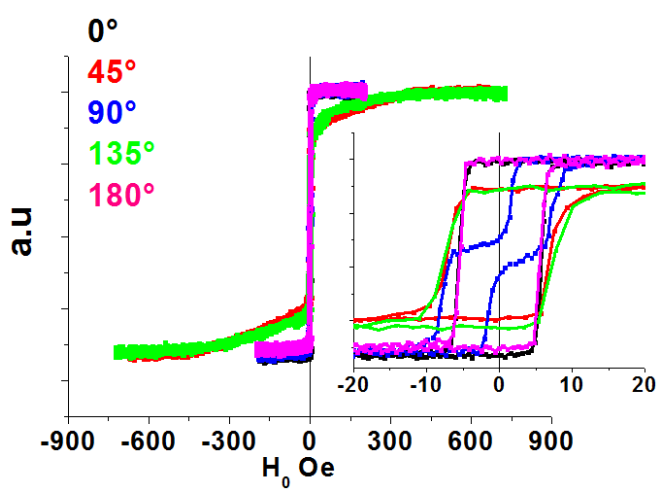

Figure 4.20: Hysteresis cycle for sample N°2. The inset shows the difference between two easy axes (0° and 90°).

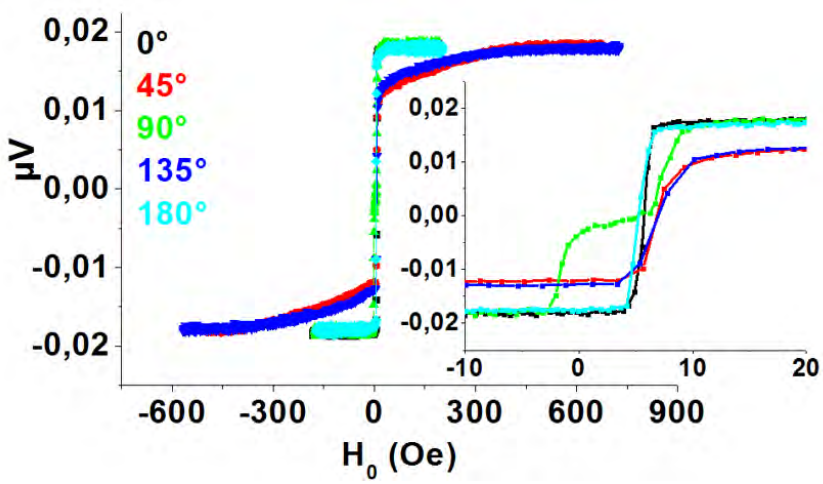

Figure 4.21: LMOKE cycles after symmetry procedure. The magnetic field is applied in the four magnetic axes directions.

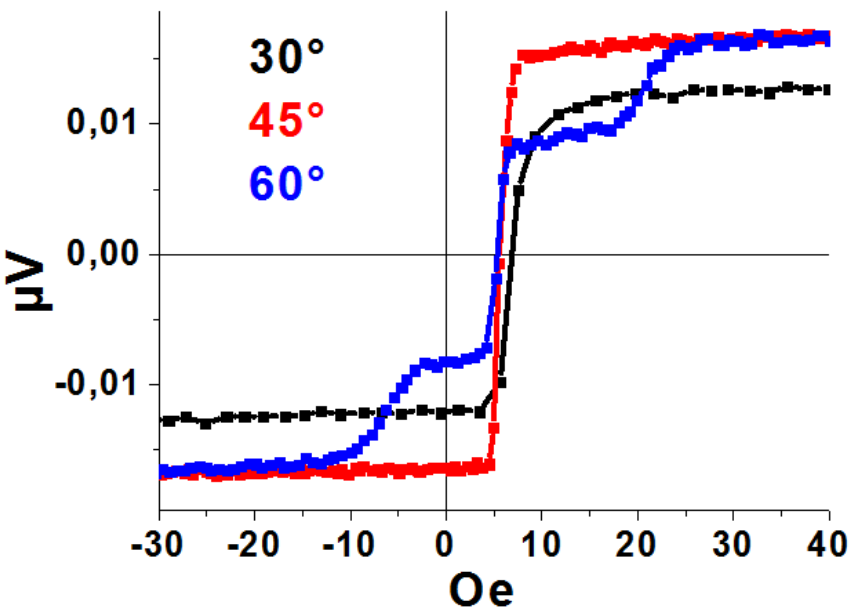

Figure 4.22: LMOKE measurements at α_H= 30°, 45° and 60° showing different switching mechanisms.

- **Switching mechanisms**

In order to understand the different magnetic switching mechanisms observed in samples N°1 and N°2 as a function of α, we have simulated the switching process with the micromagnetic solver OOMMF. Calculations were performed with a 3D package. The size of

the sample is 2 µm x 2 µm x 40 nm with a cell size of 5 nm. Due to high numbers of cells, calculations were running using the HPC resources from CALMIP super-calculator in Toulouse. The easy axes reflecting the cubic anisotropy are the X and Y directions in Figures 4.24 and 4.25. The value of the anisotropy field is set to $\mu_0 H_k$ = 35 mT. Moreover, a uniaxial anisotropy with amplitude $\mu_0 Hu$ is superposed with the X-axis. The sample is first saturated with a 100 mT external field applied with an angle α with respect to the +X direction. The field is then decreased in one step down to 20 mT. For the switching process the field is decreased down to -50 mT by steps of 1 mT and from -50 mT to -100 mT in one step.

Even if the effect of the superposed uniaxial anisotropy is more visible in sample N°2 than in sample N°1, the basic mechanisms are similar. The only difference relies on the amplitude of the uniaxial anisotropy field $\mu_0 H_u$ which is more important in sample N°2 than in sample N°1. Here in the simulation we arbitrary set the value $\mu_0 H_u$ = 1 mT, we will see that this value is in agreement with the one obtained by FMR measurements.

An example of the simulated switching mechanisms for fields applied at 30° or 60° from the easy axis 1 are presented in figures 4.24 and 4.25 respectively. The basic mechanisms are the same for every angle of the applied field. We start from saturation in the positive direction. By decreasing the field, the magnetization first rotates on the edge of the samples, parallel to the X or Y axis, depending if α is inferior or superior to 45°, respectively. This leads to 90 degrees domain walls as expected in cubic magnetic system. When α >45°, the effect of the additional anisotropy allows for switching of edge domains before the applied field is reversed. If α<45°, the magnetization stays in the X direction even at zero field due to the uniaxial anisotropy.

When the field is reversed (H_0 < 0 mT), the situation is first similar whatever the angle α. Due to the additional anisotropy in the X direction, the magnetization will form domains in the center of the sample with magnetization pointing preferentially alternatively in the + and - X direction (figure 4.24-c and 4.25-c). These domains are separated by cross ties domain walls as generally observed in soft magnetic systems with thickness around 50 nm. The edge domains are separated from the central domains by 90° domain walls. This leads to classical flux closure magnetic configuration and corresponds to a net magnetization equal to zero, i.e. at the coercive field.

Once this magnetic configuration is reached, the situation differs depending if α > 45° or α < 45°. If α < 45°, the switching occurs through the growing of the central magnetic domain pointing in the –X direction (Figure 4.24-d). As this direction is the most energetically favorable due to the uniaxial anisotropy, this process allows for abrupt transition. Then the saturation is reached with a rotation of the magnetization toward the direction of the applied field. Now if α > 45°, the switching occurs through the propagation of the 90° domain walls in order to favor domains with magnetization pointing in the –Y direction (see figure 4.25-d and 4.24-e). However, this is energetically less favorable since the uniaxial anisotropy tends to keep the magnetization in the –X direction. Therefore it is probable that the plateaus observed for α = 60° in figure 4.19 and 4.22 corresponds to the field necessary to move the 90° domain walls to the center of the sample. Finally saturation is also reached after rotation of the magnetization toward the direction of the applied field.

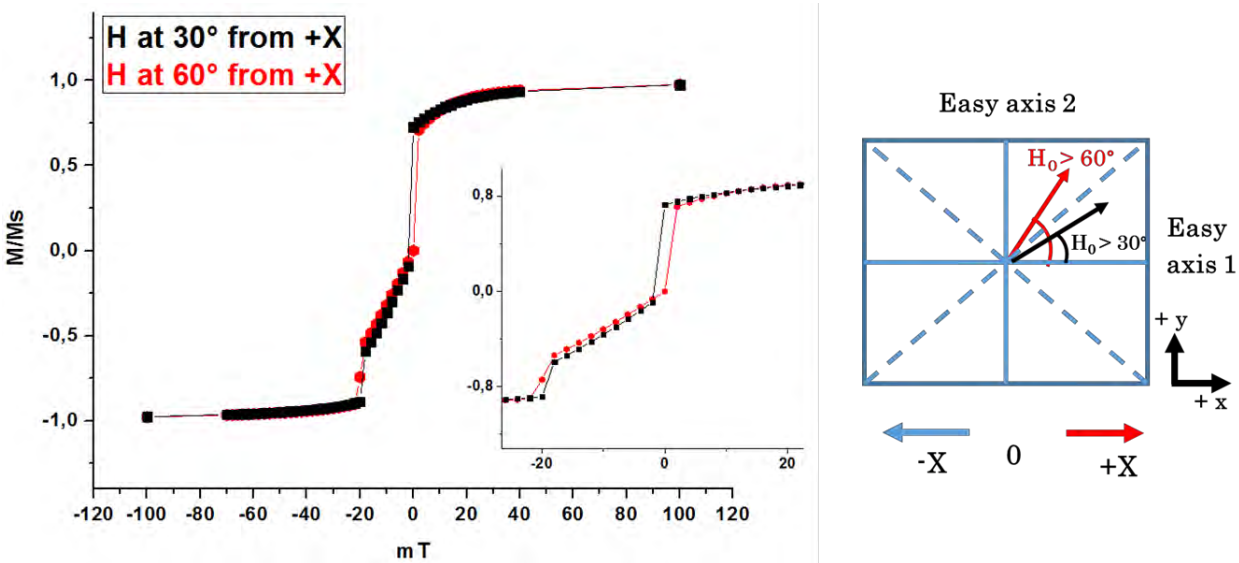

Figure 4.23: The field is swept from positive to negative fields with steps of 2 mT. The insert is a zoom around zero field. The additional uniaxial anisotropy is aligned with the easy axis 1 direction, *i.e.* the +X direction as shown in the scheme on the right.

An example of the simulated hysteresis curves with OOMMF is shown in fig 4.23. The situation is here similar to what we observe for sample N°2. Indeed, when the field is applied with α>45°, the average magnetization parallel to the applied field, M, tends to zero before switching the applied field. This corresponds to the rotation of the magnetization toward the X direction (the direction of the uniaxial anisotropy). When α< 45° the magnetization still shows a high value at it is in a stable position.

While we recover also the fact that the saturation is reached at higher field when α>45°, we observe some plateau for both directions of the applied field. Also the saturation field is almost an order of magnitude higher than in the experiment. We believe that such discrepancies comes from the size of the simulated sample. Indeed, as it is only few µm², it is much more difficult to saturate the edge of the sample due to the local demagnetizing field. This effect is also present of real samples but as they are mm², edge effects are negligible in the magnetic response of the sample. The second effect of the size of the simulated sample is a much lower density of domain walls that can be created to switch the magnetization as compared to real samples. These two effects naturally increase the saturation fields.

Let's note that it is very difficult to estimate the value of this uniaxial anisotropy from the MOKE measurement. Indeed, as the switching occurs through domain wall nucleation and propagation, no direct value of μ_0Hu can be obtained from the measurement of μ_0Hc. Moreover, the amplitude of this anisotropy is much lower than the value of the cubic anisotropy and it is very difficult to distinguish both contributions in the measurement of the saturation field within the uncertainty of the measurement. Finally, direct comparison with micromagnetic simulations is also tricky. Indeed, the measured samples are 3 x 3 mm² while the simulated sample is 5 x 5 µm². Size effect plays an important role for the value of the switching field, first because of the effect of the dipolar field and for the nucleation and propagation of domain walls. Then micro magnetic simulations allow to determine the basic

mechanisms but don't give absolute values of the uniaxial field. FMR measurements will show that this additional anisotropy has an amplitude below 20 Oe.

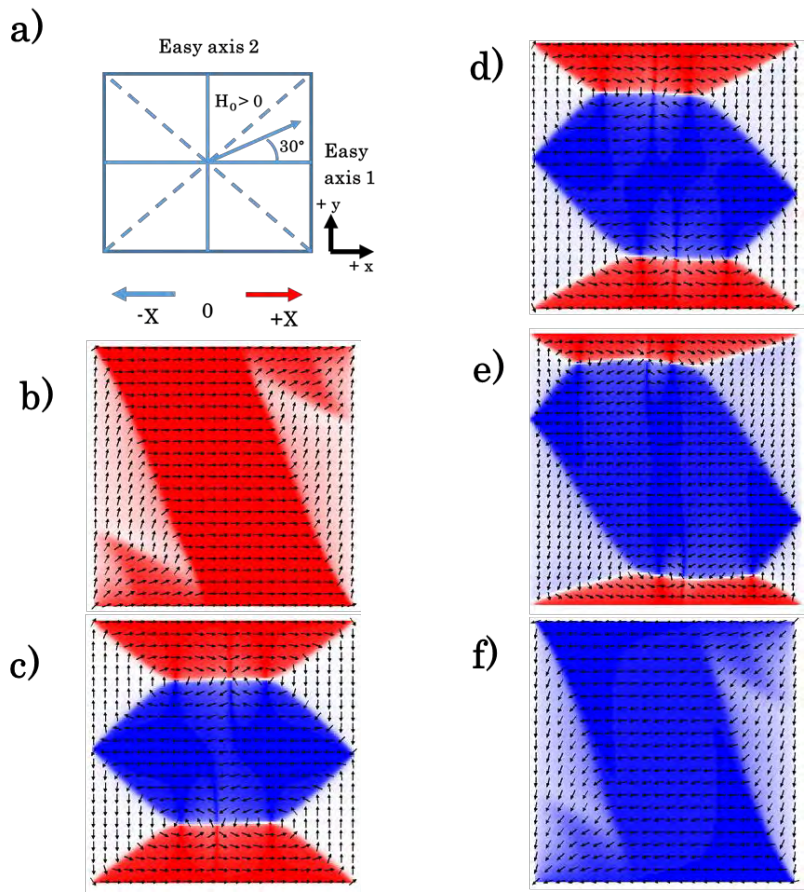

Figure 4.24: simulated switching mechanisms for fields applied at 30° from the easy axis 1. Switching from positive b) to negative f) applied field occurs through the growing of the central magnetic domain pointing in the –X direction as shown in c), d) and e).

Finally, we need to discuss the origin of the additional uniaxial anisotropy. Up to now there is no clear explanation for it. In a previous work [11 Ortiz], we suggested that uniaxial anisotropy in CMS deposited on MgO could originate from the presence of terraces on the surface of MgO substrate crystals. Indeed, some studies suggest that nanometer-scale steps in MgO substrate induce an in-plane magnetic easy direction perpendicular to the step edge. This effect was also accounted for the uniaxial anisotropy in Fe_3O_4//MgO(001) [12 McGuigan], Fe//W(001), [13 Chen], Fe//Ag(001), and Fe//Au(001) thin films [14 Leeb]. The mentioned references, [12-14], suggested that the origin of this magnetic anisotropy can arise from the preferential alignment of structural defects with step edges. While Leeb *et al.* pointed out that the magnitude of the magnetic anisotropy is determined by the large lattice out-of-plane mismatch which gives rise to strong strain in the vicinity of monoatomic steps.

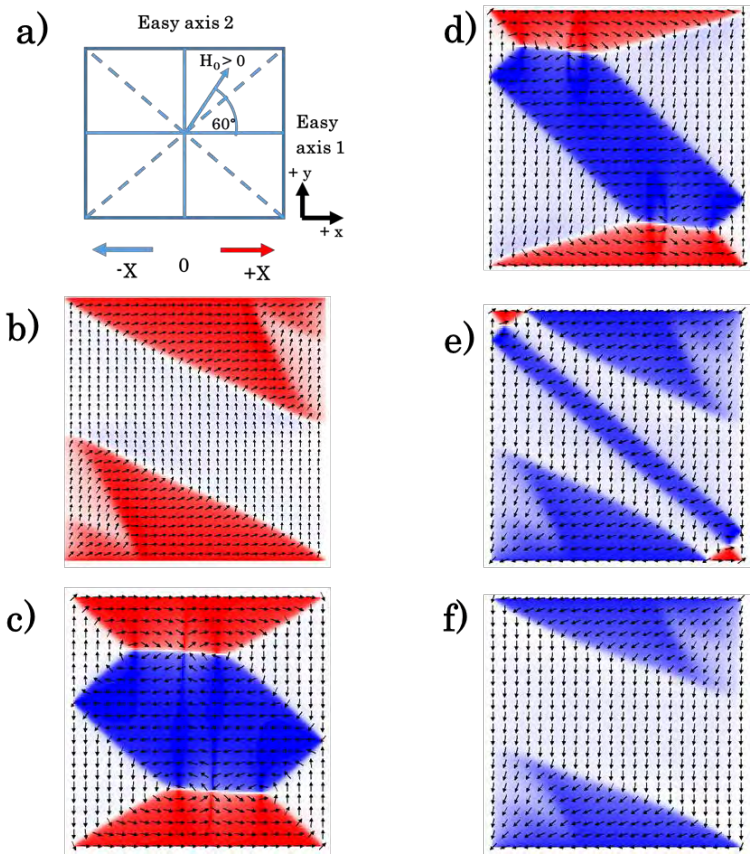

Figure 4.25: simulated switching mechanisms for an external field applied at 60° from the easy axis 1. The switching occurs through the propagation of the 90° domain walls in order to favor domains with magnetization pointing in the negative Y direction as shown in d) and e).

Additionally, the lattice mismatch between the substrate and the thin films is often accounted for a tetragonal distortion of the cell, with the product a^2c constant (iso-volume distortion), inducing strain anisotropy. This strain anisotropy has been often considered as the origin of the superposed magnetic uniaxial anisotropy observed in many cubic systems. The uniaxial anisotropy has been found to be either in one of the cubic easy axis direction, for example in Co_2FeAl [16 Belmeguenai], or in one of the cubic hard axis, for example in Iron [15 Baker]. However, Pandey *et al.* [3, 17 Pandey] have recently studied the magneto elastic anisotropy induced by lattice mismatch for thin films of CMS deposited on either MgO or STO substrate. In their work they observe a clear out of plane anisotropy induced in the CMS deposited on STO, but no significant magneto-elastic anisotropy is induced for CMS deposited on MgO.

As demonstrated by X-ray diffraction, our samples show also a tetragonal distortion which could be the origin of the uniaxial anisotropy in our sample. Even if our films are completely relaxed, we will see that FMR measurements prove this superposed uniaxial anisotropy. In the next chapter, we will show that ion irradiation increases the out of plane deformation of the alloy which goes along an increased amplitude and a rotation of the uniaxial anisotropy, supporting the idea that the tetragonal distortion is at the orgin of the uniaxial anisotropy.

4.2.2 Domain walls observation by Lorentz microscopy

As presented in chapter 3, Lorentz microscopy is a powerful tool to image and study the geometry of domain and domain walls in a ferromagnetic material. Here we apply this technique to study the shape of the domain walls in the CMS samples and verify the validity of the switching mechanisms presented in the previous section.

Experiments were carried out at the CEMES laboratory by Dr. Luis Alfredo Rodriguez using Hitachi HF-3300 (I2TEM-Toulouse) microscope operated at 300 kV. The I2TEM microscope is especially dedicated to study magnetic samples by electron holography and Lorentz microscopy. It is equipped with an image corrector (CEOS B-COR) to correct off-axial aberrations and has a cold field emission gun that emits highly coherent electrons with a very high brightness of about ~ 10^7 A/cm^2.sr. These two features allow resolving magnetic contrasts with a very good signal-to-noise ratio. Examples of TEM Lorentz mode images are presented in Figure 4.25 for sample N°3.

This sample has been dedicated to this experiment and prepared for an in-plane view sample preparation. We note that, no magnetic field has been applied prior to the observation, so it is observed as inserted in the TEM sample holder. As explained in chapter 3, contrasts due to domain walls can be observed when defocusing the image as shown in Figure 4.25-b and 4.25-c. Clearly we observe the different features predicted by micromagnetic simulations. Indeed, we observe mainly 90° domain walls, especially close from the edge of the central hole (this is done to decrease locally the thickness of the sample so the incoming electrons are able to penetrate the material). Moreover, we also observe some particular contrast as shown in Figure 4.25-c corresponding to a zoom of the yellow box in Figure 4.25-b. Here we recognize the cross-tie domain walls which appear around the coercive field in the MOKE experiments.

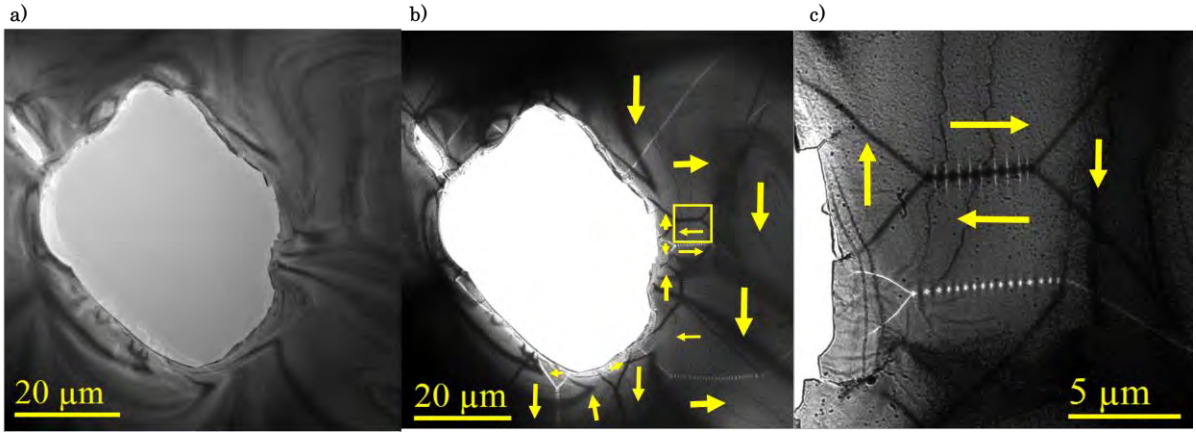

Figure 4.25: Low-magnification Lorentz images for the sample N°3 recorded at a) in-focus and b) out-of-focus conditions. In c), a zoom image of b) to observe the exotic magnetic contrast (yellow box). The intensity contrast has been forced in the defocus images to enhance the visualization of DWs. The yellow arrows show the direction of the magnetization deduced from the out of focus image in the different domains.

A closer look of the cross-tie domain wall is presented in Figure 4.26. They can be understood as a succession of vortex states with the same polarity and chirality. The white contrast observed in Figure 4.26-a. corresponds to the zone for which spins of two surrounding vortices

rotates in opposite direction. In this part, the Y component of the magnetization points either in the + or – direction leading to a difference of contrast as sketched in Figure 4.26-d.

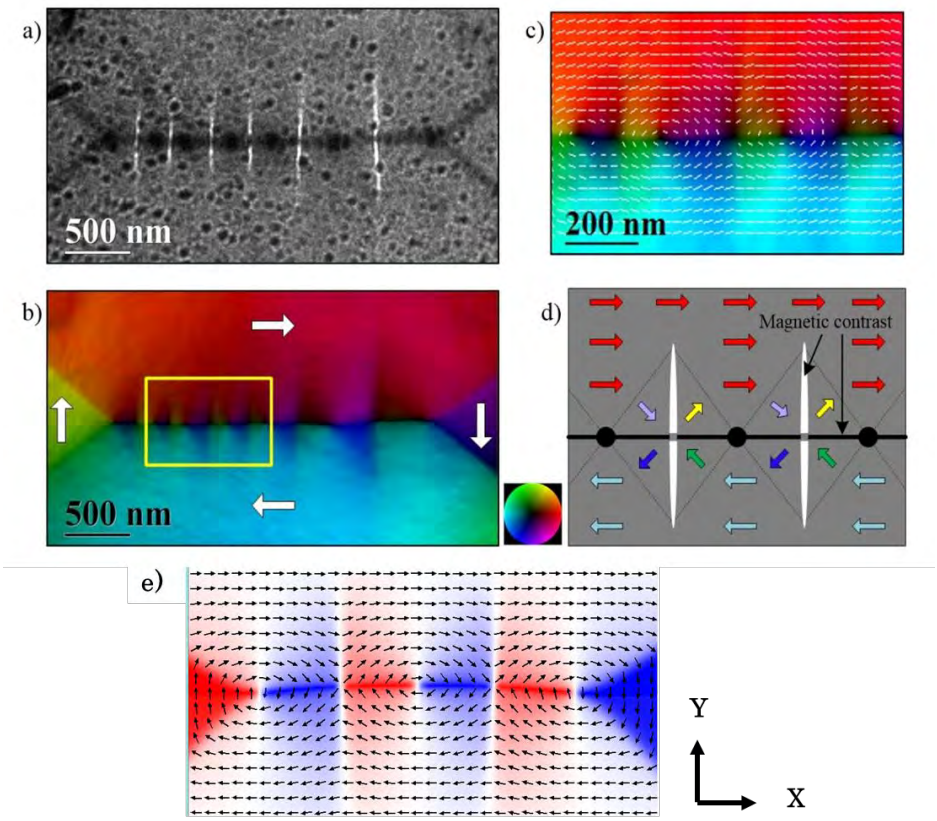

Figure 4.26: (a) Defocus image recorded around a complex DW configuration. (b) Magnetic color map of (a) by solving TIE. White arrows represent the average magnetization orientation of each domain. (c) A zoom of the yellow box in (b) where white lines represent the magnetic flux. (d) A simple cartoon representing the magnetic structure of the DW. Color arrows represent the local magnetization orientation while bright/dark lines and dark spots correspond to the magnetic contrast observed in the defocus image. e) OOMMF simulations of cross tie domain walls.

4.2.3 FMR Dynamic properties measurements

Ferromagnetic Resonance (FMR) is a common and powerful technique which is used to extract the magnetic parameters of a ferromagnetic material. In this section we will present the different geometry used in this work to extract the magnetization, the gyromagnetic ratio, the anisotropy and the exchange values of the three samples. Then we will present the measurement of the linewidth and discuss the value of the Gilbert damping extracted from the FMR.

4.2.3.1 Extraction of magnetic parameters.

- **Methodology:**

As presented in chapter III, in our FMR set-up, a microwave voltage is injected in the stripline and a modulation technique is used to measure the absorbed power signal by the magnetic film placed on the stripline. This technique allows for a direct inductive coupling between the stripline and the sample. The lateral dimensions of the studied samples range between 4*4 for samples of series N°1 and 3*3 mm^2 for series N°2 and N°3. These dimensions are bigger than the stripline width (400 µm). This leads to a non-uniform excitation field and thus we are not in a pure FMR geometry where the microwave excitation field is uniform over the sample. Indeed, we are in a configuration of surface spin waves excitation. However, considering the maximum wave vector that can be excited k=2π/L with L = 400 µm, and taking into account the corrections to the FMR frequency (chapter 2 equation 2.78), we find that that the effect of the finite size of the stripline shifts the resonance frequency by an amount of approximately 4 MHz which corresponds to a field shift of about 0.2 mT. Such a shift value is below the uncertainty of our measurement which is about 0.3 mT. Therefore, considering a uniform mode, formulas 2.54 to 2.56 will be applied to recover the magnetic parameters of the samples.

A typical FMR spectrum for different excitation frequencies is presented in Figure 4.27. The magnetic field is scanned from 0 to 450 mT. We can see that the signal corresponds to the derivative of the imaginary part of the susceptibility. However, and as explained previously, signals always contain a small contribution from the real part of the susceptibility due to the sample length, allowing for a small propagation effect, and also because the propagating mode of the stripline is not purely TEM. Then our data are fitted with a function of the form:

$$Y \propto cst + \frac{d\chi'}{dH}\cos\varphi + \frac{d\chi''}{dH}\sin\varphi \tag{4.14}$$

With φ an arbitrary dephasing angle and $\chi = \frac{cst}{(\gamma H_0 - \gamma H_{res}) - i\alpha(\frac{\gamma \Delta H}{2\alpha})} = \chi' + i\chi'' = \frac{cst(H-H_{res})}{(H-H_{res})^2+(\frac{\Delta H}{2})^2} + i\frac{cst(\frac{\Delta H}{2})}{(H-H_{res})^2+(\frac{\Delta H}{2})^2}$

It can be seen in figure 4.27 that the angle φ, in this case, is very small (< 10°). The Symbols correspond to experimental data, while the full lines are the fit obtained from equation 4.14. From the fit we are able to deduce the value of the applied field at the resonance as well as the linewidth of the signal ΔH which allows to study the relaxation parameters, that will be presented in section 4.2.3.2. Interestingly, we will show that the different CMS samples studied in this manuscript show some clear asymmetry of the resonance peaks due to multiple resonance with very close resonance fields and linewidths.

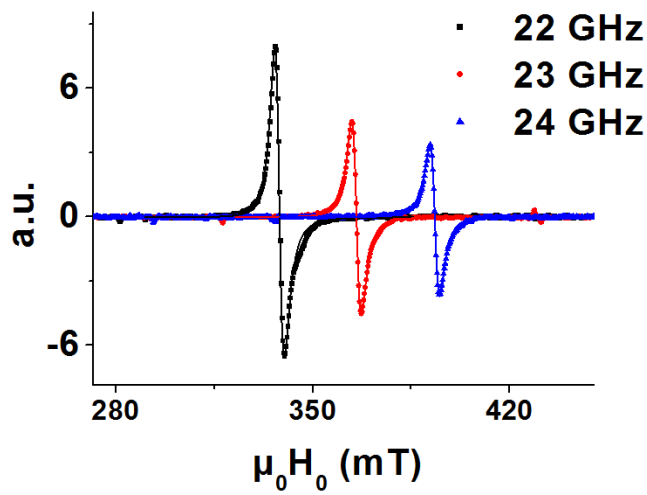

Figure 4.27: A typical FMR spectra at different frequencies.

In our work, FMR measurements have been performed in different geometries depending on the applied magnetic field orientation with respect to the film's surface. In the first case, the external magnetic field is applied in the plane of the sample (*i.e.* $\theta_H = 90°$). The maximum external field can reach about 450 mT and the air gap is 8 cm. In this geometry the external field has been applied in either the easy or hard axes directions for measurements of H_{res} vs. *fres* (Figure 4.28-a). For this measurement the sample is rotated and the electromagnet is kept at a fixed angle with respect to the sample holder. It allows staying always in the "Surface Spin Waves configuration". We also performed measurements of the resonance field H_{res} as a function of the angle φ_H of the external field with respect with one easy axis at constant excitation frequency (Figure 4.28-b). In the latter, the electromagnet is rotated with respect to the sample holder with a relative angle variation between 0 and 180°. Let's note that when $\varphi_H \sim 90°$, we are in the Magnetostatic Backward Volume Waves (MSBVW) configuration. However, here also the field shift due to MSBVW is close to 0 MHz. Moreover, we verified that we observe the same resonance field if φ_H =90° or if φ_H=0° when the sample is rotated by 90°. The only difference relies on the measured amplitude signal which is much smaller if φ_H = 90° as the pumping field is parallel to the magnetization.

In the second experimental geometry, the field is applied perpendicular to the plane of the layer (*i.e.* $\theta_H = 0°$). An example of such measurement is presented in Figure 4.28-c). In this configuration, we modify the poles of the electromagnet so the magnetic field can reach a value of 1.6 T and the air gap is decreased to 2 cm.

By fitting all the different dispersion relations *fres* vs. μ_0H_0 and H_{res} vs. φ, we were able to extract the values of the gyromagnetic ratio $\gamma/2\pi$, the magnetization μ_0Ms and the anisotropy field μ_0Hk. The latter parameter being the simplest one to determine as it corresponds to the inflexion point in the *fres* s. μ_0H_0 curve in the in-plane hard axis direction (figure 4.28 a).

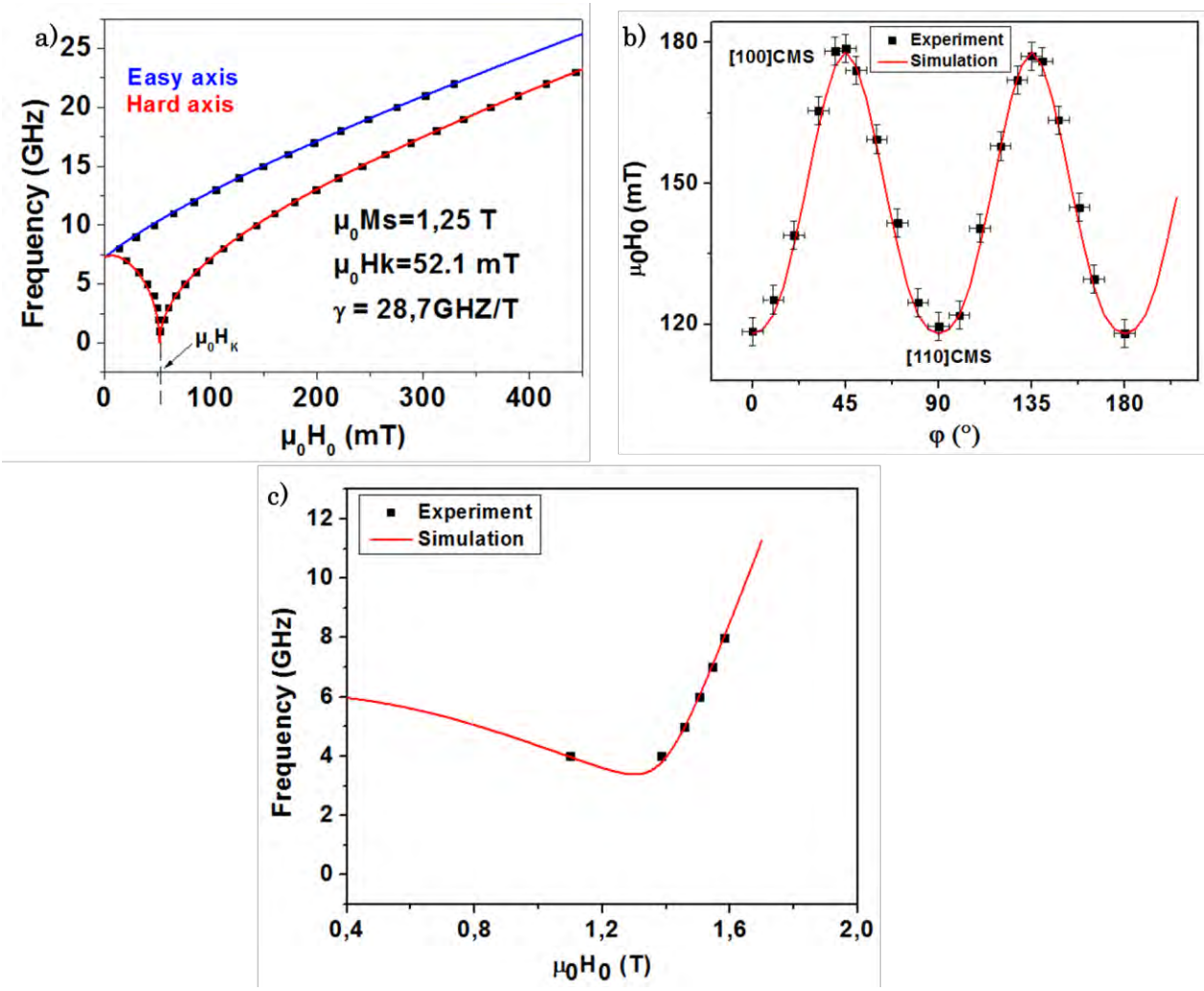

Figure 4.28: Example of measurements for the different experimental configurations used in this work. In a), dispersion relation *fres* vs. $\mu_0 H_0$ for in-plane measurements. The points corresponds to experimental data and the solid lines to the fit using equations 2.54 and 2.55. b), FMR angular measurements of $\mu_0 H_0$ vs. φ at 13 GHz. c) Out-of-plane measurements of *fres* vs. $\mu_0 H_0$. The line corresponds to the fit using equation 2.56.

We will now present the results of FMR spectra for the reference samples of the three series and try to correlate the magnetic properties to the structural analysis presented in sections 4.1.2 and 4.1.3.

- **<u>Sample N°1:</u>**

Two examples of recorded absorption spectra are shown in Figure 4.29. The first one presents the FMR signal for an applied field parallel to the easy axes, *i. e.* [110] and [1$\bar{1}$0], (Fig. 4.29-b) while the second one corresponds to an applied field parallel to the hard axes, *i. e.* [100] and [010] (Fig. 4.29-c). The excitation frequency field is 16 GHz for all those mentioned spectra measurements.

The major feature encountered in this sample is that two peaks are clearly visible for one easy axis direction while two peaks are always visible in the two hard axis directions. As these measurements are carried out in the saturated regime, the two peaks cannot be accounted for the non-saturated modes like edge modes for example. Our assumption is that they correspond to two distinct crystal order phases with different magnetic parameters. This assumption is supported by the structural investigation presented in sections 4.1.2 and 4.1.3. Indeed, we showed that this sample presents about 75% of $L2_1$ order and about 25% of B2 phases. Then we believe that these two crystal orders present two different set of magnetic parameters. Our assumption is also supported by FMR measurements on other kind of materials such as Co_2MnGe [18 Belmegeunai] for example which exhibit multiple peaks due to different crystal orders. Let's note that even if FMR is an inductive technique, and so the amplitude of the signal is supposed to be proportional to the magnetic volume of the crystal order, it is very difficult to relate one peak to one crystal order as it is. Indeed, the amplitude of the signal strongly depends on its linewidth.

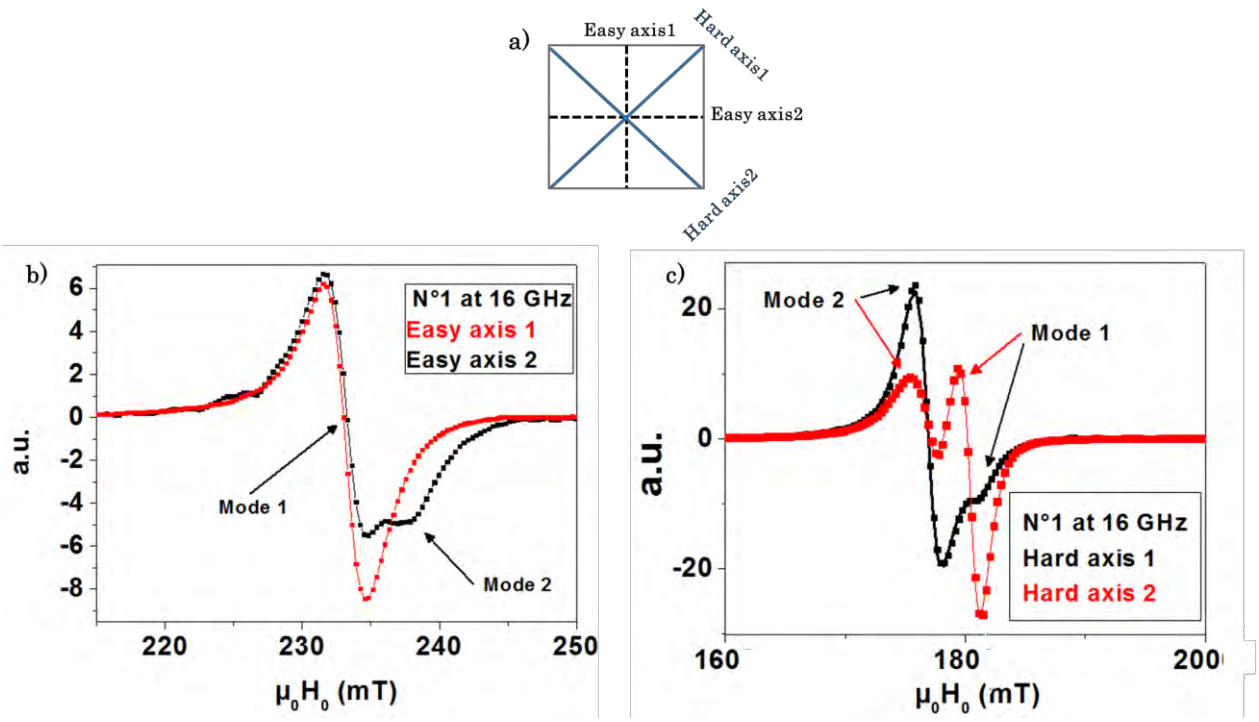

Figure 4.29: a) a schematic presentation of easy and hard axes directions in CMS sample. FMR absorption spectra of N°1 at 16 GHz for both b) and c) with two modes along easy and hard axis.

Another interesting feature is the shape of the different peaks. Indeed, while we can observe two peaks for the easy axis 2, we observe only a single asymmetric peak for the easy axis 1 for all excitations frequencies. The asymmetry shape of the peak reflects the fact that the two modes are "mixed". Similarly, for the hard axis, the amplitude of the two respective peaks seems to be inverted when the sample is rotated from one hard axis to the other. This result can only be explained if something is breaking the fourfold symmetry of the system, at least for one of the two crystal orders. Indeed, it is sufficient that only one mode shows an asymmetric behavior to modify the entire spectrum.

Naturally, one can think about the uniaxial anisotropy detected by MOKE measurements. If the anisotropy is aligned with the easy axes, one expects a shift of the resonance fields between the two easy axes while the FMR signals in the hard axes are at the same positions. This is what we observe, within the uncertainty of our measurement, a shift in the easy axis resonance at least for the mode 2 as shown in figure 4.30.

Moreover, another difference we observe when fitting the experimental data, is that the amplitude of the different peaks are always different. For example, the amplitude ratio of the primary peak/ secondary peak in the fitted curves has a value of 1.5 in figure 4.30-a) and 6 for the blue fitted curve in 4.30-b. Despite different amplitude ratios depending on the orientation of the field, we always observe a peak with lower amplitude in agreement with the fact that we have different crystal order in the sample with different volume. Therefore we believe that the two resonance modes exhibit anisotropy of the linewidth as a function of the direction of the applied field. This effect is expected in crystals as the damping tensor reflects the symmetry of the system. However the two hard axes on one hand and the two easy axes on the other hand should be equivalent. Here, we believe that the relaxation differs for every direction of the applied field. We will develop this point in the next subsection 4.2.3.2 devoted to the damping and relaxation mechanisms.

Let's note that it is more difficult to define the value of the linewidth for each mode when the field is applied in the easy axis 1. Indeed we show in Figure 4.30-b two examples (red and blue lines) of simulated signals which are in very good agreement with the experimental data. While the resonance fields are the same as for the easy 1, the amplitude and linewidths of the two modes are different, especially for mode 2. Then it is extremely difficult to get a precise measurement of the linewidth of the two modes if the peaks are not sufficiently resolved. To show how much the two peaks are mixed, we also fitted this curve with a single peak (green line), and the agreement is also very good. However the dephasing between the real and imaginary part φ reaches 18°, which is quite important. This is why we can state that when a peak is very asymmetric, it contains most probably two resonant modes. The situation is quite similar when the field is applied in the hard axis 1 direction. Even if the mode 1 is clearly visible, it is very difficult to determine with a good precision the value of the linewidth if the peak is not well resolved.

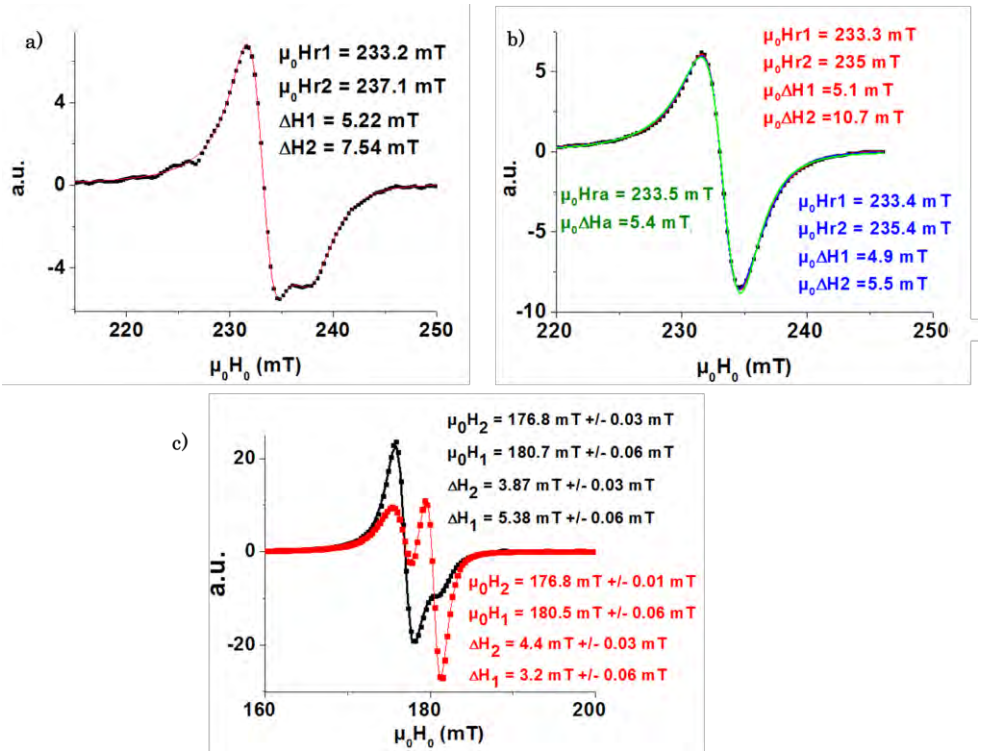

Figure 4.30: absorption spectra at 16 GHz as a function of external field for CMS N°1 along the two easy axes in a) and b) and the two hard axes in c). Experimental data are presented as points and the solid lines correspond to linear fit with different adjustment parameters using equation 4.14.

In order to determine the magnetic parameters corresponding to the two modes, we use the spectra for which the peaks are well resolved. The evolution of the resonance field as a function of frequency for in-plane and out-of-plane configuration are presented in Figure 4.31-a) and 4.31-d, respectively. Only one easy and one hard axes are drawn here. Figure 4.31-b is a zoom on the black box in Figure 4.31-a, to show the small difference between the two phases. Figure 4.31-c corresponds to the angle measurement of the resonant field as a function of the in-plane angle between the applied field and the easy axis at 13 GHz. The solid lines in the different curves correspond to the adjustment using equations 2.54 to 2.56.

In figure 4.31-a, we also show the first standing spin wave modes (SSW) measured in the direction of the easy axis 1 and hard axis 1 direction. This mode is an exchange dominated excitation in the thickness of the layer that appears at lower magnetic fields than the uniform mode as shown in Figure 4.31-e. It allows to extract the value of the exchange constant, A, Indeed, in the in-plane configuration and for an external field applied either parallel to the easy or hard axis, the dispersion relation that relates the resonance frequency of the SSW to the applied field (following equation 2.85 in chapter 2) is expressed as:

SSW Easy axis: $$\boldsymbol{f_{res} = \frac{\mu_0\gamma}{2\pi}\left[\left(H_0 + H_k + \frac{2A}{\mu_0 M_s}k_{z,n}^2\right)\left(H_0 - \frac{H_k}{2} + \frac{2A}{\mu_0 M_s}k_{z,n}^2 + M_s\right)\right]^{1/2}} \quad (4.15)$$

SSW Hard axis: $$\boldsymbol{f_{res} = \frac{\mu_0\gamma}{2\pi}\left[\left(H_0 - H_k + \frac{2A}{\mu_0 M_s}k_{z,n}^2\right)\left(H_0 - H_k + \frac{2A}{\mu_0 M_s}k_{z,n}^2 + M_s\right)\right]^{1/2}} \quad (4.16)$$

Where $\boldsymbol{k_{z,n}^2} = \frac{\boldsymbol{n\pi}}{\boldsymbol{d}}$, with $\boldsymbol{d}$ being the thickness of the CMS layer (≈42 ±1 nm), $\boldsymbol{n}$ corresponds to the pinning mode and $\boldsymbol{A}$ is the exchange stiffness constant. To calculate the exchange value, we consider the first excitation mode with n=1. Moreover we consider a perfect pinning at the surfaces. These assumptions are supported by the fact that, even if the film thickness is well below the skin depth, the amplitude of the microwave field is slightly different between the two surfaces of the sample. The pumping field being non-uniform in the thickness of the layer, it allows for the excitation of the first mode. Rigorously, the pinning parameters p and the mode index $\boldsymbol{n}$ in equation 2.84 could be determined if we could have observed at least 3 standing spin waves modes [19 Wigen]. However, the frequencies of the modes with n>1 are higher than 30 GHz, the limit of our microwave source. Finally, as the signal is very small it is impossible to distinguish the contribution of the two respective phases and the exchange value is calculated considering the parameters of mode 1.

The deduced parameters for μ_0Ms, μ_0Hk, the gyromagnetic ratio $\gamma/2\pi$ and the exchange value A are presented in table 4.4. We obtain very similar values of the magnetic parameters for each mode observed in the FMR spectrum. First the magnetization values are very close from the theoretical prediction. Taking into account the lattice parameters obtained by X-ray diffraction, we get 4.88 and 4.85 $\mu_B/f.u$ for modes 1 and 2 respectively, to compare with the theoretical prediction of 5 μ_B for perfect $L2_1$ or B2 structure. This result is also in very good agreement with the structural studies. Then we attribute the two resonance modes to the B2 and $L2_1$ crystal order. The small decrease of the magnetic moment as compared to theoretical value is most probably due to a small amount of Co-Si exchange in each phase (we remind that the Co/Si exchange parameters has been found to be around 0.04 for this sample). We confirm the average value of the magnetization with PPMS measurement (Figure 4.32). We obtain average magnetization amplitude of 1.26 ± 0.02 T for CMS Heusler alloy. The uncertainty on the PPMS measurement is due to the uncertainty on the exact dimension of the sample.

The main difference between the two modes concerns the anisotropy. First we succeeded to fit the angle dependence of the resonant field of mode 2 taking into account a very small uniaxial anisotropy of $\mu_0 H_u$ ~0.9 mT in the easy axis 2 direction, as expected from MOKE measurement. This superposed anisotropy seems to be absent for mode 1. In order to fit this uniaxial anisotropy for mode 2, we include in the calculation of the total energy of the system a term of the form $K_u.\mathrm{Sin}^2(\beta)$, with β the angle of the magnetization with respect to easy axis 1.

We also deduced cubic anisotropy values which are more important than the values generally reported for CMS deposited on MgO, for example, [20 Yilgin, 21 Gaier] but equivalent to the ones previously reported by Ortiz *et al*. This can be related to the deduced value of the g factor calculated from $g = \frac{\gamma * 2m_e}{|e|}$. Indeed we obtain values of g ≈ 2.05 (considering the mass of a free electron) for both modes. This value is in agreement with reported values in literature for CMS ([4 Belmeguenai, 2 Rameev, 23 Hamrle and 1 Ortiz]) of 2.05 or 2.04.

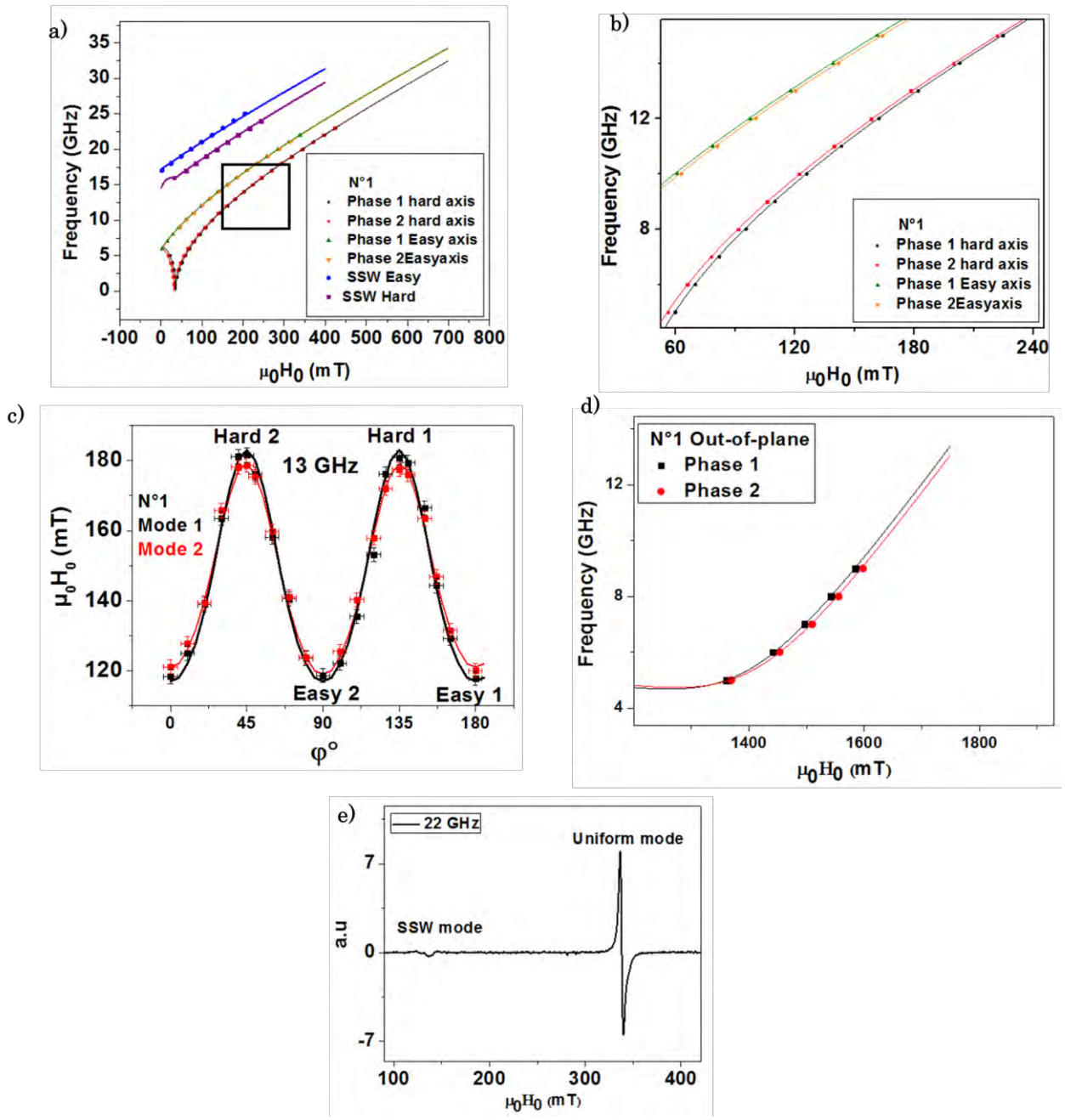

Figure 4.31: Dispersion relation f_{res} vs. $\mu_0 H_0$ in CMS N°1 for a) in-plane and d) out-of-plane configuration. Figure b) corresponds to a zoom on the two modes for the black box in a). c) Angular dependence of the resonance field at 13 GHz. e) FMR signal at 22 GHz in the easy direction showing both the FMR and SSW modes.

According to the Kittel formalism for ferromagnetic material with small orbital moment, g can be related to the ratio of orbital over spin moment such as $(g-2) = 2\left(\frac{\mu_L}{\mu_S}\right)$. Then we believe that our sample shows a small contribution from orbital moment. As the anisotropy relates the orbital and spin moment through the spin-orbit coupling, the orbital

contribution is maybe the origin of the large value of the cubic anisotropy. This assumption will be supported by the effect of ion irradiation on the cubic anisotropy in chapter V. Moreover, the slightly lower value of the anisotropy constant for the mode 2 could be expected in the B2 phase due to the disorder on the Mn and Si sites which change the local environment of the Mn atoms carrying most of the magnetic moment. Therefore, we attribute the mode 2 to the B2 order and the mode 1 to the $L2_1$ order. Further study of the FMR linewidth (see next subsection) wil support this assumption.

Finally, we found a value of the exchange constant, ***A***, close to the values reported in literature for $L2_1$ structure. Indeed the exchange constant is found to range between 19 and 23 pJ/m as mentioned in [24 Ritchie, 23 Hamrle and 3 Pandey]. This exchange constant value is in a good agreement with the values of the magnetization. Indeed the magnetization depends on the splitting of spin up and down energy states which is related to the strength of the exchange spitting.

CMS sample N°1	Magnetization saturation Ms (T)	Anisotropy field H_k (mT)	Anisotropy constant $K_c=\frac{H_K*\mu_0 M_s}{2}$ (KJ/m³)	Uniaxial Anisotropy field (mT)	Gyromagnetic ratio $\frac{\gamma}{2\pi}$ (GHz/T)	Exchange constant ***A*** (PJ/m)
Phase 1	1.26 ±0.02	36±0.2	-18.042±0.2		28.7±0.1	19±0.5
Phase 2	1.25 ±0.02	33±0.2	-16.91±0.2	0.9	28.7±0.1	

Table 4.4: Magnetic parameters of the CMS reference sample N°1 for the two phase measured by FMR.

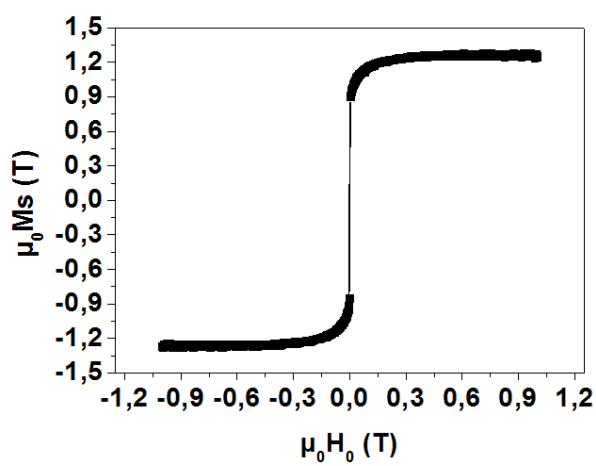

Figure 4.32: PPMS measurements on CMS N°1 with an average magnetization of 1.26 T.

- **<u>Sample N°2:</u>**

Similar treatment has been conducted on sample N°2. Examples of the different measurements are shown in Figure 4.33. For this sample we were only able to distinguish one resonance peak. However, we still notice an asymmetry of the peak shape which could mean that we have two modes with very similar magnetic parameters that are mixed in the

measured spectra. We also note a small shift of the resonant field of 1.7 mT for the easy axis 2. This shift does not exist for the hard axes (within the precision of the alignment of the applied field with respect to the hard axis, which is less than 1°). This means that we have a uniaxial anisotropy superposed to the easy axis 2, confirming the MOKE experiment. The presence of the additional uniaxial anisotropy allows fitting the angle dependence of the resonance field as a function of the angle φ (Figure 4.33-e).

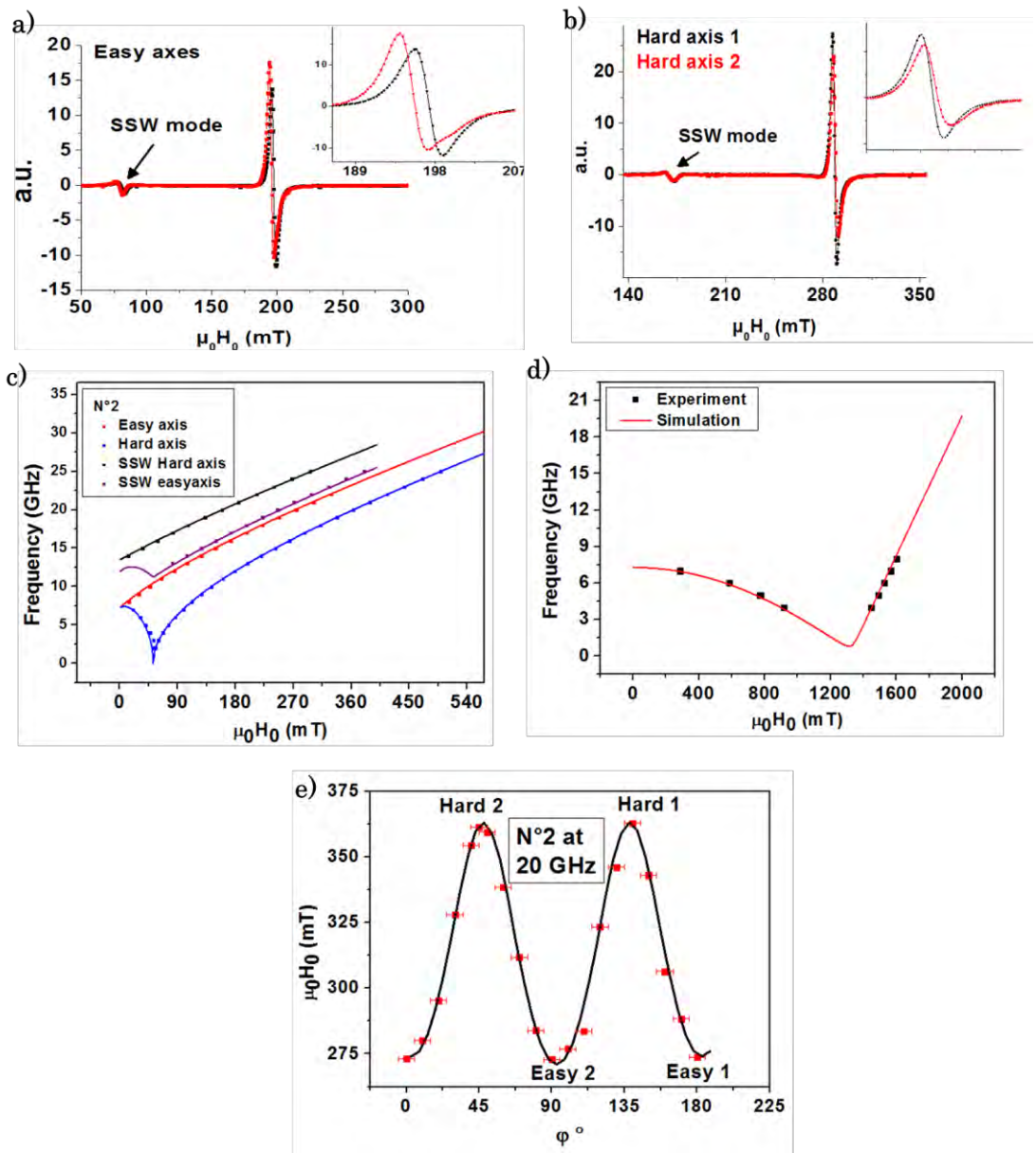

Figure 4.33: FMR absorption spectra for CMS N°2 for in-plane configuration along a) easy axes at 18 GHz and b) hard axes at 17 GHz. f_{res} vs $\mu_0 H_0$ for c) in-plane and d) out-of-plane configurations. In e), angular dependence of resonance fields at 20 GHz.

The magnetic parameters extracted from the simulation are presented in table 4.5. The amplitude of the uniaxial anisotropy $\mu_0 Hu$ is found to be about 1.5 mT. While we observe the

same value of gyromagnetic ratio as for sample N°1, the cubic anisotropy constant is much higher while the exchange constant is almost half of sample N°1. It is surprising to have an increased value of the cubic anisotropy without any change of the gyromagnetic ratio. The value of the gyromagnetic ratio $\gamma/2\pi$ means that the amplitude of the orbital and spin moment are similar to sample N°1. The increased cubic anisotropy signifies an increased spin orbit interaction. Then it is most probably the value of the spin orbit constant, λ_{SO}, which must differ from sample N°1.

Moreover, the magnetization amplitude and exchange constant are found to be lower than for the sample N°1. Even if no quantitative study of atomic disorder have been conducted on this sample we already stated that it shows some degree of $L2_1$ order but Co/Mn, Co/Si and Mn/Si exchanges are fairly to be considered. Dealing with the Mn/Si disorder (B2 type disorder), Gaier *et al.* have obtained an exchange value of 18 pJ/m for the pure B2 phase. Therefore, we assume the reduced value of the magnetization and exchange amplitudes to be related to an important Co/Mn and/or Co/Si disorders.

	Magnetization saturation Ms (T)	Anisotropy field H_k (mT)	Anisotropy constant $K_c=\frac{H_K*\mu_0 M_s}{2}$ (KJ/m^3)	Uniaxial anisotropy field H_u (mT)	Gyromagnetic ratio $\frac{\gamma}{2\pi}$ (GHz/T)	Exchange constant $\boldsymbol{A}$ (PJ/m)
CMS sample N°2	1.24 ±0.02	53±0.2	-26.14±0.2	1.5±0.2	28.8±0.1	10±0.5

Table 4.5: Magnetic parameters of sample N°2 deduced from FMR measurements presented in figure 4.33.

- **<u>Sample N°3:</u>**

The situation for sample N°3 is somewhere between samples N°1 and N°2. Indeed, as shown in Figure 4.34-a and 4.34-b, two modes are visible for the applied field parallel to the hard 2 direction while it is barely visible above 19 GHz in the easy axis 1 direction. For the two other magnetic directions only a single resonance peak is observed.

The main difference with sample N°1 is that not only the amplitude of the peaks change when going from the hard axis 1 to the hard axis 2, but also the position of the peaks with a clear shift of mode 1 of about 5 mT at 19 GHz. Even if HAADF-STEM only shows $L2_1$ order for this sample, we believe that it most probably shows some inclusions of B2 order in the matrix. The $L2_1$ order being clearly predominant over the B2 phase in terms of volume. Due to the difficulty to separate both contributions in the FMR spectra (except for the hard axis 2), only the magnetic parameters will be extracted for the main mode corresponding to the $L2_1$ phase.

Once again, the shift of resonance field when going from one hard axis to the other can be explained by the presence of an additional uniaxial anisotropy. However this time it is superposed with the hard axis 1 (let's note that most probably the minority mode shows no additional anisotropy). Our assumption is also supported by angle measurements that are perfectly fitted considering the main mode with a superposed uniaxial anisotropy (figure 34-d) in the hard axis 1 direction. As already mentioned, tetragonal distortion of the cell has been

proved to induce such kind of anisotropy in Iron for example in the case of doping with Dy atoms. This situation is different from sample N°1 and N°2 for which we observed a uniaxial anisotropy superposed to the easy axis. The first explanation for this difference could be the amplitude of the out of plane lattice parameter which is higher for the sample N°3 than for sample N°1. Another possibility relies on the nature of the atomic plane being either the Co planes or the Mn-Si planes in contact with the MgO substrate. However, further structural characterization studies would be necessary to clarify this point.

The values for the different magnetic parameters obtained from the different fits are presented in table 4.6. The cubic anisotropy, exchange and gyromagnetic factor values are similar to sample N°1 while the magnetization is slightly lower. This can be due to the higher Co-Si exchange deduced from by X-ray diffraction with Cu source.

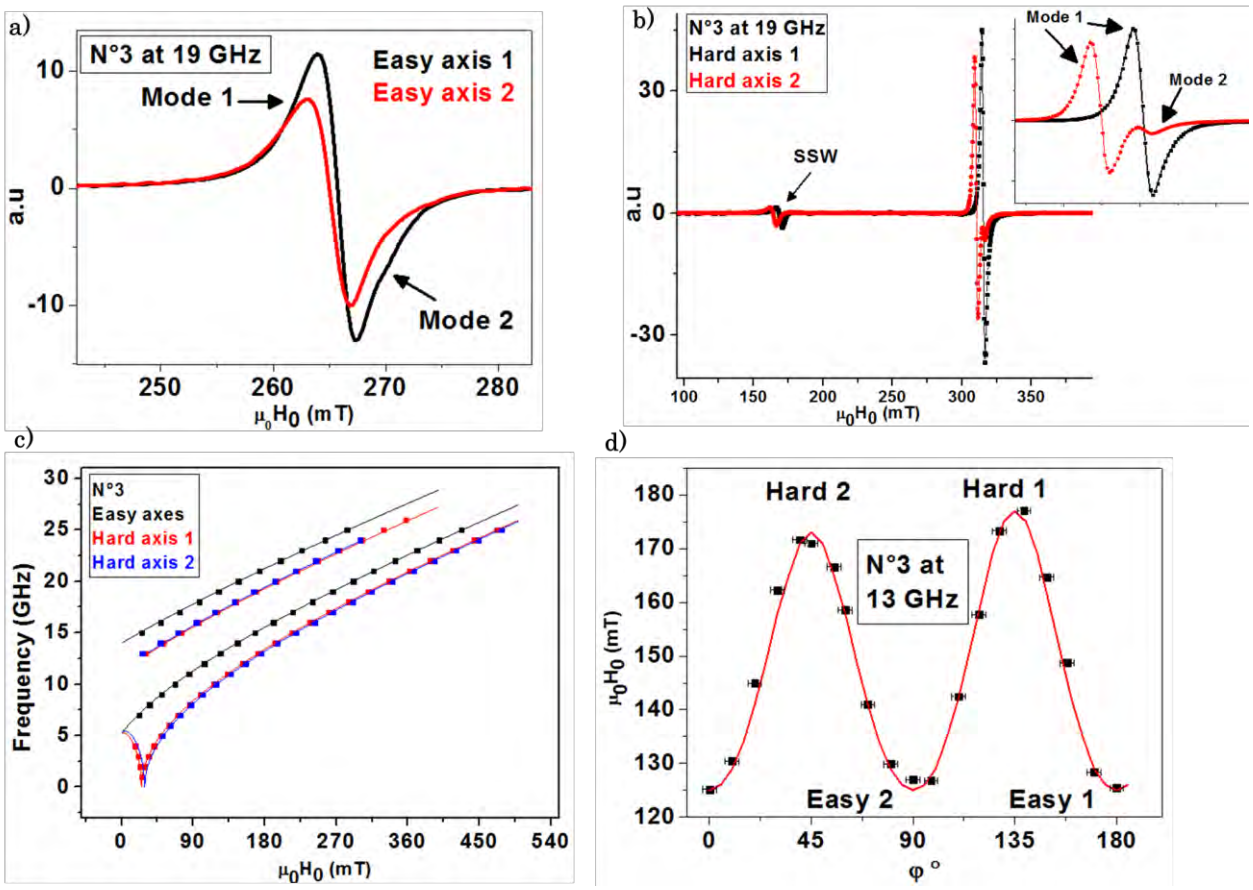

Figure 4.34: FMR absorption spectra for CMS N°3 for in-plane configuration along a) easy axes and b) hard axes at 19 GHz. c) f_{res} vs. H_0 for in-plane SSW and uniform mode configurations. In d), angular dependence of resonance fields at 13 GHz.

	Magnetization saturation Ms (T)	Anisotropy field H_k (mT)	Anisotropy constant $K_c=\frac{H_K*\mu_0 M_s}{2}$ (KJ/m^3)	Uniaxial anisotropy field H_u (mT)	Gyromagnetic ratio $\frac{\gamma}{2\pi}$ (GHz/T)	Exchange constant $\boldsymbol{A}$ (PJ/m)
CMS sample N°3	1.25 ±0.01	29±0.5	-14.4±0.2	2±0.1	28.7±0.1	18±0.5

Table 4.6: Magnetic parameters obtained for sample N°3 from FMR measurements presented in figure 4.34.

In the next subsection, the different measurements of the linewidth in different configurations and the deduced value of the gilbert damping coefficient α are presented for the three studied samples.

4.2.3.2 Study of dynamic relaxation: anisotropic damping

Heusler alloy and especially Co_2MnSi is supposed to show very small damping coefficient as compared to other ferromagnetic materials. This hypothesis is based on the half metallic behavior of these compounds which limits spin-flip events. Theoretical calculations have predicted Gilbert damping constant α down to $0.6*10^{-4}$ [25 Liu]. To our knowledge, values reported in literature for α in CMS range between 2.10^{-3} and 3.10^{-3} for best. However, recently, two studies have reported lower damping values. The first one by Qiao *et al.* [26 Qiao] with $\alpha \sim 9.9*10^{-4}$ for one easy axis direction without mentioning the other directions. Moreover they have reported that their sample grow in a $L2_1$ crystalline order but the deduced magnetic moment is only 2.8 $\mu_B/f.u$ which is much below the theoretical prediction. Also in Qiao et al. study, they have linked the possible lower values of gilbert damping to a lower values of magneto-crystalline cubic anisotropy constant as in their study they have a value of $5.1*10^4$ erg/cc (5.1 KJ/m^3) for the in-plane four fold anisotropy constant K. The second study was done in the PhD work of A. Neggache on electronic properties on $Co_{1.5}Fe_{1.5}Ge$ and CMS alloys. They claim values of $\alpha \sim 1*10^{-3}$ [27 Andrieu].

An interesting feature in literature is that only very few studies report any eventual anisotropy of the Gilbert damping constant. In Yilgin *et al.* [20 Yilgin], they show a damping constant of $3*10^{-3}$ for one easy axis and $6*10^{-3}$ for one hard axis. It is useful to remind that, in crystal, the damping is normally described as a matrix reflecting the symmetry of the crystal. Anisotropic damping is generally reported in uniaxial materials. However, it is generally assumed in cubic systems that the damping factor is equal for equivalent crystal directions. In our work we show that our samples must probably present different values of α constant even for equivalent crystal directions.

- **<u>Sample N°1:</u>**

As already explained, it is very difficult to give precise values of the linewidth for the two modes when the resonance peaks are mixed up, as shown in figure 4.30. This is the reason why in the easy axis 1 direction, we consider only a single resonant peak and we attribute the

linewidth to the mode 1 (which will be shown to correspond to the most predominant $L2_1$ order). In addition, the mixing of the two peaks makes difficult the measurement of the linewidth in the hard axis 1 direction for the mode 1, as can be seen by the strong variations of the green dots in figure 4.35 c. Then for this crystal direction we do not give value of the damping coefficient of the mode 1. Also we do not present the linewidth of the two modes for the out of plane configuration due to the small number of point measured in the saturated regime as shown in Figure 4.28-e.

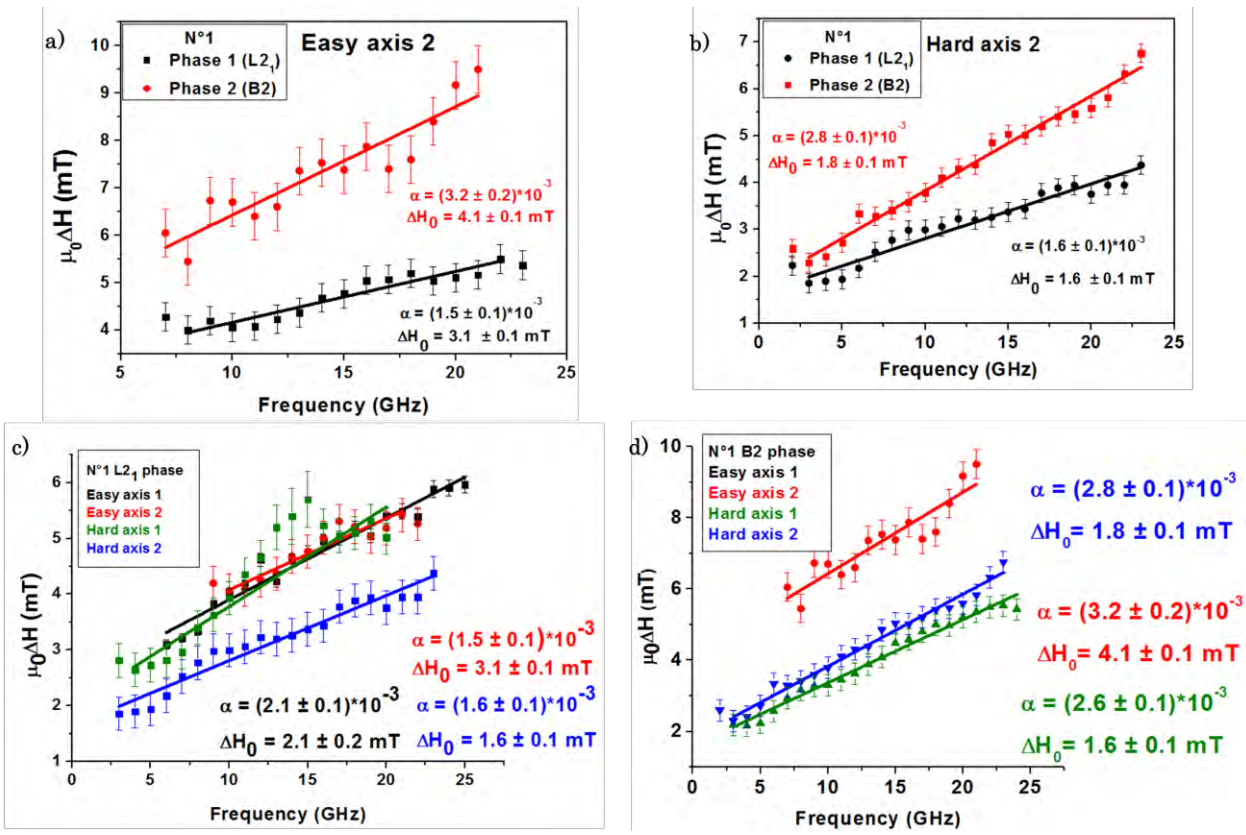

Figure 4.35: line width measurements as a function of the applied frequency along easy and hard axes for the two observed $L2_1$ and B2 phases of sample N°1. In a) and b) the two modes are distinguished for easy 2 and hard 2 axes, respectively. While in c) and d), line width values ($\Delta \boldsymbol{H}$) of $L2_1$ and B2 phases and their linear fit are traced for each easy and hard axis showing their corresponding damping coefficient $\boldsymbol{\alpha}$ and $\Delta \boldsymbol{H_0}$.

In Figure 4.35-a) and 4.35-b we compare the linewidth of the two resonance peaks measured either in the 2 easy or in the 2 hard directions. Clearly, the mode 1 shows lower values of the linewidths than the mode 2, reinforcing the idea that the mode 1 corresponds to the $L2_1$ order and the mode 2 to the B2, as the latter grows in the form of crystallites in the $L2_1$ matrix. Then in the following we will consider the two peaks to correspond to the $L2_1$ and B2 modes and we will refer the mode 1 as the $L2_1$ mode and the mode 2 as the B2 mode.

The linewidths in the different directions of the crystal are presented in figure 4.35-c for the $L2_1$ mode and in figure 4.35-d for the B2 mode. For both modes, it appears that the linewidth amplitudes depend on the direction of the applied field. However, for both the $L2_1$ and B2 modes, it appears that the damping coefficient is roughly constant for each direction.

Then the difference in the linewidth seems to be essentially related to the variation of the extrinsic contributions ΔH_0. Indeed, for the $L2_1$ order, the α value is equivalent for the easy axis 2 and the hard axis 2. We found values of 1.5 and $1.6*10^{-3} \pm 0.1*10^{-3}$, respectively. These values are very good with respect to other reported values for CMS and are similar to the ones reported for Co_2FeAl [16 Belmeguenai]. In the hard axis 1, the dispersion is pretty important which avoids a precise value of α. Finally, α is found to increase for the easy axis 1 with a value of about $2.1*10^{-3}$. The difference between the two easy axes is most probably due to the fact that in the easy axis 1 direction, the $L2_1$ and B2 peaks are hardly dissociated and then it naturally increases the measured linewidth. Similarly, the α value for the B2 order in the easy axis 2 appears to be higher than for the hard axes. However, we can see in Figure 4.35-c that the dispersion in the experimental data is very important as the amplitude of the peak in the FMR signal is weak and mixed up with the $L2_1$ mode. Then it is difficult to clearly state about a potential anisotropic behavior of α in the B2 order. In conclusion, from these measurements, we do not observe neither the expected cubic symmetry nor a clear difference between the damping coefficient in the easy and hard axis directions, as reported by others.

Further insight can be obtained from the evolution of the linewidth as a function of the in plane angle φ of the applied field (φ scan) presented in figure 4.36-c and 4.36-d for the $L2_1$ and B2 modes, respectively. The determination of the exact value in this configuration is very difficult for two reasons. As both peaks does not show the same dependence with the angle φ (as shown by the simulations in Figure 4.31-c), the mixing of the mode and then uncertainty on the linewidth values, is reinforced for most of the angle φ. The second reason is due to the decrease of signal amplitude with φ. Indeed, in these measurements we change the orientation of the field as sketched in the figure 4.36. As already stated, the microwave magnetic field generated by the stripline turns from the magnetization perpendicular to parallel when φ = 90°. This last configuration corresponds to the excitation of backward volume waves and the coupling between the microwave field and the magnetization is minimum. An example of such effect is shown in fig 4.36-a. Then it becomes very complicated to get a precise measurement of the different linewidth when the signal is almost of the order of the experimental noise.

Despite the experimental limitations, we clearly observe some variations of the linewidth as a function of φ for both modes. In principle, the linewidth as a function of φ is supposed to reflect the cubic anisotropy [16 Belmeguenai] due to the $\frac{\partial f}{\partial H}$ term in equation 2.38. For the $L2_1$ mode, we observe two minima of the linewidth, one at 45° corresponding to the hard axis 2, and one at 110° with the smallest linewidth. Additionally, the linewidth at 0° (easy axis 1) and 135° (hard axis 1) are similar while it is lower around 90° (easy axis 2). While we already explained that the linewidth in hard axis 1 is difficult to obtain with precision, we do not have a clear explanation why a minimum appears at 110°. For the B2 mode, the expected fourfold symmetry is observed with minima at 45° and 135° and some "plateau" appearing for the easy 2 direction which may be related to the superposed uniaxial anisotropy.

While the main expected feature of the dependence of the linewidth as a function of the angle is recovered in the φ scans, the study of the angular dependence of α requires further analytical simulations. Indeed, a full treatment of the linewidth amplitude as a function of either the angle φ or as a function of the resonance frequency must be carried out taking into account different contributions. In literature the linewidth in FMR measurement is expressed as:

$$\Delta H = \Delta H_{Gilbert} + \Delta H_{inh} + \Delta H_{mos} + \Delta H_{2mag} \tag{4.17}$$

With:

- $\Delta H_{Gilbert} = \frac{\alpha}{\frac{\partial(2\pi f)}{\partial H}} \frac{\gamma}{M_S}(E_{\theta\theta} + \frac{1}{sin^2\theta_{eq}} E_{\varphi\varphi})$, which is angle dependent but reduced to $\frac{\alpha 2\pi f}{\gamma}$ for symmetry axes.
- $\Delta H_{mos} = \left|\frac{\partial H_{res}}{\partial \varphi_h}\right|_{res} \Delta\varphi_h$, where $\Delta\varphi_h$ is the average spread of easy axis anisotropy direction. This term is evaluated at the resonance. This contribution vanishes along the easy and hard axis directions.
- ΔH_{inh} reflects the inhomogeneous contribution to the linewidth due to local fluctuations such as roughness, thickness, local defects etc… It is frequency and angle dependent and its contribution is generally adjusted experimentally.
- ΔH_{2mag} is the 2 magnons contribution presented in chapter 2 section 2.5. This term is linear in frequency and angle dependent. It is more important in the easy axis than in the hard axis. It vanishes in the out of plane configuration.

An example of a complete treatment of the different term has been performed by Belmeguenai *et al.* on Co_2FeAl Heusler alloy [16 Belmeguenai]. An interesting feature of their work is that the damping constant α measured from the ΔH vs. f_{res} curves in the symmetry axes is of the form $\alpha + \frac{\Gamma_0}{H_{eff}}$, where α is the intrinsic damping constant and Γ_0 is a constant due to 2 magnons scattering. **Therefore, the values presented in our work must be seen as effective damping, and upper limits of the real intrinsic values of α.**

However one limitation of this treatment is that α is always considered as a constant and angular dependence of the linewidths is adjusted through a full set of constant parameters. In order to fit all these parameters it is necessary to have measurement of the linewidth vs. the out of plane angle θ_h which is not accessible with our set-up. It is also worth mentioning that a lower limit of α can be obtained from the measurement of ΔH vs. f_{res} in the out of plane configuration since the extrinsic broadening due to 2 magnons is avoided.

In conclusion, the measured values of the damping coefficient for the $L2_1$ phase are found to be better than most of the reported values up to now. Additional measurements are needed in order to state about the intrinsic value of the damping parameter and its possible anisotropic character. The variations of the linewidth amplitude as a function of the crystal directions are then accounted to come mainly from variations of the extrinsic contributions ΔH_0. This term is generally accounted for all the inhomogeneous contribution to the linewidth related to the structure of the material, *i.e.* from atomic dislocations to the mosaicity effect. It is worth noting that this constant seems to be always higher for easy axes than for hard axes, whatever the $L2_1$ or B2 order. We believe that this is due to the presence of the misfit dislocation array (see Figure 4.14 for example) in the [100] and [0$\bar{1}$0] directions of the CMS to relax the strain with the MgO substrate. These dislocations are sites for spin waves scattering leading to an increased extrinsic contribution to the linewidth. The large values of ΔH_0 seen for all measurements can be accounted also for the crystal inhomogeneity.

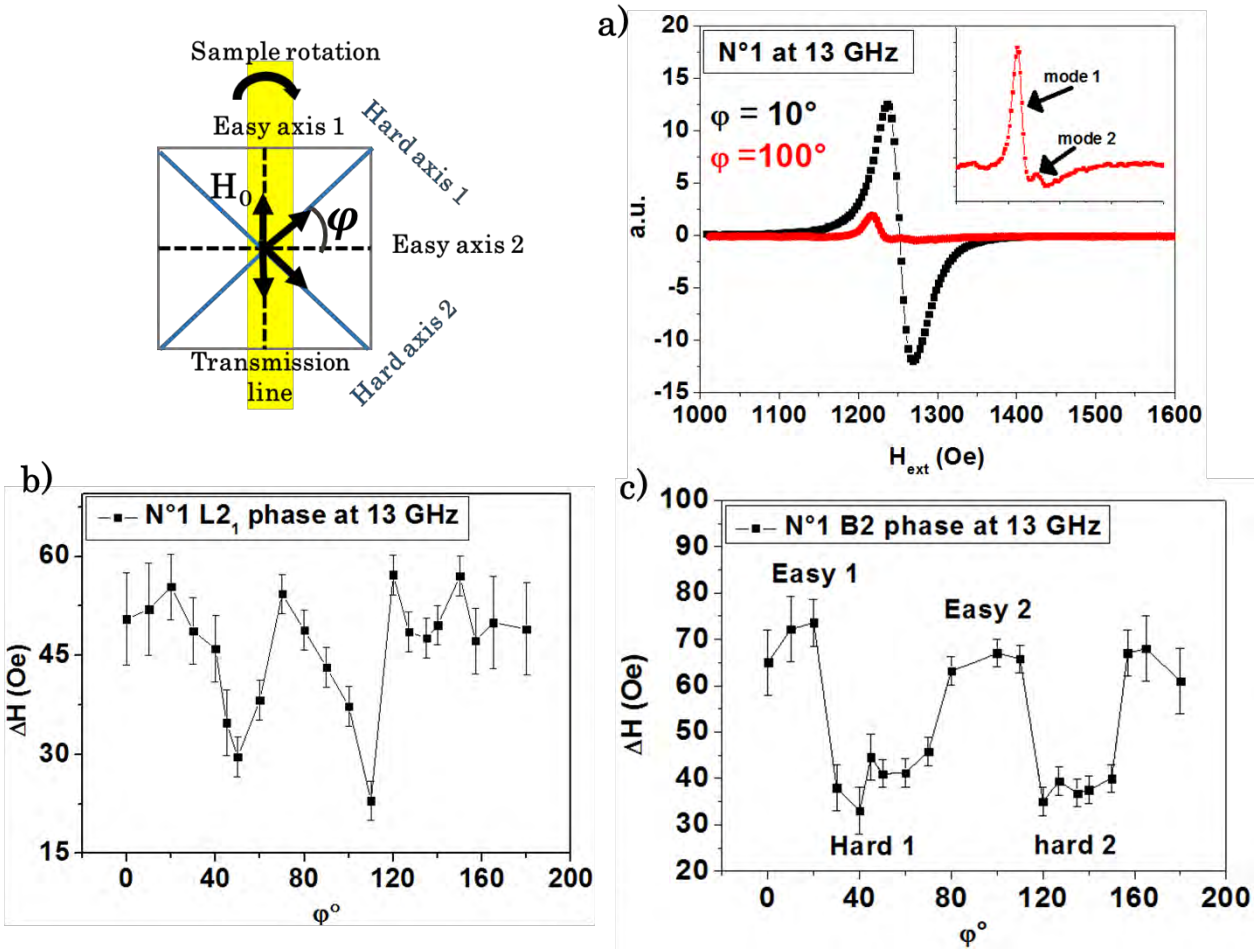

Figure 4.36: Sketch of the experimental configuration where the external field is rotated in the plane of the sample. In a), FMR spectra of sample N°1 at 10 and 100° from the easy axis 1 showing the decreasing amplitude of the signal when the applied external field gets perpendicular to the RF field. b) and c) corresponds to linewidths as a function of $\boldsymbol{\varphi}$ for $L2_1$ and B2 phases (experimental data are presented as points with connected lines to visualize the evolution of $\Delta\boldsymbol{H}$).

- **<u>Sample N°2:</u>**

The results of ΔH vs. f_{res} and ΔH vs. φ treatments are shown in figure 4.37-a) and 4.37-b. Even if the asymmetry of the FMR peak makes us believe that this sample also shows some inhomogeneity of the crystal order, we treated it as a single phase. However, the potential mixing of the different resonance peaks could be the origin of an overestimation of the linewidth and then of α.

Globally, the linewidths in the four crystal directions are quite similar, except for the hard axis 2 which shows the smallest α ($2.3*10^{-3}$). In addition, the highest α value is found for the other hard axis. All α values are found to be higher than for the $L2_1$ phase measured in sample N°1. This confirms that the $L2_1$ order is not the predominant phase in this sample and that the atomic disorder increases the average damping in the alloy.

Further insight can be found in the φ scan measurement performed at 20 GHz presented in Figure 4.37-b). Interestingly, the fourfold symmetry is recovered even if the symmetry of the curve is not perfect. This measurement does not completely reflects the evolution of the ΔH vs. f_{res} curves at 20 GHz in Figure 4.37-a. One possible explanation for this difference relies on the coupling between the magnetization and the RF field. Indeed if, as we believe, this sample shows some minority crystal order, the contribution to the signal of this one most probably vanishes with φ, leaving only the contribution of the main phase for angles different from 0° or 180°. However, this effect could explain the difference of linewidth amplitude between the two easy axes but not between the two hard axes, for which the orientation of the pumping field with respect to the magnetization is similar (45 and 135°).

Then we wonder if the difference observed in the φ scans reflect some magneto-mechanic coupling, in relation with the presence of the uniaxial anisotropy in the easy axis 2 direction. To validate this assumption it is necessary to reproduce the phi scan measurement starting from another crystal direction. For example, starting with the sample oriented in one hard direction, the two easy axes would be equivalently excited at 45° and 135° and so the effect of the minority crystal order on the linewidth will be equivalent. Unfortunately such measurements could not be performed on this sample before the end of this thesis.

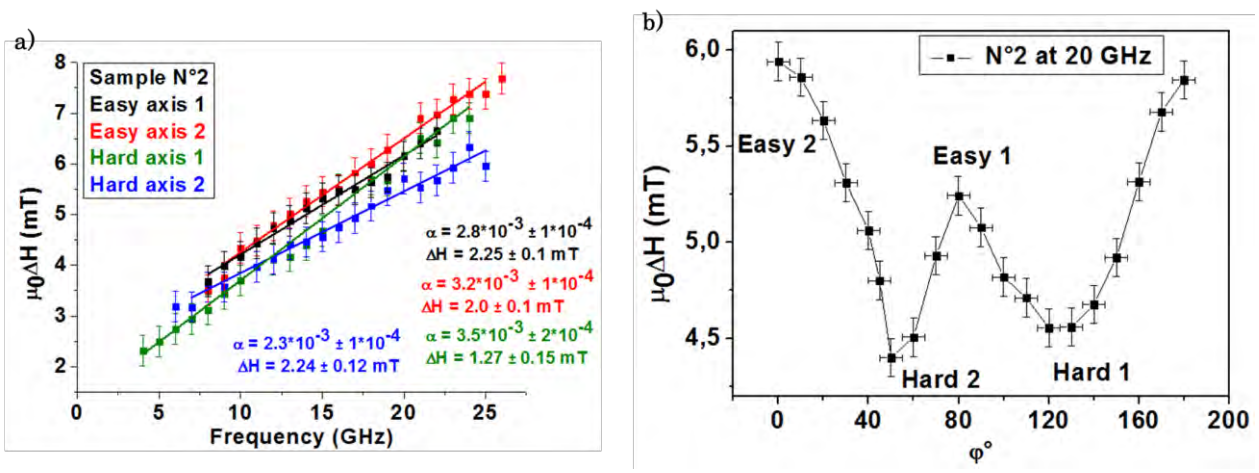

Figure 4.37: a) sample N°2 line width measurements as a function of the applied frequency along the two easy and hard axes with their corresponding damping coefficient $\boldsymbol{\alpha}$ and $\Delta\boldsymbol{H_0}$. b) Anguar dependence of the line width at 20 GHz. Experimental data are presented as squares. The line is a guide for the eyes.

In conclusion, the linewidth of this sample seems to be mainly governed by the chemical disorder in the matrix which increases the damping value as compared to the $L2_1$ order. However some differences in the damping value are observed as a function of the direction, for example between the two hard axis, and difference in the linewidth amplitudes are recovered in φ scans. As for the sample N°1, inhomogeneity contributions have most probably to be considered but additional magneto-mechanic effects could be at the origin of the observations. At this point we cannot discriminate between these different contributions.

- **<u>Sample N°3:</u>**

Results of the ΔH vs. f_{res} and ΔH vs. φ for sample N°3 are presented in figures 4.38-a,b and 4.38-c. φ scans have been performed starting either in an easy axis direction or in a hard axis direction.

The best α value is down to 1.9* 10^{-3}, which is very good taking into account the presence of a second minority crystal order, as shown in figures 4.34-a and 4.34-b. We clearly observe that the linewidth amplitudes for the easy axes are higher than for the hard axes. It appears that both the damping and the extrinsic contributions ΔH0 are always higher for easy axes than for hard axes. For the ΔH0, we assume that it comes from the organization of the lattice mismatch as proposed for the sample N°1.Then this sample seems to exhibit an anisotropic behavior of its linewidth and a possible cubic anisotropy of the damping parameter.

We notice that the values of the linewidth and of the damping are very close for the two hard directions. Then it seems that no correlation appears between the uniaxial anisotropy (aligned with the hard axis 1) and the linewidth in the hard axes. However we observe some difference of the linewidth and of the damping coefficient between the two easy axes (considering the uncertainty of the calculation of α from the dispersion of the experimental values of ΔH)[1]. This behavior is also recovered in the φ scans performed at 13 GHz presented in figure 4.38 b and c. To verify that the difference of linewidth between the two easy axis in the φ scans in 4.38 b were not related to the variation of the amplitude of the pumping field with φ, we did the same experiment starting with the sample oriented in a hard axis direction (4.38 c), allowing for the same amplitude of the excitation field for both easy axis. The clear fourfold symmetry is recovered in each case, with a pronounced difference between the two easy axes.

Then it is clear that this sample shows an anisotropic behavior of its linewidth and we believe that it is also the case for the damping coefficient. In any case our result is not in agreement with other reported work. First, we find that the damping is lower for the hard axes directions than for the easy axes directions, in opposite to the work of Yilgin *et al*. In addition, we believe that the damping coefficient for the two easy directions is slightly different. As for sample N°2, we wonder if magneto mechanic effects could be at the origin of this behavior. Indeed, a clear difference in the damping value of the two hard axes was observed for sample N°2 when the uniaxial anisotropy was aligned with an easy axis. For the sample N°3 the situation is inversed as the difference of damping is observed in the easy axes when the uniaxial anisotropy is aligned with a hard axis.

[1] Let's note that one source of dispersion of the experimental points for the determination of the linewidth in the easy axis 2 direction comes from the mixing of the $L2_1$ majority mode and the minority one.

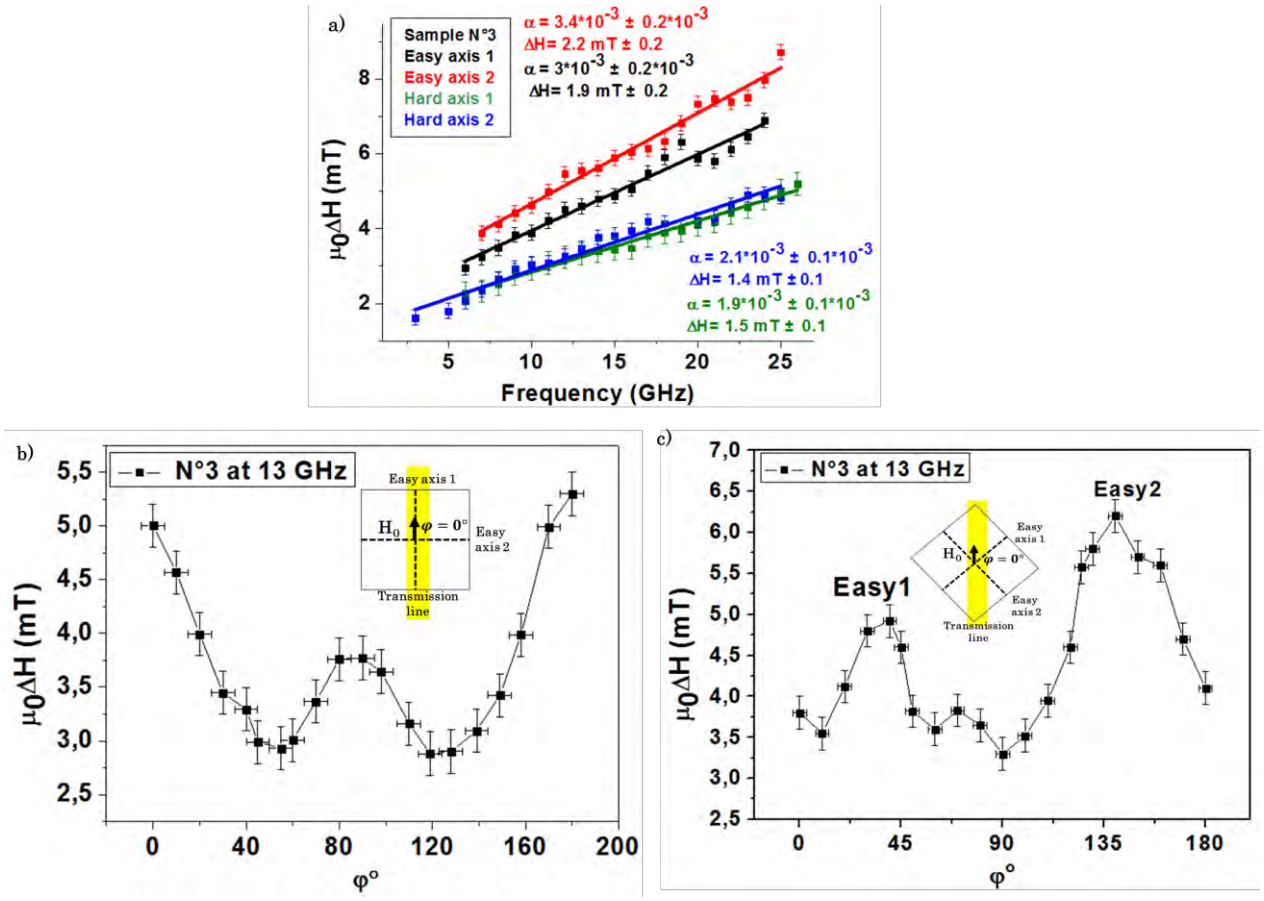

Figure 4.38: a) sample N°3 linewidth measurements as a function of the resonance frequency along the four magnetic directions. Figures b) and c) show the line width values (experimental data are presented as points with connected lines to visualize the evolution of $\Delta \boldsymbol{H}$) as a function of φ at 13 GHz starting from easy and hard axis, respectively.

At the end of this section, a summary of the extracted relaxation parameters for the three samples is given in the following table.

Sample	Easy axis1	Easy axis 2	Hard axis 1	Hard axis 2
N°1 Phase $L2_1$ Phase B2	$\boldsymbol{\alpha} = (2.1\pm\mathbf{0.1})*10^{-3}$ $\boldsymbol{\Delta H_0} = \mathbf{2.1\ mT}$ –	$\boldsymbol{\alpha} = (1.5\pm\mathbf{0.3})*10^{-3}$ $\boldsymbol{\Delta H_0} = \mathbf{3.1\ mT}$ $\alpha = (3.2\pm0.1)*10^{-3}$ $\Delta H_0 = 4.1$ mT	– $\boldsymbol{\alpha} = (2.6\pm\mathbf{0.1})*10^{-3}$ $\boldsymbol{\Delta H_0} = \mathbf{1.6\ mT}$	$\boldsymbol{\alpha} =(1.6\pm\mathbf{0.1})*10^{-3}$ $\boldsymbol{\Delta H_0} = \mathbf{1.6\ mT}$ $\alpha = (2.8\pm0.1)*10^{-3}$ $\Delta H_0 = 1.8$ mT
N°2	$\boldsymbol{\alpha} = (2.8\pm\mathbf{0.1})*10^{-3}$ $\boldsymbol{\Delta H_0} = \mathbf{2.3\ mT}$	$\boldsymbol{\alpha} = (3.\mathbf{2} \pm \mathbf{0.1})*10^{-3}$ $\boldsymbol{\Delta H_0} = \mathbf{1.9\ mT}$	$\boldsymbol{\alpha} = (3.5\pm\mathbf{0.1})*10^{-3}$ $\boldsymbol{\Delta H_0} = \mathbf{1.3\ mT}$	$\boldsymbol{\alpha} = (2.3\pm\mathbf{0.1})*10^{-3}$ $\boldsymbol{\Delta H_0} = \mathbf{2.4\ mT}$
N°3	$\boldsymbol{\alpha} = (3\pm\mathbf{0.1})*10^{-3}$ $\boldsymbol{\Delta H_0} = \mathbf{1.9\ mT}$	$\boldsymbol{\alpha} = (3.4\pm\mathbf{0.1})*10^{-3}$ $\boldsymbol{\Delta H_0} = \mathbf{2.2\ mT}$	$\boldsymbol{\alpha} = (1.9\pm\mathbf{0.1})*10^{-3}$ $\boldsymbol{\Delta H_0} = \mathbf{1.5\ mT}$	$\boldsymbol{\alpha} =(2.1\pm\mathbf{0.1})*10^{-3}$ $\boldsymbol{\Delta H_0} = \mathbf{1.4\ mT}$

Table 4.7: damping factor $\boldsymbol{\alpha}$ and extrinsic line width $\boldsymbol{\Delta H_0}$ values for both the two easy and hard axes of the three samples N°1, N°2 and N°3.

4.3 Conclusion

In conclusion of this chapter, we demonstrated that our films present several characteristics.

- First, the sample N°1 and N°3 present two crystal orders. For the sample N°1 the two phase corresponds to the $L2_1$ and B2 order phases, the first being majority. This is confirmed by HAADF-STEM analysis which also shows a complete relaxation of our sample by the presence of misfit dislocation at the interface between the CMS layer and the MgO substrate. The $L2_1$ order has also been found to be the main phase in sample N°3. However a second resonance peak observed in FMR let us think that a minority B2 order is also present in this sample. Finally a small amount of Co-Si exchange (4 to 6 %) is found for these two samples.
- The situation of the sample N°2 is different. While the presence of $L2_1$ order has been observed by X-ray, it is not the main phase in the material. Unfortunately we could not perform structural analysis on this series of samples. However, the smaller amplitude of the magnetization as compared to the other samples let us think that Co/Mn and or Co/Si disorder is more important than for the two other samples.
- MOKE measurements have shown small coercive fields of about 1 mT for the reference samples of series N°1 and N°2. The switching process has been assumed to arise from the propagation of either cross tie or 90° domain walls depending on the orientation of the applied field with respect to the easy axis.

- MOKE and FMR measurements have shown that all samples exhibit a cubic anisotropy as expected, with an additional uniaxial anisotropy which can be aligned either with an easy or a hard axis. The amplitude of the cubic anisotropy is few tens of mT. These values are higher than the one reported in literature but in agreement with our previous study [11 Ortiz]. The amplitude of the uniaxial anisotropy varies from a few tenth to 2 mT. While the origin of this uniaxial anisotropy is still under debate, we attribute it to the tetragonal distortion of the cell observed by X-ray diffraction.
- FMR measurements allowed extracting the static and dynamic magnetic parameters of the samples. The magnetization, or magnetic moment, is found to be in good agreement with the expected value of $L2_1$ or B2 order for samples N°1 and N°3. The small discrepancies with respect to theoretical predictions are accounted to the presence of Co/Si exchange.
- The exchange constant value is in agreement with reported values except for sample N°2, for which the disorder on Co sites is believed to be responsible of the decrease magnetization and exchange values. Further investigation, for example via Brillouin Light Scattering measurement, would be necessary to determine if it is really the exchange value constant which is lower than other samples or if it is related to a modification of the pinning constant due, for example, to surface effect.
- The gyromagnetic ratio is found to be 28.7 GHz/T, leading to a g value of 2.05, showing a small magnetic contribution from orbital moment.
- FMR linewidth studies as a function of the frequency or angle φ has been carried out. Based on other works, the values of the damping coefficient obtained in our samples are believed to be upper limits to the intrinsic damping. This is due to inhomogeneity contributions and 2 magnons scattering. The best value of the measured α is $1.6*10^{-3}$, which is to our knowledge close from the best values reported in CMS. In most cases the best α values are found in hard axis directions, unlike other work reported in literature.
- ΔH vs. $f$res and ΔH vs. φ measurements let us think for some anisotropic behavior of the linewidth for all samples. However, experimental conditions, especially mixing modes, leads to strong uncertainty of the measurement. Further analytical analysis, especially taking into account the mosaicity of the sample and the two magnon processes, is needed to conclude on this point and especially on an eventual anisotropy of the damping coefficient.

Chapter 4 References:

[1] G. Ortiz Hernandez, « Elaboration et étude des propriétés physiques de couches minces monocristallines d'alliage de Heusler à faible amortissement magnétique pour composants hyperfréquences », Université de Toulouse, Université Toulouse III-Paul Sabatier, 2013.

[2] O. Gaier, « A study of exchange interaction, magnetic anisotropies, and ion beam induced effects in thin films of Co2-based Heusler compounds », Ph. D. dissertation, Technical University of Kaiserslautern, 2009.

[3] H. Pandey, P. C. Joshi, R. P. Pant, R. Prasad, S. Auluck, et R. C. Budhani, « Evolution of ferromagnetic and spin-wave resonances with crystalline order in thin films of full-Heusler alloy Co2MnSi », *J. Appl. Phys.*, vol. 111, nº 2, p. 023912, janv. 2012.

[4] M. Belmeguenai, F. Zighem, D. Faurie, H. Tuzcuoglu, S.-M. Chérif, P. Moch, K. Westerholt, et W. Seiler, « Structural and magnetic properties of Co2MnSi thin films », *Phys. Status Solidi A*, vol. 209, nº 7, p. 1328‑1333, juillet 2012.

[5] P. J. Webster, « Magnetic and chemical order in Heusler alloys containing cobalt and manganese », *J. Phys. Chem. Solids*, vol. 32, nº 6, p. 1221‑1231, 1971.

[6] V. Niculescu, K. Raj, T. J. Burch, et J. I. Budnick, « Correlation of the internal fields, magnetic moments, and site preferences in Fe 3- x Mn x Si alloys », *Phys. Rev. B*, vol. 13, nº 7, p. 3167, 1976.

[7] Y. Takamura, R. Nakane, et S. Sugahara, « Quantitative analysis of atomic disorders in full-Heusler Co[sub 2]FeSi alloy thin films using x-ray diffraction with Co Kα and Cu Kα sources », *J. Appl. Phys.*, vol. 107, nº 9, p. 09B111, 2010.

[8] D. T. Cromer, « Compton Scattering Factors for Spherically Symmetric Free Atoms », *J. Chem. Phys.*, vol. 47, nº 6, p. 1892, 1967.

[9] C. H. MacGillavry, G. D. Rieck, et International Union of Crystallography, *International tables for X-ray crystallography. Vol. 3, Vol. 3,*. Birmingham: Published for the International Union of Crystallography by the Kynoch Press, 1968.

[10] T. Mewes, « Separation of the first- and second-order contributions in magneto-optic Kerr effect magnetometry of epitaxial FeMn/NiFe bilayers », *J. Appl. Phys.*, vol. 95, nº 10, p. 5324, 2004.

[11] G. Ortiz, A. García-García, N. Biziere, F. Boust, J. F. Bobo, et E. Snoeck, « Growth, structural, and magnetic characterization of epitaxial Co2MnSi films deposited on MgO and Cr seed layers », *J. Appl. Phys.*, vol. 113, nº 4, p. 043921, 2013.

[12] L. McGuigan, R. C. Barklie, R. G. S. Sofin, S. K. Arora, et I. V. Shvets, « In-plane magnetic anisotropies in Fe 3 O 4 films on vicinal MgO(100) », *Phys. Rev. B*, vol. 77, nº 17, mai 2008.

[13] J. Chen et J. L. Erskine, « Surface-step-induced magnetic anisotropy in thin epitaxial Fe films on W(001) », *Phys. Rev. Lett.*, vol. 68, nº 8, p. 1212‑1215, février 1992.

[14] T. Leeb, M. Brockmann, F. Bensch, S. Miethaner, et G. Bayreuther, « In-plane magnetic anisotropies in Fe films on vicinal Ag(001) and Au(001) surfaces », *J. Appl. Phys.*, vol. 85, nº 8, p. 4964‑4966, avr. 1999.

[15] A. A. Baker, A. I. Figueroa, G. van der Laan, et T. Hesjedal, « Tailoring of magnetic properties of ultrathin epitaxial Fe films by Dy doping », *AIP Adv.*, vol. 5, nº 7, p. 077117, juill. 2015.

[16] M. Belmeguenai, H. Tuzcuoglu, M. S. Gabor, T. Petrisor, C. Tiusan, D. Berling, F. Zighem, T. Chauveau, S. M. Chérif, et P. Moch, « Co2FeAl thin films grown on MgO

substrates: Correlation between static, dynamic, and structural properties », *Phys. Rev. B*, vol. 87, nº 18, p. 184431, mai 2013.

[17] H. Pandey, P. K. Rout, Anupam, P. C. Joshi, Z. Hossain, et R. C. Budhani, « Magnetoelastic coupling induced magnetic anisotropy in Co_2(Fe/Mn)Si thin films », *Appl. Phys. Lett.*, vol. 104, nº 2, p. 022402, janv. 2014.

[18] M. Belmeguenai, F. Zighem, T. Chauveau, D. Faurie, Y. Roussigne, S. M. Cherif, P. Moch, K. Westerholt, et P. Monod, « Structural, static and dynamic magnetic properties of Co2MnGe thin films on a sapphire a-plane substrate », *J. Appl. Phys.*, vol. 108, nº 6, p. 063926‑063926‑6, sept. 2010.

[19] P. E. Wigen, C. F. Kooi, M. R. Shanabarger, et T. D. Rossing, « Dynamic Pinning in Thin-Film Spin-Wave Resonance », *Phys. Rev. Lett.*, vol. 9, nº 5, p. 206‑208, sept. 1962.

[20] R. Yilgin, Y. Sakuraba, M. Oogane, S. Mizukami, Y. Ando, et T. Miyazaki, « Anisotropic intrinsic damping constant of epitaxial Co2MnSi Heusler alloy films », *Jpn. J. Appl. Phys.*, vol. 46, nº 3L, p. L205, 2007.

[21] O. Gaier, J. Hamrle, S. J. Hermsdoerfer, H. Schultheiß, B. Hillebrands, Y. Sakuraba, M. Oogane, et Y. Ando, « Influence of the L21 ordering degree on the magnetic properties of Co_2MnSi Heusler films », *J. Appl. Phys.*, vol. 103, nº 10, p. 103910, mai 2008.

[22] B. Rameev, F. Yildiz, S. Kazan, B. Aktas, A. Gupta, L. R. Tagirov, D. Rata, D. Buergler, P. Gruenberg, C. M. Schneider, S. Kämmerer, G. Reiss, et A. Hütten, « FMR investigations of half-metallic ferromagnets », *Phys. Status Solidi A*, vol. 203, nº 7, p. 1503‑1512, mai 2006.

[23] J. Hamrle, O. Gaier, S.-G. Min, B. Hillebrands, Y. Sakuraba, et Y. Ando, « Determination of exchange constants of Heusler compounds by Brillouin light scattering spectroscopy: application to Co_2MnSi », *J. Phys. Appl. Phys.*, vol. 42, nº 8, p. 084005, avr. 2009.

[24] L. Ritchie, G. Xiao, Y. Ji, T. Y. Chen, C. L. Chien, M. Zhang, J. Chen, Z. Liu, G. Wu, et X. X. Zhang, « Magnetic, structural, and transport properties of the Heusler alloys Co 2 MnSi and NiMnSb », *Phys. Rev. B*, vol. 68, nº 10, sept. 2003.

[25] C. Liu, C. K. A. Mewes, M. Chshiev, T. Mewes, et W. H. Butler, « Origin of low Gilbert damping in half metals », *Appl. Phys. Lett.*, vol. 95, nº 2, p. 022509, 2009.

[26] S.-Z. Qiao, J. Zhang, Y.-F. Qin, R.-R. Hao, H. Zhong, D.-P. Zhu, Y. Kang, S.-S. Kang, S.-Y. Yu, G.-B. Han, S.-S. Yan, et L.-M. Mei, « Structural and Magnetic Properties of Co_2 MnSi Thin Film with a Low Damping Constant », *Chin. Phys. Lett.*, vol. 32, nº 5, p. 057601, mai 2015.

[27] S. Andrieu, A. Neggache, T. Hauet, T. Devolder, A. Hallal, M. Chshiev, A. M. Bataille, P. Le Fèvre, et F. Bertran, « Direct evidence for minority spin gap in the Co_2MnSi Heusler alloy », *Phys. Rev. B*, vol. 93, nº 9, p. 094417, mars 2016

Chapter 5: Effect of He^+ ions irradiation on structural and magnetic properties of CMS Heusler alloys

In this chapter we investigate the effect of He^+ ion irradiation on structural and magnetic properties of the three studied CMS samples presented in chapter 4 as follows:

- **Samples of series N°1**: the same substrate has been cut in 4 equivalent pieces of 5 x 5 mm². One is the reference sample presented in chapter IV and the three others have been irradiated at fluences of $1*10^{15}$, $5*10^{15}$ and $1*10^{16}$ ions/cm². The structural properties of this series of samples have been studied by X-ray diffraction for the four samples and by HAADF-STEM for the reference and $1*10^{16}$ irradiated samples. The magnetic properties have been studied by MOKE for the reference and $1*10^{16}$ irradiated samples and by FMR and PPMS magnetometry for the four samples.

- **Sample of series N°2:** this series of samples have been cut into 6 pieces of 3 x 3 mm². One piece is the reference sample presented in chapter IV. The irradiation doses for the other samples are $1*10^{14}$, $1*10^{15}$, $4*10^{15}$, $1.2*10^{16}$ and $1*10^{17}$ ions/cm². X-ray diffraction φ scan measurement was only performed on the reference sample to check the existence of $L2_1$ phase, even with a weak signal, by CEMES Co source diffractometer (Figure 4.9). Thus, we were not able to conduct a quantitative study of the atomic disorder on this series. The magnetic properties have been studied by MOKE for the reference sample and by FMR for all samples.

- **Sample of series N°3**: This series of samples have been cut into 5 pieces of 3 x 3 mm². One piece is the reference sample presented in chapter IV. The irradiation doses for the other samples are $1*10^{14}$, $1*10^{15}$, $1*10^{16}$ and $1*10^{17}$ ions/cm². X-ray diffraction measurements with Cu source has been performed on the reference, $1*10^{16}$ and $1*10^{17}$ irradiated samples. HAADF-STEM analysis have been performed on the reference and $1*10^{17}$ irradiated samples. The magnetic properties have been studied only by FMR for all the samples.

The different results obtained for the reference samples of the three series have been presented in the previous chapter. In this chapter we will begin with the simulations of the effect of irradiation with He+ ions on the structural disorder of the CMS. Then we will present

the structural analysis performed by X-ray diffraction and HAADF-STEM on series N°1 and N°3. The last part of this chapter will focus on the evolution of the magnetic parameters induced by the irradiation, with respect to the structural modifications.

5.1 Irradiation with Helium ions (He^+) at 150 keV

In the present thesis, the species used for ion irradiation is helium ions. The main goal of using light ions, such as He^+, was to investigate how the introduction of a controlled disorder is possible to promote the advent of partially disordered phases. Moreover, the high kinetic energy is chosen to first avoid He^+ implantation in the CMS layer and also to minimize local defects at low doses. Indeed, ion irradiation can be considered in a very simplified approach to act as an annealing process for low doses which can lead to structural improvement. He^+ ions irradiation has been used in previous work done by [1-3 Fassbender] to modify the magnetic properties of Pt-Co system, resulting from ion-induced interfacial mixing. Also, an enhancement of chemical ordering and long-range order $L1_0$ in FePt and FePd thin films by 130 KeV He^+ irradiation was reported by Ravelosona *et al.*[4,5 Ravelosona]. Based on the mentioned magnetic and structural properties presented in the previous chapter, Ion irradiation of high energy (150 KeV) of different fluences doses range from 10^{14} to 10^{17} ions/cm^2 will impact our CMS thin films

In our experiments we focused our work on a Co_2MnSi layer with a thickness of 42 and 50 nm. Prior to the experiment, the irradiation process was simulated using either the well-known SRIM software (Stopping and Range of Ions in Matter) or a homemade IPROS code [6-8]. These softwares are based on Monte-Carlo binary collision process. From the output results, it is then possible to estimate the Helium range and the concentration distribution of displaced atoms in the ternary layer.

The starting point of the calculation was to reduce as much as possible the presence of helium atoms in the Heusler layer and for this reason an energy of 150 keV was chosen. In the following section the results of the simulation will be analyzed.

5.1.1 Simulation of Co_2MnSi irradiation with He^+ ions

Prior to ion irradiation, the appropriate parameters to predict the helium distribution as well as the damage impact of the bombardment on the structural properties of the Heusler layer were carried out. For this purpose, simulations of the irradiation process were performed using Monte-Carlo binary collision softwares [6-8].

In the case of He^+ irradiation of Co_2MnSi two criteria must be fulfilled: (i) a low concentration of helium atoms in the active layer and (ii) a low defect density induced by ion bombardment. These are the major conditions to ensure a suitable improvement of the structural and magnetic properties of the Heusler layer, at least for low fluences. To perform this work an atomic density of 8.85x1022 atoms/cm^3 for the Heusler film was used and about 300000 incoming He ions with an energy of 150 keV were launched.

Figure 5.1 shows the simulated Helium concentration profile as a function of depth for a fluence of $1x10^{14}$ ions/cm^{-2}. Let's keep in mind that the CMS layer of 42 or 50 nm thickness

is deposited on MgO substrate and covered by a capping layer of MgO (10 nm) to prevent oxidation. The simulation was performed for the CMS monolayer of stoichiometric composition (50% Co, 25% Mn and 25 % Si atoms). From figure 5.1, we have deduced the projected range Rp=486 nm of helium in CMS layer. The profile clearly shows that the peak of the implantation concentration is located in the MgO substrate and that the depth at which most of the ions stopped in the sample is far below the CMS layer. In figure 5.2 the He ion concentration was plotted in log scale for 3 increasing fluences. The figure shows that in the CMS region the concentration of He is about 0.1% of the peak value and may be considered as negligible.

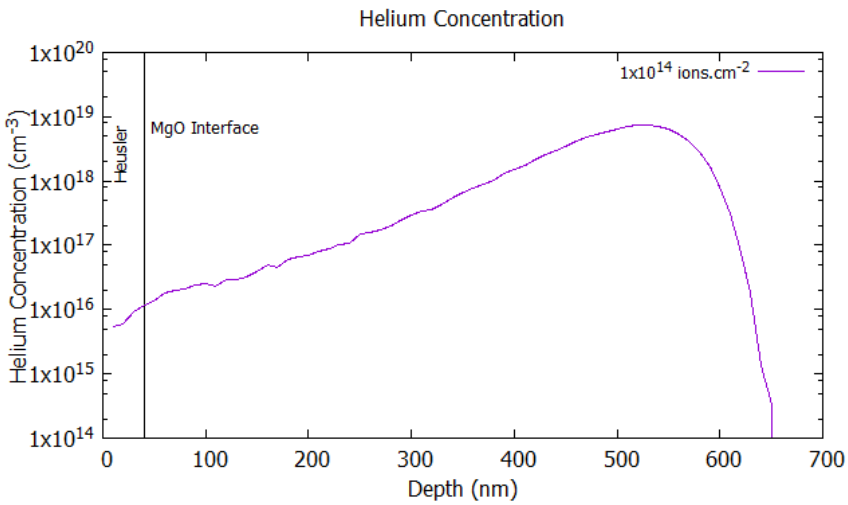

Figure 5.1: Helium concentration as a function of depth.

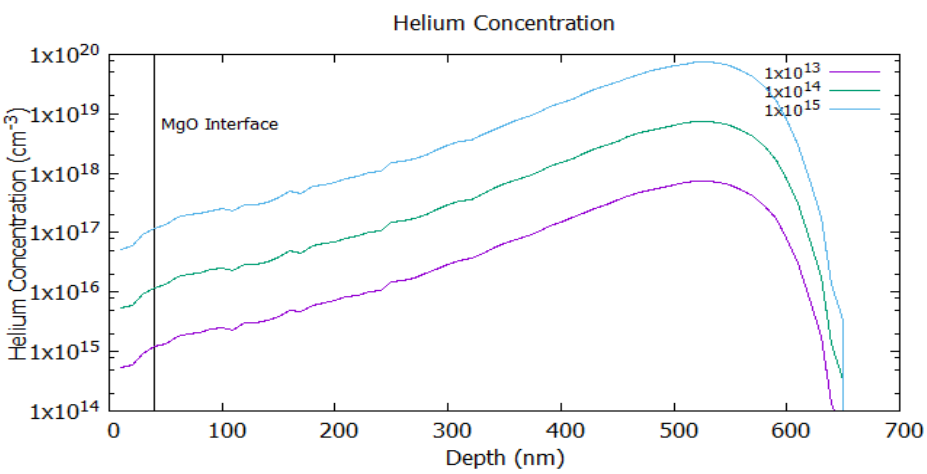

Figure 5.2: distribution of different concentration doses of He^+ ions at 150 KeV as a function of CMS layer depth.

In order to estimate the number of defects created along the helium ion trajectory, we plotted in figure 5.3 the vacancy concentration of each element of the CMS film as a function of depth. The total damage introduced into the crystal lattice at a particular fluence of $1x10^{14}$ ions/cm^2 can be estimated taking into account that most displacements resulted in creation of Frenkel

pairs the majority of which instantly recombines leaving only about less than 10% of surviving vacancies [9 Bernas]. We can notice that in this case the remaining vacancy density is in the range of 10^{19} cm^{-3} either for Si, Co or Mn. Then finally the experimental fluence was varied from $1x10^{14}$ up to $1x10^{17}$ ions/cm^2.

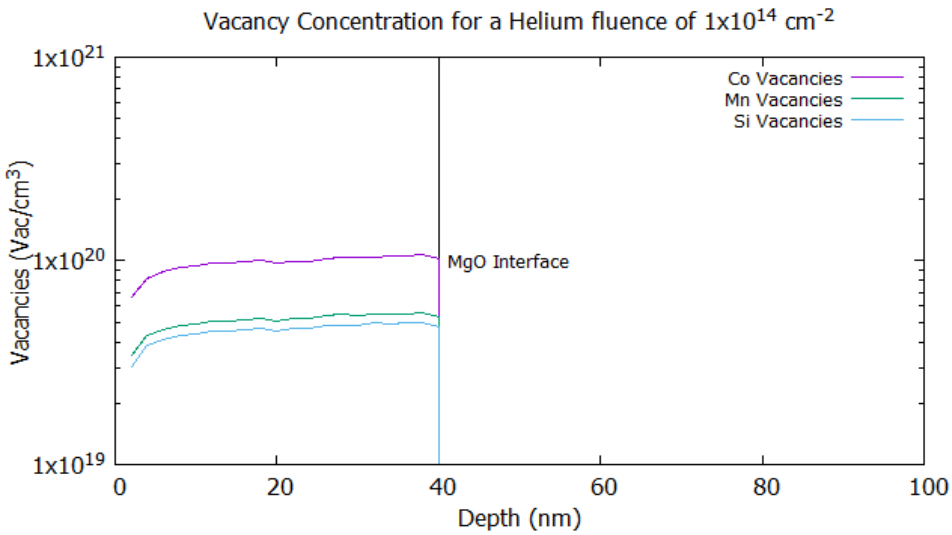

Figure 5.3: Vacancy concentration as depth or Vacancy concentration of Co,Mn and Si for 10^{14} ions/cm^2 at the Mgo/CMS interface.

5.2 Induced atomic disorder by X-ray diffraction and STEM

Sample N°1 series:

The effect of ion irradiation on the atomic disorder of Heusler alloy has been studied with the same methodology as presented in chapter IV for the reference samples. A complete study has been performed with Cu and Co source on the four samples of N°1 series.

Examples of the diffraction pattern recorded as a function of either Co or Cu sources for the different peaks of interest are summarized in figure 5.4. For each sample the calibration of the peak position is performed on its corresponding MgO peak. Therefore, we do not consider any deformation in the MgO under irradiation. This assumption is supported by the fact that He^+ ions are stopped at several hundreds of nanometer away from the interface. We assume a constant value of the MgO lattice parameter at the interface with the CMS.

The first observation is that the (111) diffraction peak is still observable for fluences up to 10^{16} ions/cm^2 meaning that either the $L2_1$ (or $D0_3$) order is still present in the material. We also observe a global decrease of the intensity peak as the fluence increase, which goes along an increased linewidth. This is typical for the presence of local defects such as vacancies created by the collision cascade of He^+ ions.

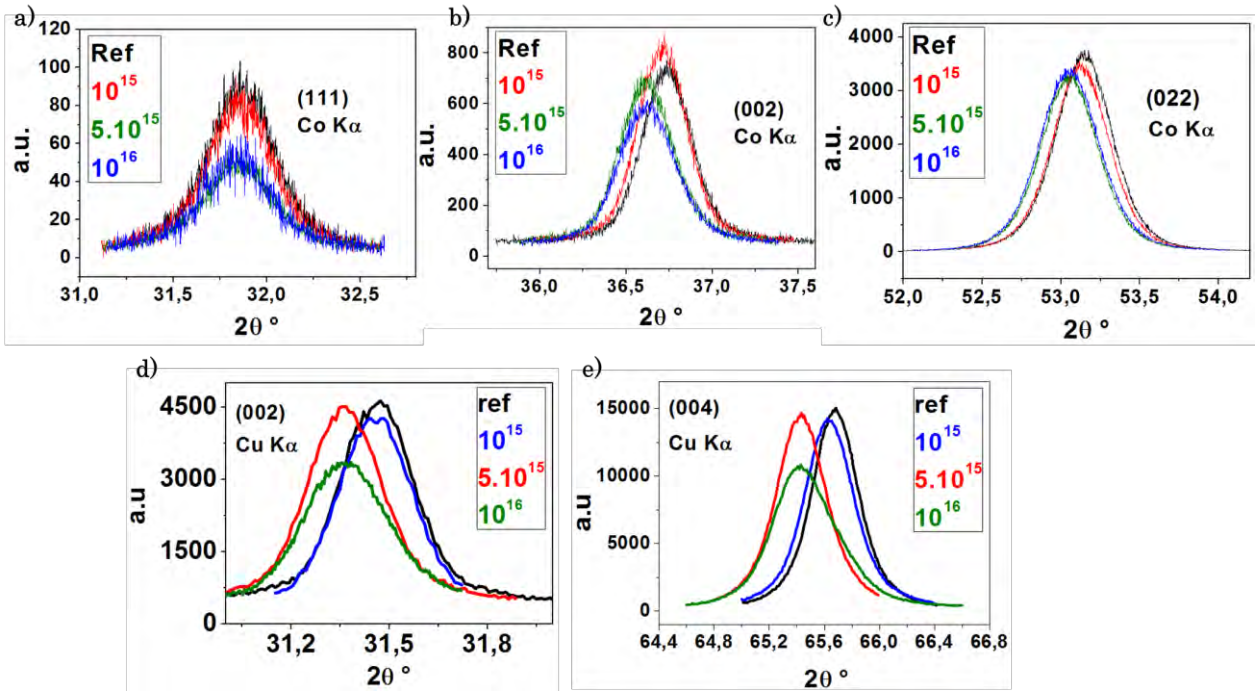

Figure 5.4: X-ray diffraction 2$\boldsymbol{\theta}$ scan for reference and 3 irradiated samples of N°1 for Co and Cu diffractometer sources. a), b) and c) represents the 111,002 and 022 peaks acquired by Co source. d) and e) presents the 002 and 004 peaks acquired by Cu source.

Interestingly, we also observe with both sources a shift in the (002) diffraction peak towards low angles compared to the reference sample peak position, indicating an increase of the out-of-plane lattice parameter of CMS with the increase of ion fluence. With the Co source, we also observe a shift in the (022) diffraction peak while the (111) peak is kept almost at the same Bragg angle (from 31.86° to 31.83°). Calculating the lattice parameters (table 5.1) from the 2$\boldsymbol{\theta}$ Bragg angle of the three peaks with the Co source, we find that only the out-of-plane lattice parameter **c** varies from 5.67 Å for the reference sample to 5.69 Å for the 5.10^{15} and 10^{16} ions/cm² irradiated sample, while the in-plane parameter is kept constant and equals to 5.63 Å. Same values of the **c** parameters are obtained from the diffraction peaks with the Cu source. Then the most obvious conclusion of this observation is that the irradiation induces a tetragonal distortion of the cell but then the volume of the cell is not kept constant with respect to the reference sample.

GPA analysis performed on HAADF-STEM images obtained from the sample irradiated at 10^{16} ions/cm² have shown similar values of strain deformation as for the reference sample. An example of strain calculation is shown in Figure 5.5. As for the sample reference, we found the out of plane strain of the order of 34 ± 1.5% with respect to the MgO, and no particular additional strain effect is observed as compared to the reference sample. This is not surprising. Indeed, the strain in the CMS layer is calculated with respect to the MgO. The difference of out-of-plane lattice parameter measured by X-ray for the CMS would lead theoretically to a change in the strain with respect to the MgO from $\boldsymbol{\varepsilon_{zz}}$ = 34.6% to 35%, so the variation is below the uncertainty of the *GPA* analysis. For the in plane deformation, which is supposed to be constant according to the X-ray diffraction, we found an average value

for the irradiated sample of ε_{xx} = -5.1 ± 0.4 %. This is slightly higher than for the reference sample. This could be due to an eventual modification of the MgO parameters under irradiation. However the observed difference between the reference sample and the irradiated one is also of the order of the experimental uncertainty. Then, we believe that *GPA* analysis is not sensitive enough to detect such small variations of strain induced by the ion irradiation as the experimental uncertainty is of the order of the expected variation.

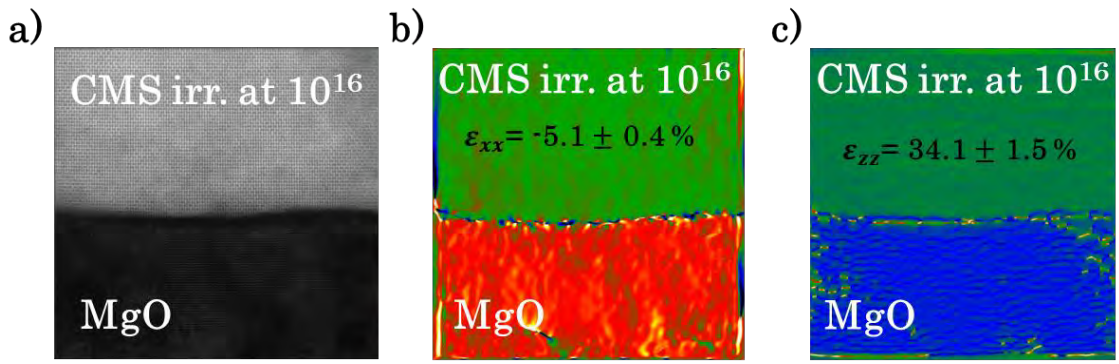

Figure 5.5: GPA analysis performed on sample N°1 irradiated at 10^{16} ions/cm^2 shows the in-plane and out-of-plane deformation of -5.1 ±0.4 and 34.1 ±1.5, respectively.

	REF (Å)	10^{15} (Å)	$5*10^{15}$ (Å)	$1*10^{16}$ (Å)
a	5.63	5.63	5.63	5.63
c	5.67	5.68	5.69	5.69

Table 5.1: lattice parameter of sample N°1 reference and irradiated ones as a function of the ion fluence.

In order to determine the different disorder parameters for the four series of sample N°1, the same methodology presented in chapter IV is used for the reference sample. The results for the deduced α, β and γ are presented in figure 5.6. For all samples, we observe that the β parameter, i.e. Co/Si disorder, remains almost constant (0.04 ± 0.02) whatever the ion fluence is used. Additionally α increases from 0.14 ± 0.01 to 0.22 ± 0.01 for the reference sample and the 10^{16} irradiated one, respectively. There is a clear step at $5*10^{15}$ for α. Similarly the γ parameter, *i.e.* Co/Mn disorder, increases significantly for fluences above $5*10^{15}$. For lower fluences, the Co-Mn substitution (γ) is not detectable within the uncertainty of the measurements, meaning it is less than 0.02.

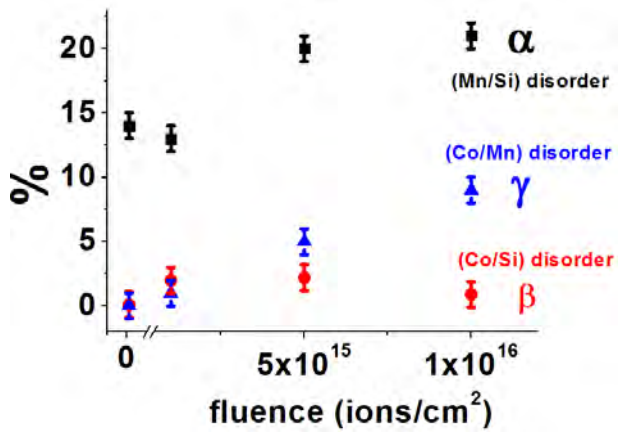

Figure 5.6: ***α, β and γ*** atomic disorder percentage of sample N°1 series as a function of the irradiated fluences used.

In order to state about the organization of the induced atomic disorder observed by X-Ray diffraction, HAADF-STEM has been performed on the sample irradiated at 10^{16} ions/cm².

While the B2 order in the reference sample is only observed in small regions of similar size as the black box in Figure 4.13-a in chapter IV, it can be observed in more extended areas for a fluence of 10^{16} ions/cm². This is shown in Figure 5.7-a. The B2 order can be observed either from the intensity profile presented in Figure 5.7-b corresponding to the lines in figure 5.7-a or statistically over the selected area (black box in figure 5.7-a as shown in figure 5.7-c). Similar values for the STEM intensity of the Mn and Si columns are measured while the intensity corresponding to the Co columns remains higher[2]. On other part of the sample we still observe the $L2_1$ order (Figure 5.7-d). Based on this result and in addition to the observed increase of the α parameter, we suggest that ion irradiation induces a $L2_1$ to B2 transformation in this sample. Moreover we suggest that the transformation occurs around the initial B2 grains.

Dealing with the increase Co-Mn exchange, we already mentioned that HAADF-STEM is not sensitive to this atomic exchange as the Z numbers of both atoms are very close. Therefore, it is difficult to state about either $D0_3$ grains grow in the initial matrix or if this atomic exchange occurs as punctual defects in the entire alloy, including in the B2 phase. This issue can be addressed via magnetization amplitude measurements with PPMS. Indeed we show in Figure 5.12 that the decrease of the magnetization observed for the alloy is in agreement with a model in which we consider a B2 order with magnetization 1.25 T and a L21'[3] phase with decreasing magnetization. With this model, the calculation of the average magnetization is done considering a volume of the B2 phase proportional to $\alpha/0.5$ (α = 0.5 corresponding to a full B2 order) and a L21' phase proportional to $1-\alpha/0.5$. The result of the calculation for the magnetization of this $L2_1$' phase is presented in table 5.2. The obtained

[2] Note here that the denotation Mn and Si does not have a real signification as we are not able to distinguish the two elements. Then we arbitrarily set the first atomic column in blue to be the Mn and the red to be the Si in figure 5.7-a. We did the same denotation in figure 5.9-a.

[3] The denotation $L2_1$' is proposed in order to remind that the initial $L2_1$ phase has been submitted to atomic disorder and does not correspond anymore to a "pure" $L2_1$ order.

value of the magnetization is in agreement with the one obtained from the FMR measured presented in section 5.3.2. Then we think that the Co/Mn exchange arises only in the $L2_1$ phase in this material. The last remaining question to answer is to know if the atomic exchange leads to $D0_3$ grains in the $L2_1$ matrix or if it only appears as local defects. This question is difficult to answer based on the measurements performed in this work. However, if $D0_3$ grains would grow in the initial $L2_1$ matrix, we could expect additional resonant peaks in FMR. This is not the case, then we believe that the Co/Mn exchange arises as local defects in the $L2_1$ matrix.

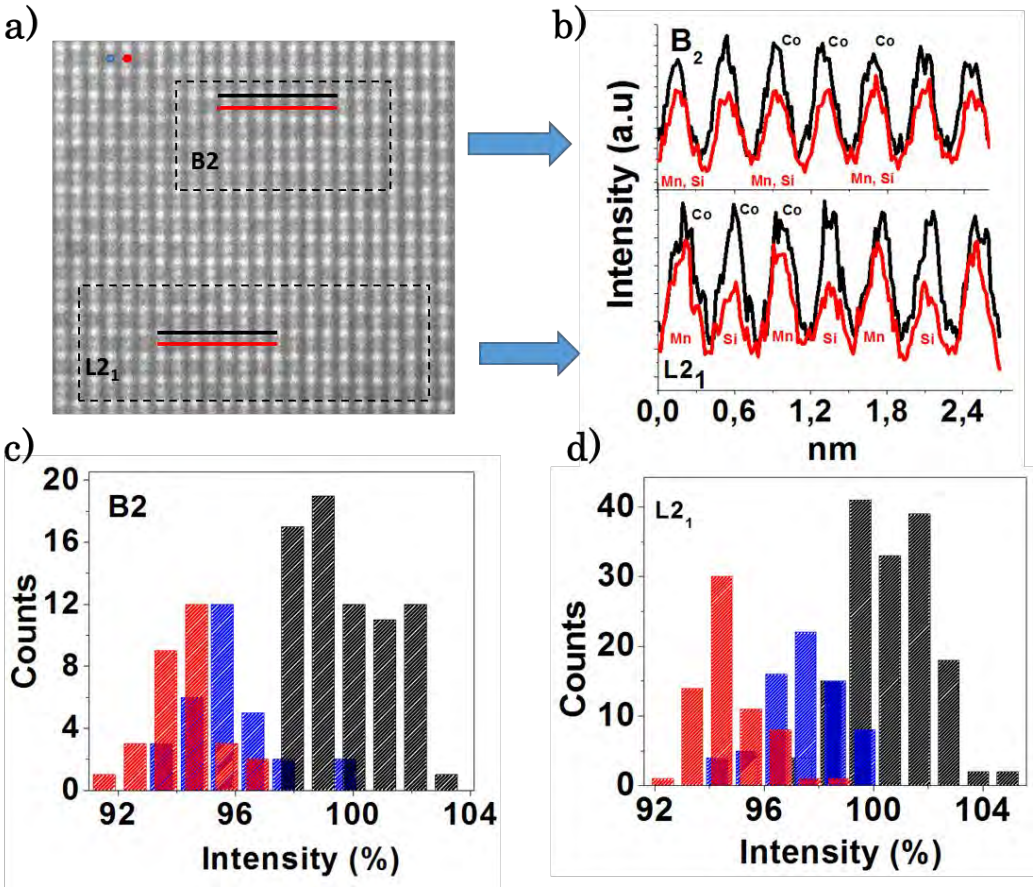

Figure 5.7: effect of irradiation on the atomic order seen by HAADF-STEM image in a) with a profile intensity on two selected lines indicating $L2_1$ and B2 regions in b). Statistics were done on selected areas to distinguish the two phases in c) and d).

<u>Sample N°3 series:</u>

For the samples of series N°3, only X-ray diffraction with the Cu source has been performed to follow the effect of the ion irradiation. This is due to the small size of the samples as the intensity of the diffraction peak are too small to be detected with the Co source diffractometer at the INSA.

The evolution of the (002) and (004) peaks for samples irradiated at 10^{16} and 10^{17} ions/cm² are shown in figure 5.8. Similarly to sample N°1, we observe an increase of the out of plane deformation but it is found to be more important than for the samples N°1. Indeed the out of plane lattice parameter is found to be 5.70, 5.72 and 5.73 Å for the reference, 10^{16} and 10^{17} ions/cm² irradiated samples respectively. These values are very important as compared to the expected one and bigger than for sample N°1. Unfortunately no GPA analysis could be performed on these samples as the MgO zone is not observable on the HAADF-STEM images. Then we could not study the eventual deformation of the CMS with respect to the substrate.

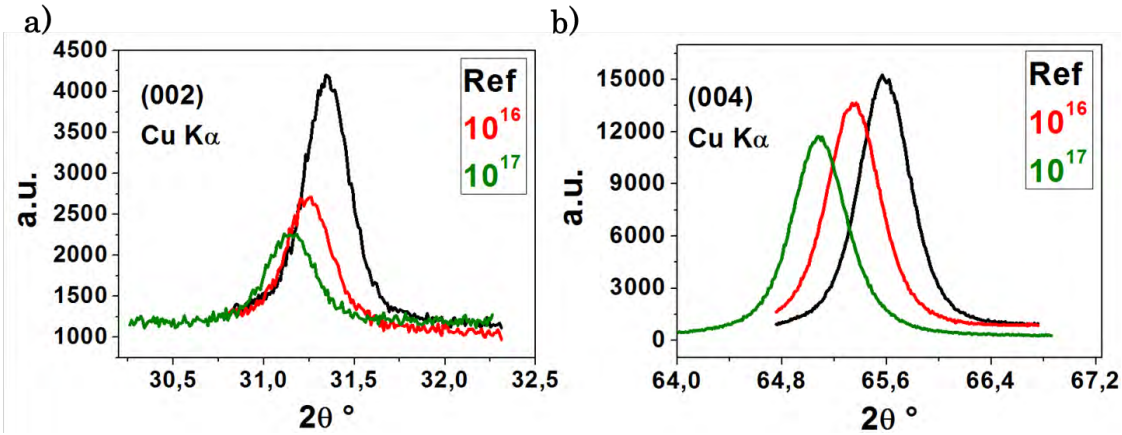

Figure 5.8: Evolution of 002 and 004 diffraction peaks as a function of irradiation fluence for the reference, irradiated at 10^{16} and 10^{17} ions/cm² of N°3 series samples performed by Cu source diffractometer.

As the measurements were done with the Cu source, we can calculate the evolution of the Co/Si exchange. The β parameter is found to vary from 0.06 to 0.15 and 0.22 for the irradiated sample at 10^{16} and 10^{17} ions/cm², respectively. Comparing the samples irradiated at 10^{16} for series N°1 and N°3, we observe a clear difference in the evolution of β disorder parameter. While it was found to be roughly constant for the N°1 series, it increases by more than a factor 2 for the N°3 series at 10^{16} ions/cm².
This behavior is surprising and one of the most important conclusions we can state is that the different samples do not show the same behavior under irradiation. This is a potential problem for the reproducibility of the method and implies a full study of the structural order for each sample to understand their magnetic properties.

HAADF-STEM has been performed on the sample irradiated at 10^{17} ions/cm² for N°3 series. An example of HAADF-STEM image is shown for the [110] direction of CMS in Figure 5.9. The statistics of the maximum amplitude of each atomic column performed on a zone of 20 x 22 atomic columns are shown in figures 5.9-e and 5.9-f. We clearly see that the Mn and Si intensities are very similar and below the intensity of Co. This is similar to what we observed for sample N°1. However, the main difference with the sample irradiated at 10^{16} ions/cm² of the N°1 series is that here we do not observe variations from one zone of the sample to another. This sample looks quite homogeneous with only punctual variations of local intensities in the Mn/Si amplitude that could reflect some remaining $L2_1$ order as shown by the blue circles in figure 5.9-c. HAADF-STEM performed in the [100] direction presented in

figure 5.9-b, confirms that the Mn/Si columns have lower intensities than the Co columns (figure 5.9-d).

At first sight, this sample can then be concluded to be almost completely in the B2 order. However this result is not in agreement neither with the value of β determined by X-ray nor by the FMR measurements presented in section 5.3.2, for which two crystal orders are well separated at 10^{17} ions/cm². First, the β value is close from the expected value for a pure A2 crystal order (α, β and γ are equal to ½, ¼ and ¼, respectively for A2) but this phase would be revealed in HAADF-STEM by having the same STEM intensities for all atomic columns, including the Co ones, due to the random distribution of the atoms on the different atomic sites. This is clearly not observed in our experiment for which the Co intensity is always above the one of the Si or Mn columns. Then we do not think that the A2 order is present.

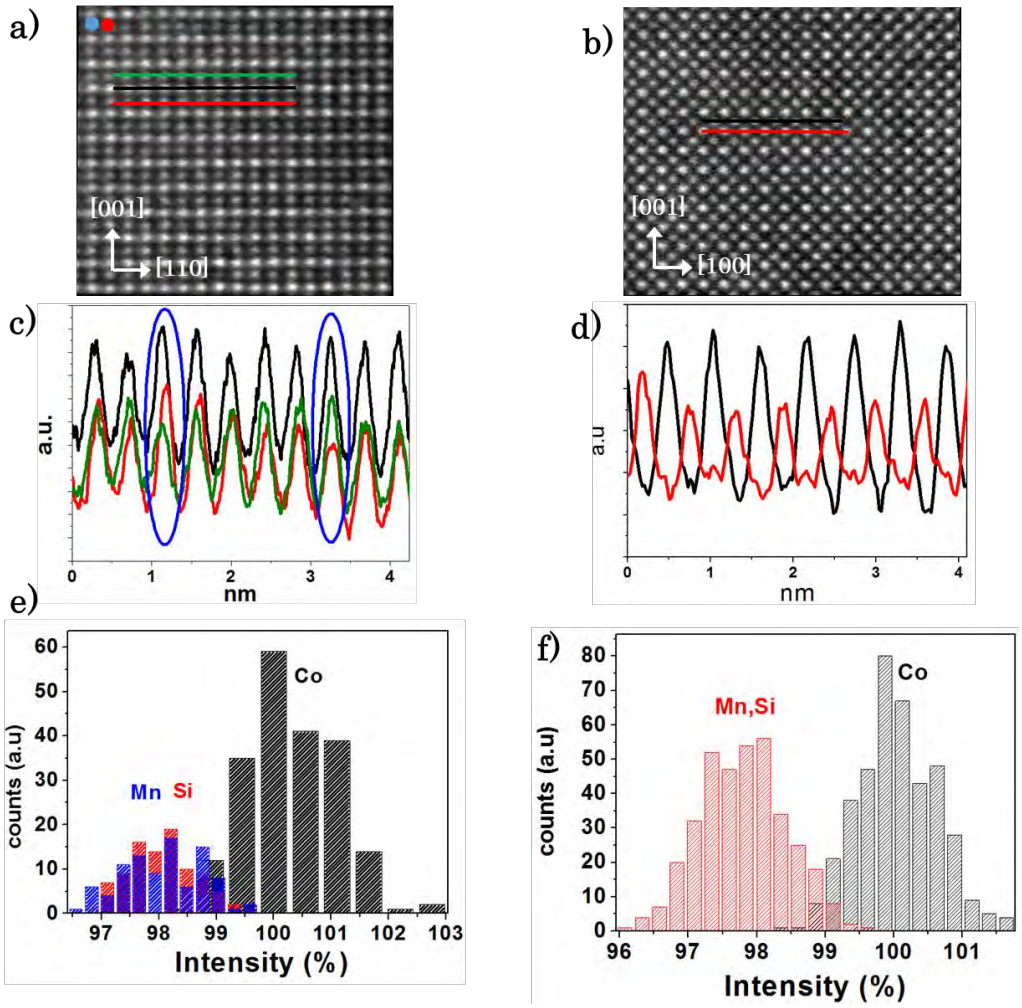

Figure 5.9: HAADF-STEM has been performed on the sample irradiated at 10^{17} ions/cm² for the series N°3 along [110] and [100] CMS directions in a) and b) respectively. Intensity profiles in c) show some remaining $L2_1$ regions in blue circles while in d) Mn and Si are indistinguishable. Statistics in e) and f) show that Co has higher intensities than Mn and Si.

Based on the evolution of the disorder parameters observed in the samples of series N°1, we propose the following scenario, sketched on figure 5.10. We believe that starting from a $L2_1$ order, the effect of irradiation is to induce 2 kinds of transformation. The first one is a $L2_1$-B2 transition as shown for sample N°1 and in agreement with the STEM profile in sample N°3 and FMR measurements presented below. The second transformation concerns only the remaining $L2_1$ phase for which we believe that Co/Mn exchange first occurs, similarly to sample N°1. Then, above a threshold fluence, Co-Si exchange takes place for the Co atoms being on the Mn sites. In this manner, Co atoms can be found on Si sites, leading to a high β value, but Si atoms are not on Co sites, explaining the remaining high intensity of Co columns in STEM. Indeed as Co and Mn gives the same STEM intensities (as a first approximation), this double exchange scenario would lead to high intensity on Co/Mn columns and lower intensities in randomly distributed Mn/Si/Co columns and this phase would not be very different in HAADF-STEM image from a B2 order. This phase could be considered as a mix of $D0_3$ and B2 phase, but not to the A2 order as no Si would be found on Co sites. Let's note that this scenario does not avoid Co/Si exchange also in the B2 order, which most probably occurs at very high fluence.

If this double exchange scenario is right, it also means that our model for the calculation of the disorder parameters is incorrect, at least for fluence of 10^{17}. Indeed, this model implicitly considers the symmetric exchange of the atoms positions. This would not be the case for double exchange. A complete model for calculating the atomic disorder parameters would need a set of individual rate of presence of each chemical entity on each atomic site. Also the presence of local defects should be taken into account in the model to consider the decrease of the peak amplitude. However, this approach leads to too many unknown parameters and is not realistic. Then the model used in this work has most probably to be limited to low irradiation fluence.

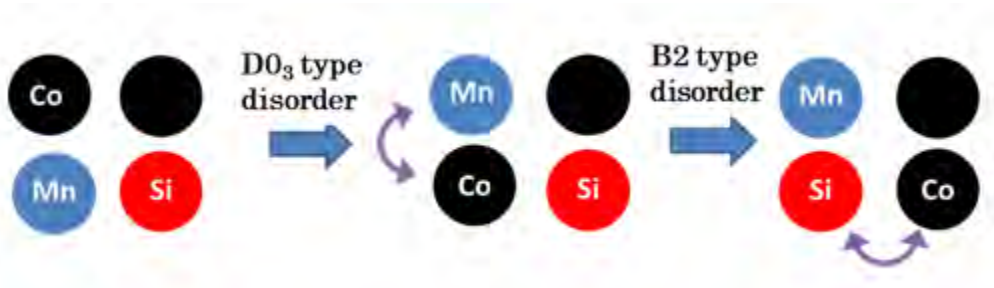

Figure 5.10: proposed scenario of the irradiation effect on CMS samples starting from $L2_1$ phase to D03 (Co-Mn disorder) and then a B'2 (Co-Si disorder) phase.

Several conclusions can be stated from the structural analysis of the irradiated sample. First, out of plane deformation is induced by the He+ irradiation. In addition, local defects in the alloy appear for ions fluence above 10^{16} ions/cm².

The mechanical distortion is accompanied by a modification of the local atomic arrangement as demonstrated by the evolution of the disorder parameters for the sample of series N°1. Based on this series of sample we believe that, for low ion fluence, the B2 order is favored with respect to the $L2_1$ order, especially if the B2 order is already present. Additionally, we believe that above a threshold fluence, most probably around $5*10^{15}$ or 10^{16} ions/cm², Co/Mn swap occurs due to the low

energy formation of this kind of defects. Then ion irradiation seems to be inappropriate for improving the $L2_1$ order in Co_2MnSi, as it nucleates most probably some local defects of $D0_3$ type. However ion irradiation is confirmed to improve the B2 order, as observed by Gaier *et al*. However neither HAADF-STEM nor X-ray diffraction allows to state about the presence of Co/Mn swap in the created B2 phase.

For higher fluences, the partial results obtained from X-ray diffraction and HAADF-STEM imaging performed on the samples of the series N°3 let us think that a potential double exchange arises in the $L2_1/D0_3$ order. Indeed, the only possibility to explain the contrast in STEM is to consider that no (or only few) Si atoms get to the position of Co atoms. Moreover, the presence of Co atoms on Si sites is coherent with both the STEM contrast and the high value of the β parameter. This assumption can be partially supported by the calculated energy formation of Co antisite realized by Piccozzi *et al* [10 Picozzi]. They have found relatively low value of 0.8 eV which, corroborated to the presence of local defects in the matrix, allow for the displacement of Co atoms far from their original site.

Let us now focus on the effect of ion irradiation on the magnetic properties of the alloy. We will first show how the basic properties of the magnetic material, such as the average magnetization amplitude and coercive fields are affected. Then we will present dynamic measurement which will allow studying more in details the effect of irradiation on local anisotropies and on the evolution of magnetic parameters for the different crystal order as a function of the ion fluence. Finally the last part of this chapter will be devoted to the presentation of preliminary results on the effect of ion irradiation on the dynamic relaxation.

5.3 Modifications of magnetic properties by He^+ ions irradiation

To study the effect of the ion irradiation on the coercive field and magnetization amplitude, MOKE has been performed on the sample of the series N°1 irradiated at 10^{16} ions/cm² while PPMS measurements have been performed on the four samples of the series. The results of these experiments are presented in the next subsection.

5.3.1 Static magnetic properties

Basically, similar features as for the reference samples are recovered. However, few differences can be observed. The most obvious observation concerns the amplitude of the coercive field μ_0Hc. While similar values of μ_0Hc were observed for the reference sample as a function of the angle α between the direction of the applied field and the easy axis, the irradiated sample shows a clear difference between the easy and hard directions as can be seen in Figure 5.11-a. This reflects an increase of the crystal anisotropy, in agreement with the values of the saturation field presented in Figure 5.11-b. This will also be confirmed by FMR measurements.

The increase of the coercive fields is typical in switching mechanisms dominated by the propagation field. Indeed, point defects are generally assumed to decrease the nucleation field of magnetic domains via a reduction of the local energy landscape. However, point defects acts as a friction term in the dissipative process during the propagation of the domains.

Therefore, an increase of the coercive fields can be accounted for an increase of the propagation field. This is due to the fact that the domain wall widths, being of a few tens of nanometer for Neel walls, average the effect of local defects over large distance. The friction arises from local distortion of the domain around point defects. A complete review of these processes can be found in the book "Magnetic Domains" by Hubert and Schäfer [12 Hubert & Schäfer].

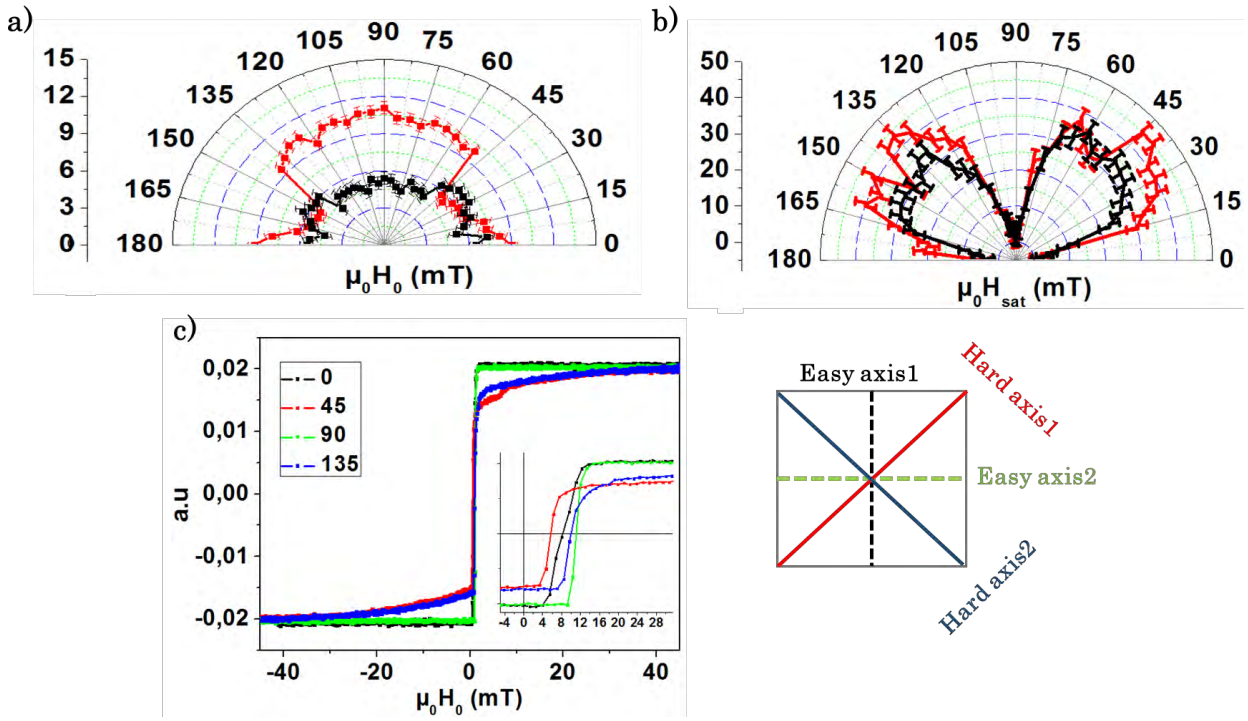

Figure 5.11: Coercive field (a) and saturation field (b) as a function of the applied field direction with respect to the easy axis, where the black and red curves correspond respectively to the reference sample of series N°1 and irradiated one at 10^{16} ions/cm². C) Example of LMOKE signal after symmetry process, showing the different switching mechanisms in the different directions.

Additionally to the anisotropic behavior of the coercive fields, we also observe that the two easy axes and the two hard axes do not show similar magnetic switching mechanisms. This is shown in figure 5.11-c. As the four axes behave differently, one can think that some uniaxial anisotropy tilted with respect to the easy axis appears. FMR measurements presented in the next sub-section will show that no uniaxial anisotropy is present at 10^{16} ions/cm². Then the origin of these differences between the 4 axes is not clear. However, as demonstrated by the structural analysis and further by FMR measurements, this sample shows clearly two different phases with different magnetic parameters (μ_0Ms, $\mu_0 H_k$). Then, as MOKE measures the average magnetic properties of the sample, it is extremely difficult to distinct the magnetic behavior of an individual phase and we believe that the observed differences are accounted for the different behavior of the two phases.

PPMS magnetometry measurements have also been performed on the four samples of N°1series. The result of the calculated magnetization amplitude is shown in figure 5.12. We clearly observe a decrease of magnetization with an ion fluence above 10^{15} ions/cm². The uncertainty of the magnetization is due to the uncertainty on the exact dimensions of each

sample measured with a precision of a few microns. Magnetization values are reported in table 5.2. Considering that the samples are made up of the B2 crystal order with a magnetization of 1.25 T and a second phase with varying magnetization amplitude due to $D0_3$ type disorder, we can evaluate the magnetization of the second phase by considering the volume ratio of each phase. As explained in section 5.2, the volume of the B2 phase is calculated with respect to the full B2 order as $\alpha/0.5$. The values of α are given in figure 5.6. The volume of the second phase is then 1- $\alpha/0.5$. Magnetization values of the second phase are presented in table 5.2. We will see that FMR measurements are in good agreement with this approach and then support our initial assumption of two distinct crystal orders, one being the B2 order with constant magnetization and the second one having a decreasing magnetization.

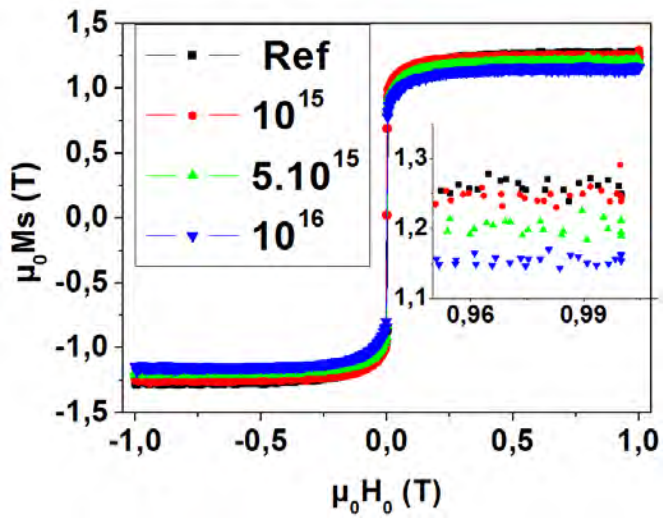

Figure 5.12: PPMS average magnetization measurements for the four samples of N°1 series.

N°1 sample at different Fluences (ions/cm²)	μ_0Ms (T) measured	Proportion of B2 phase (1.25 T) (α/0.5)	Proportion of second phase (1 - α/0.5)	μ_0Ms second phase (T)
REF	1.25 ± 0.02	0.28	0.72	1.25± 0.02
10^{15}	1.25 ± 0.02	0.26	0.74	1.25± 0.02
$5*10^{15}$	1.2 ±0.02	0.4	0.6	1.16± 0.02
10^{16}	1.16 ± 0.02	0.41	0.59	1.1± 0.02

Table 5.2: magnetization values of N°1 series for both phases.

5.3.2 FMR measurements of irradiated samples: effect of irradiation on magnetic parameters

- **<u>Sample N°1 series:</u>**

FMR measurements have been performed on the four samples of N°1 series to extract the magnetic parameters of each crystal phase as a function of the ion fluence. Examples of

the evolution of the FMR spectra at 18 GHz in easy 2 and hard 2 directions are presented in figures 5.13-a and 5.13-b. The spectra are shifted vertically for convenience. As can be seen the evolution is quite complex. The general behavior is the separation of the two peaks corresponding to the $L2_1$ and B2 crystal order we stated for the reference sample. Considering the structural analysis presented above, we assume that the peak showing almost a constant resonance field value corresponds to the B2 order, as this phase seems to be favored by the irradiation, while the peak showing an evolution of the resonance field is assumed to correspond to an evolution of the $L2_1$ matrix. We will see that the extracted magnetic parameters support this assumption. For convenience in the following we will denote the two peaks as the $L2_1$ and B2 peaks.

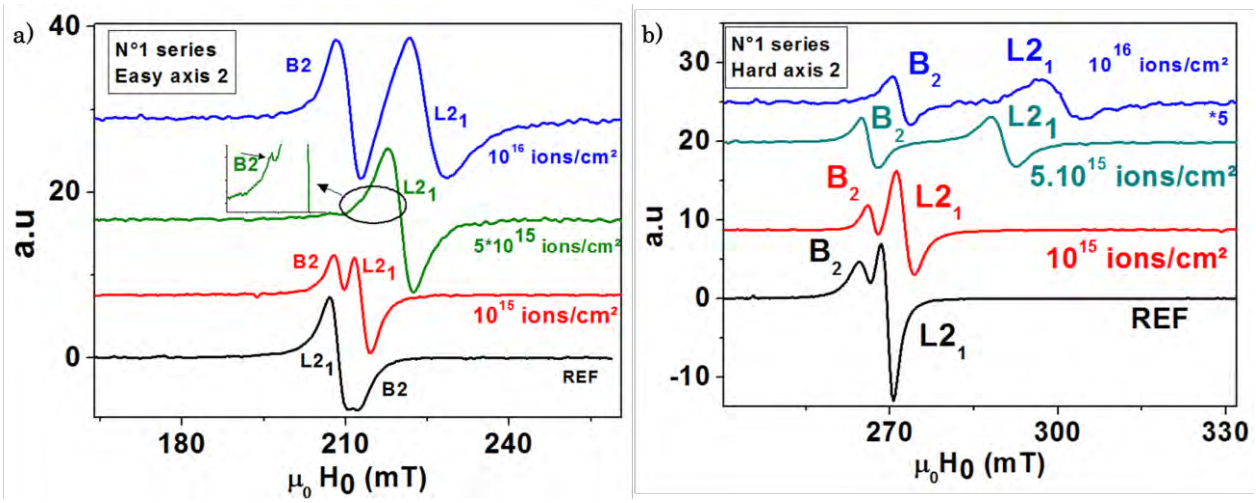

Figure 5.13: Evolution of FMR spectra peaks at 18 GHz of N°1 series samples as irradiation fluence increases for easy axis 2 in a) and hard axis 2 in b).

An important feature of these measurements is that the observation of the $L2_1$ and B2 peaks depends on the ion fluence. Starting with the fluence of 10^{15} ions/cm², we observe a strong mixing of the B2 and $L2_1$ peaks especially when the external field is applied parallel to the easy axis 2 and hard axis 2. This is shown in figure 5.13 and also in figure 5.14 presenting the FMR spectra at 16 GHz in the four directions for the reference sample and 10^{15} ions/cm². The zoom in figure 5.14-b shows that the B2 peak can still be observed for the hard axis 2 direction. For the easy axis 2, it is not possible to separate both phases. We then assume the same resonance field for both phases in the easy 2 direction. The mixing of the two modes can be accounted for either a shift of the resonance peak or for different linewidth of the two peaks depending on the orientation of the applied field. In fact, both effects participate to the mixing of the modes.

Fitting the f_{res} vs. $\mu_0 H_0$ curves (figures 5.14-c and 5.14-d) for the two peaks allows recovering the different magnetic parameters. Several differences are observed as compared to the reference sample. The first one is that one resonance peak corresponds to a crystal phase with lower magnetization amplitude (1.22 T). For the $L2_1$ phase, the situation is different. Indeed, the effect of irradiation is to strongly decrease the magnetization amplitude along with the exchange constant. This is in agreement with the theoretical prediction of reduced spin splitting caused by Co/Mn exchange by Picozzi *et al.* [10 Picozzi]. The second phase shows a magnetization of 1.25 T in agreement with our assumption that the irradiation

favors the B2 order in the alloy. Concerning the cubic anisotropy amplitude, both phases show similar values compared to the reference sample.

The main difference with the reference sample is the appearance of a uniaxial anisotropy aligned at about 23° from easy axis 2. This effect is most probably related to the tetragonal deformation observed by X-ray diffraction. We remind that MOKE measurements for the reference sample made us think that a small uniaxial anisotropy was aligned with one easy axis. Then we think that the tetragonal distortion allows for the rotation of the anisotropy direction in the plane of the layer. However, we do not know if this effect can be caused by an eventual interface effect with the MgO as we made the assumption that the MgO lattice parameter is not influenced by the irradiation.

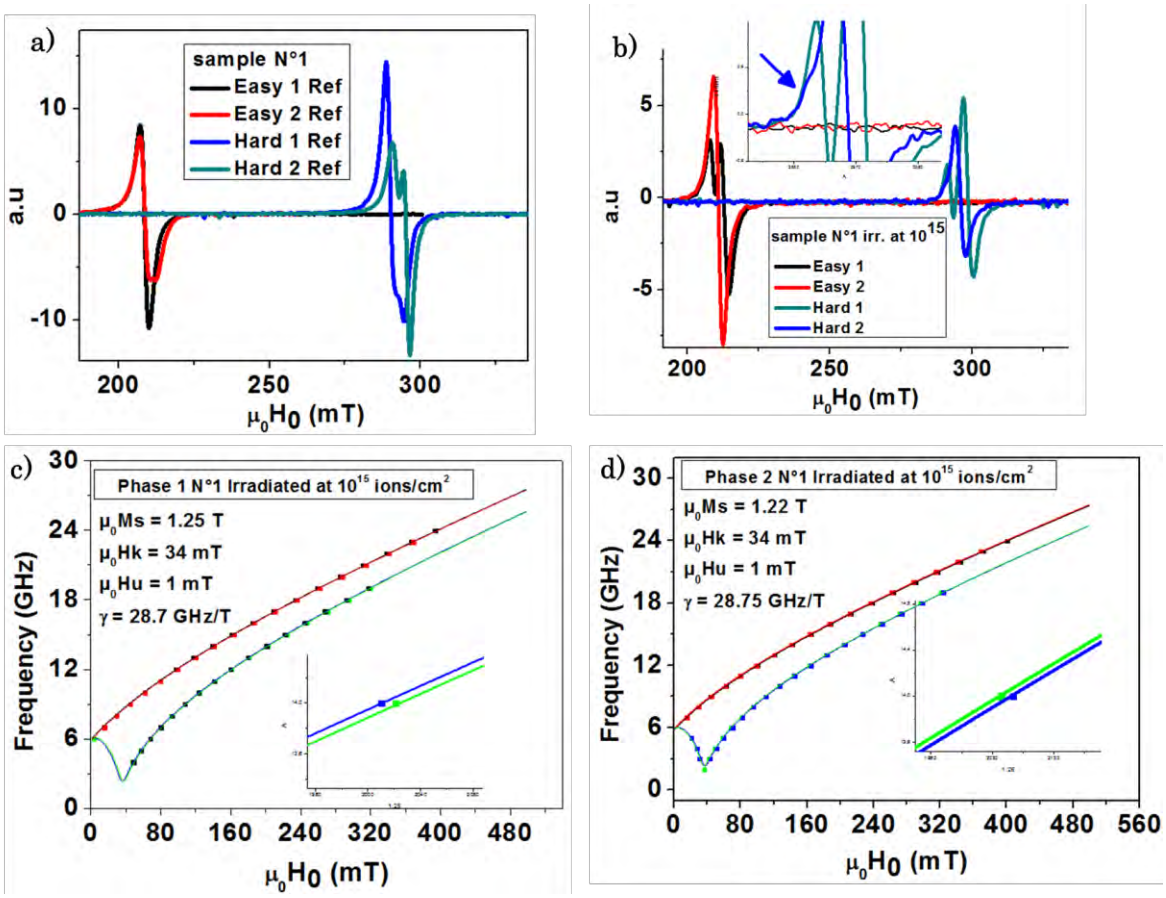

Figure 5.14: a) and b) presents the four easy and hard directions FMR spectra at 16 GHz of N°1 reference and irradiated at 10^{15} ions/cm^2.In c) and d) f_{res}vs. μ_0H$_0$ curves for both phases of N°1 irradiated at 10^{15} ions/cm^2.

Similar treatment is applied for fluences of $5*10^{15}$ and 10^{16} ions/cm^2. At $5*10^{15}$ fluence, we now observe that the position of the peaks for the L2$_1$ and B2 phases respectively are superposed for the two easy axes while a shift is observed for the two hard axes (figure 5.15-a). This means that the uniaxial anisotropy is now superposed to a hard axis (hard axis 2 in our case) direction. At 10^{16} fluence, the effect of the uniaxial anisotropy has disappeared as the position of both L2$_1$ and B2 peaks superpose for the two easy and the two hard axes (figure 5.15-b). While the tetragonal distortion was found to increase between $1*10^{15}$ and $5*10^{15}$

ions/cm², which could explain the increased amplitude (see table 5.3) and rotation of the uniaxial anisotropy, the fact that the uniaxial anisotropy disappears at 10^{16} while the out-of-plane parameter is the same means that the internal strain have been relaxed. Then we believe that the amplitude of the uniaxial anisotropy is most probably related with the internal mechanical strain, the relaxation of the latter being mediated by the increased number of vacancies by the irradiation.

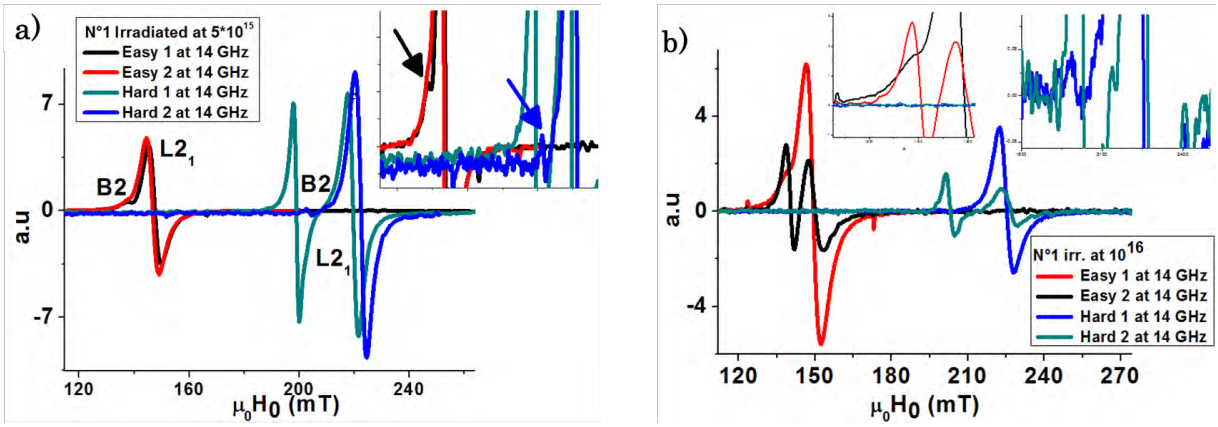

Figure 5.15: FMR absorption spectra obtained for the four easy and hard axes directions for a) N°1 irradiated at $5*10^{15}$ and b) N°1 irradiated for 10^{16} ions/cm² fluence.

Figure 5.16 presents the evolution of the f_{res} vs $\mu_0 H_0$ for all fluences of N°1 series for each crystal order. For convenience and clarity, only one easy and one hard axis for each fluence is presented. The deduced magnetic parameters obtained from these curves are summarized in table 5.3. Despite the increasing uniaxial anisotropy, the B2 crystal order shows similar magnetic parameters whatever the ion fluence.

Additionally, we observe an increase of the cubic anisotropy and of the gyromagnetic ratio. The latter shows that the orbital moment increases with disorder. The study of the linewidth presented in the next subsection will show that the spin-orbit coefficient λ_{SO} is roughly constant as a function of the dose. Then the increased orbital moment seems to be the origin of the increased anisotropy and decreased g value.

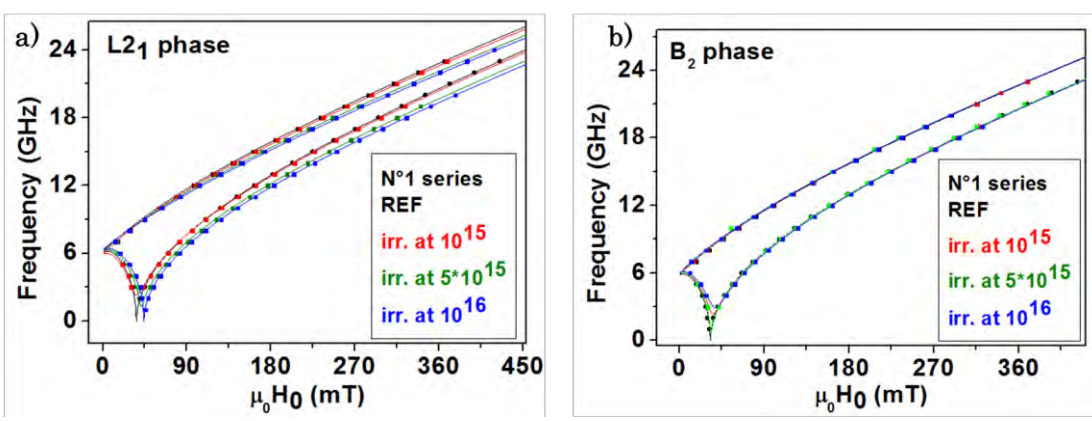

Figure 5.16: Evolution of the f_{res} vs. $\mu_0 H_0$ curves for both phases of N°1 series. In a) shows the $L2_1$ phase evolution as irradiation dose increases while in b) all curves have the same behavior and are identified for the B2 phase.

N°1 series (ions/cm^2)	Ref	Irr. at 10^{15}	Irr. at $5*10^{15}$	Irr. at 10^{16}
μ_0Ms1 (T)	1.26± 0.02	1.22± 0.02	1.14± 0.02	1.1± 0.02
μ_0Ms2 (T)	1.25± 0.02	1.25± 0.02	1.25± 0.02	1.25± 0.02
μ_0Hk$_1$ (mT)	36± 0.2	34± 0.2	42± 0.2	45± 0.2
μ_0Hk$_2$ (mT)	**32 ± 0.2**	33± 0.2	35± 0.2	36± 0.2
γ_1 (GHz/T)	28.7± 0.1	28.7± 0.1	28.8± 0.1	28.9± 0.5
γ_2 (GHz/T)	28.7± 0.1	28.7± 0.1	28.7± 0.1	28.7± 0.3
φ_u (deg)	0	23 ± 2	45 ± 2	0
μ_0H$_u$ (mT)	< 1	1 ± 0.2	1.9 ± 0.1	0
A1 (pJ/m)	19 ± 0.1	18 ± 0.1	12.8 ± 0.1	13± 0.1
A2 (pJ/m)	-	-	-	-

Table 5.3: Magnetic parameters extracted from FMR spectra for the L2$_1$ and B2 order as a function of the fluence for N°1 series.

Finally, we want to emphasize an important feature that is observable particularly for the $5*10^{15}$ and 10^{16} ions/cm² fluences. We will show that similar effect appears for the sample of series N°3. As already mentioned the resonant peak corresponding to the B2 order shows strong variations of its amplitude depending on the orientation of the applied field. As we already said, mode mixing is a possible reason for this, especially in the easy axes directions. This is particularly true for the fluence of $5*10^{15}$. However, this assumption is no longer valid for 10^{16} as no uniaxial anisotropy induces any shift of the resonant modes. Furthermore, the two peaks are well separated for the hard axes direction even at $5*10^{15}$. Then, we do not believe that mode mixing is in cause.

Therefore, one has to consider the different effects that contribute to the amplitude of the FMR signal. The first is the damping. When the linewidth increases, the FMR maximum amplitude decreases since the total microwave power absorbed is constant. However, and despite the strong uncertainty of the deduced linewidth due to the weakness of the signal, we did not observe a very significant difference of the linewidth for the B2 order between the two hard axes. The second contribution to the FMR amplitude is the volume of magnetic material that interacts with the pumping field. As this resonant peak corresponds to the growing B2 phase in the matrix, this result could imply a preferential orientation of the growing crystallite. However, we did not observe such effect in HAADF-STEM images. Moreover we did not find any reasonable configurations that would break the symmetry between the two hard axes. It cannot be related neither to some partial relaxation of the strain since this would imply a shift of the resonance peaks when switching from one hard axis to the other. We will

show that similar effect appears for the N°3 series. Unfortunately, at this time we do not have any explanation or hypothesis that could explain this observation.

- **<u>Sample N°2 series:</u>**

The evolution of FMR spectra recorded at 19 GHz as a function of the irradiation fluence for the two easy and two hard axes are presented in Figures 15.7-a and 15.7-b, respectively. The most interesting feature relies on the evolution of the peak position for the easy axes. We start from the reference sample for which the uniaxial anisotropy is superposed on easy axis 2. The resonance field of easy axis 2 is lower than that of easy axis 1 while for both hard axes the resonance fields are superposed. At 10^{14} ions/cm², there is first an increase of the field shift for the two easy and two hard axes meaning that the uniaxial anisotropy is not superposed anymore with the easy axis 2. Increasing the fluence up to 10^{15}, we observe that both resonance fields of the two easy axes are superposed while they are not for the two hard axes, meaning that now the uniaxial anisotropy is superposed to the hard axis 1.

At $5*10^{15}$ and 10^{16} ions/cm², we recover a field shift for the four axes but the position of the easy axis 1 and 2 is inversed as compared to the reference sample[4]. This means that now the uniaxial anisotropy is between the hard axis 1 and easy axis 1. Finally, at 10^{17} ions/cm², the uniaxial anisotropy is found to be aligned with the easy axis 1.

Then the effect of the ion irradiation for this sample is to rotate the uniaxial anisotropy from the easy axis 2 to the easy axis 1 (as schematically drawn in figure 5.18). Based on the structural properties of samples of series N°1 and N°3 with irradiation, we state that this rotation is linked to the increase out of plane parameter of the alloy. The values of the amplitude of this anisotropy obtained from the f_{res} Vs. $\mu_0 H_0$ curves (Figure 5.18), are presented in table 5.4. It shows that it first increases for fluence up to $5*10^{15}$ and then decreases for higher fluence. This result confirms the observation for samples of series 1, *i.e.* the direction and amplitude of the anisotropy is strongly dependent on the value of the out of plane deformation.

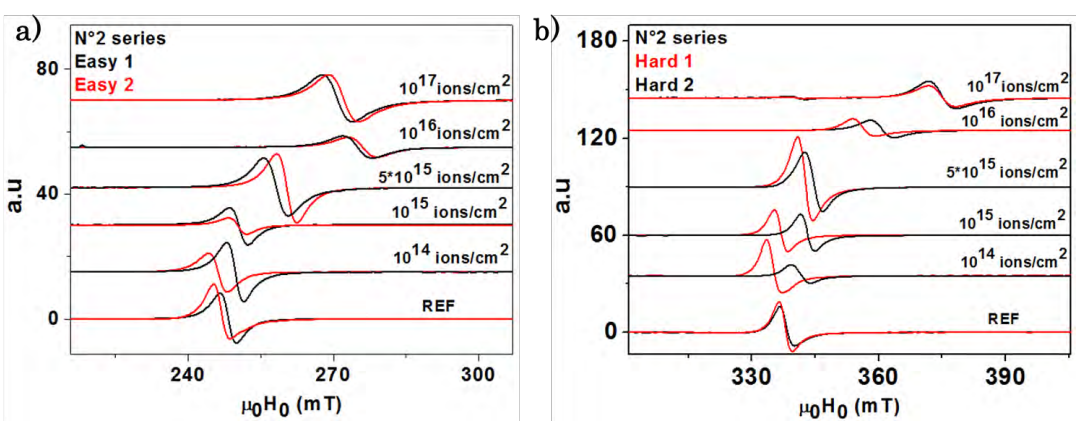

Figure 5.17: Absorption spectra as a function of magnetic external Field H_0 for N°2 series samples at 19 GHz along the two easy and the two hard axes in a) and b) respectively.

[4] While we find similar values of the amplitude and orientation of the uniaxial anisotropy for $5*10^{15}$ and 10^{16} ions/cm² (see table 5.4), the field shift in the hard axis appears lower at 10^{15} in figure 5.17-b. This is due to a very small misalignment of the applied external field with the hard axis. The misalignment is about 0.5 °.

The magnetic parameters extracted from the f_{res} vs. $\mu_0 H_0$ curves are presented in table 5.4. As for the $L2_1$ crystal order of series N°1, we observe a decrease of the magnetization and exchange constant with the ion fluence which could be accounted for an increase Co/Mn and/or Co/Si exchange. A difference with the first series deals with the amplitude of the cubic anisotropy which is found here to be roughly constant up to 10^{17} ions/cm², the only fluence for which a clear increase is observed. Also, the gyromagnetic ratio is first found to jump up to 29.1 GHz/T at 10^{14} and then to be constant with the fluence. Then the relation between the gyromagnetic value and the cubic anisotropy is slightly different as for the $L2_1$ order in series N°1. Indeed the increase in γ is not correlated to an increase of $\mu_0 H_k$ at 10^{14} ions/cm². This could mean that the increase orbital moment is compensated by a decrease of the λ_{SO} coupling amplitude. For fluence between 10^{14} and 10^{16} there is no variations of γ while $\mu_0 H_k$ is roughly constant as could be expected. Then at 10^{17} both $\mu_0 H_k$ and γ are found to increase as for series N°1. Maybe this particular behavior has to be correlated to the Co/Si exchange as observed for samples of series N°3. The lack of structural information for this series of sample avoid to state about the origin of the behavior of the magnetic parameters.

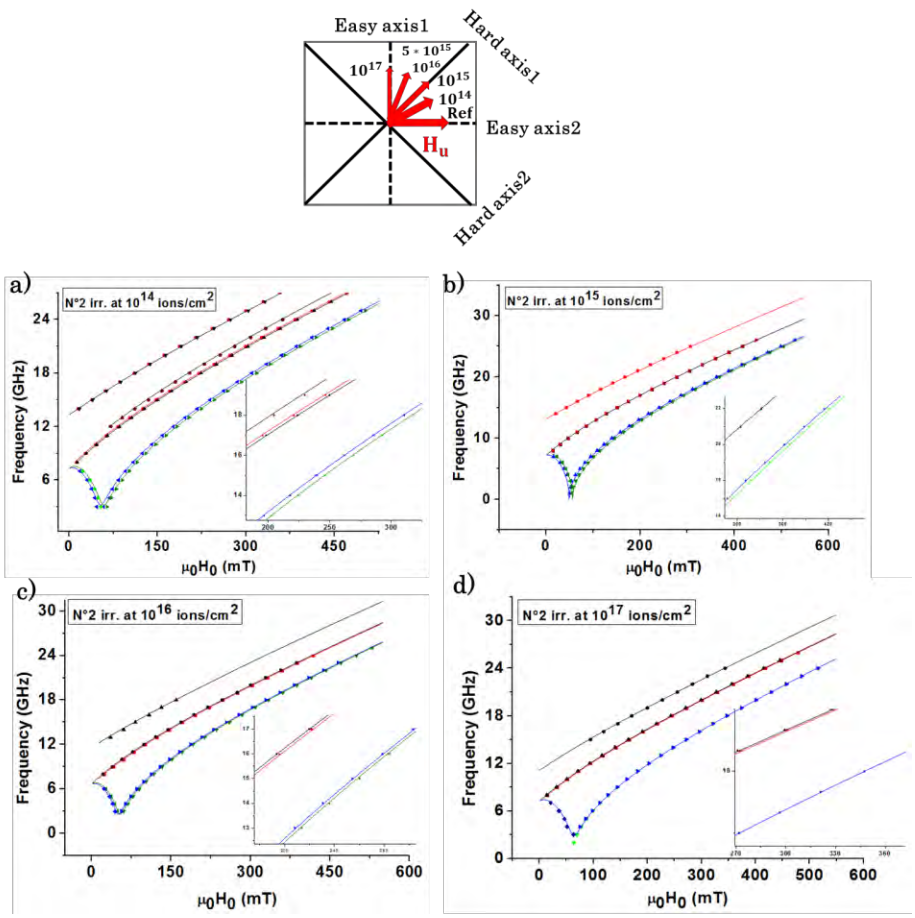

Figure 5.18: f_{res} vs. H_0 curves for N°2 series irradiated samples at 10^{14}, 10^{15}, 10^{16} and 10^{17} ions/cm² in a), b) c) and d) respectively. The box shows the uniaxial anisotropy rotation from Easy axis 2 for reference sample to Easy axis 1 at 10^{17} ions/cm².

N°2 series (ions/cm²)	Ref	Irr. at 10^{14}	Irr. at 10^{15}	Irr. at $5*10^{15}$	Irr. at 10^{16}	Irr. at 10^{17}
μ_0Ms1 (T)	1.24± 0.02	1.21± 0.02	1.20± 0.02	1.14 ±0.02	1.07± 0.02	1.03± 0.02
μ_0Ms2 (T)						1.25± 0.03
μ_0Hk$_1$ (mT)	51± 1	52± 0.2	52± 0.2	49± 0.2	49± 0.2	60±0.2
μ_0Hk$_2$ (mT)						60± 0.2
γ_1 (GHz/T)	28.8 ±0.1	29.1 ±0.1	29.1±0.1	29.1±0.1	29.1± 0.1	29.2± 0.1
γ_2 (GHz/T)						28.7± 0.1
φ_u (deg)	0	30 ± 2	45 ± 2	65 ± 2	60 ± 2	90 ± 2
μ_0H$_u$ (mT)	1.2 ±0.2	3.5± 0.2	3.5 ±0.2	3.5 ±0.2	2± 0.2	1±0.2
A1 (pJ/m)	10±0.2	9.3 ±0.2	9.1 ±0.2	8.3 ±0.2	7 ±0.2	5.4 ±0.2

Table 5.4: Magnetic parameters extracted from FMR spectra for N°2 series as a function of the fluence.

Finally, we also observed the apparition of a second resonant peak at high fluence, which most probably corresponds to a second crystal order phase. It can be seen in figure 5.19-a) that the peak is barely visible in the hard axis 2 direction at 10^{16} ions/cm² (figure 5.19-a) while it can be detected for both hard axes at 10^{17} ions/cm² (figure 5.19-a). In the easy axes we were not able to separate this resonance peak from the main one. Then, in figure 5.19-b we only present the evolution of the position of the resonant peaks in the hard axes for a fluence of 10^{17} ions/cm². Combined with the small amplitude of the signal, the determination of the exact peak position is difficult and then the determination of the magnetization and gyromagnetic ratio has low precision However, the estimation of the magnetization amplitude and gyromagnetic ratio is in agreement with the values found for the B2 order for the samples of series 1 while the cubic anisotropy is the same as for the $L2_1$ phase of the reference sample.

In conclusion, this series of samples show similar behavior to that of the series N°1 but with differences for some magnetic parameters, especially for the anisotropy and gyromagnetic values. These differences are most probably to be related to different chemical order between the references samples N°1 and N°2, as shown in chapter IV. While the lack of structural information avoids a better understanding of the evolution of the magnetic parameters as a function of the type of atomic disorder, it seems that ion irradiation favors again the apparition of the B2 order from the initial matrix.

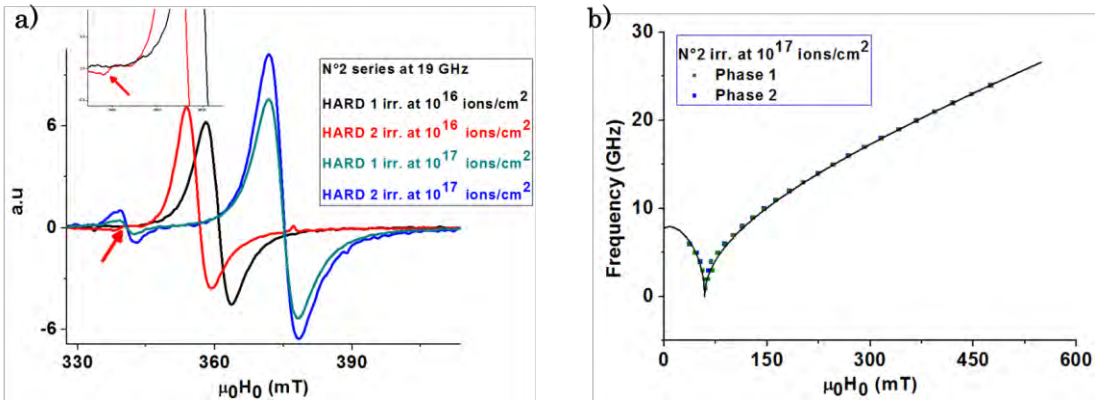

Figure 5.19: FMR absorption spectra comparison at 16 GHz of hard 1 and hard 2 axes of N°2 series samples irradiated at 10^{16} and 10^{17} ions/cm² in a). In b), the evolution of hard axes resonant peaks of N°2 sample irradiated at 10^{17} ions/cm².

- **<u>Sample N°3 series:</u>**

As stated in chapter IV, the reference sample of this series exhibits a clear $L2_1$ crystal order. However a very small additional peak was detected in the hard axis 2 direction (the one supporting the uniaxial anisotropy) that we accounted for a second crystal order which is most probably the B2 order, based on the results of the samples of series N°1. In the following we will call this second peak the minority peak in reference to its very small amplitude.

The evolution of the FMR spectra with the ion fluence is shown in figure 5.20. In figure 5.20-a only the easy axis 1 is shown for clarity as the two easy axes resonance always superposed at all fluence. In figure 5.20-b we show the evolution of the two hard axes. Clearly, the uniaxial anisotropy in the hard axis is visible for all fluence. However, the main effect of the irradiation is to switch the direction of the uniaxial anisotropy from the hard axis 2 to the hard axis 1 at 10^{16} ions/cm².

We begin with the effect of ion irradiation on the magnetic properties of the main $L2_1$ phase. Examples of f_{res} Vs $\mu_0 H_0$ curves for the main peaks are presented in figure 5.21. The values of the magnetic parameters extracted from this curves are summarized in table 5.5. We found typically two different behaviors depending on the ion fluence.

For 10^{14} and 10^{15} ions/cm², we observe a decrease of the magnetization amplitude and exchange constant. The values of the magnetization and exchange are roughly similar to the ones reported for $L2_1$ order of the samples of series N°1 at similar fluence. In addition the values of the cubic anisotropy are roughly constant at these fluence, as for sample of series N°1 and N°2, while the gyromagnetic constant slightly increases. This is similar to the situation encountered for the sample N°2 and is maybe due to the higher rate of Co/Si exchange observed for this sample as compared to the series N°1. Also the uniaxial anisotropy stays always aligned with hard axis 2 direction but its amplitude slightly decreases. We attribute this decrease to the fact that the out of plane lattice parameter of the reference sample of series N°3 corresponds to the maximum value of the sample irradiated at 10^{16} ions/cm² of the series N°1. Then we think that the sample of series N°3 has already overpassed

the "elastic" limit for which the uniaxial anisotropy was found to increase. Once again, it confirms the relation between the amplitude of the anisotropy and of the deformation.

At 10^{16} and 10^{17} ions/cm², the magnetic parameters evolve drastically. Similar features as for the sample of series N°1 are observed for the magnetization, cubic anisotropy, exchange[5] and gyromagnetic ratio. We note that the decrease of the magnetization and, to a less extent, the exchange constant is more important while the gyromagnetic ratio is found to increase much more than for series N°1. Here also we assume that this is due to the higher Co/Si exchange. One possible scenario is that the modification, with a Co atom having a higher atomic number Z, of the local environment around the Mn atoms, that carry most of the magnetic moment in Co_2MnSi, leads to an increase of orbital magnetic moment on the Mn atoms. The most striking feature appearing at these fluence concerns the direction of the uniaxial anisotropy which switches from the hard axis 2 to the hard axis 1 direction at 10^{16} ions/cm², along with a decrease of its amplitude as expected from the relaxation of the strain. Increasing further the fluence to 10^{17} ions/cm², the anisotropy slightly rotates toward the easy axis 1 but its amplitude increases again to a large value of about 4.5 mT. The explanation for this effect is not clear. We believe that at such high fluence, in addition to the strong chemical reorganization in the $L2_1$ phase, some internal modifications of the cell appears such as an orthorhombic deformation with different in plane lattice parameters, leading to modification of the atomic magnetic interactions. Then we have no clue about the magnetic properties of such a "new" crystal order with different chemical and physical organization and further structural analysis, in particular a full atomic disorder model and deformation measurements would be necessary to state about the local arrangement of the atoms.

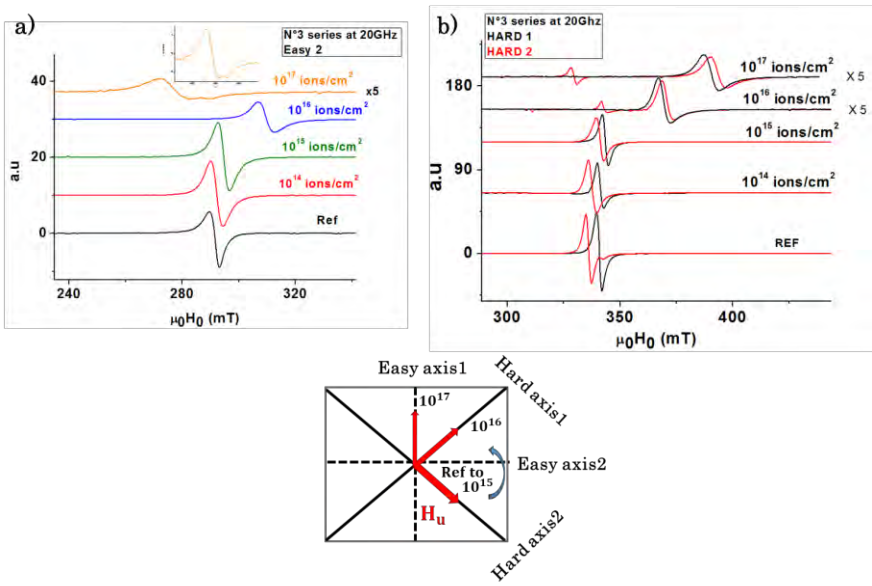

Figure 5.20: Absorption spectra as a function of magnetic external field $\mu_0 H_0$ for N°3 series samples at 20 GHz along the two easy and the two hard axes in a) and b) respectively. The box shows the uniaxial anisotropy rotation from hard axis 2 for reference sample to easy axis 1 at 10^{17} ions/cm²

[5] The exchange constant cannot be measured at fluence of 10^{17} ions/cm². Indeed the FMR signal decreases with the ion fluence and the exchange mode becomes undetectable at the microwave power used in this experiment.

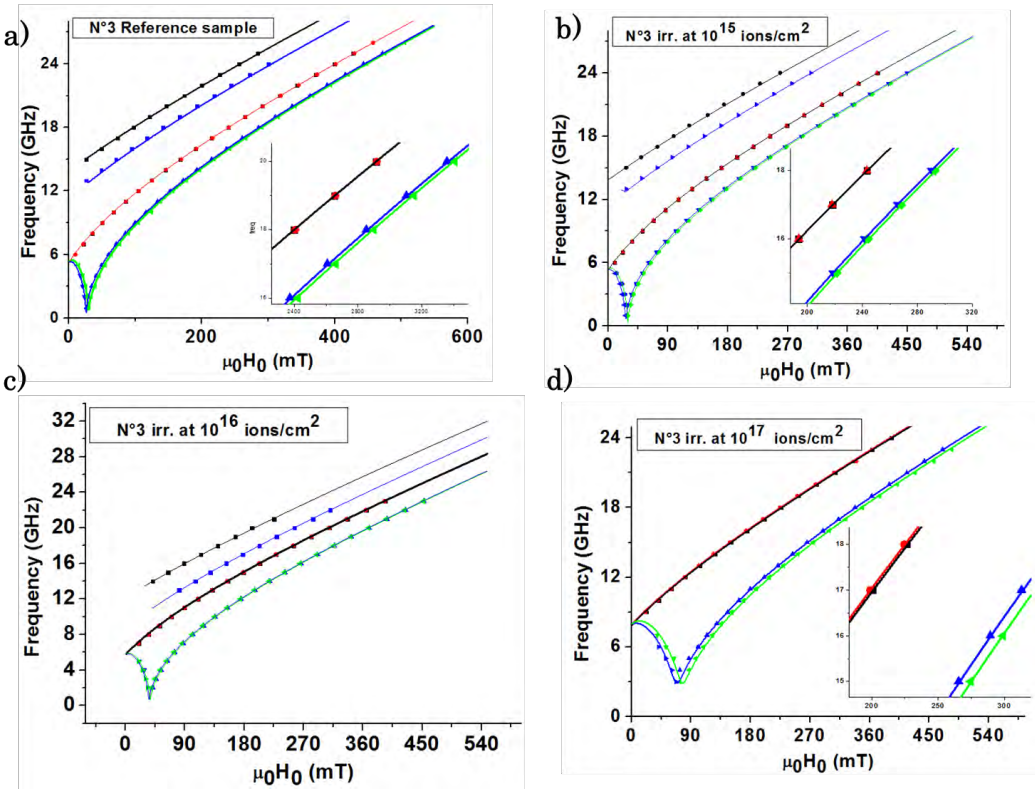

Figure 5.21: f_{res} vs. $\mu_0 H_0$ curves for N°3 series for reference in a) and irradiated samples at 10^{15}, 10^{16} and 10^{17} ions/cm² in b), c) and d) respectively.

Now let's return to the behavior of the minority peaks as a function of the ion fluence. Between 10^{14} and 10^{16} ions/cm², we are not able to detect it anymore, neither in hard axis 2 nor in easy axis 1 (as for the reference sample). Most probably because it is mixed up with the majority peak. Reaching 10^{16} ions/cm², it is visible again in the hard axis 2 direction. Increasing further the fluence to 10^{17}, both peaks become detectable in the hard axis 2 and easy axis 1 directions, as for the reference sample. This is shown in figures 5.22-a and 5.22-b. Likewise the samples of N°1 series, here we were not able to detect the second peak for the two other magnetic directions. At this point we are not able to explain why we cannot observe it in the four directions. Interestingly, the resonance field for the minority peak at fluence of 10^{17} is similar to the one of the reference sample. From the *fres* vs. $\mu_0 H_0$ curve at 10^{17} ions/cm² (Figure 5.22-c) we extract the magnetic parameters of this phase. We find that they are very close to the magnetic parameters of the reference sample) initial crystal order. As for N°1 series, we believe that it corresponds to the reinforcement of the B2 order, which would also show a small amount of Co-Si disorder as its magnetization amplitude is slightly lower than for the N°1 series.

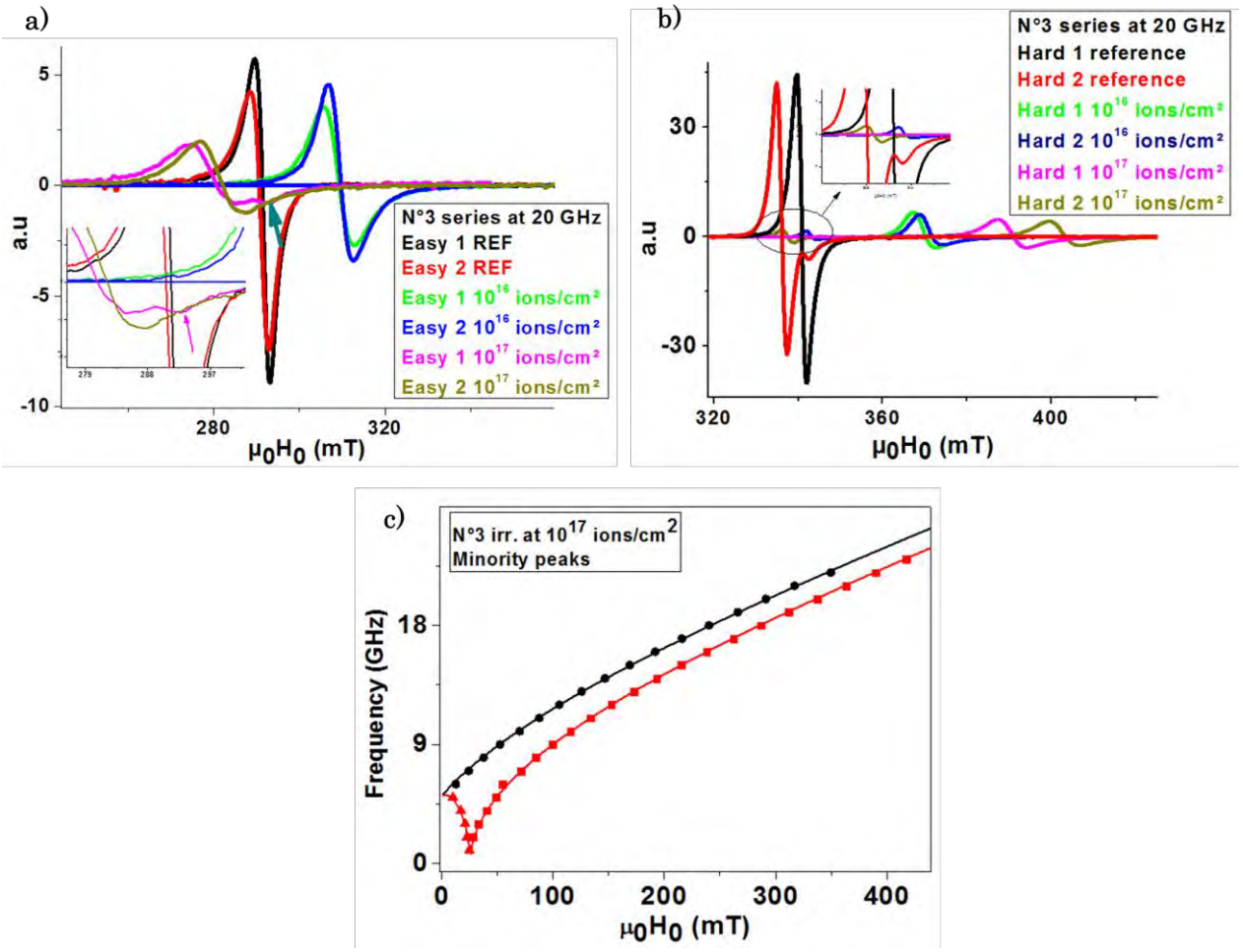

Figure 5.22: In a) and b) Comparison of the two easy and two hard axes respectively FMR absorption spectra at 20 GHZ for N°3 series for reference and irradiated samples at 10^{16} and 10^{17} ions/cm². Figure c) f_{res} vs. $\mu_0 H_0$ at lower magnetic fields (minority peaks) are traced forN°3 sample irradiated at 10^{17} ions/cm².

N°3 series (ions/cm²)	Ref	Irr. at 10^{14}	Irr. at 10^{15}	Irr. at 10^{16}	Irr. at 10^{17}
μ_0Ms1 (T)	1.25 ±0.02	1.24±0.02	1.21± 0.02	1.06± 0.02	1.02± 0.02
μ_0Ms2 (T)					1.24 ±0.02
μ_0Hk$_1$ (mT)	28± 0.5	28±0.5	28± 0.5	36.5 ± 0.5	69 ± 0.5
μ_0Hk$_2$ (mT)					25.5 ±0.5
γ_1 (GHz/T)	28.7± 0.1	28.8± 0.1	28.85 ± 0.1	29.4 ± 0.1	30.2 ±0.1
γ_2 (GHz/T)					28.7 ±0.2
φ_u (deg)	45 ±1	45 ±1	45 ± 1	135 ±1	140 ±2
μ_0H$_u$ (mT)	2 ± 0.2	1.8 ±0.2	1.8 ± 0.2	1 ± 0.2	4.5 ±0.2
A1 (pJ/m)	18±0.1	18 ± 0.1	17.5± 0.1	12±0.1	

Table 5.5: Magnetic parameters extracted from FMR spectra for N°3 series as a function of the fluence.

In conclusion, The L2$_1$ order of this series of samples shows similar behavior for the magnetic parameters than the samples of series N°1, even if the variations as a function of the fluence are more pronounced here. Also, this series shows some interesting behavior of the uniaxial anisotropy which has to be related to the cell distortion induced by the irradiation, and also the chemical modification of the main phase. A full understanding of the evolution of the magnetic parameters implies a complete structural analysis for fluence above 10^{16} ions/cm².

It is very interesting as it allows to state about the structural origin of the uniaxial anisotropy observed in many systems, especially in Co_2MnSi or Co_2FeSi but most probably also for Iron and others that show cubic anisotropy. In addition the fact that the amplitude of the anisotropy decreases at fluence above 10^{16} ions/cm² is also in agreement with a relaxation of the starin for high deformation and high density of local defects.

5.3.3 Effect of He⁺ irradiation on the Gilbert Damping

- **Sample N°1 series:**

The study of the linewidth as a function of the ion fluence for the $L2_1$ and B2 order for the series of N°1 sample is presented in figure 5.23. In this figure we only present the evolution of the linewidth for the magnetic directions for which the two peaks are sufficiently well resolved to avoid a too important uncertainty, as for example of strong mixing of the two modes. This is why we do not show the linewidth of the B2 order in the easy directions for fluence of $5*10^{15}$ ions/cm². The values of the damping factor with the extrinsic linewidth of N°1 series are presented in table 5.6

Two main features are observed depending on the crystal order. For the B2 order, the linewidth first decrease for a fluence of 10^{15} ions/cm², with a very clear improvement of the extrinsic contribution ΔH_0. It is also accompanied by an enhancement of the effective damping coefficient, especially in the easy axis direction for which the value is almost divided by 2. This behavior for relatively low fluence is most probably to be related to the improvement of the long range order of the B2 phase as demonstrated by Gaier *et al* [10 Gaier]. As already mentioned, irradiation acts similarly as a local temperature annealing at low fluences. Then, as the size of the B2 crystallite grows, the coherence of the precession for this crystal phase is improved, decreasing the extrinsic linewidth. Then we believe that it is the inhomogeneity contribution (variation of μ_0Ms, μ_0Hk, crystallite size etc...) to the extrinsic damping coefficient that decreases. For higher fluences, the damping coefficient is found to be roughly equivalent as for the reference sample while the ΔH_0 increases. This is in agreement with the inclusion of local point defects induced by the irradiation which is probably at the origin of two magnons scattering process.

For the $L2_1$ phase, the situation is different. Irradiation is found to increase both the effective damping coefficient and the ΔH_0 contribution for the easy and the hard axis directions. The increase of the extrinsic contribution is most probably of the same origin as for the B2 order. However, the origin of the evolution of the intrinsic contribution α is most probably to be related to the chemical disorder in the matrix. Indeed, the α parameter is strongly dependent on the local atomic arrangement as it can modify either the spin-orbit mediated relaxation mechanisms (see chap II) or the orbital and spin magnetic moments and then the **g** values for example. We recall that in the Kamberský model of relaxation in ferromagnets [13, 14 Kamberský and 15 pelzl], the damping coefficient is related to the Gilbert relaxation coefficient G through the relation α=G*4π/($\mu_0 M_s \gamma$). In addition, the Gilbert damping coefficient G depends on the g value and on the spin-orbit coupling coefficient λ_{SO} through the relation $G_{os} = (\gamma\hbar/2)^2 Z_f \lambda_{so}^2 (g-2)^2 \tau$. In figure 5.24, we report on the evolution of the Gilbert damping constant G as a function of (g-2)² calculated with the values of table 5.3. For this crystal order, the g value increases for all fluences. Of course, we have only a few points but we can see that either for the easy or hard axis, the relation is almost linear, meaning that the amplitude of the spin-orbit coupling λ_{SO} is probably constant with the ion fluence. This result shows that the damping coefficient is here dominated by spin-orbit interaction without spin-flip interaction (what is called ordinary damping in the Kamberský model).

This interesting result has to be emphasized on as one could expect some spin flip scattering at the Fermi level. Indeed, the decrease of the magnetization amplitude was accounted for a the Co/Mn exchange and so on the closure of the energy band gap for spin up and spin down states. This result also impacts the understanding of the evolution of the

crystal anisotropy. Indeed, in the model of Bruno [16 Bruno], the crystal anisotropy is roughly proportional to λ^2_{SO}, as for the Gilbert damping. As this parameter is found constant we can assume that the increase anisotropy is related to the increase of orbital moment μ_L as g increases with the ration μ_L/μ_S.

Therefore, our conclusion is that the Co-Mn exchange induces in this sample an increase of the orbital moment in the $L2_1$ phase which goes along with an increase of the g values and of the anisotropy. For the B2 order, ion irradiation is found to be an interesting technique to improve the microwave linewidth as long as the fluence is kept relatively low. Based on the results of Gaier *et al* we assume that this effect is related to the improvement of the long range order for this crystal phase. The other interesting feature is the fact that the effective damping of the B2 order is not especially impacted by the irradiation while the extrinsic contribution is.

From a fundamental point of view, ion irradiation is then particularly interesting to probe the different contributions to the dynamic relaxation mechanisms depending on the initial crystal order, as for example the effect of local defects on the extrinsic mechanisms or the relation between the energy spin gap and the intrinsic relaxation.

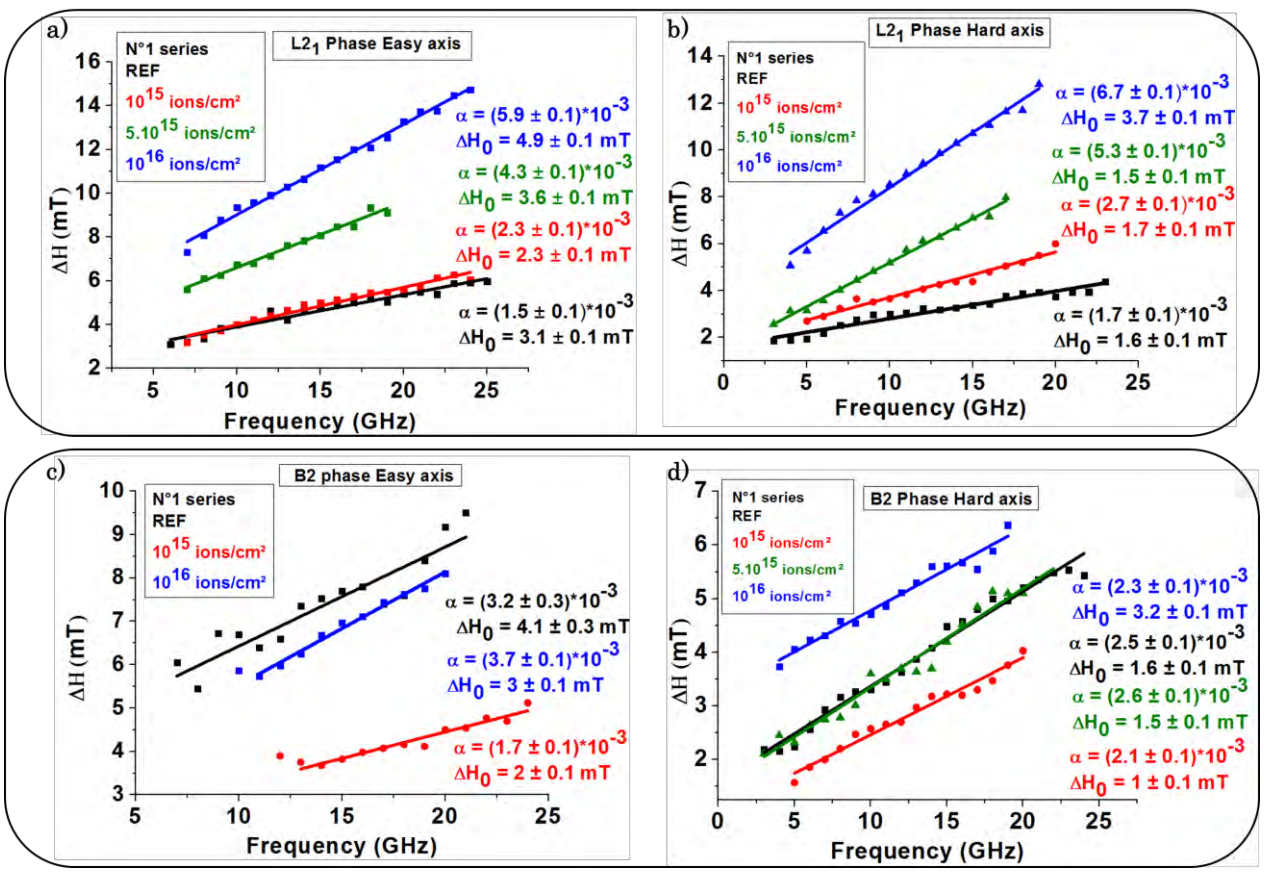

Figure 5.23: Evolution of linewidth measurements ΔH vs. f_{res} for N°1 series for both $L2_1$ and B2 phases. In a) and b) we can see the evolution of damping coefficient and extrinsic linewidth contribution ΔH_0 for $L2_1$ phase as irradiation dose increases, while in c) and d) the damping factor is kept almost constant for B2 phase with an increase in ΔH_0.

N°1 series ions/cm²	$L2_1$ Easy axis	B2 Easy axis	$L2_1$ Hard axis	B2 Hard axis
Ref	$\boldsymbol{\alpha} = (1.5\pm\mathbf{0.1})*10^{-3}$ $\Delta\boldsymbol{H_0} = \mathbf{3.1\ mT}$	$\boldsymbol{\alpha} = (3.2\pm\mathbf{0.3})*10^{-3}$ $\Delta\boldsymbol{H_0} = \mathbf{4.1\ mT}$	$\boldsymbol{\alpha} = (1.7\pm\mathbf{0.1})*10^{-3}$ $\Delta\boldsymbol{H_0} = \mathbf{1.6\ mT}$	$\boldsymbol{\alpha} = (2.5\pm\mathbf{0.1})*10^{-3}$ $\Delta\boldsymbol{H_0} = \mathbf{1.6\ mT}$
Irr. at 10^{15}	$\boldsymbol{\alpha} = (2.3\pm\mathbf{0.1})*10^{-3}$ $\Delta\boldsymbol{H_0} = \mathbf{2.3\ mT}$	$\boldsymbol{\alpha} = (1.7\pm\mathbf{0.1})*10^{-3}$ $\Delta\boldsymbol{H_0} = \mathbf{2\ mT}$	$\boldsymbol{\alpha} = (2.7\pm\mathbf{0.1})*10^{-3}$ $\Delta\boldsymbol{H_0} = \mathbf{1.7\ mT}$	$\boldsymbol{\alpha} = (2.1\pm\mathbf{0.1})*10^{-3}$ $\Delta\boldsymbol{H_0} = \mathbf{1\ mT}$
Irr. at $5*10^{15}$	$\boldsymbol{\alpha} = (4.3\pm\mathbf{0.1})*10^{-3}$ $\Delta\boldsymbol{H_0} = \mathbf{3.6\ mT}$	-	$\boldsymbol{\alpha} = (5.3\pm\mathbf{0.1})*10^{-3}$ $\Delta\boldsymbol{H_0} = \mathbf{1.5\ mT}$	$\boldsymbol{\alpha} = (2.6\pm\mathbf{0.1})*10^{-3}$ $\Delta\boldsymbol{H_0} = \mathbf{1.5\ mT}$
Irr. at 10^{16}	$\boldsymbol{\alpha} = (5.9\pm\mathbf{0.1})*10^{-3}$ $\Delta\boldsymbol{H_0} = \mathbf{4.9\ mT}$	$\boldsymbol{\alpha} = (3.7\pm\mathbf{0.1})*10^{-3}$ $\Delta\boldsymbol{H_0} = \mathbf{3\ mT}$	$\boldsymbol{\alpha} = (6.7\pm\mathbf{0.1})*10^{-3}$ $\Delta\boldsymbol{H_0} = \mathbf{3.7\ mT}$	$\boldsymbol{\alpha} = (2.3\pm\mathbf{0.1})*10^{-3}$ $\Delta\boldsymbol{H_0} = \mathbf{3.2\ mT}$

Table 5.6: damping factor $\boldsymbol{\alpha}$ and extrinsic line width $\Delta\mathbf{H_0}$ values for both one easy and one hard axis of $L2_1$ and B2 phases in the series of sample N°1 reference and irradiated samples.

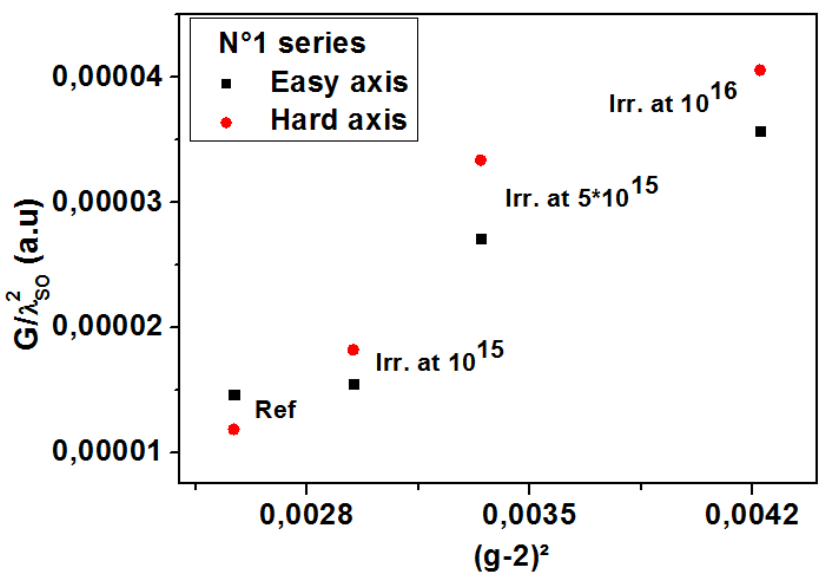

Figure 5.24: Gilbert coefficient $G/\boldsymbol{\lambda_{SO}^2}$ as a function of $(g-2)^2$ for the $L2_1$ order in the easy (black) and hard (red) directions. The values given on the graph corresponds to the different fluence at which $(g-2)^2$ has been calculated.

.

- **<u>Sample N°2 series:</u>**

The evolution of the linewidth for each magnetic direction as a function of the fluence is shown in figure 5.25. Basically, the damping coefficient in every direction is found to be

roughly constant for fluence up to $5*10^{15}$ ions/cm², similarly as for the B2 crystal order of series N°1. However, it increases at higher fluence, as for the $L2_1$ crystal order in series N°1. This behavior is similar to the one observed for the samples of series N°3 (see below). The increase at high fluence is most probably to be related to the strong increase of the atomic disorder above $5*10^{15}$ in agreement with the sharp decrease of the magnetization of the $L2_1$ phase. Concerning the extrinsic contribution ΔH_0, it is found to increase with the ion fluence, especially above $5*10^{15}$, in agreement with enhanced scattering events due to the increased density of defects.

We also notice that for fluences of 10^{14} and 10^{15} ions/cm², for which the internal structure is barely modified, the damping coefficient is found to improve in the hard 1 direction as compared to the reference sample but the ΔH_0 is at the same time increased by almost a factor of two. The observed difference of α are well above the uncertainty of the measurement. However, the origin of this effect is not clear. Indeed, we know that the order of the $L2_1$ phase is not improved at this fluence since the magnetization amplitude decreases. So the improvement of α cannot be related to some improvement of the chemical ordering. If the origin relies on inhomogeneity in the samples, both the ΔH_0 and α would show the same behavior, which is not the case. It is also particularly surprising that such effect appears only in one direction. It is maybe to be related to the rotation of the uniaxial anisotropy toward the hard axis 1 at 10^{15} ions/cm² meaning that mechanical strain could plays a role in the amplitude of the intrinsic damping in Co_2MnSi. However, further experiments are needed to validate this hypothesis, especially phi scans that are not performed on the irradiated samples of this series.

In conclusion, as compared to the series of sample N°1, the series of N°2 shows some feature similar to the B2 and $L2_1$ crystal order. Additionally, it is possible that the presence of the uniaxial anisotropy modifies the intrinsic damping in particular magnetic axis. However, the global behavior at high fluence is in agreement with the first series.

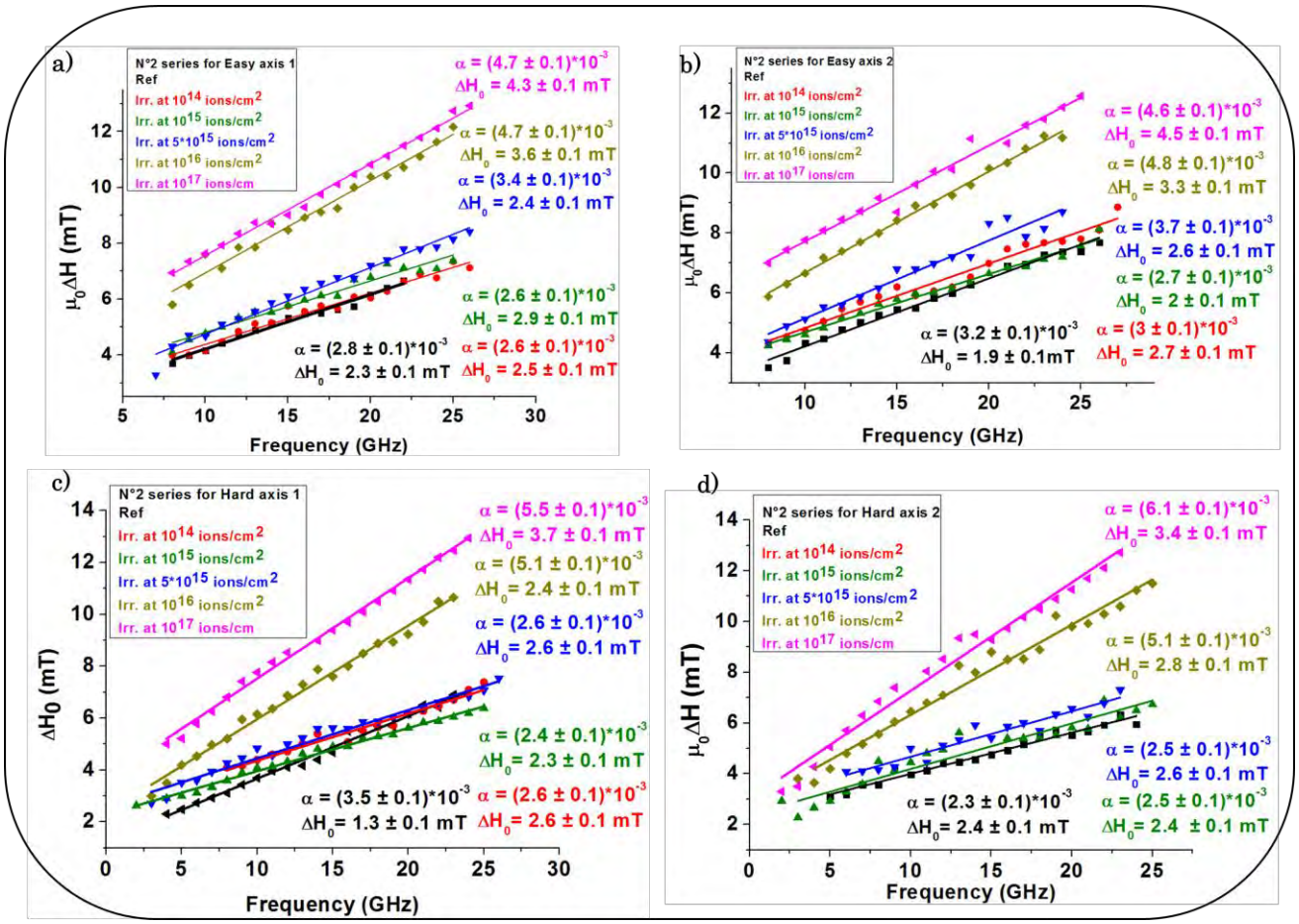

Figure 5.25: Evolution of damping coefficient and extrinsic linewidth contribution ΔH_0 as a function of irradiation dose from ΔH vs. f_{res} measurements for N°2 series along the two easy and two hard axes.

Finally we compare, the value of the linewidths in the hard axes direction for the two modes observed at 10^{17} ions/cm². We clearly observe, in Figure 5.26, that the second phase presents a lower linewidth with lower damping and ΔH_0, as expected from the improvement of B2 order. However, the values of the damping are higher than for the samples of series N°1 exhibiting clear B2 order. This is in agreement with our assumption that this sample exhibit Co/Si exchange even in the B2 phase. The damping factor and extrinsic line width values of N°2 are presented in Table 5.7.

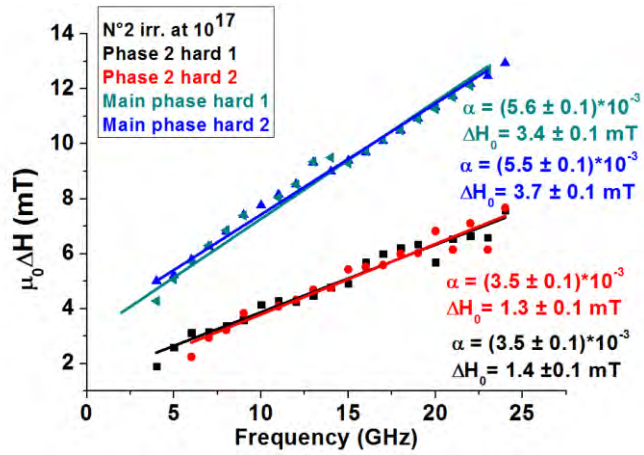

Figure 5.26: Comparison between the two phases in hard axis 1 and 2 for sample N°2 irradiated at 10^{17} ions/cm² as the damping factor $\boldsymbol{\alpha}$ and extrinsic linewidth $\Delta \boldsymbol{H_0}$ is lower for the second phase than the main phase.

N°2 series (ions/cm²)	Easy axis1	Easy axis 2	Hard axis 1	Hard axis 2
Ref	$\boldsymbol{\alpha} = (2.8 \pm \mathbf{0.1})*10^{-3}$ $\Delta \boldsymbol{H_0} = \mathbf{2.3\ mT}$	$\boldsymbol{\alpha} = (3.2 \pm \mathbf{0.3})*10^{-3}$ $\Delta \boldsymbol{H_0} = \mathbf{1.9\ mT}$	$\boldsymbol{\alpha} = (3.5 \pm \mathbf{0.1})*10^{-3}$ $\Delta \boldsymbol{H_0} = \mathbf{1.3\ mT}$	$\boldsymbol{\alpha} = (2.3 \pm \mathbf{0.1})*10^{-3}$ $\Delta \boldsymbol{H_0} = \mathbf{2.4\ mT}$
Irr. at 10^{14}	$\boldsymbol{\alpha} = (2.6 \pm \mathbf{0.1})*10^{-3}$ $\Delta \boldsymbol{H_0} = \mathbf{2.5\ mT}$	$\boldsymbol{\alpha} = (3 \pm \mathbf{0.1})*10^{-3}$ $\Delta \boldsymbol{H_0} = \mathbf{2.7\ mT}$	$\boldsymbol{\alpha} = (2.6 \pm \mathbf{0.1})*10^{-3}$ $\Delta \boldsymbol{H_0} = \mathbf{2.6\ mT}$	-
Irr. at 10^{15}	$\boldsymbol{\alpha} = (2.6 \pm \mathbf{0.1})*10^{-3}$ $\Delta \boldsymbol{H_0} = \mathbf{2.9\ mT}$	$\boldsymbol{\alpha} = (2.7 \pm \mathbf{0.1})*10^{-3}$ $\Delta \boldsymbol{H_0} = \mathbf{2\ mT}$	$(2.4 \pm \mathbf{0.1})*10^{-3}$ $\Delta \boldsymbol{H_0} = \mathbf{2.3\ mT}$	$\boldsymbol{\alpha} = (2.5 \pm \mathbf{0.1})*10^{-3}$ $\Delta \boldsymbol{H_0} = \mathbf{2.4\ mT}$
Irr. at $5*10^{15}$	$\boldsymbol{\alpha} = (3.4 \pm \mathbf{0.1})*10^{-3}$ $\Delta \boldsymbol{H_0} = \mathbf{2.4\ mT}$	$\boldsymbol{\alpha} = (3.7 \pm \mathbf{0.1})*10^{-3}$ $\Delta \boldsymbol{H_0} = \mathbf{2.6\ mT}$	$\boldsymbol{\alpha} = (2.6 \pm \mathbf{0.1})*10^{-3}$ $\Delta \boldsymbol{H_0} = \mathbf{2.6\ mT}$	$\boldsymbol{\alpha} = (2.5 \pm \mathbf{0.1})*10^{-3}$ $\Delta \boldsymbol{H_0} = \mathbf{2.6\ mT}$
Irr. at 10^{16}	$\boldsymbol{\alpha} = (4.7 \pm \mathbf{0.1})*10^{-3}$ $\Delta \boldsymbol{H_0} = \mathbf{3.6\ mT}$	$\boldsymbol{\alpha} = (4.8 \pm \mathbf{0.3})*10^{-3}$ $\Delta \boldsymbol{H_0} = \mathbf{3.3\ mT}$	$\boldsymbol{\alpha} = (5.1 \pm \mathbf{0.1})*10^{-3}$ $\Delta \boldsymbol{H_0} = \mathbf{2.4\ mT}$	$\boldsymbol{\alpha} = (5.1 \pm \mathbf{0.1})*10^{-3}$ $\Delta \boldsymbol{H_0} = \mathbf{2.8\ mT}$
Irr. at 10^{17}	$\boldsymbol{\alpha} = (4.7 \pm \mathbf{0.1})*10^{-3}$ $\Delta \boldsymbol{H_0} = \mathbf{4.3\ mT}$	$\boldsymbol{\alpha} = (4.6 \pm \mathbf{0.1})*10^{-3}$ $\Delta \boldsymbol{H_0} = \mathbf{4.5\ mT}$	$\boldsymbol{\alpha} = (5.5 \pm \mathbf{0.1})*10^{-3}$ $\Delta \boldsymbol{H_0} = \mathbf{3.7\ mT}$	$\boldsymbol{\alpha} = (6.1 \pm \mathbf{0.1})*10^{-3}$ $\Delta \boldsymbol{H_0} = \mathbf{3.4\ mT}$

Table 5.7: damping factor $\boldsymbol{\alpha}$ and extrinsic line width contribution $\Delta \boldsymbol{H_0}$ values for N°2 series reference and irradiated samples along the two easy and two hard axes.

- **<u>Sample N°3 series:</u>**

For this series of sample we always observe that the linewidths for the easy axes are bigger than for the hard axes whatever the ion fluence. This is shown in figure 5.27, which presents the linewidths in the four magnetic directions at different fluence for the $L2_1$ order. Moreover the easy axis 2 shows higher linewidth and effective damping than the easy axis 1, except at 10^{16} and 10^{17} ions/cm² for which the situation is inversed.

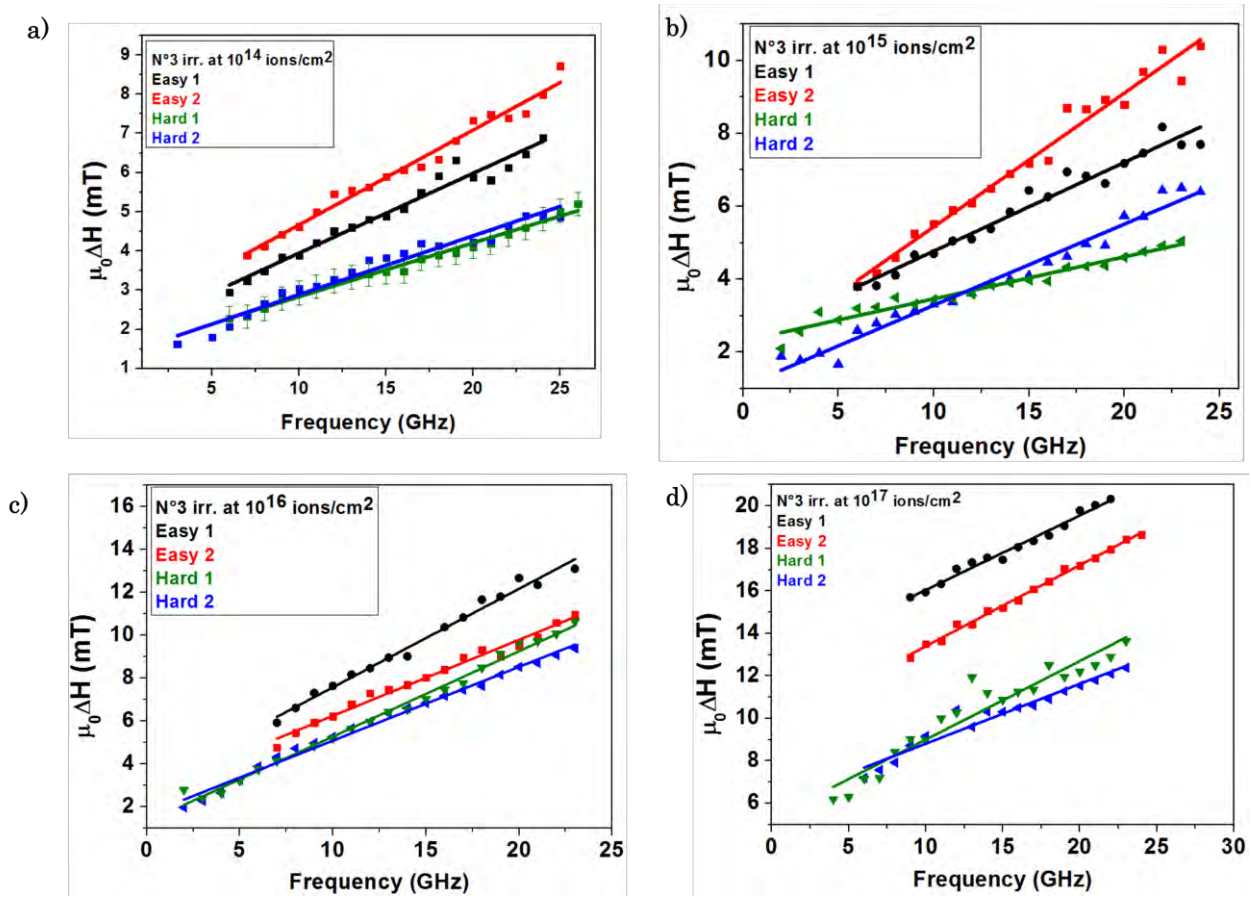

Figure 5.27: $\Delta \boldsymbol{H}$ vs. $\boldsymbol{f_{res}}$ measurements of N°3 series irradiated samples from 10^{14} to 10^{17} ions/cm² along the 4 axes directions shows clearly that the easy axes have higher $\Delta \boldsymbol{H}$ than hard axes.

In figure 5.28 we present the evolution of the linewidth in each magnetic direction as a function of the ion fluence of sample N°3 series. Same general tendencies as for the samples of series N°1 and N°2 are visible, i.e., an increase of the effective damping coefficient and extrinsic contribution ΔH_0 with the ion fluence up to 10^{16} ions/cm². However at 10^{17}, the damping coefficient tends to saturate while the ΔH_0 becomes very important, the latter point being in agreement with the expectation of the TRIM simulations (figure 5.3).

At 10^{14} and 10^{15} ions/cm², the evolution of the linewidth is similar to the situation encountered for the samples of series N°2. Indeed for all directions, the linewidths are roughly

similar as a function of the fluence, except for the hard axis 2 for which a clear increase at 10^{14} of the α is observed. This increase is accounted for the mixing of the $L2_1$ and B2 resonance at this fluence, as shown in figure 5.20-b. The values of damping factor and extrinsic line width of N°3 are presented in Table 5.8.

At 10^{16} some particular feature appears. In addition to the fact that the linewidth of the easy axis 1 becomes more important than the linewidth of the easy axis 2, we observe that the increase damping coefficient for the hard and easy axes 1 increase much more than the one of the hard and easy axes 2. Interestingly this change arises for the fluence for which the uniaxial anisotropy is found to switch from one hard axis to the other. It is possible that this measurement shows the effect of the mechanical deformation of the value of the intrinsic damping in the Co_2MnSi. However this tendency is not observed anymore at 10^{17} ions/cm². Maybe it is due to the fact that the material has suffered strong internal chemical and mechanical deformation at this fluence, changing drastically the relaxation mechanisms. Then it is possible that this measurement shows the effect of the mechanical deformation of the value of the intrinsic damping in the Co_2MnSi but it is very difficult to conclude of this point as the effect at very high fluence does not confirm the tendency. Further measurements at some intermediate fluence between $5*10^{15}$ and 10^{17} should be necessary to follow the evolution of the damping with more precision. Also, a full structural characterization of the lattice parameter and deformation is needed.

As the gyromagnetic ratio and cubic anisotropy were found to increase with the fluence, we also studied the evolution of $G/\boldsymbol{\lambda_{SO}^2}$ as a function of $(g-2)^2$. The result is shown in Figure 5.29 for fluence up to 10^{16} ions/cm². We consider only the $L2_1$ crystal order and we compare it with the one calculated for the samples of series N°1 and N°3 in the hard axis. Clearly, for the sample of series N°3, we do not observe the same linear variation as for series N°1. This demonstrates that the damping is not governed only by ordinary scattering in this sample and spin flip scattering processes are allowed. The difference between the series N°1 and N°3 may have to be related to the different Co/Si exchange that arises for sample N°3, meaning that this kind of disorder strongly modifies the intrinsic relaxation mechanisms.

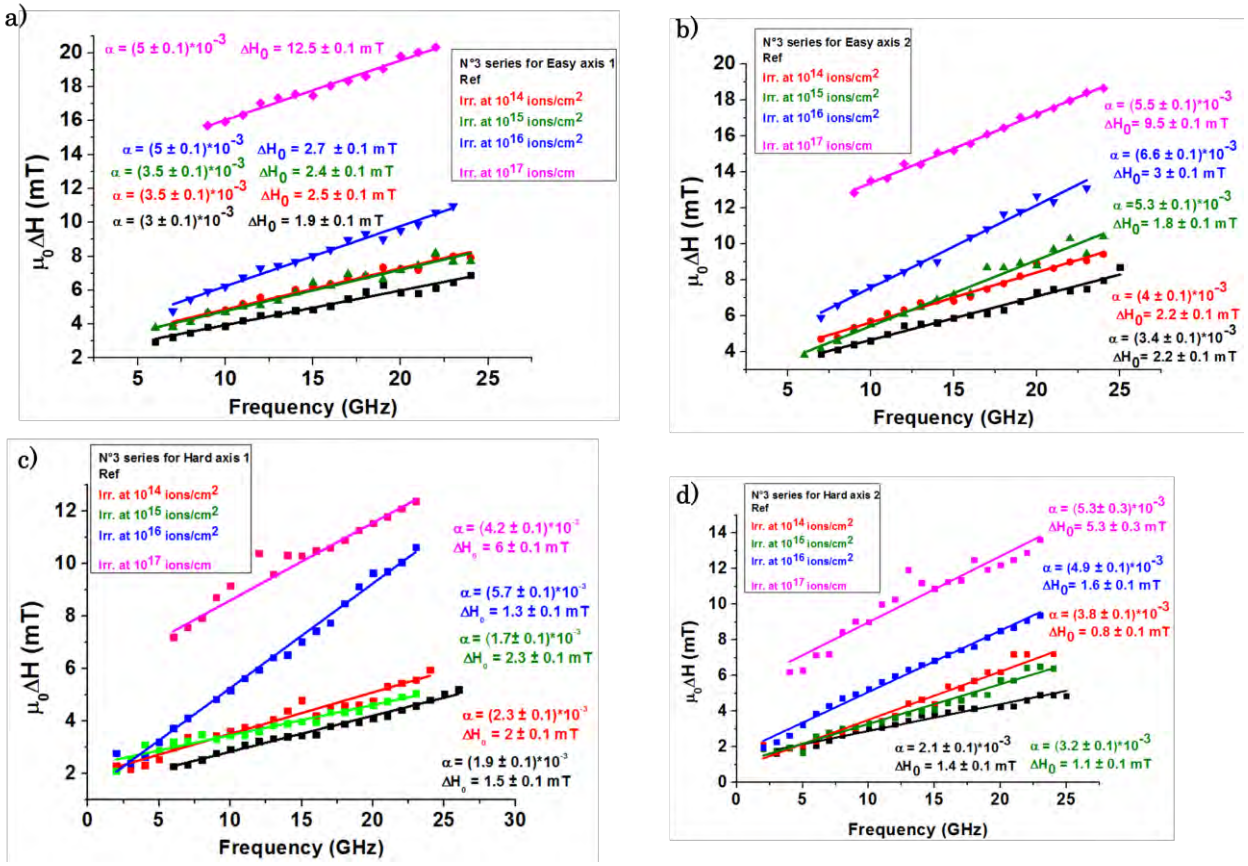

Figure 5.28: Evolution of damping coefficient and extrinsic linewidth contribution ΔH_0 as a function of irradiation dose from ΔH vs. f_{res} measurements for N°3 series along the two easy and two hard axes.

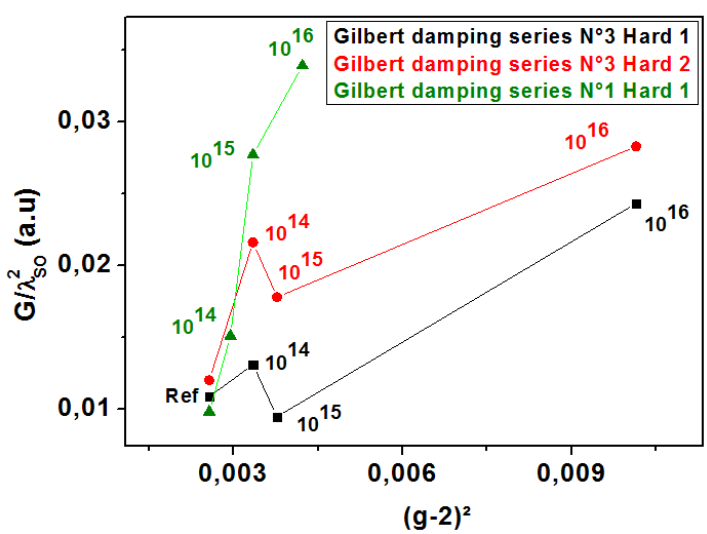

Figure 5.29: A comparison between the evolution of G/λ_{SO}^2 as a function of $(g-2)^2$ along one hard axis for N°1 series and two hard axis for N°3 series.

Finally, the values of the linewidth for the two crystal orders at 10^{17} ions/cm² in figure 5.30 are compared. Clearly, the expected B2 order shows much narrower linewidths as compared to the main phase. Indeed, we find some values of the effective damping down to $1.5*10^{-3}$ in the hard axis direction, which is very good taking into account the induced disorder by irradiation.

N°3 series ions/cm²	Easy axis1	Easy axis 2	Hard axis 1	Hard axis 2
Ref	$\boldsymbol{\alpha}$ =(3±**0.1**)*10^{-3} $\Delta \boldsymbol{H_0} = \mathbf{1.9\ mT}$	$\boldsymbol{\alpha}$ =(3.**4** ± **0.1**)*10^{-3} $\Delta \boldsymbol{H_0} = \mathbf{2.2\ mT}$	$\boldsymbol{\alpha}$ = (1.9±**0.1**)*10^{-3} $\Delta \boldsymbol{H_0} = \mathbf{1.5\ mT}$	$\boldsymbol{\alpha}$ =(2.1±**0.1**)*10^{-3} $\Delta \boldsymbol{H_0} = \mathbf{1.4\ mT}$
Irr. at 10^{14}	$\boldsymbol{\alpha}$ = (3.5±**0.1**)*10^{-3} $\Delta \boldsymbol{H_0} = \mathbf{2.5\ mT}$	$\boldsymbol{\alpha}$ = (4±**0.1**)*10^{-3} $\Delta \boldsymbol{H_0} = \mathbf{2.2\ mT}$	$\boldsymbol{\alpha}$ = (2.3±**0.1**)*10^{-3} $\Delta \boldsymbol{H_0} = \mathbf{2\ mT}$	$\boldsymbol{\alpha}$ =(3.2±**0.1**)*10^{-3} $\Delta \boldsymbol{H_0} = \mathbf{1.1\ mT}$
Irr. at 10^{15}	$\boldsymbol{\alpha}$ = (3.5±**0.1**)*10^{-3} $\Delta \boldsymbol{H_0} = \mathbf{2.4\ mT}$	$\boldsymbol{\alpha}$ =(5.3±**0.1**)*10^{-3} $\Delta \boldsymbol{H_0} = \mathbf{1.8\ mT}$	(1.7±**0.1**)*10^{-3} $\Delta \boldsymbol{H_0} = \mathbf{2.3\ mT}$	$\boldsymbol{\alpha}$ =(3.8±**0.1**)*10^{-3} $\Delta \boldsymbol{H_0} = \mathbf{0.8\ mT}$
Irr. at 10^{16}	$\boldsymbol{\alpha}$ = (5±**0.1**)*10^{-3} $\Delta \boldsymbol{H_0} = \mathbf{2.7\ mT}$	$\boldsymbol{\alpha}$ =(6.**6** ± **0.1**)*10^{-3} $\Delta \boldsymbol{H_0} = \mathbf{3\ mT}$	$\boldsymbol{\alpha}$ = (5.7±**0.1**)*10^{-3} $\Delta \boldsymbol{H_0} = \mathbf{1.3\ mT}$	$\boldsymbol{\alpha}$ =(4.9±**0.1**)*10^{-3} $\Delta \boldsymbol{H_0} = \mathbf{1.6\ mT}$
Irr. at 10^{17}	$\boldsymbol{\alpha}$ = (5±**0.1**)*10^{-3} $\Delta \boldsymbol{H_0} = \mathbf{12.5\ mT}$	$\boldsymbol{\alpha}$ = (5.5±**0.1**)*10^{-3} $\Delta \boldsymbol{H_0} = \mathbf{9.5\ mT}$	$\boldsymbol{\alpha}$ = (4.2±**0.2**)*10^{-3} $\Delta \boldsymbol{H_0} = \mathbf{6\ mT}$	$\boldsymbol{\alpha}$ =(5.3±**0.3**)*10^{-3} $\Delta \boldsymbol{H_0} = \mathbf{5.3\ mT}$

Table 5.8: damping factor $\boldsymbol{\alpha}$ and extrinsic line width $\Delta \boldsymbol{H_0}$ values for N°3 series reference and irradiated samples along the two easy and two hard axes.

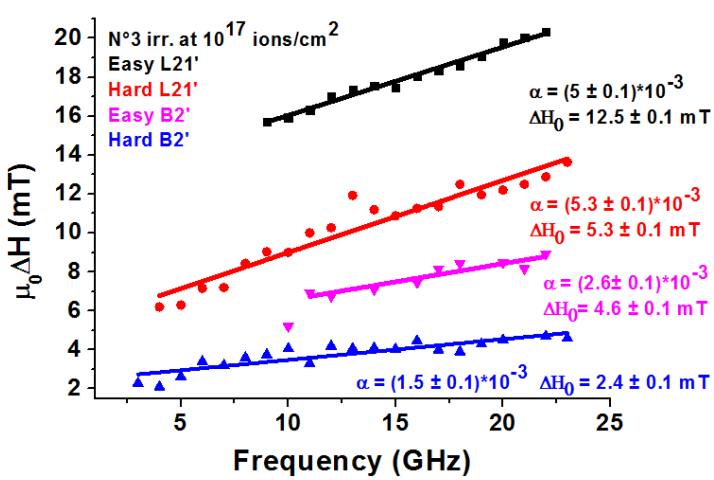

Figure 5.30: A comparison of the damping factor $\boldsymbol{\alpha}$ and the linewidth ΔH_0 for two crystal order of N°3 sample irradiated at 10^{17} ions/cm².

In conclusion, this series of samples shows similar behavior as the sample of series N°1 and N°2 with an increased intrinsic and extrinsic contribution at fluence above 10^{16} ions/cm². However the study of the Gilbert coefficient shows that relaxation mechanisms must differ in this series as compared to the series N°1. We also observed that the intrinsic damping of the B2 order induced by ion irradiation is much lower than for the modified $L2_1$' phase, as we reach values of $1.5*10^{-3}$ in the hard axis direction. Finally, it is possible that the mechanical strain play a role in the value of the damping coefficient but further experiments at intermediate fluence are required to validate our assumption.

Conclusion

In conclusion, we have presented three series of samples which shows different magnetic behaviors and different initial atomic disorder. The main observations are summarized below:

- Structural analysis performed by X-ray and HAADF-STEM imaging have shown that ion irradiation induces atomic disorder in Co_2MnSi alloys, especially for fluence above $5*10^{15}$ ions/cm². For the three series of samples we assume that ion irradiation favors the B2 crystal order to the cost of the $L2_1$ order. On the other hand, the structural analysis performed on the series N°1 and N°3 shows that the $L2_1$ order is submitted to a Co-Mn ($D0_3$ type) disorder and/or Co-Si exchange.

- Ion irradiation has been found to increase the out of plane lattice parameter of the alloy. This induces a tetragonal (and maybe orthorhombic at fluence of 10^{17} ions/cm² for the series N°3) distortion of the unit cell. At the same time, in each series of samples, we observe the rotation and modification of the amplitude of the uniaxial anisotropy when increasing the fluence, until the material is fully relaxed. Then we believe that structural deformation and uniaxial anisotropy must be related, the latter being a consequence of the mechanical strain induced by lattice deformation.

- The local defects induced by ion irradiation have been showed to increase the coercive field of the samples of series N°1, meaning that the switching mechanism of this series is governed by propagation effects.

- The static magnetic parameters (Ms, Hk, A) has been found to be unaffected by irradiation for the B2 order. For the $L2_1$ order, ion irradiation induces a decrease of the magnetization and exchange amplitude while the cubic anisotropy and gyromagnetic ratio increases. We assume that it is due to the modification of the local environment of the Mn atoms. We believe that atomic disorder on Co sites (i.e. Co/Mn or Co/Si exchange) leads to a closing of the spin splitting at the Fermi level, inducing a lower magnetization and exchange values, in agreement with theoretical predictions in literature. Moreover the atomic disorder is assumed to increase the orbital moment on the Mn atoms and the spin-orbit coupling, explaining the behavior of the gyromagnetic ratio and anisotropy.

The effect of ion irradiation on the FMR linewidth has been found to depend on the initial crystal order:

- For the B2 order, we observe on series N°1 a clear improvement of the extrinsic contribution ΔH_0 for fluence up to 10^{15} ions/cm², which is in agreement with previous report by Gaier *et al* of the improvement of long range order in B2 phase at low fluence. At higher fluence the ΔH_0 increases in agreement with the creation of local defects such as vacancies and interstitial in the alloy. We also observed that the effective damping α was roughly constant, even at high fluence such as 10^{17} for the series N°2 and N°3. This means that most probably the B2 order is not summited to strong chemical atomic disorder. On the samples of series N°2 and N°3, the value of the effective damping of the expected B2 order at 10^{17} ions/cm² has been found in very good agreement with the value of the B2 phase for the series N°1.

- For the $L2_1$ phase, the general tendency is an increase of the effective damping with the fluence. This is in agreement with the reduced magnetization if spin-flip scattering relaxation is allowed, and also with the increased spin-orbit interaction observed for the cubic anisotropy. Beside this, the effective α was found to be improved in the direction of the uniaxial anisotropy for the series N°2 at low fluence, while it was found to be degraded for the series N°3. Finally, we were not able to state about the possible relation between the mechanical deformation induced in the matrix and the evolution of the effective damping. Further studies such as angle dependence of the linewidths, and measurements are intermediate fluence for which the relaxation appear are required to conclude on this point.

Chapter 5 References:

[1] J. Fassbender, D. Ravelosona, et Y. Samson, « Tailoring magnetism by light-ion irradiation », *J. Phys. Appl. Phys.*, vol. 37, nº 16, p. R179, août 2004.

[2] J. Fassbender et J. McCord, « Control of saturation magnetization, anisotropy, and damping due to Ni implantation in thin $Ni_{81}Fe_{19}$ layers », *Appl. Phys. Lett.*, vol. 88, nº 25, p. 252501, 2006.

[3] J. Fassbender, S. Poppe, T. Mewes, A. Mougin, B. Hillebrands, D. Engel, M. Jung, A. Ehresmann, H. Schmoranzer, G. Faini, K. j. Kirk, et J. n. Chapman, « Magnetization Reversal of Exchange Bias Double Layers Magnetically Patterned by Ion Irradiation », *Phys. Status Solidi A*, vol. 189, nº 2, p. 439‑447, février 2002.

[4] D. Ravelosona, C. Chappert, H. Bernas, D. Halley, Y. Samson, et A. Marty, « Chemical ordering at low temperatures in FePd films », *J. Appl. Phys.*, vol. 91, p. 8082‑8084, 2002.

[5] D. Ravelosona, C. Chappert, V. Mathet, et H. Bernas, « Chemical order induced by ion irradiation in FePt (001) films », *Appl. Phys. Lett.*, vol. 76, nº 2, p. 236, 2000.

[6] J. F. Ziegler et J. P. Biersack, « The Stopping and Range of Ions in Matter », in *Treatise on Heavy-Ion Science*, D. A. Bromley, Éd. Springer US, 1985, p. 93‑129.

[7] « James Ziegler - SRIM & TRIM ». [En ligne]. Disponible sur: http://www.srim.org/.

[8] Radiation Effects and Defects in Solids: Incorporating Plasma Science and Plasma Technology - Volume 141, Issue 1-4 .

[9] H. Bernas, J.-P. Attané, K.-H. Heinig, D. Halley, D. Ravelosona, A. Marty, P. Auric, C. Chappert, et Y. Samson, « Ordering Intermetallic Alloys by Ion Irradiation: A Way to Tailor Magnetic Media », *Phys. Rev. Lett.*, vol. 91, nº 7, août 2003.

[10] S. Picozzi, A. Continenza, et A. Freeman, « Role of structural defects on the half-metallic character of Co2MnGe and Co2MnSi Heusler alloys », *Phys. Rev. B*, vol. 69, nº 9, mars 2004.

[11] O. Gaier, J. Hamrle, B. Hillebrands, M. Kallmayer, P. Pörsch, G. Schönhense, H. J. Elmers, J. Fassbender, A. Gloskovskii, C. A. Jenkins, C. Felser, E. Ikenaga, Y. Sakuraba, S. Tsunegi, M. Oogane, et Y. Ando, « Improvement of structural, electronic, and magnetic properties of Co2MnSi thin films by He+ irradiation », *Appl. Phys. Lett.*, vol. 94, nº 15, p. 152508, avr. 2009.

[12] A. Hubert and R. Schäfer, *Magnetic domains: the analysis of magnetic microstructures*. Berlin ; New York: Springer, 1998.

[13] V. Kamberskỳ, « On ferromagnetic resonance damping in metals », *Czechoslov. J. Phys. B*, vol. 26, nº 12, p. 1366–1383, 1976.

[14] V. Kamberský, « Spin-orbital Gilbert damping in common magnetic metals », *Phys. Rev. B*, vol. 76, nº 13, oct. 2007.

[15] J. Pelzl, R. Meckenstock, D. Spoddig, F. Schreiber, J. Pflaum, et Z. Frait, « Spin–orbit-coupling effects on g-value and damping factor of the ferromagnetic resonance in Co and Fe films », *J. Phys. Condens. Matter*, vol. 15, nº 5, p. S451, 2003.

[16] P. Bruno, «Tight-binding approach to the orbital magnetic moment and magnetocrystalline anisotropy of transition-metal monolayers. Phys. Rev. B 39, 865 (1989).

Conclusion and Perspective

Heusler alloys are known to exhibit very special magnetic features, such as half metallicity and low damping coefficient, as a function of the degree of atomic order in the material. These properties are highly required for the development of spintronics devices based on magnetoresistance or spin torque effects. In this work, we offered to get a deeper insight into the correlation between the magnetic and structural properties of the Co_2MnSi alloy by studying the evolution of its static and dynamic magnetic parameters when submitted to He^+ ion irradiation at 150 KeV. Our work was based on the results obtained by Gaier et *al.* showing that He^+ ion irradiation at low fluences improves the long range B2 order in Co_2MnSi. In addition to the fundamental aspect of our approach, one of our goals was to study the possibility of improving the atomic order, even in the $L2_1$ phase, and then decreasing the dynamic damping of the material down to the theoretical predictions by Liu *et al.* ($\sim 0.6 * 10^{-4}$). Another goal was to study the effect of atomic disorder on the fundamental dynamic relaxation mechanisms by a proper control of the structure of the material.

For this purpose, several experimental techniques have been combined. Structural characterization has been achieved through X-ray diffraction in normal and anomalous conditions for a quantitative description of atomic disorder, while electron microscopy and especially HAADF-STEM imaging has been used to study the local organization of the atomic structure. Beside this, ferromagnetic resonance, MOKE and PPMS magnetometry allowed the determination of the static and dynamic magnetic parameters of the alloy. In this manuscript, we have chosen to present the experimental results observed for three series of samples. This choice is due to the difference of evolution of the structural and magnetic properties for each series.

In chapter IV, we first studied the structure and the magnetic properties of the reference samples of each series. Each sample is a thin film, with a thickness between 40 and 50 nm, grown on MgO substrate by sputtering. The CMS films verify the expected epitaxial relationship (001)[110] // MgO(001)[100]], indicating a 45° rotation of the CMS on the MgO substrate in order to minimize the lattice mismatch. Moreover, *GPA* analysis, performed from HAADF-STEM images, on the reference sample of series N°1 shows that the films are fully relaxed.

One of the major results presented in this chapter is that the structure of the three reference samples is slightly different. First, X-ray diffraction demonstrated that the unit cell is tetragonal with an out-of-plane lattice parameter of 5.67 and 5.69 Å for the reference samples of series N°1 and N°3, respectively. Moreover, the chemical atomic disorder was found to be different from one sample to the other. For example, the reference sample of series N°1 exhibits small crystallites with B2 order inside a $L2_1$ matrix. The rate of Co-Si exchange for this sample has been found to be below the uncertainty of the measurement, *i.e.* below 2%. $L2_1$ order was also found for the reference sample of series N°3 but the Co-Si exchange rate was found to be about 6% while no B2 order was observable in HAADF-STEM images. This means that the B2 order is either absent or that crystallites are too small to induce a variation of contrast in HAADF-STEM images. Unfortunately a complete structural analysis could not be performed on the reference sample of series N°2. Only X-ray diffraction performed with a

diffractometer equipped for small samples has been carried out. A very small amplitude of the (111) superlattice diffraction peak was observed for this sample. Based on the results obtained for the two other samples, it is possible that it grows either mainly in the B2 phase and/or in the $L2_1$ phase with strong Co-Si exchange.

The three reference samples also show different magnetic behaviors. For example, in FMR measurements, the reference samples of series N°1 and N°3 exhibit two resonance peaks, that we attribute to the $L2_1$ and B2 crystal order, while the reference sample of N°2 series exhibit only a single peak that we attributed to a disordered $L2_1$ phase. The values of the magnetization, exchange and gyromagnetic ratio for the three samples are in good agreement with reported values in the literature for $L2_1$ and B2 crystal order. One interesting feature of our samples concerns the anisotropy. Indeed the amplitude of the cubic anisotropy is more important than the one reported in literature for CMS deposited on MgO substrate. In addition, we observe the presence of a small uniaxial anisotropy which is aligned either with an easy axis for the samples of series N°1 and N°2 or with a hard axis for sample N°3. The origin of this additional anisotropy is accounted for the out-of-plane deformation of the unit cell but it is worth to mention that the effect of the chemical disorder cannot be eliminated.

We also studied the FMR linewidth of the three samples. Interestingly, we observe an anisotropic behavior of the linewidth and of the intrinsic damping coefficient. As explained in chapter 4, we measure in fact an effective damping coefficient that takes into account several contributions. Then further analytical analysis, especially taking into account the mosaicity of the sample and the two magnon processes, is needed to state about the origin of this anisotropy and conclude about an isotropic or anisotropic damping constant. One important result of this chapter is that the best effective damping coefficient is found for the reference sample of series N°1 for which we were able to separate the contribution of the B2 and the $L2_1$ order. We obtained an effective damping down to $1.6*10^{-3}$, which is better than most of the reported work up till now. Then, two main conclusions for this part can be emphasized on. The first one is that the understanding of the magnetic behavior and the determination of the static and dynamic parameters of the Co_2MnSi must include a full structural analysis of the material, including a study of the atomic disorder and mechanical strain in the material. To our knowledge such kinds of studies are rarely performed. In addition, we believe that the presence of the atomic disorder is at the origin for the reported values of α in literature which are generally between $6*10^{-3}$ and $3*10^{-3}$, almost one order of magnitude above the theoretical predictions. In our case we also believe that the values of α determined by the ΔH vs. f_{res} curves are the upper limit of the intrinsic coefficient, as many contributions to the linewidth arise. Then, if improving the crystallinity of our samples, we could expect to reach intrinsic damping coefficient down to 10^{-3}, as recently reported by Andrieu *et al.* in Co_2MnSi grown by MBE on MgO substrate.

In chapter 5, we studied the effect of ion irradiation on the structural and magnetic properties of the alloy. In the first part of this chapter we present simulations of the expected damages induced by the irradiation. While these simulations give the order of magnitude of the maximum damage that can be induced, it shows that local point defects such as vacancies or interstitial cannot be neglected for fluence above 10^{16} ions/cm².

The effect of irradiation on the structure of the alloy is found to depend on the original structure of the material. Indeed, for the samples of series N°1, we demonstrated that the irradiation favors the B2 order to the cost of the $L2_1$ phase. In addition, Co-Mn exchange is found to rise in the $L2_1$ matrix while Co-Si exchange is kept roughly constant up to 10^{16} ions/cm². The study of the magnetic parameters for the three series of samples makes us

believe that ion irradiation always favors the B2 order in every sample. This confirms the result obtained by Gaier *et al*. For the samples of series N°3, only X-ray diffraction with a Cu source have been performed so only the Co-Si exchange rate could be studied. We found a strong increase of this parameter with the ion fluence. However, such atomic exchange was not detected in the HAADF-STEM analysis. Indeed we observed a very uniform contrast, similar to the one expected for B2 order. Therefore, we propose a scenario in which a double exchange mechanism appears in the $L2_1$ matrix. We believe that Co-Mn and Mn-Si exchange are first induced at low fluences, similarly as for N°1 series. Then we believe that it is the Co atoms which are on the Mn sites that switch their position with Si atoms. Further structural analysis will be needed to validate our assumption.

In addition to the chemical disorder, we observe that the irradiation increases the out-of-plane lattice parameter of the samples of series N°1 and N°3. For the samples of series N°3 only the out-of-plane parameters have been measured due to the experimental configuration of the diffractometer. However, for the series of sample N°1, we could verify that the in-plane lattice parameters are kept constant for fluences up to 10^{16} ions/cm², meaning that the volume of the unit cell (a^2c) is not constant during the deformation.

The effect of the ion irradiation on the magnetic parameters of the alloy is presented in the last part of chapter 5. We find two different effects depending on the crystal order. The general tendencies are the following. Surprisingly the magnetic parameters of the B2 order are almost constant whatever the fluence. The only effect of irradiation is an increase of the extrinsic contributions ΔH_0 to the FMR linewidth, in agreement with the increased numbers of local defects. This again confirms that ion irradiation favors the B2 order in Co_2MnSi. For the $L2_1$ order the situation is different. Due to the induced atomic disorder, the values of the magnetization and exchange are found to decrease, in agreement with theoretical predictions of the loss of half metallicity with structural disorder. More interestingly we observed an increase of the gyromagnetic ratio and cubic anisotropy which reflects an increase of the orbital magnetic moment and spin-orbit interaction in the material.

In addition, one of the most striking features in our experiments is that the uniaxial anisotropy is found to rotate in the plane of the layer when increasing the ion fluence. Moreover its amplitude is found to increase for fluence up to $5*10^{15}$ ions/cm². At 10^{16} ions/cm² the uniaxial anisotropy amplitude decreases. We believe that the increase of the anisotropy amplitude is related to an elastic deformation of the unit cell when the decrease at 1016 can be accounted for the relaxation of the internal strain, which can be mediated by the structural defects induced by irradiation. Finally the anisotropy amplitude increases again for fluence of 10^{17} ions/cm². For such high fluence, the strong internal modifications of the chemical order along with some irreversible mechanical distortions (such as orthorhombic deformations for example) have to be considered. The possibility offered by ion irradiation to follow the evolution of the uniaxial anisotropy as a function of the deformation allows to clarify the origin of the uniaxial anisotropy. This result is of particular interest since it can be extended to other magnetic systems presenting the same behavior.

Finally, we studied the effect of ion irradiation on the linewidth of the different samples. As already stated, the intrinsic effective damping for the B2 order seems to be constant with the fluence. The extrinsic contributions were even found to be improved for the samples of series N°1 at fluence below 10^{15} ions/cm², reflecting the improvement of the long range order of this phase. For the $L2_1$ order, the general tendency is an increased of the damping coefficient, especially at high fluence due to the modification of the local environment around the Mn atoms. However, we also observed that for the samples of series N°2 and N°3, there could be some relation between the evolution of the uniaxial anisotropy and a potential improvement of the damping in some particular magnetic directions. This

appears only at fluence below 10^{15} ions/cm². At this point, it is not possible to state clearly on this assumption. Additional experiments are needed. Especially it would be necessary to study the linewidth in directions close to the direction of the uniaxial anisotropy.

Finally we would like to emphasize on some strange features observed for the second resonant peak appearing in the samples of N°2 and N°3 series at high fluence, and to a less extent in N°1 series. From the dispersion curves f_{res} vs H_0 in one easy and one hard axis directions obtained for this resonance,, we deduced in agreement with the reported values for a B2 order. However, this resonance shows strong variations of its amplitude depending on the magnetic directions and ion fluence. It is even completely undetectable for two directions for the samples of N°3 series. At the time we write this manuscript we do not have any explanations for these observations.

In conclusion, it is clear that ion irradiation at low fluences can be a very efficient tool to improve the B2 order in Co_2MnSi. This technique can be of particular interest since this crystal order is supposed to show a half metallic behavior. Therefore, we believe that it can be a credible complementary technique to temperature annealing to improve the order of this crystal phase in Heusler alloy. We also demonstrated that the atomic disorder and maybe mechanical strain are two key parameters to optimize the magnetic properties of Co_2MnSi in view of spintronic applications. While a much better control of the growing condition must be fulfilled to get reproducible effects, the very low damping measured in our work demonstrates the potential of Co_2MnSi to develop low energy consumption microwave devices, or spin torque memories. We believe that damping coefficient down to 10^{-3} or below are achievable in a very "pure" crystal, making of this material one of the most interesting ferromagnetic materials compatible with microelectronics processes.

From a fundamental point of view, ion irradiation is also very interesting to study the effect of disorder on the dynamic relaxation mechanisms. For example, starting from a thin film with B2 order, ion irradiation can be used to control the density of defects and study the evolution of the extrinsic contributions to the linewidth. The main interest being that, all the other magnetic parameters would be kept constant. It is also an interesting technique to probe fundamental interaction in the material such as the correlation between the spin-orbit interaction and the intrinsic damping coefficient. In this work we only get very preliminary results on this entanglement for N°1 series samples. In addition, ion irradiation offers the possibility to study the spin-flip and non spin-flip relaxation mechanisms by controlling the atomic disorder, and so the energy bandgap for spin up and spin down, in the material. For this the best configuration would be to start with a single crystal of $L2_1$ order. The main difficulty encountered in our work to get a deeper understanding of these different contributions was to separate the contributions to the linewidth of the different crystal order present in the as deposited material. One key issue for the future of this work will be the improvement of deposition condition to reduce the atomic disorder and phase mixing in the alloy.

Sommaire Thèse

Les matériaux demi-métalliques sont aujourd'hui particulièrement attractif pour les dispositifs à électronique de spin ainsi que les dispositifs micro-ondes.. Ces matériaux ont une propriété unique, ils se comportent comme métal pour une orientation du spin et en tant que semi-conducteur pour l'autre avec un écart au niveau de fermi qui conduit à une polarisation de spin de 100%. Un exemple de de matériaux demi-métalliques est la famille des alliages d' Heusler. Ces alliages ont été découverts en 1903 par F. Heusler [1 Heusler] en combinant 3 éléments non magnétiques tel que Cu_2MnAl qui se comporte comme un matériau ferromagnétique. Après cette découverte, de nombreux autres composés ont également été ajoutés à cette famille. En 1983, De Groot et al. [2 De Groot] ont montré le comportement demi-métallique du composé NiMnSb; cette découverte a conduit à un grand intérêt pour l'étude des alliages Heusler. Une autre propriété importante, qui est d'un intérêt particulier dans ce manuscrit de thèse, est le faible coefficient d'amortissement Gilbert dans ces composés qui est prévu pour être en dessous de 10^{-3} dans certains cas comme le Co_2MnSi, soit un ordre de grandeur environ meilleur que la plupart des métaux ferromagnétiques classiques. La combinaison de la polarisation en spin et du faible amortissement de Gilbert sont importants pour le retournement de l'aimantation dans les dispositifs STT MRAM.

Depuis lors, diverses combinaisons atomiques ont été testées comme par exemple des composés à base de cobalt Heusler. Au cours des 10 dernières années, le travail expérimental est axé sur la qualité de la croissance et les différentes propriétés magnétiques des alliages d'Heusler. Dans ce travail, nous sommes intéressés à l'étude des propriétés magnétiques et structurales des alliages Co_2MnSi.

Bien que le grand intérêt dans ces alliages ont été démontrées théoriquement (polarisation de spin élevée et faible Gilbert facteur d'amortissement $0,6 * 10^{-4}$ [3 Liu]) expérimentalement ces propriétés ont rarement été observées. Une raison possible de ces écarts réside dans la présence de désordre cristallin dans les matériaux réels. En effet,

Les alliages d'Heusler cristallisent en 4 phases différentes (pour les « full Heusler ») et en fonction de la position des atomes dans le réseau, le comportement magnétique est impacté.

Les alliages de type full Heusler à base de cobalt ont une composition chimique de type Co_2YZ. Ils cristallisent de préférence dans la structure $L2_1$ (groupe d'espace Fm3m). La cellule unitaire cubique est composée de quatre sous-réseaux interpénétrés de type FCC et les atomes sont placés suivant des positions de Wyckoff (1/4, 1/4, 1/4) pour le Co et la (0, 0, 0) et (1/2, 1/2, 1 / 2), pour Y et Z respectivement. La phase $L2_1$ est la phase la plus ordonnée des alliages d'Heusler. Si les atomes sont mal placés ou occupés de façon aléatoire dans la cellule unitaire, la phase ordonnée est modifiée. Trois autres phases cristallines, peuvent ainsi ête cristallisée, les phases B2 et $D0_3$ partiellement ordonnée et la phase A2 complètement désordonnée. La phase B2 correspond à une répartition aléatoire des atomes Y et Z dans la cellule unitaire, mais en gardant les atomes de Co dans leurs positions initiales. L'échange de Co et d'atomes Y donne la structure $D0_3$. La phase complètement désordonné A2 est formée lorsque tous les atomes sont occupés de façon aléatoire dans la cellule unité [4 Bacon and

Plant, 5 Webster, 6 Trudel]. La figure 1 donne une présentation schématique des quatre phases différentes du CMS.

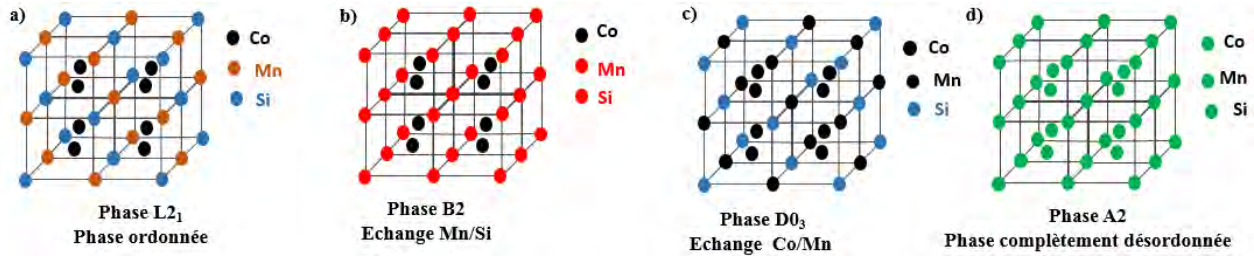

Figure1: présentation schématique des quatre phases cristalline pour le Co_2MnSi a) $L2_1$, b) B2, c) $D0_3$ et A2.

Les propriétés structurales de l'alliage à base de Co sont très sensibles aux conditions de dépôt et en particulier la nature du substrat, afin de minimiser le désaccord de maille définie comme: $\frac{a_{deposited\ film} - a_{substrate}}{a_{substrate}}$. Ou a est le paramètre de maille

Dans la littérature, les substrats les plus connus pour déposer des alliages d'Heusler sont le MgO et le GaAs. L'un des principaux intérêts de l'utilisation de substrat MgO concerne les jonctions tunnel magnétiques (MTJ), tandis que des substrats de GaAs permettent l'injection de spin dans des semi-conducteurs. GaAs a un paramètre de maille de 5,65 Å tandis que celle de MgO est 4.21 Å (Figure 1.2). Ceci conduit à un meilleur accord de maille pour GaAs où les alliages à base de Co Heusler croissent cube sur cube. Pour MgO, la croissance épitaxiale est réalisée par une rotation de l'axe du CMS à 45 ° par rapport à la direction <100> du MgO. Le désaccord de maille théorique entre le Co_2MnSi et le MgO est ≈ - 5,1% (Figure 2).

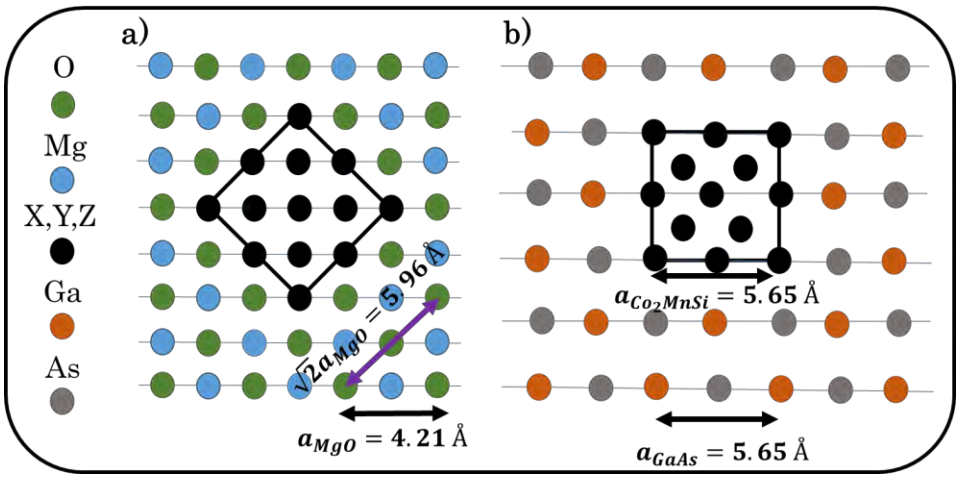

Figure 2: e présentation schématique de la croissance épitaxial du Co_2MnSi sur a) MgO et b) GaAs.

Le comportement magnétique de ces alliages dépend fortement de la phase structurale dans laquelle il croît. Théoriquement Picozzi et al [7 Picozzi] ont montré que dans les phases $L2_1$ et B2, ont une valeur de l'aimantation d'environ 5 µb /f.u. (1,3 T), même lorsque le Mn et le Si échangent leurs positions dans le réseau pour former la phase B2. Le comportement demi-métallique du CMS est montré théoriquement avec une " band gap" au niveau de fermi pour la phase $L2_1$ avec un faible Gilbert coefficient d'amortissement de $6 * 10^{-5}$. Le CMS présente une anisotropie cubique avec une constante d'anisotropie négative. Ainsi l'axe de facile aimantation est orienté dans les diagonales du cube (directions <111>) et l'axe de difficile aimantation est le long des arêtes du cube (directions <100>). Beaucoup d'études ont été menées sur les phases $L2_1$ et B2. Cependant peu d'études ont été menées s sur les phases de $D0_3$ et A2. Théoriquement, Picozzi et al. ont également étudié l'effet de la réorganisation atomique sur l'aimantation moyenne lorsque en présence d'échange de type Co/Mn (échange de type $D0_3$). Ils ont montré une diminution de l'aimantation à saturation à 4,5 µb /f.u. (1,16 T) mais aucune information sur les variations de l'anisotropie ou du facteur d'amortissement ne sont donnés. Pour la phase A2 aucune information n'a été trouvée sur le comportement magnétique de cette phase.

Ainsi l'objectif de ce travail consiste à étudier et comprendre les corrélations entre les propriétés structurales et magnétiques du CMS à l'échelle atomique. Pour atteindre cet objectif, nous avons utilisé la technique d'irradiation ionique. Dans ce processus des ions sont accélérés et pénètrent dans un solide pour modifier les propriétés physiques et chimiques par interaction nucléaire et électronique. Dans une vision simplifiée, l'irradiation ionique peut être considérée comme un transfert d'énergie cinétique des ions incidents aux atomes du réseau. La fluence est définie comme le nombre d'ions / cm2. A faible fluence, l'irradiation agit comme un recuit local où le transfert d'énergie cinétique conduira à un léger mouvement des atomes localement pouvant amener une réorganisation chimique locale. Pour les fortes fluences, l'accumulation d'énergie transmise aux atomes du cristal leur permettra de se déplacer sur de plus grandes distances et créer des défauts ponctuels de types lacunes ou interstitielles dans le matériau.

Dans ce travail nous avons utilisé des ions He+ accélérés par une tension de 150 KeV. Nous avons déterminé les fluences de travail à partir de simulations d'endommagement du CMS avec le logiciel IPROS développé dans notre laboratoire. Ce logiciel permet de simuler l'endommagement d'un matériau amorphe et de composition stœchiométrique (50% de Co, 25% de Mn et 25% Si). En plus les simulations sont réalisées à 0K et négligent les potentielles recombinaisons atomiques à température ambiante. A partir des simulations deux caractéristiques importantes peuvent être obtenues (figures 3-a et 3-b). La première est quelles ions parcourent environ 600 nm dans le MgO (dans notre cas 42 nm), Le deuxième est le nombre de lacunes créées. Par exemple pour une fluence de 10^{16} ions/cm², nous obtenons presque 1 lacunes pour 100 atomes de CMS. Cependant, du fait des limitations évoquées ci-dessus, ce chiffre est surévalué et ne donne qu'une limite haute de l'endommagement possible.

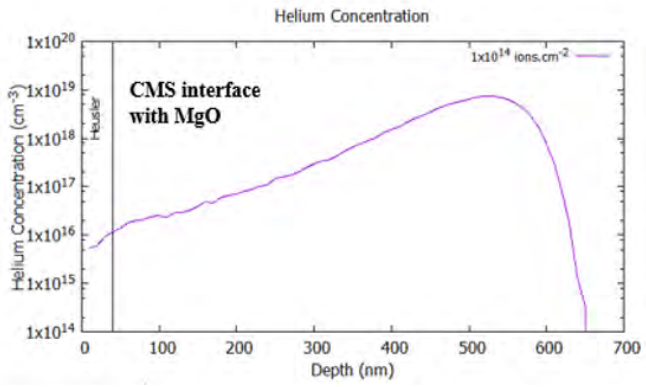

Figure 3-a: concentration d'Hélium en fonction de la profondeur.

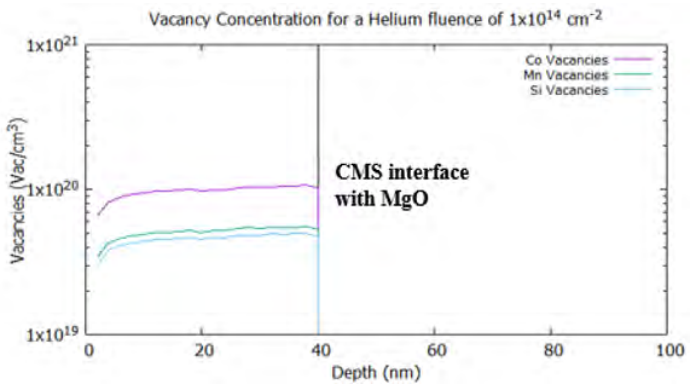

Figure 3-b: concentration de lacunes de Co, Mn et Si pour une fluence de 10^{14} ions / cm2..

Plusieurs techniques expérimentales ont été utilisées pour étudier les propriétés structurales et magnétiques de nos échantillons Nous avons déposé par pulvérisation cathodique des films minces de 40 nm d'épaisseur de CMS sur des substrats de MgO. Notre bâti est équipé d'un RHEED pour contrôler in situ le type de croissance du CMS. Les conditions de dépôt (température de dépôt et de recuit, $T_{deposition}$ et T_{recuit}) ont été optimisées après contrôle in situ de la croissance 2D par RHEED, comme illustré sur la figure 4. Les conditions optimales ont été définies comme Tdep = 600 ° C et Trecuit = 750 ° C.

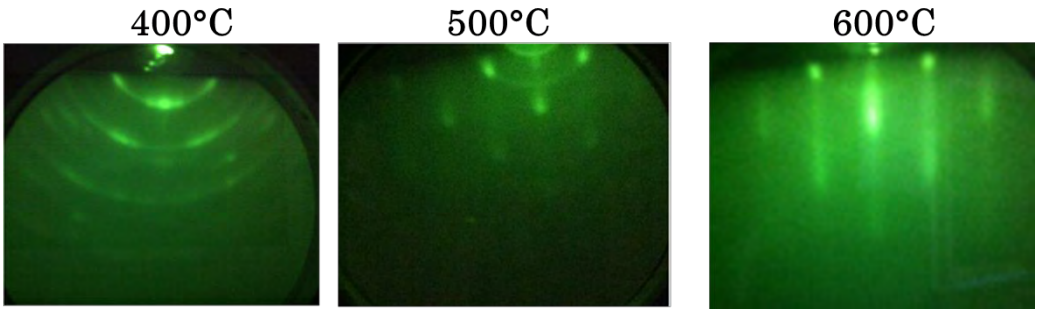

Figure 4: cliché RHEED de CMS à des températures de dépôt différentes.

L'épaisseur du CMS varie de 40 à 50 nm et à la fin du procédé, une couche de 10 nm de MgO a été déposée pour empêcher l'oxydation de l'échantillon. Après avoir réalisé l'échantillon, la diffraction par rayons X et la microscopie électronique en transmission (TEM) sont utilisés pour étudier la structure et le désordre atomique de nos échantillons. La diffraction de rayons X est un outil qui permet de caractériser la structure à l'échelle macroscopique. La première chose que nous avons vérifiée est la relation d'épitaxie du CMS avec le MgO avec une rotation de la maille du CMS par rapport au MgO. De plus, la diffraction de rayons X permet d'avoir accès au différents échange atomique et donc aux phases cristallines en présence. En effet, dans le CMS, certains pics de diffraction apparaissent quel que soit la phase cristalline. On les appelle les pics fondamentaux (par exemple (220)). Cependant des pics de sur-structure peuvent apparaitre en fonction du type de désordre présent dans le matériau. Par exemple le pic de diffraction (111) apparait en présence des ordres cristallins $L2_1$ ou $D0_3$. Un problème majeur dans la littérature est que la présence de ce pic de diffraction est généralement attribuée directement à la présence de la phase $L2_1$, ce qui est faux. Ainsi, afin d'avoir accès à l'ensemble des types de désordre présent dans nos échantillons nous avons suivis l'approche développé par Niculescu et al. [8 Niculesci] et employé par Takamura [9 Takamura] dans le cas du Co_2FeSi. Dans ce modèle trois paramètres de désordre sont définis α, β et γ. α corresponds au nombre d'atome de Mn sur les sites de Si par formule unité, β est le nombre d'atome de Co sur les sites de Si et γ est le nombre d'atomes de Co sur les sites du Mn. Ces paramètres de désordre sont ensuite introduit dans le calcul des facteurs de structures des différents plans de diffraction et dans le calcul de l'intensité diffractée tel que :

$$I_{hkl} \approx L_{hkl(\theta)} P_{hkl(\theta)} |F_{hkl}|^2 \frac{1}{\sin\theta_{hkl}} \qquad \text{Eq.1}$$

$$\mathrm{F}_{111} \propto (1-2\alpha-\beta)(f_{\mathrm{Mn}} - f_{\mathrm{Si}}) + (\gamma-\beta)(f_{\mathrm{Co}} - f_{\mathrm{Mn}}) \qquad \text{Eq.2}$$

$$\mathrm{F}_{002} \propto (1-2\beta)(f_{\mathrm{Co}} - f_{\mathrm{Si}}) + (1-2\gamma)(f_{\mathrm{Co}} - f_{\mathrm{Mn}}) \qquad \text{Eq.3}$$

$$\mathrm{F}_{022} = \mathrm{F}_{004} \propto 2f_{\mathrm{Co}} + f_{\mathrm{Mn}} + f_{\mathrm{Si}} \qquad \text{Eq.4}$$

Dans cette méthode, trois rapports d'intensités entre les pics de sur-structure hkl et le pic fondamental doivent être évalués afin d'obtenir α, β et γ.

Afin d'obtenir ces trois paramètres, nous avons utilisé deux diffractomètres, l'un équipé avec une source de cuivre au seuil Kα et l'un équipé d'une source de cobalt au seuil Kα. L'utilisation du premier permet d'obtenir α et β car le facteur de diffusion du Co et du Mn à cette énergie étant très proches (figure 5-a) le second terme du membre de droite des équations 2 et 3 disparaissent. En revanche ces termes réapparaissent au seuil Kα du Co, permettant ainsi de retrouver le paramètre γ.

Pour étudier l'effet de l'irradiation, l'échantillon déposé a été coupé en 4 morceaux, la référence et 3 échantillons irradiés à 150 keV de fluences 10^{15}, $5 * 10^{15}$ et 10^{16} ions/cm^2, respectivement.

La figure 6 présente différents pics de diffraction de l'échantillon de référence et des échantillons irradiés où l'on peut voir clairement le décalage des pics de diffraction vers des angles plus faibles pour les pics 022, 022 et 004. A partir de ces spectres, on peut d'abord obtenir le paramètre de maille du CMS. Les valeurs obtenues sont résumées dans le tableau

1. Nous observons que l'irradiation augmente la déformation tétragonale du réseau, tout en gardant les paramètres dans le plan constant à 5,63 Å. Cette distorsion tétragonale affectera l'anisotropie magnétique présentée dans la section suivante.

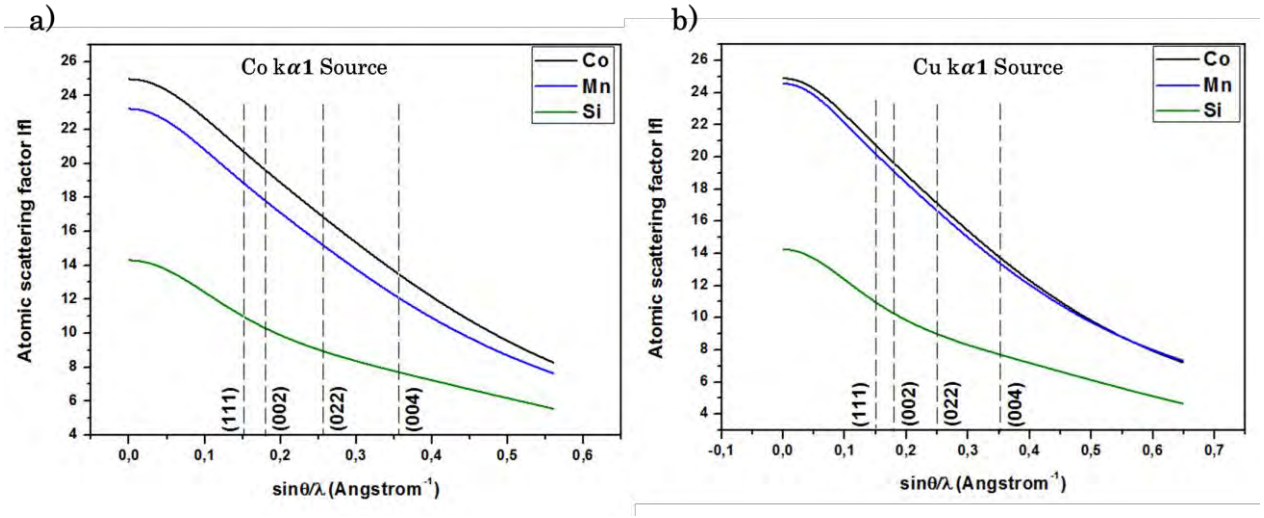

Figure 5: facteurs de diffusion atomique du Co, Mn et Si en fonction of $\frac{sin\theta_{hkl}}{\lambda}$ pour les sources de a) Co kα1 et b) Cu kα1.

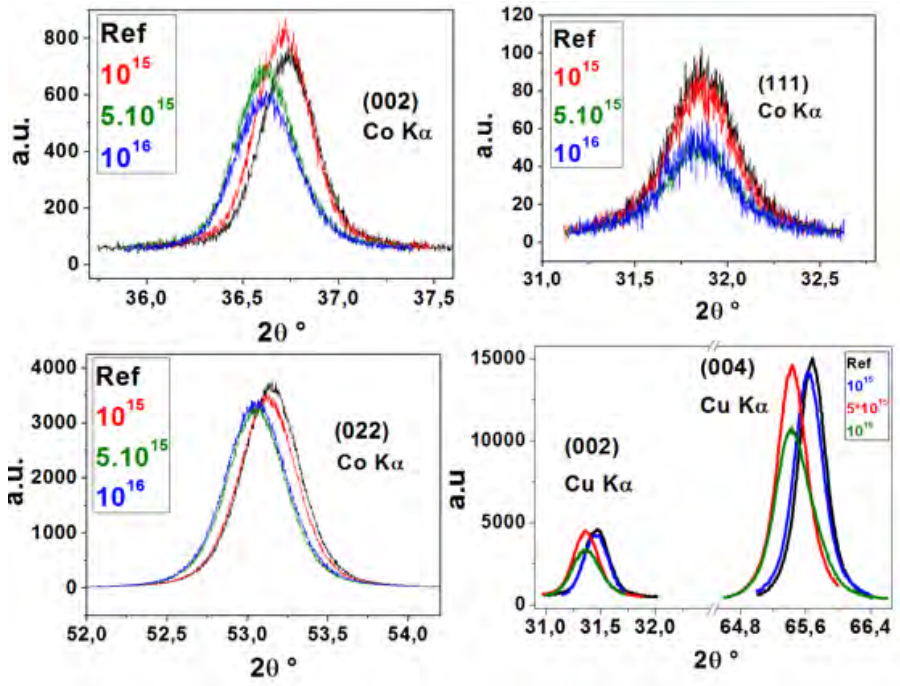

Figure 6: Diffraction des rayons X . 2$\boldsymbol{\theta}$ scan pour l'échantillon de référence et les 3 échantillons irradiés pour les sources de Co et Cu. a), b) et c) représente les 111,002 et 022 pics acquis avec la source de Co. d) et e) présente les pics 002 et 004 acquis avec la source de Cu.

fluence	a (Å)	c (Å)
Ref	5.63	5.67
10^{15}	5.63	5.68
5×10^{15}	5.63	5.69
10^{16}	5.63	5.69

Tableau 1: paramètres de maille dans le plan et hors plan en fonction de la fluence.

α, β et γ ont été évalués aussi pour la référence et les échantillons irradiés. Pour l'échantillon de référence, nous avons mesuré $\alpha(Mn/Si) = 0.14 \pm 0.01, \beta(Co/Si)$=0.03 $\pm$0.02 et $\gamma(Co/Si) = 0.01 \pm 0.01$. A partir de ce résultat, nous pouvons conclure que l'échantillon de référence présente environ 75% de phase $L2_1$ et 25% de phase B2 (le taux de désordre CO/Si étant très faible nous le négligeons ici) L'évolution des taux de désordre en fonction de la fluence sont présentés sur la figure 7. Le désordre Mn/Si (type B2) augmente avec la fluence alors qu'à la plus forte fluence le désordre de type Co / Mn apparaît. Enfin le désordre de type Co / Si reste à peu près constant avec la fluence. . Ainsi avec l'irradiation nous avons montré qu'il était possible d'induire des désordres atomiques de type B2 et $D0_3$.

Afin de comprendre l'organisation des différents désordre à l'échelle atomique, nous avons réalisé des mesures HAADF-STEM (High Angular Angle Dark Field Scanning Transmission Electron Microscopy') au laboratoire INA à Saragosse. Cette technique permet à la fois d'observer l'organisation structurale du matériau à l'échelle atomique mais aussi d'avoir une information chimique puisque le contraste des colonnes atomiques est proportionnel au numéro atomique de l'espèce chimique. ($Z\sim I^{1.7 \text{ to } 2}$). De ce fait la différence de contraste entre le Co et le Mn, et donc l'observation du désordre de type D03, est très difficile à observer.

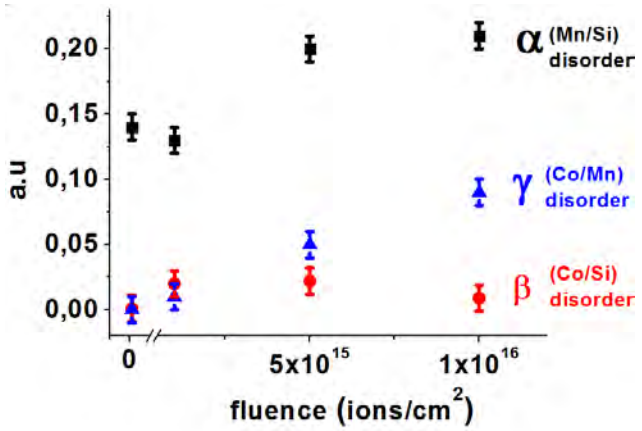

Figure 7: $\boldsymbol{\alpha, \beta}$ ***and*** $\boldsymbol{\gamma}$ paramètres de désordre atomique en fonction de la fluence.

Un exemple d'image STEM-HAADF est donné dans la figure 8-a. Un zoom sur une petite zone permet d'observer les variations d'intensité des différentes colonnes atomiques dénotées par les flèches de couleur (figure 8-b). Par exemple pour la ligne en noire les colonnes atomiques montrent un maximum d'intensité correspondant aux colonnes de Co. Pour les lignes rouges et vertes nous observons une alternance de haute et faible intensité, typique de l'alternance des atomes de Mn et Si dans une structure de type $L2_1$. La différence d'intensité entre les atomes de Co et Mn étant très faible, une manière de discrétiser ces deux types d'atomes consiste à réaliser une étude statistique du maximum d'intensité de chaque colonne comme le montre sur la figure 9. Un résultat important de cette mesure est la présence de petite zone ou l'alternance d'intensité entre le Mn et le Si disparait. Ceci correspond à des zones cristallisées dans la phase B2. (Figure 9-b).

La même méthode a été appliquée sur l'échantillon le plus irradié avec une fluence de 10^{16} ions/cm² La différence principale avec l'échantillon de référence concerne la taille des zones de type B2 qui sont beaucoup plus grande (figure 10). Ceci confirme es résultats obtenus par diffraction X montrant que la phase B2 est favorisée par l'irradiation ionique, en défaveur de la phase $L2_1$. Concernant le désordre de type D03, celui-ci est difficilement observable par STEM-HAADF. Cependant des mesures magnétiques permettent de statuer sur l'organisation de ce désordre au sein du matériau.

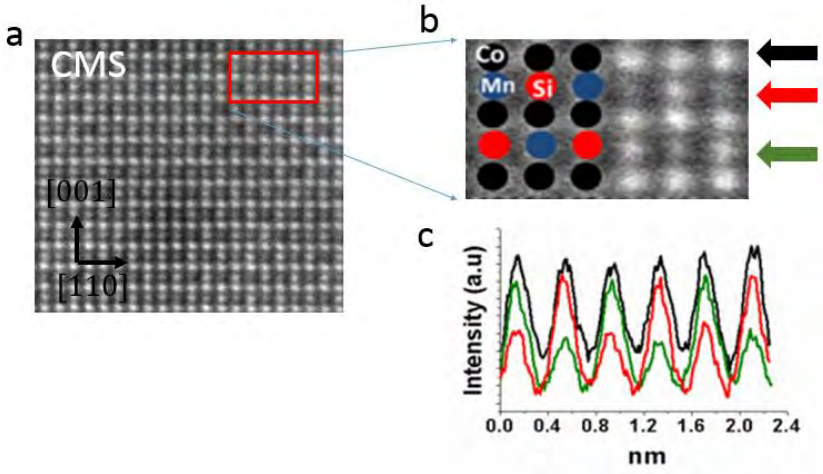

Figure 8: a) Image STEM-HAADF du CMS. b) zoom sur 6x 6 colonnes atomiques délimité par le rectangle rouge en a). (C) profil d'intensité des lignes indiquées par les flèches en b).

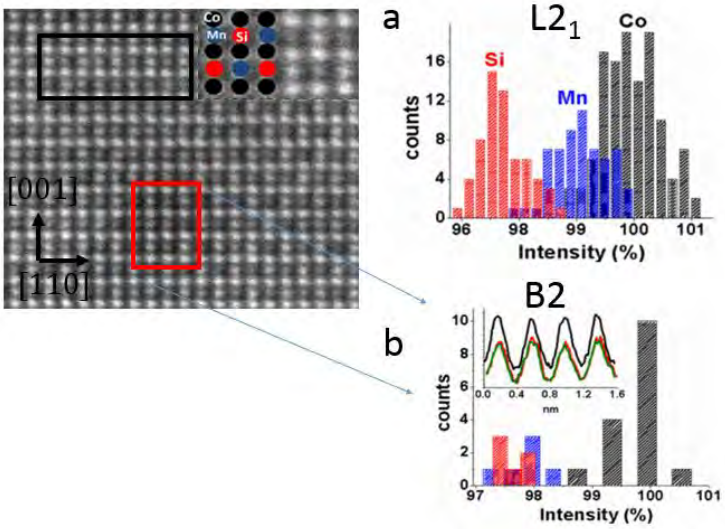

Figure 9: (a) L'analyse statistique du profil d'intensité obtenu sur une région de 11 x 23 colonnes atomiques délimité par la zone en noire (a) ou rouge (b) dans l'image STEM.

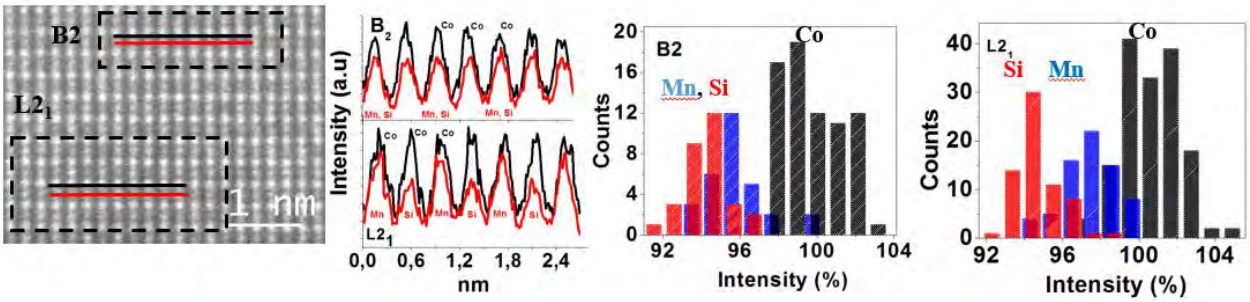

Figure 10: Image STEM-HAADF sur l'échantillon irradié à 1016 ions/cm². Les statistiques ont été effectuées sur les colonnes atomiques délimitées par les zones entourées en a).

La deuxième partie du travail de thèse a consisté à étudier l'effet du désordre atomique sur les propriétés magnétiques du CMS par résonance ferromagnétique (RFM). La RFM décrit la précession uniforme de l'aimantation lorsque celle-ci est mise hors de sa position d'équilibre définie par la direction du champ effectif H_{eff} (qui est défini par la somme des énergies magnétiques mises en jeu). L'équation du mouvement de l'aimantation est définie dans l'équation 5. Afin de permette le retour à l'équilibre de l'aimantation, un terme de relaxation de type frottement visqueux et décrit par le Gilbert facteur d'amortissement α est introduit.

$$\frac{d\vec{M}}{dt} = -\gamma\, \mu_0 \left(\vec{M} \wedge \vec{H}_{eff} \right) \quad + \quad \frac{\alpha}{M} \left(\vec{M} \wedge \frac{d\vec{M}}{dt} \right) \qquad \text{Eq.5}$$

Pour étudier les propriétés magnétiques, nous avons développé au CEMES une technique RFM présentée schématiquement dans la figure 11. Le principe est le suivant. L'échantillon de CMS est placé au-dessus d'une ligne de transmission micro-ruban constituée d'une couche d'or de largeur de 400 nm sur un substrat d'alumine.. Une courante micro-onde (0.1 – 30 GHz) est injectée dans la ligne Afin d'exciter l'aimantation. Le porte objet est placé entre les pôles d'un électro-aimant pouvant délivrer jusqu'à 1.5 T dans un entrefer de 2 cm ou 0.6 T dans un entrefer de 8 cm. La mesure consiste à balayer la valeur du champ magnétique extérieur en gardant une fréquence d'excitation micro-ondes constante. A la résonance, nous mesurons par une technique de modulation du champ externe la dérivée de la puissance électromagnétique absorbée par l'échantillon. Cette modulation est réalisée grâce à deux bobines de Helmholtz placée autour du porte objet. La figure 12 présente un spectre RFM typique qui peut être mesuré avec notre set-up. Le champ de résonance est définie comme la valeur pour laquelle le signal est égal à zéro et la largeur de raie ΔHpp définie par la largeur pic à pic dans notre mesure peut être reliée au facteur de relaxation via la relation $\Delta H_{pp} = \frac{1}{\sqrt{3}} \Delta H$, avec ΔH la valeur FMR réelle.

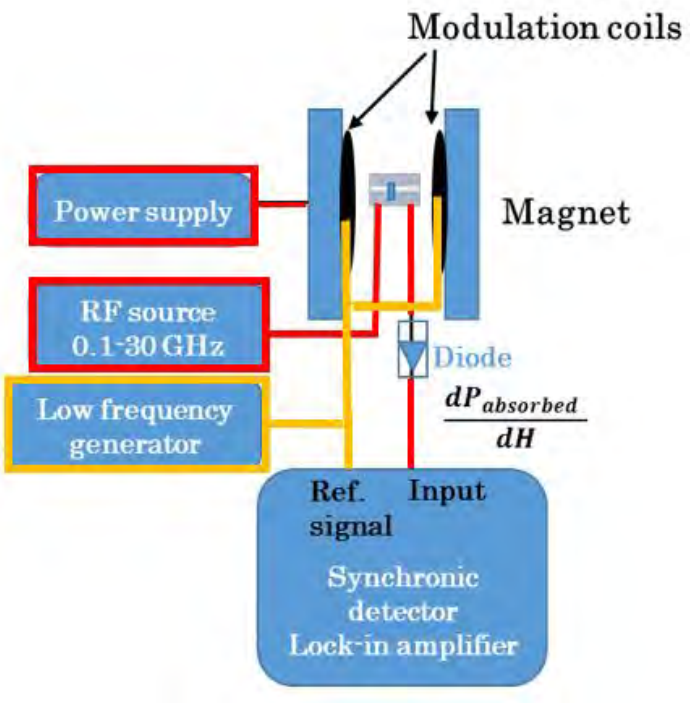

Figure 11: illustration schématique de la configuration FMR.

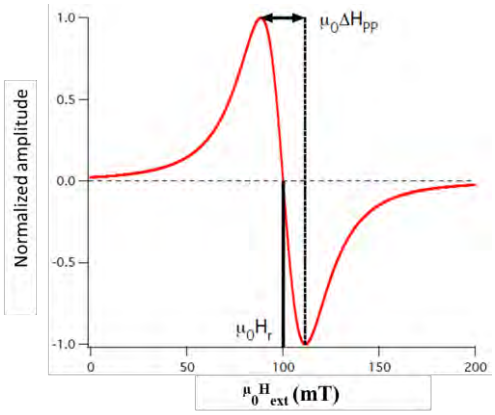

Figure 12: Signal FMR mesurée en fonction du champ extérieur appliqué.

Le spectre FMR de l'échantillon de CMS de référence est présenté sur la figure 13. Deux pics de résonance sont clairement visibles en accord avec la présence des phases B2 et $L2_1$ déterminées par diffraction X et STEM-HAADF. La même chose est observée quel que soit la direction d'application du champ par rapport aux directions cristallines. Un point important à prendre en considération est le mélange des modes qui rendent difficile

l'évaluation précise de la largeur de raie dans certaines directions d'application duc champ extérieur.

En effet, alors que nous pouvons observer clairement deux pics pour l'axe de difficile aimantation N° 2 (dans le CMS il y a deux axes faciles et deux axes difficiles orientés tous les 45°), on observe un seul pic asymétrique pour l'autre axe difficile N°1. Cependant la forme asymétrique du pic reflète le fait que les deux modes sont "mélangés". De même, pour l'axe facile, l'amplitude des deux pics respectifs semble être inversée lorsque le champ extérieur est appliqué d'un axe facile à l'autre.

Les mesures FMR sont réalisées avec un champ magnétique parallèle ou perpendiculaire au plan de la couche de CMS. Dans e premier cas, notre montage permet de tourner le champ magnétique autour de l'échantillon. Les paramètres magnétiques sont obtenus à partir des courbes de dispersion f_{res} Vs H_0 ou H_0 est l'amplitude du champ appliqué. Pour cela, les données expérimentales (F_{res} vs. H_{res}) sont ajustées avec l'équation de Smit-Belger ; Les paramètres magnétiques obtenus par cette méthode sont résumés dans le tableau 2.

$$\omega_{res} = \frac{\gamma}{M_s \sin\theta_{eq}} [(E_{\theta\theta}E_{\varphi\varphi} - E_{\theta\varphi}{}^2)]^{1/2} \qquad \text{Eq.6}$$

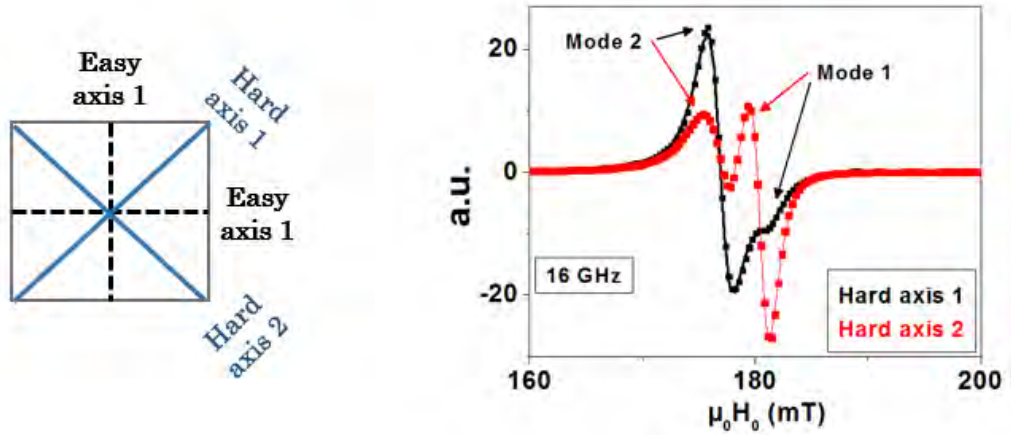

Figure 13: Les spectres d'absorption à 16 GHz en fonction du champ externe à deux axes durs.

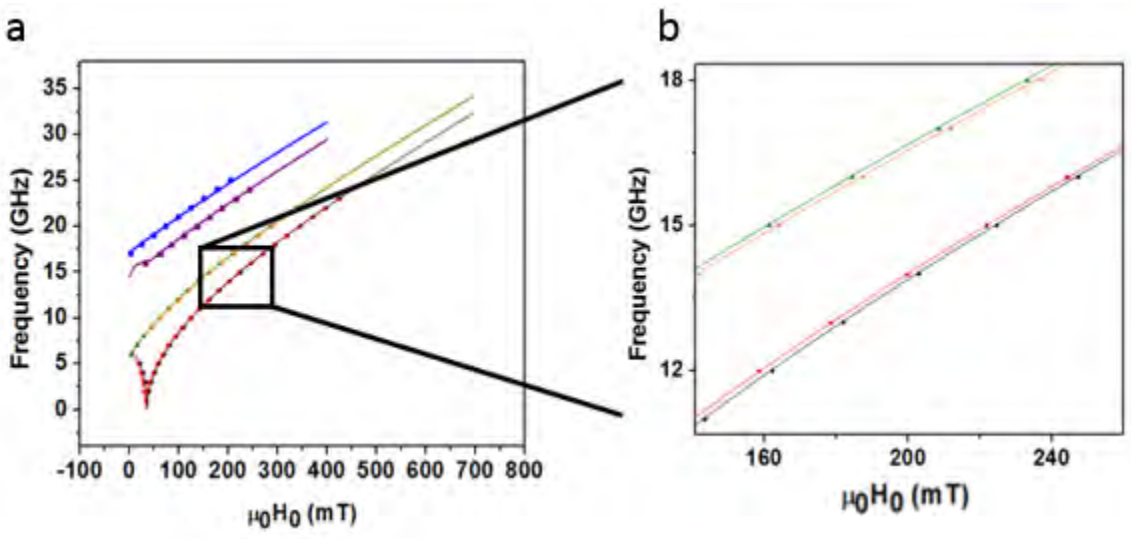

Figure 14: a) relation de dispersion F_{res} vs. $\mu_0 H_0$ pour l'échantillon de référence pour un champ appliqué dans le plan de la couche. A droite, zoom sur les deux modes délimitées par la boîte noire en a).

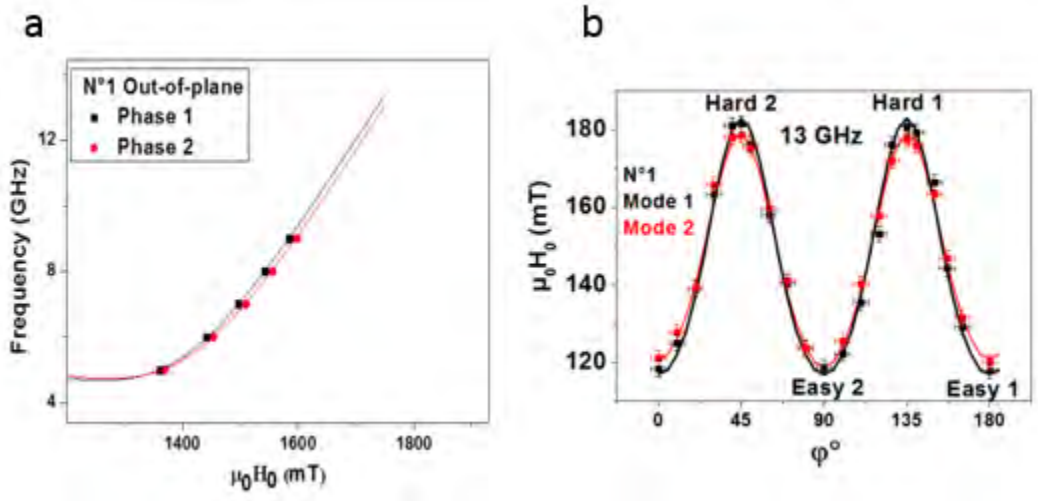

Figure 15: relation de dispersion pour l'échantillon de référence pour un champ appliqué perpendiculairement au plan de la couche. b) dépendance angulaire du champ de résonance à 13 GHz pour un champ appliqué dans le plan de la couche.

Les valeurs de l'aimantation à saturation sont en très bon accord avec la valeur théorique de la phase $L2_1$ (~ 5 μ_B / f.u) [10 Galanakis]. En nous basant sur les mesures de largeurs de raies présentées ci-dessous, nous attribuons la phase 1 à l'ordre $L2_1$ et la phase 2 à l'ordre B2. Ceci est en bon accord également avec l'amplitude des pics FMR, plus faible dans le cas de l'ordre B2 en raison d'un volume plus faible dans l'échantillon. Les valeurs d'aimantation légèrement plus faible que celles prédites par la théorie peuvent s'expliquer par la présence d'une très faible quantité de désordre Co/Si comme montré par diffraction X.

Concernant le champ d'anisotropie cubique, nous obtenons une amplitude plus élevée que celles généralement reportées dans la littérature mais similaire aux celles obtenues dans les travaux de G. Ortiz au CEMES [11 Ortiz]. La valeur du rapport gyromagnétique de 28,7 GHz / T (facteur de Landé g = 2.05) reflète une petite contribution du moment orbital, où, pour un électron libre du facteur de Landé g = 2. Le dernier paramètre magnétique à commenter est la constante d'échange. Pour mesurer cette constant nous mesurons le premier mode d'excitation non linéaire en épaisseur dans le spectre FMR. Le signal correspondant étant très faible, nous l'attribuons à la phase majoritairement en présence dans l'échantillon, à savoir la phase $L2_1$. La valeur déduite de la constante d'échange est en bon accord avec les autres valeurs rapportées dans la littérature [12 Ritchie, 13 Hamrlé and 14 Pandey].

CMS Reference sample	Magnetization saturation M_s (T)	Anisotropy field $\mu_0 H_k$ (mT)	Gyromagnetic ratio $\gamma/2\pi$ (GHz/T)	Exchange constant A (pJ/m)
Phase 1	1.26 ±0.02	36 ±0.2	28.7±0.1	19±0.5
Phase 2	1.25 ±0.02	33 ±0.2	28.7±0.1	

Tableau 2 : valeurs magnétique de la référence pour les deux phases.

La figure 16 présente l'évolution du spectre FMR à 18 GHz en fonction de la fluence. Alors que la position du pic correspondant à l'ordre B2 reste à une position à peu près constante, celle du pic correspondant à l'ordre $L2_1$ évolue vers les valeurs de champ plus élevées. Ceci implique une modification des paramètres magnétiques de cette phase. De plus, à la fluence la plus élevée, nos n'observons toujours que deux pics. Ainsi, nous pouvons conclure que le désordre de type $D0_3$ induit par l'irradiation doit probablement apparaitre de manière aléatoire dans la partie initialement $L2_1$ de l'échantillon de référence. Sinon si ce désordre s'organisait sous a forme de « grains » par exemple, nous pourrions attendre trois pics FMR ($L2_1$, B2, D03).

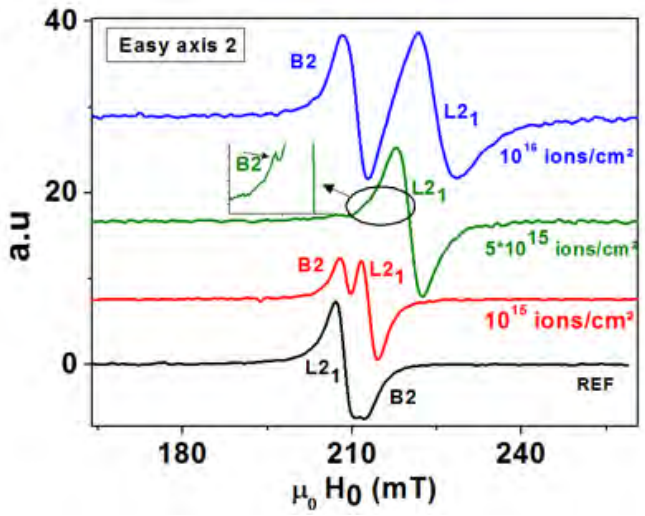

Figure 16: Evolution du spectre FMR à 18 GHz en fonction de la fluence. Le champ extérieur est appliqué parallèlement à un axe facile.

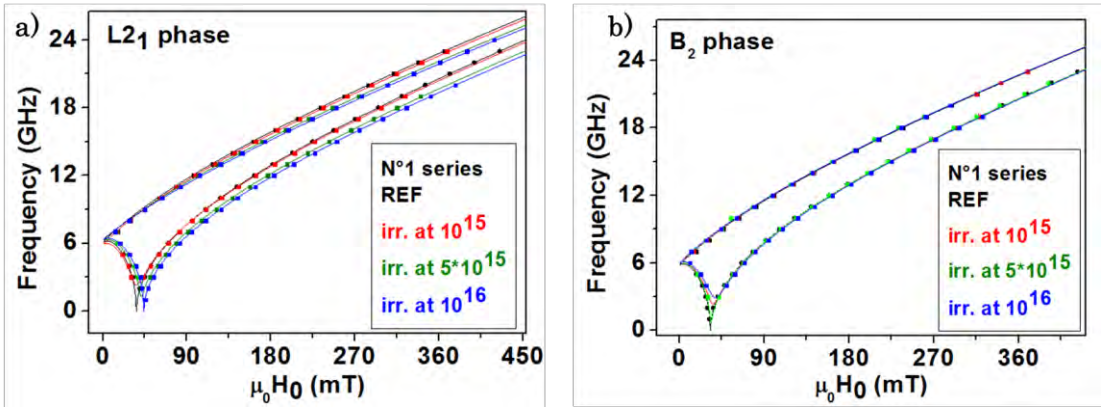

Figure 17: Evolution des courbes f_{res} vs. $\mu_0 H_0$ pour les deux phases en fonction de la fluence.

Pour la phase B2, les paramètres magnétiques très des courbes de dispersion montrent que ceux-ci sont constants avec la fluence, excepté une petite augmentation de l'anisotropie cubique (tableau 3).

CMS B2 phase	Reference	Irr. 10^{15}	Irr. 5×10^{15}	Irr. 10^{16}
Magnetization saturation M_s (T)	1.25 ±0.02	1.25 ±0.02	1.25 ±0.02	1.25 ±0.02
Anisotropy field $\mu_0 H_k$ (mT)	32 ±0.2	33 ±0.2	35 ±0.2	36 ±0.2
Gyromagnetic ratio $\gamma/2\pi$ (GHz/T)	28.7±0.1	28.7±0.1	28.7±0.1	28.7±0.3

Tableau 3 : valeurs magnétique de la phase B2 en fonction de la fluence.

Pour la phase $L2_1$, la situation est plus complexe. En effet nous observons une diminution très forte de l'aimantation à saturation et du constant échange alors que la valeur de l'anisotropie cubique et du facteur gyromagnétique augmentent fortement (figure 18).

A diminution de la valeur du moment magnétique et de l'échange peut s'expliquer à partir des travaux de Picozzi et al. [15 Picozzi] dans lequel la densité d'état pour les spins up et down ont été calculés ab-initio pour une structure parfaite de type $L2_1$ et pour une structure comprenant un échange de type Co/Mn. Ils ont ainsi démontré (figure 19) que des états localisés pour les spins minoritaires apparaissent au niveau de Fermi, ce qui diminue le moment magnétique totale de la maille élémentaire (à 4,5 µB / fu). De plus ils ont observé un léger décalage en énergie des spins minoritaires qui peut s'apparenter à une diminution de l'échange. Il est intéressant de noter que la diminution de Ms dans nos échantillons est plus élevé que les valeurs attendues par le calcul.

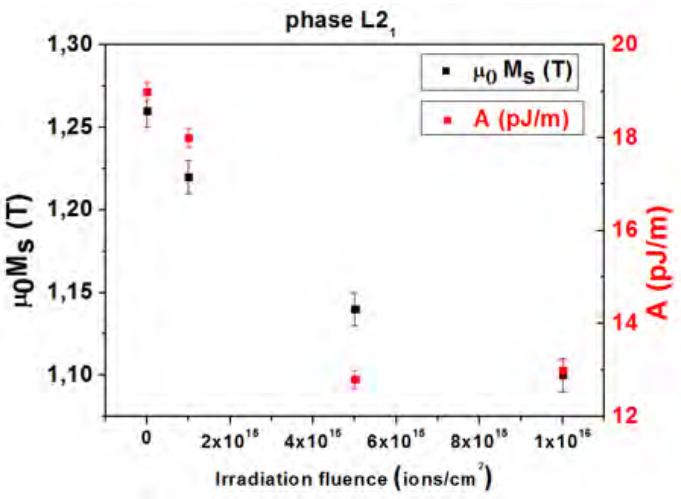

Figure 18: Evolution de l'aimantation à saturation et de la constante d'échange en fonction de la fluence.

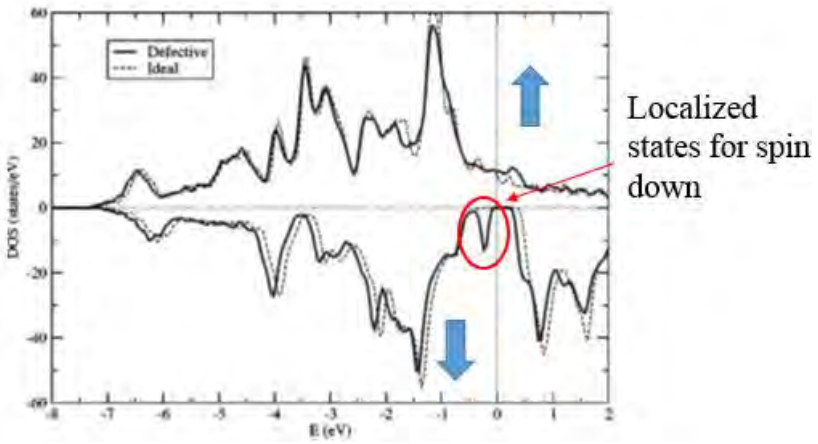

Figure 19: Densité d'états résolues en spins pour une structure idéale ($L2_1$) et une structure comprenant un désordre de type Co / Mn qui est typique pour l'ordre $D0_3$.

Afin d'expliquer l'évolution de l'anisotropie cubique et du rapport gyromagnétique en fonction de fluence, nous rappelons que ces deux termes dépendent de l'amplitude des moments magnétiques orbitaux et de spins. En effet le rapport gyromagnétique est liée au facteur de Landé "g" par la formule suivante:

$$\gamma = \frac{g*|e|}{2m_e} \quad \text{with} \quad (g-2) = 2\frac{\mu_L}{\mu_s}$$

Alors que l'augmentation de l'anisotropie cubique est due à une augmentation éventuelle des moments orbitaux comme décrit par Bruno et al. [16 Bruno] par cette formule:

$$\Delta E_{SO} = \lambda\left[(L.S)_{hard} - (L.S)_{easy}\right] = \frac{\lambda}{4\mu_B}\left(\mu_L^{easy} - \mu_L^{hard}\right) > 0$$

Ainsi, nous pensons que l'augmentation de l'anisotropie cubique et du facteur gyromagnétique sont probablement lié à l'augmentation du moment magnétique orbital avec le désordre.

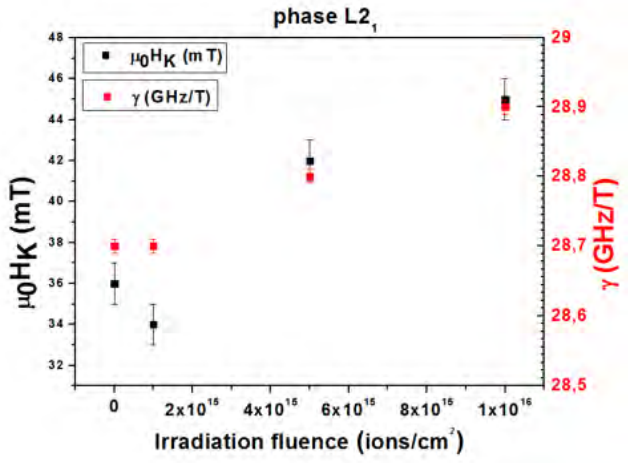

Figure 20: Evolution du champ d'anisotropie cubique et du rapport gyromagnétique en fonction de la fluence

Un autre paramètre magnétique important auquel nous nous sommes intéressés est la présence d'une faible anisotropie uniaxiale dans le plan des couches. Bien que l'apparition d'une telle anisotropie est un phénomène connu dans les films minces, son origine physique est encore débattue. Un mécanisme souvent avancé est un effet de magnéto-mécanique induit par un effet de contrainte à l'interface avec le substrat. D'autres études proposent que cette anisotropie provienne de la morphologie du substrat (présence de terrasses par exemple). Des études GPA menées à partir de l'imagerie STEM-HADDF a montré que nos échantillons sont parfaitement relaxés et donc l'anisotropie est peut être liée à un effet d'interface avec le substrat.

Dans l'échantillon de référence celle-ci est alignée avec un axe facile mais nous observons que son amplitude et la direction évolue sous l'effet de l'irradiation.

La figure 21 présente l'évolution de l'amplitude d'anisotropie uni-axiale μ_0H_u et sa direction par rapport à l'axe de facile aimantation en fonction du paramètre de maille hors plan. La dépendance quasi linéaire observée laisse penser que l'origine de l'anisotropie réside dans la déformation intrinsèque de la maille de l'Heusler. Etant donné que les paramètres dans le plan sont constants il semblerait que la déformation induise une contrainte interne induisant l'anisotropie. Ceci est confirmé à la plus haute fluence, 10^{16}, pour lequel le matériau est parfaitement relaxé et pour lequel l'anisotropie disparaît. Nous pensons que ce résultat obtenu ici sur l'alliage Co_2MnSi peut être appliqué à d'autres systèmes ferromagnétiques.

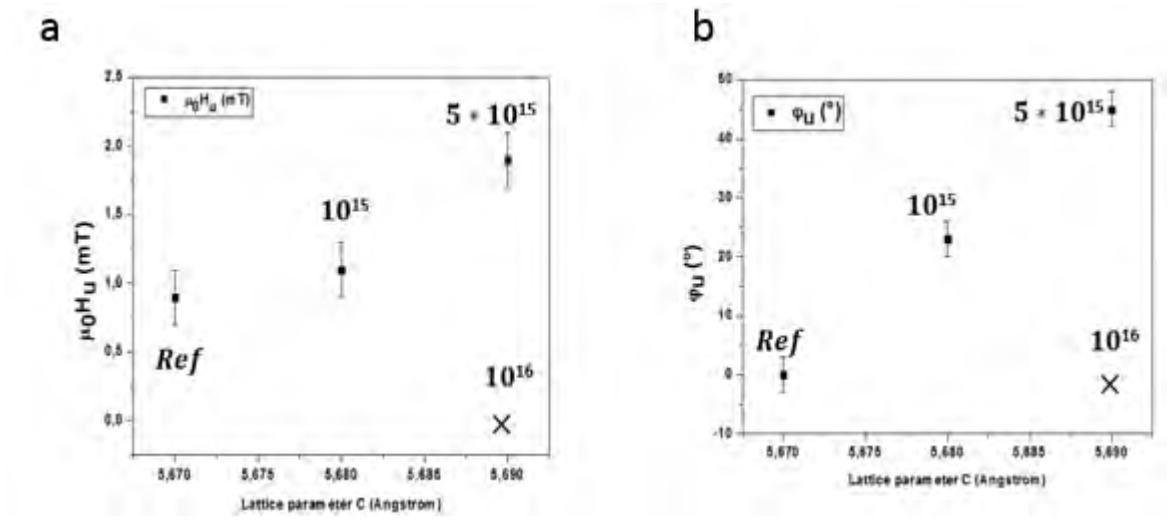

Figure 21: Evolution de l'amplitude de l'anisotropie uni-axiale $\mu_0 H_u$ (a) et de son orientation par rapport à l'axe facile φ_u (b) en fonction du paramètre du réseau hors plan.

Enfin la dernière partie de notre étude a porté sur l'étude de la largeur de raie dynamique en fonction du désordre cristallin.

La largeur de raie dynamique est particulièrement importante d'un point de vue technologique puisqu'elle représente les pertes d''énergie. Ceci est particulièrement important par exemple pour des applications de type guides d'ondes micro-ondes ou pour des systèmes en spintronique à base de transfert de spins. Théoriquement le coefficient de relaxation intrinsèque α a été calculé à $0{,}6*10^{-4}$. Cependant expérimentalement la valeur la plus proche récemment rapportée est de $7 * 10^{-4}$ [17 Andrieu].

L'évolution de la largeur de raie ΔH pour les pics $L2_1$ et B2 dans l'échantillon de référence sont présentés dans la figure 22. Ici nous ne présentons les résultats que dans le cas où les deux pics sont bien distincts. La dépendance en fréquence de la largeur de raie est généralement écrite sous la forme

$$.\Delta H = \frac{2\pi f \alpha}{\gamma} + \Delta H_0,$$

Avec α le coefficient de relaxation de Gilbert (intrinsèque) et ΔH_0 les pertes extrinsèques. Nous observons que la pente, et donc la valeur de α, est la même pour les directions faciles et difficiles, nous observons une différence de la contribution extrinsèque. Ce résultat n'est pas clair mais il se peut qu'il soit relié à l'orientation des plans de dislocations dans le MgO permettant de relaxer le CMS. Nous observons également que la valeur du coefficient de relaxation est plus faible pour la phase $L2_1$ en accord avec les prédictions théoriques. De plus la valeur obtenue dans la phase $L2_1$ est une des meilleures reportées jusqu'ici dans la littérature.

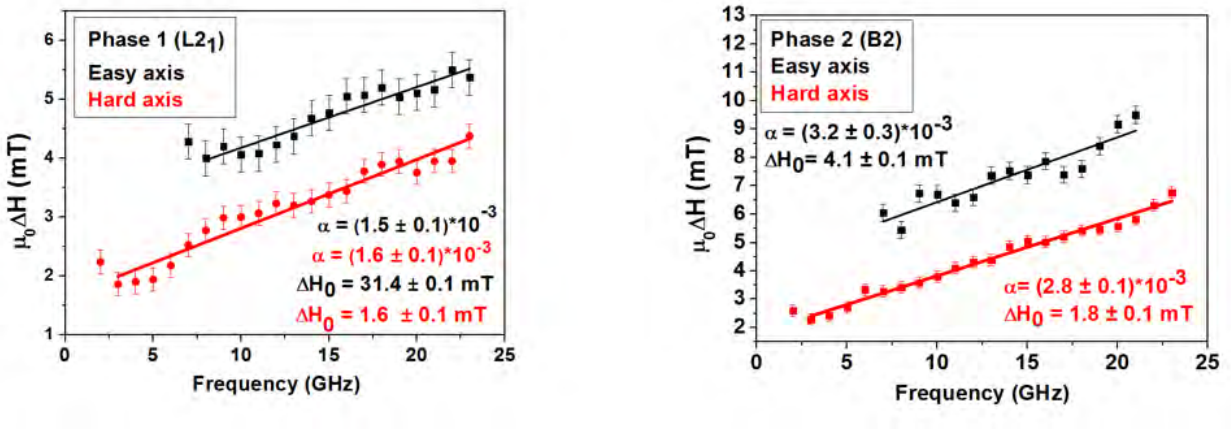

Fgure 22 : Largeur de raie en fonction de la fréquence pour un champ appliqué le long des axes faciles et difficiles pour les deux phases observée $L2_1$ (gauche) et B2 (droite) pour l'échantillon de référence.

L'évolution de la largeur de raie pour chaque phase en fonction de la fluence est présentée sur les figures 23 et 24. Dans le cas de la phase $L2_1$ nous observons clairement une augmentation de α avec la fluence, et donc du désordre. Ici peut s'expliquer par la présence des états de spins minoritaires calculés par Piccozzi et al. En effet, ces derniers permettent une diffusion inter bandes avec retournement du spin augmentant ainsi le coefficient de relaxation (dans le modèle de Kamberski du la relaxation dans les métaux ferromagnétiques [18, 19 Kamberski]). Pour la phase B2 en revanche nous n'observons pas de variation de α, ce qui est en bon accord avec l'hypothèse initiale qu'aucun désordre chimique autre que Mn/Si (donc B2) n'apparait dans les zones de type B2. Cependant nous observons une variation importante des contributions extrinsèques. A faible fluence celles-ci diminuent. Une explication possible est l'effet de recuit local apparaissant avec l'irradiation, ce qui peut entrainer une augmentation du paramètre d'ordre longue portée dans les zones B2 [20 Gaier]. En revanche, à plus forte fluence les contributions extrinsèques augmentent fortement en raison de la création de défauts de structure, en accord avec les simulations IPROS.

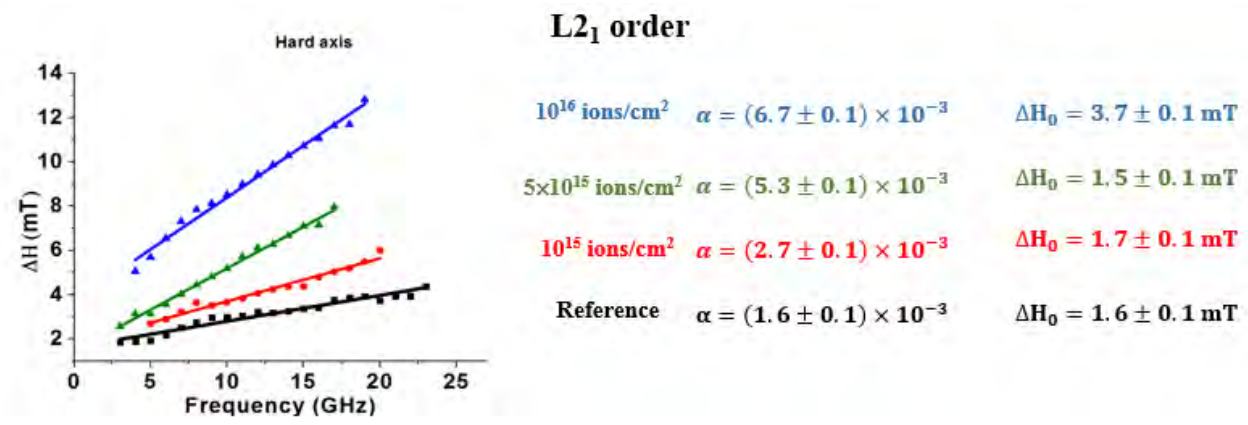

Figure 23: Evolution avec la fluence de la largeur de raie pour la phase $L2_1$ pour un champ appliqué dans une direction de difficile aimantation.

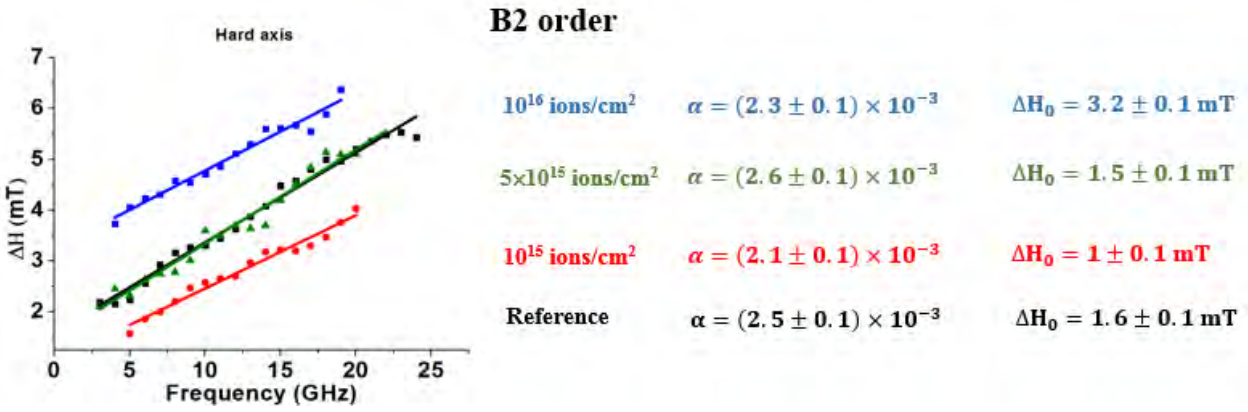

Figure 24: Evolution avec la fluence de la largeur de raie pour la phase B2 pour un champ appliqué dans une direction de difficile aimantation.

En conclusion de ce travail:

La caractérisation complète des propriétés du Co_2MnSi implique à la fois la caractérisation structurale et magnétique du matériau.

Intérêt pour la science des matériaux:

• l'échange Mn/Si ne semble avoir aucun impact sur les propriétés magnétiques statiques mais la valeur du facteur d'amortissement est plus élevée que pour la phase ordonnée $L2_1$.

• L'irradiation aux ions He^+ favorise la phase B2: cette technique peut ainsi s'avérer complémentaire des techniques de recuit dans certains procédés industriels

• l'échange Co/Mn affecte considérablement les paramètres magnétiques statiques et dynamiques, de manière plus importante que ce que des calculs ab-initio laissent prévoir. Les résultats préliminaires sur l'échange Co/Si semble similaire à l'effet de Co/Mn.

• la déformation tétragonale induit dans le plan une anisotropie uni-axiale. Ceci pose la question de la validité de notre approche pour d'autres métaux ferromagnétiques.

• Les résultats préliminaires sur la relaxation dynamique:

• Meilleur amortissement observé dans l'ordre $L2_1$ ($1.5*10^{-3}$).

• Amélioration de la largeur de raie pour la phase B2 à faible fluence.

• L'anisotropie de la largeur de raie est démontrée, mais l'anisotropie du coefficient de relaxation ne peut pas être statuée en l'état

References:

[1] F. Heusler, W. Starck, and E. Haupt, Verh. DPG 5, 220 (1903)."

[2] R. A. De Groot, F. M. Mueller, P. G. Van Engen, et K. H. J. Buschow, « New class of materials: half-metallic ferromagnets », *Phys. Rev. Lett.*, vol. 50, nº 25, p. 2024–2027, 1983.

[3] C. Liu, C. K. A. Mewes, M. Chshiev, T. Mewes, et W. H. Butler, « Origin of low Gilbert damping in half metals », *Appl. Phys. Lett.*, vol. 95, nº 2, p. 022509, 2009.

[4] G. E. Bacon et J. S. Plant, « Chemical ordering in Heusler alloys with the general formula A2BC or ABC », *J. Phys. F Met. Phys.*, vol. 1, nº 4, p. 524, juill. 1971.

[5] P. J. Webster, « Magnetic and chemical order in Heusler alloys containing cobalt and manganese », *J. Phys. Chem. Solids*, vol. 32, nº 6, p. 1221‑1231, 1971.

[6] S. Trudel, O. Gaier, J. Hamrle, et B. Hillebrands, « Magnetic anisotropy, exchange and damping in cobalt-based full-Heusler compounds: an experimental review », *J. Phys. Appl. Phys.*, vol. 43, nº 19, p. 193001, mai 2010.

[7] S. Picozzi, A. Continenza, et A. J. Freeman, « Co 2 Mn X (X = Si , Ge, Sn) Heusler compounds: An *ab initio* study of their structural, electronic, and magnetic properties at zero and elevated pressure », *Phys. Rev. B*, vol. 66, nº 9, sept. 2002.

[8] V. Niculescu, K. Raj, T. J. Burch, et J. I. Budnick, « Correlation of the internal fields, magnetic moments, and site preferences in Fe 3- x Mn x Si alloys », *Phys. Rev. B*, vol. 13, nº 7, p. 3167, 1976.

[9] Y. Takamura, R. Nakane, et S. Sugahara, « Analysis of L21-ordering in full-Heusler Co2FeSi alloy thin films formed by rapid thermal annealing », *J. Appl. Phys.*, vol. 105, nº 7, p. 07B109, avr. 2009.

[10] I. Galanakis, P. H. Dederichs, et N. Papanikolaou, « Slater-Pauling behavior and origin of the half-metallicity of the full-Heusler alloys », *Phys. Rev. B*, vol. 66, nº 17, p. 174429, nov. 2002.

[11] G. Ortiz Hernandez, « Elaboration et étude des propriétés physiques de couches minces monocristallines d'alliage de Heusler à faible amortissement magnétique pour composants hyperfréquences », Université de Toulouse, Université Toulouse III-Paul Sabatier, 2013.

[12] L. Ritchie, G. Xiao, Y. Ji, T. Y. Chen, C. L. Chien, M. Zhang, J. Chen, Z. Liu, G. Wu, et X. X. Zhang, « Magnetic, structural, and transport properties of the Heusler alloys Co 2 MnSi and NiMnSb », *Phys. Rev. B*, vol. 68, nº 10, sept. 2003.

[13] J. Hamrle, O. Gaier, S.-G. Min, B. Hillebrands, Y. Sakuraba, et Y. Ando, « Determination of exchange constants of Heusler compounds by Brillouin light scattering spectroscopy: application to Co2MnSi », *J. Phys. Appl. Phys.*, vol. 42, nº 8, p. 084005, avr. 2009.

[14] H. Pandey, P. C. Joshi, R. P. Pant, R. Prasad, S. Auluck, et R. C. Budhani, « Evolution of ferromagnetic and spin-wave resonances with crystalline order in thin films of full-Heusler alloy Co2MnSi », *J. Appl. Phys.*, vol. 111, nº 2, p. 023912, janv. 2012.

[15] S. Picozzi, A. Continenza, et A. Freeman, « Role of structural defects on the half-metallic character of Co2MnGe and Co2MnSi Heusler alloys », *Phys. Rev. B*, vol. 69, nº 9, mars 2004.

[16] P. Bruno, « Physical origins and theoretical models of magnetic anisotropy », in *Ferienkurse des Forschungszentrums Julich*, 1993.

[17] S. Andrieu, A. Neggache, T. Hauet, T. Devolder, A. Hallal, M. Chshiev, A. M. Bataille, P. Le Fèvre, et F. Bertran, « Direct evidence for minority spin gap in the $\mathrm{C}{\mathrm{o}}_{2}\mathrm{MnSi}$ Heusler compound », *Phys. Rev. B*, vol. 93, nº 9, p. 094417, mars 2016.

[18] V. Kamberskỳ, « On ferromagnetic resonance damping in metals », *Czechoslov. J. Phys. B*, vol. 26, nº 12, p. 1366–1383, 1976.

[19] V. Kamberský, « Spin-orbital Gilbert damping in common magnetic metals », *Phys. Rev. B*, vol. 76, n° 13, oct. 2007.

[20] O. Gaier, J. Hamrle, S. J. Hermsdoerfer, H. Schultheiß, B. Hillebrands, Y. Sakuraba, M. Oogane, et Y. Ando, « Influence of the L21 ordering degree on the magnetic properties of Co2MnSi Heusler films », *J. Appl. Phys.*, vol. 103, n° 10, p. 103910, may 2008.